

Editors:

Lori Tamura Arthur L. Robinson Elizabeth Moxon

Editorial Assistance:

Molly Stoufer

Design, layout, photography:

Berkeley Lab's Technical and Electronic Information Department (TEID) Creative Services

The editors gratefully acknowledge the ALS users and staff for their contributions, advice, and patience.

Available to DOE and DOE Contractors from the Office of Scientific and Technical Communication, P.O. Box 62, Oak Ridge, TN 37831. Prices available from (615) 576-8401.

Available to the public from the National Technical Information Service, U.S. Department of Commerce, 5285 Port Royal Road, Springfield, VA 22161.

Ernest Orlando Lawrence Berkeley National Laboratory is an equal opportunity employer.

Disclaimer

This document was prepared as an account of work sponsored by the United States Government. While this document is believed to contain correct information, neither the United States Government nor any agency thereof, nor The Regents of the University of California, nor any of their employees, makes any warranty, express or implied, or assumes any legal responsibility for the accuracy, completeness, or usefulness of any information, apparatus, product, or process disclosed, or represents that its use would not infringe privately owned rights. Reference herein to any specific commercial product, process, or service by its trade name, trademark, manufacturer, or otherwise, does not necessarily constitute or imply its endorsement, recommendation, or favoring by the United States Government or any agency thereof, or The Regents of the University of California. The views and opinions of authors expressed herein do not necessarily state or reflect those of the United States Government or any agency thereof, or The Regents of the University of California.



This work was supported by the Director, Office of Science, Office of Basic Energy Sciences, Materials Sciences Division, of the U.S. Department of Energy under Contract No. DE-AC03-76SF00098.

Contents

Welcome from the Directoratev			
ote from the UEC Chairv.			
Science Highlightsx			
Feature: Nanomagnetism Up Closex			
Condensed Matter Physicsx			
Materials Sciencex			
Environmental and Earth Sciencex			
Structural Biologyx			
Atomic and Molecular Sciencex			
New X-Ray Techniquesx			
Facility Reportx			
Feature: Reflections on the ALSx			
Operationsx			
Accelerator Physicsx			
Experimental Systemsx			
Scientific Supportx			
User Servicesx			
Special Eventsx			
About the ALS			
ALS Advisory Panelsx			
ALS Staffx			
Facts and Figuresx			
2003 Publicationsx			

Jim Krupnick, Division Deputy for Planning; Ben Feinberg, Division Deputy for Operations; and Neville Smith, Division Deputy for Science.



Welcome from the Directorate

We welcome you to this 2003 edition of the Advanced Light Source (ALS) Activity Report. We hope that you enjoy reading it and that you will send us your comments. The ALS has had another successful year in providing a reliable, high-quality beam, and our users have continued to generate outstanding science, a sampling of which will be presented in the following pages. The number of users surpassed 1600 in 2003 and will likely exceed 2000 in a few years.

The present and near future of the ALS appear to be on a steady course, so the activities of the management have turned increasingly toward strategic planning. Three events in 2003 serve to illustrate our situation and current thinking.

First, we were asked to participate in the formulation of a 20-year roadmap for major Department of Energy (DOE) facilities. At a meeting in February of a specially formed subcommittee of the DOE's Basic Energy Sciences Advisory Committee (BESAC), Neville Smith, Division Deputy for Science, presented a vision for an upgrade that would keep the ALS at the cutting edge for several decades. This plan was enthusiastically received, and progress on its first phase, conversion to "top-off" operation, is already underway. At the same meeting, ALS staff member Mike Martin made a pitch for a coherent infrared center (CIRCE), a small storage ring that would provide extremely intense terahertz radiation. This proposal was very well received by the subcommittee, which recommended that a national consensus for such a facility first be established. The subcommittee arrived at a similar conclusion for the visionary and farsighted proposal for a linac-based ultrafast x-ray source (LUX) presented by Berkeley Lab scientists Steve Leone and John Corlett.

The second event was the funding by the DOE of an meV-resolution beamline (MERLIN). With this event, all available straight sections at the ALS are now either built out, under construction, or funded. The only

WELCOME FROM

THE DIRECTORATE

avenue for further development of the straight sections is to go around the ring progressively retiring the older insertion devices and replacing them, based on well-defined strategic goals, with more advanced, application-specific, half-length insertion devices that allow two beamlines where previously there was only one. Some liken this never-ending process to continuously repainting the Golden Gate Bridge. We prefer the expression that ALS Director Daniel Chemla learned on the streets of Paris in 1968: "permanent revolution."

The third event was the celebration in October of our tenth year of operation. In a special session at our Users' Meeting, David Attwood (the first ALS Scientific Director) and Jay Marx (ALS Director during the construction period) offered a riveting, and often humorous, account of the early struggles in establishing the credentials of the ALS and the challenges of building such an exquisite machine. The proof of the pudding, as they say, is in the eating. With a decade of excellent accomplishment behind us, we look forward, through a well-thought-out upgrade strategy, to remaining at the cutting edge for several more decades.

A note concerning ALS Director Daniel Chemla

On December 15, 2003, ALS Director Daniel Chemla was admitted to the University of California (UC) San Francisco hospital for surgery to remove an arteriovenous malformation in his cerebellum. The best prognosis at the time was that he would be in intensive care for four to five days and then be home for the holidays. However, because of the need for a second operation and other complications, he was not released from intensive care until January 6,

2004. After a couple of months of rehabilitation, he returned home on March 19, 2004, where, as of this writing, he is slowly regaining his strength. While we all look forward to his return to the ALS, it will not be for some time. In the meantime, his responsibilities, including the preparation of this introduction, are being shared by his three deputies, Ben Feinberg, Jim Krupnick, and Neville Smith, who are moving forward in implementing the agenda that Daniel has very clearly laid out for 2004.



ALS Director Daniel Chemla addressed the crowd assembled for the opening session of the 2003 Users' Meeting.



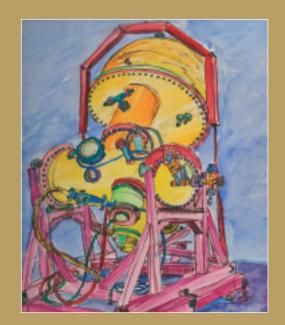
Jennifer Doudna, UEC Chair for 2003.

Note from the UEC Chair

During the past year it has been my pleasure to serve the ALS user community as Chair of the Users' Executive Committee (UEC). The UEC represents the 1600+ users of the ALS in a variety of venues, including discussions with ALS management, the wider scientific and lay communities, and DOE leadership. Issues of ongoing importance to users, including facilities access, housing and support, and planning for the future of the ALS, as well as the immediate needs of particular user groups, were addressed in meetings with ALS management and staff and through continual informal discussions. Exciting progress occurred in several areas, thanks to the hard work of users and the staff and managers at both the ALS and DOE.

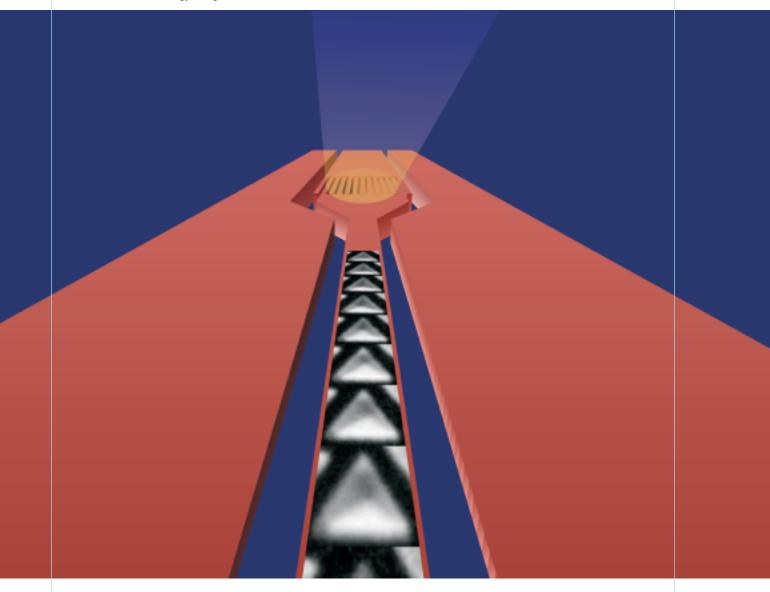
Several developments at the ALS over the past year are particularly exciting for users. The planned ALS upgrades, conceived and designed over many months, will provide for continuous injection of beam into the storage ring and enhanced beamline capabilities. These improvements should maintain the ALS as a cutting-edge research facility into the foreseeable future, enabling users to more efficiently conduct ongoing research as well as undertake new kinds of experiments. In addition, the planned new user support building will replace the current Building 10 adjacent to the ALS and provide much-needed experimental and office space along with seminar and meeting rooms. Plans are also in the works for new facilities to provide low-cost short- and medium-term housing for visiting ALS users. These projects are the outcome of hard work by Daniel, Neville, Ben, the ALS group leaders, and others at the ALS, together with user input and financial support from the DOE. Many thanks to these talented and dedicated people!

The ALS Users' Meeting last October, organized by UEC members Gerry McDermott and Eli Rotenberg, celebrated the tenth anniversary of the ALS. As we look ahead to the next ten years, users will be called upon to work closely with the ALS management to develop and implement a shared vision for maintaining the ALS as a world-class scientific research facility. It will continue to be essential that we as a community communicate our needs and our achievements to the public and our representatives in Washington. Thanks for your support of the ALS, and as always, please contact me or any UEC member with your ideas for the ALS.



SCIENCE HIGHLIGHTS

Picosecond movie of a gyrating vortex.



Nanomagnetism Up Close

X-Ray Photoemission Electron Microscopy Looks at Exchange Bias

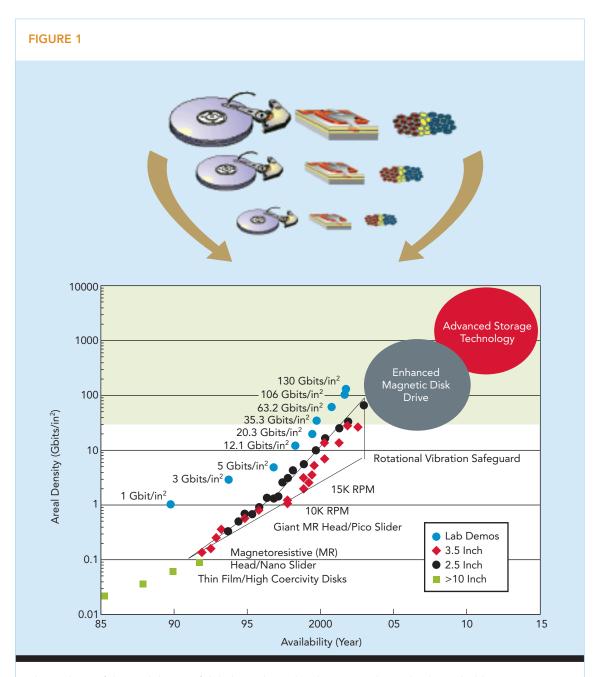
Andreas Scholl, Experimental Systems Group

Any desktop or laptop computer user knows how fast the storage capacity of hard disks is growing. Within just the last ten years, the areal density of magnetic disk drives has jumped by a factor of 1000 from 50 Mbits/in² to the current state of the art, 50 Gbits/in². The storage density now doubles every 12 months, significantly faster than that of semiconductor memory (D-RAM), which according to the famous Moore's Law doubles every 18 months (Figure 1). During the same period, the data rate, which limits the speed of a

disk drive, increased from 50 MHz to 1 GHz. To maintain this pace, we require new tools to study magnetic materials on smaller length and shorter time scales. At the ALS, we have been developing x-ray microscopes that can image the nanoscale magnetic bits on hard disks, thereby allowing researchers to both understand the basic properties of magnetic media and examine

the data-reading and -writing processes in space and in time.

X-ray photoemission electron microscopy (X-PEEM) unites the attributes of two techniques that are formidable in their own right: high-resolution electron microscopy and sensitive x-ray spectroscopy. X-PEEM is a spectromicroscopy tool that is applicable not only to



SCIENCE HIGHLIGHTS

NANOMAGNETISM UP CLOSE 3

The roadmap of the areal density of disk drives shows that the storage density has been doubling every 12 months, owing to progress in the disk, head, and media (adapted from Hitachi Global Storage Technologies).

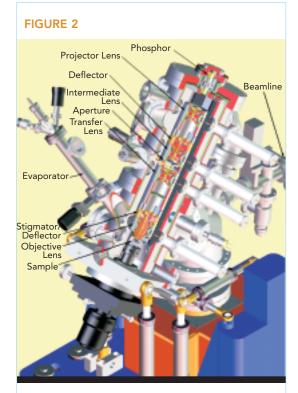
magnetic structures, such as bits and regions where magnetic moments are aligned (domains), but also to the chemical and elemental composition of the sample. X rays produced by the ALS, one of the brightest x-ray sources of the world, illuminate the sample, resulting in a photoelectron image that is then magnified a thousandfold by the optics of the microscope (Figure 2). An electronic (CCD) camera digitizes this magnified image for processing and analysis.

So far, two generations of x-ray photoemission electron microscopes have operated at the ALS, but we are working on the third. Succeeding its predecessor PRISM in 1998, the second-generation microscope, PEEM-2 was designed and built at the ALS with much-improved electron optics and an angle- and energy-selecting aperture and is now in successful operation on Beamline 7.3.1.1 with a spatial resolution around 50 nm for magnetic structures. It will be surpassed in the coming years by a much more powerful PEEM-3 instrument (see "PEEM-3 Is the Next-Generation Microscope"), now in the design and engineering stage, on a

SCIENCE HIGHLIGHTS

NANOMAGNETISM UP CLOSE

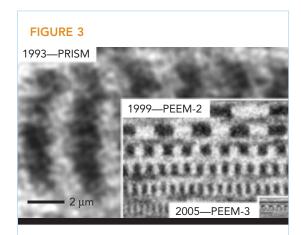
4



Schematic of the PEEM-2 microscope of the ALS.

beamline with an elliptically polarizing undulator (EPU). The increase in resolution by a factor of 10 between generations is instrumental in allowing researchers to keep pace with the rapid reduction of the bit size in disk drives, as Figure 3 shows.

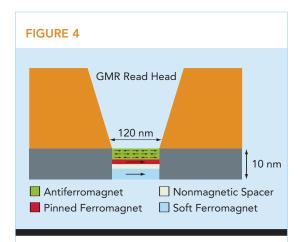
The read head in a disk drive is responsible for converting the magnetic field of a data bit into an electric signal. Today's disk drives use nanoscale, giant-magnetoresistance (GMR)



Images of magnetic bits written on a hard disk from three generations of PEEM experiments at similar magnification. The PRISM and PEEM-2 pictures are actual images; the PEEM-3 picture is simulated to demonstrate the expected improvement in resolution. The pictures also show the increase in storage density since 1993.

heads, which utilize the change in resistance of a stack of magnetic layers that occurs when the magnetization in one ferromagnetic layer is rotated parallel or antiparallel relative to the other layer (Figure 4). An important component in such magnetoelectronic devices is an antiferromagnetic layer that, while itself insensitive to external fields, can pin the magnetization of one of the ferromagnetic layers, which then acts as a magnetization reference. This pinning phenomenon is called exchange bias.

An antiferromagnet has microscopic magnetic moments that point in opposite directions, so that the macroscopic magnetization exactly vanishes. The domain structure (defined by the



Elevation view of a modern GMR read head. The sensor consists of two ferromagnetic layers separated by a nonmagnetic spacer. One of the ferromagnets is exchange biased by an antiferromagnet.

direction of the antiparallel microscopic moments) of antiferromagnetic layers and the mechanism that enables them to pin the magnetization of ferromagnets were unknown for decades, despite the technological importance of the exchangebias effect. One reason was the inability of ordinary imaging techniques to detect the magnetic structure at the interface between the ferromagnet and the antiferromagnet.

Dichroism, a difference in absorption or other optical property that appears when polarized electromagnetic radiation passes through a chiral or anisotropic system, is well known in the

FIGURE 5

Ferromagnetic domain structure in cobalt (top) and antiferromagnetic domain structure in LaFeO₃ (bottom). Both layers are exchange coupled. The images were acquired using XMCD and XMLD, respectively.

visible spectrum. X-ray microscopes use similar effects that occur at x-ray photon energies to detect ferromagnetism and antiferromagnetism, thereby opening the door to the microscopic study of exchange bias. X-ray magnetic circular dichroism (XMCD) and x-ray magnetic linear dichroism (XMLD) depend, respectively, on the circularly and linearly polarized x rays available only from a synchrotron light source like the ALS.

Figure 5 shows X-PEEM images of micronsize magnetic domains in an antiferromagnetic thin film (lanthanum iron oxide, or LaFeO₃) and a ferromagnetic thin film (cobalt) that is magnetically coupled to the antiferromagnet. Different colors symbolize different directions of the magnetic moments. It is apparent from the images that the domain structures are coupled on microscopic length scales. The correspondence between the domain structures is a first indication that exchange bias has a microscopic origin.

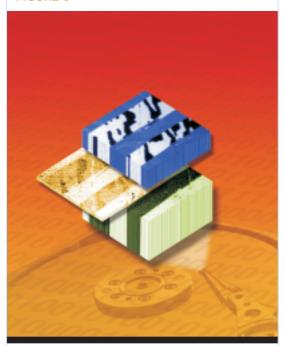
Nickel oxide (NiO) is known to possess good exchange-bias properties. When studied as a single crystal, large antiferromagnetic domains appear in X-PEEM images (Figure 6). A ferromagnetic cobalt layer, grown over the NiO by in-vacuum evaporation, exhibits ferromagnetic domains that are aligned with the magnetic domains in the antiferromagnet, very similar to what occurs in the Co/LaFeO₃ system. The mechanism of the coupling is revealed when the antiferromagnet is imaged with ferromagnetic (XMCD) contrast. Although an antiferromagnet should be nonmagnetic on macroscopic length scales, the image reveals ferromagnetic domains at its surface that mediate the coupling between the layers. These domains originate in a chemically reacted region less than a monolayer thick, which is only visible because of the high sensitivity and chemical specificity of x-ray spectromicroscopy.

Element-specific magnetization vs. applied field (hysteresis) loops measured at ALS Beamline 4.0.2, a high-brightness EPU beamline specifically designed for the study of magnetism with variably polarized light, demonstrate that the fer-

SCIENCE HIGHLIGHTS

NANOMAGNETISM UP CLOSE

FIGURE 6



Ferromagnetic structure of nickel interface spins (yellow) sandwiched between the antiferromagnet nickel oxide (green) and the ferromagnet cobalt (blue). The uncompensated spins at the surface of the antiferromagnet mediate the coupling of the ferromagnet to the antiferromagnet.

SCIENCE HIGHLIGHTS

NANOMAGNETISM UP CLOSE

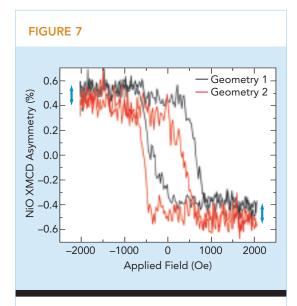
6

romagnetic signal of the antiferromagnet is due to the presence of uncompensated spins. Most of these spins rotate with an externally applied field, but a tiny fraction is pinned, as revealed by the small vertical shift of the loops (Figure 7). These pinned spins exert a magnetic force on the ferromagnet and are ultimately responsible for the exchange-bias effect. (See "Pinning Down Exchange Bias" in the Materials Science section for more detail about this result.)

The data rate in modern disk drives will soon surpass 1 GHz. At lower frequencies, the response of a magnet is governed by magnetic friction, also called damping, as the magnetic moments rotate into the direction of the applied field. At gigahertz frequencies and above, magnetization precession, a gyroscopic motion of the magnetization around an applied field (like a wobbling top), is dominant. Subnanosecond magnetic-field pulses like those of a write head therefore

initiate magnetization precession. To study such fast processes, we have developed a novel technique that utilizes the pulsed nature of x rays produced by synchrotron light sources. The 70-ps x-ray pulses of the ALS can be used like light flashes from a strobe to freeze the dynamics of a sample and to acquire a snapshot of the motion of the magnetization.

Figure 8 shows a new experiment that we developed for the microscopic study of ultrafast magnetization dynamics. A light flash from a laser activates a gallium arsenide photo switch,



Magnetic hysteresis loops of uncompensated spins at the interface between cobalt and nickel oxide. The vertical shift (blue arrows) between the loops is due to pinned spins.

which is integrated into the sample, and launches a 300-ps electrical current pulse into a waveguide (a wire that is optimized for the transmission of short pulses). The current pulse generates a short, strong magnetic field, initiating the dynamics of the magnet. After a controllable delay, an x-ray pulse illuminates the sample, generating a photoelectron image of the current state of the magnetization of the sample in the photoemission electron microscope. The CCD

PEEM-3 IS THE NEXT-GENERATION MICROSCOPE

Jun Feng, Experimental Systems Group

X-PEEM combines the power of modern synchrotron radiation absorption spectroscopy with the full-field imaging capability of a photoemission electron microscope (see "Nanomagnetism Up Close"). Existing microscopes, such as PEEM-2 at the ALS, routinely operate with a typical resolution of 50–100 nm with an electron transmission of 2–5%. However, a higher spatial resolution and a larger electron transmission are critical for many areas of nanoscience research. Design of a new aberration-corrected photoemission electron microscope, PEEM-3, is now underway at the ALS, with the goal of achieving higher transmission and 10 times higher resolution than our present PEEM-2 instrument.

A conventional X-PEEM system consists of electron lenses, the resolution of which is limited by spherical and chromatic aberrations. In contrast to light optics, the signs of the aberrations of electron lenses cannot be changed. Therefore, image errors in an electron optical system cannot be eliminated as in an optical achromat by using pairs of lenses with opposite aberrations; they can only be minimized by adjusting the geometry of the electrodes and, in the process, sacrificing the electron-beam transmission. However, an electron mirror can have aberrations of opposite sign but equal magnitude with respect to those of electron lenses, so that, in principle, the aberrations can be canceled out and the resolution can be improved, ultimately to the diffraction limit.

The critical components of PEEM-3 are the aberration-free magnetic beam separator and the electron-mirror aberration corrector (Figure 1). The beam separator produces a magnetic dipole field to bend the electron beam by 90 degrees in order to separate the corrected electron beam from the uncorrected beam, direct it to the mirror, and transfer it back to the projector column. The electron mirror has four rotationally symmetric electrodes. One electrode

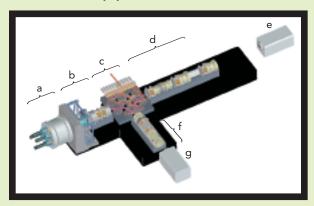


FIGURE 1

Schematic layout of the aberration-corrected x-ray photoemission electron microscope PEEM-3 at the ALS; sample manipulator (a), objective (b), beam separator (c), transfer and projector optics (d), imaging CCD (e), electron-mirror column (f), and diagnostic CCD (g).

resides at ground voltage, while the potentials of the other three electrodes serve as three free "knobs" for adjusting the focal length, chromatic aberration, and spherical aberration of the mirror. The reflecting electrode has a complex, spherical shape to counter the aberrations of the electron lenses.

A key aspect of the design is the mechanical layout. All components—the sample manipulator, the electron lenses, and the separator—are mounted on a common internal, highly stable reference plate. This arrangement allows us to achieve the stability we need, not only for good resolution in single images but also for multiple images over minutes or even hours, as in pump–probe time-resolved experiments or in collecting a set of images at different photon energies for spectroscopy.

The comparison of calculated resolution versus transmission for PEEM-2 and PEEM-3 is shown in Figure 2. Operating PEEM-3 at a voltage of 20 kV yields a point resolution of 50 nm at better than 90% transmission with the mirror corrector. The best resolution that can be achieved is 5 nm at 2% transmission, as opposed to 20 nm at 1% transmission in an ideal PEEM-2. We have designed the system to be flexible and upgradable. For example, an electronenergy filter could be added at a later date, if scientific need drives a further improvement in the resolution. Since the energy filter collects only electrons at selected kinetic energies, the filter would also make it possible to conduct spatially resolved photoemission spectroscopy experiments.

PEEM-3 will be installed on EPU Beamline 11.0.1 (also under construction) and will be used for the study of complex materials at high spatial and spectral resolution. The EPU can produce linearly polarized light of arbitrary orientation, from horizontal to vertical and left- and right-handed circularly polarized radiation with a continuous range of ellipticity. A variable-line-spacing (VLS) plane-grating monochromator will provide soft x rays in the spectral range from 100–1500 eV.

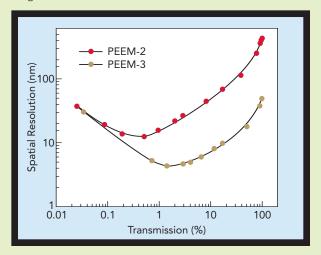


FIGURE 2

Comparison of resolution vs. transmission for PEEM-2 and PEEM-3.

SCIENCE

HIGHLIGHTS

NANOMAGNETISM UP CLOSE

Probe X-Ray Pulse Electrons Electrons 8 ns

Top: Laser pulses (red) generate a current pulse, resulting in a magnetic field that initiates the magnetization dynamics. Bottom: X-ray pulses (blue) probe the sample after a delay Δt . The electron image is detected by the photoemission electron microscope.

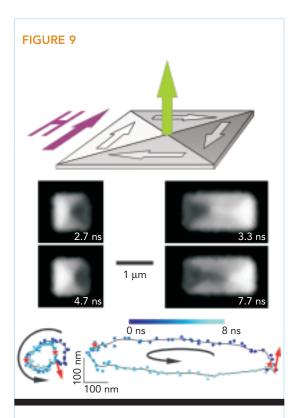
camera accumulates the signal from millions of x-ray pulses until an image of sufficient quality has been obtained.

We have applied this new technique to the study of the dynamics of magnetic vortices, peculiar magnetic structures that appear in micron-size magnetic patterns (Figure 9). The magnetization of a vortex curls around the vortex center or core, which itself has an out-of-plane magnetization. When studied by the time-resolved PEEM technique, images acquired at different times after the excitation field pulse resolve the motion of the vortex core in response to the field pulse. The gyrating trajectory of the core demonstrates that the domain motion on such short time scales is indeed governed by precession and not by friction.

With PEEM-3 and the future possibility of subpicosecond x-ray pulses, there is every chance that the future of nanomagnetism at the ALS is bright, indeed.

PUBLICATIONS

- J. Stöhr, et al., "Element-specific magnetic microscopy with circularly polarized x-rays," *Science* **259**, 658 (1993).
- S. Anders, et al., "Photoemission electron microscope for the study of magnetic materials," *Rev. Sci. Instrum.* **70**, 3973 (1999).
- A. Scholl, et al., "Observation of antiferromagnetic domains in epitaxial thin films," *Science* **287**, 1014 (2000).
- F. Nolting, et al., "Direct observation of the alignment of ferromagnetic spins by antiferromagnetic spins," *Nature* **405**, 767 (2000).
- H. Ohldag, et al., "Spin reorientation at the antiferromagnetic NiO(001) surface in response to an adjacent ferromagnet," *Phys. Rev. Lett.* **86**, 2878 (2001).
- H. Ohldag, et al., "Spectroscopic identification and direct imaging of interfacial magnetic spins," *Phys. Rev. Lett.* **87**, 247201 (2001).
- H. Ohldag, et al., "Correlation between exchange bias and pinned interfacial spins," *Phys. Rev. Lett.* **91**, 7203 (2003).
- S.B. Choe, et al., "Vortex-driven magnetization dynamics," *Science* **304**, 420 (2004).



Top: Domain structure of a magnetic vortex. Arrows symbolize the direction of the magnetization. Center: Time-resolved PEEM images of a square $(1\times 1 \text{ mm}^2)$ and a rectangular $(2\times 1 \text{ mm}^2)$ vortex pattern. Bottom: The trajectory of the gyrating vortex core is shown as function of elapsed time after the driving field pulse.

CONDENSED MATTER PHYSICS

::

Early Kinetics of Nanoparticle Formation During Femtosecond Laser Ablation

The application of heat and pressure has for centuries been a favored technique for converting materials into more useful forms. The temperatures and pressures achieved in the smelting ovens of antiquity, however, pale in comparison to conditions achievable by heating with lasers. For example, material superheated by ultrashort pulses of laser light to well above its melting temperature will rapidly expel fragments from the surface. This ablation process is of considerable practical importance, since it is used to synthesize nanoparticles, which are the focus of one of today's scientific and technological frontiers, as well as other substances like biomolecules. However, ablation is complex, and significant uncertainties remain, in part because it is difficult to study the ejected matter separately from the surface just below. To hone in on the ejected matter, Glover et al. have developed an ultrafast version of a standard x-ray technique (photoemission spectroscopy) and have demonstrated its ability to study chemical and structural evolution during the early stages (a few trillionths of a second) of ablation.

Ultrashort pulses of laser light can rapidly heat matter to extreme temperature and pressure, thereby creating exotic states of matter of both fundamental and practical interest, such as nanoparticles. Recently, our team has succeeded in recording the chemical and structural evolution of ejecta from a silicon surface as the hot, pressurized material rapidly expanded into vacuum during the early stages immediately following impulsive superheating by an intense, ultra-

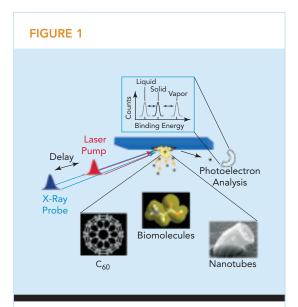
short laser pulse. The feat was made possible by developing a novel technique: ultrafast core-level photoemission spectroscopy. With foreseeable improvements in energy resolution (<< 1 eV) and time resolution (<< 1 ps), the technique will play an important role in unraveling the complex dynamics by which nanoparticles arise from an impulsively superheated material.

While direct probes with very good time resolution are essential to understanding and eventually controlling nanoparticle synthesis, development of such probes has proven difficult. Extreme initial heating implies rapid material evolution in which the ejecta undergo change while still within microns of the underlying, intact surface. Traditional ultrafast probes based on light scattering or absorption cannot separate ejecta dynamics from surface dynamics, since the light interacts with both the ejecta and the underlying surface. We have developed a high-timeresolution version of core-level photoemission spectroscopy by taking advantage of the recent synergy between intense femtosecond laser systems and high-brightness synchrotron light sources. Photoemission probes only the ejecta, since electrons escape from a layer of material thinner than the depth of material removed by ablation. As a further benefit, core-level spectroscopy offers local chemical information.

With so-called pump-probe techniques (Figure 1) at ALS Beamline 5.3.1, we have followed the early stages (0–1 ns) of the chemical and structural evolution of the silicon ejecta by observing shifts in a photoemission peak with picosecond time resolution. We observed that shortly after laser heating, the silicon 2p photoemission peak shifted to lower binding energy, a key to identifying the initial ejecta phase (Figure 2). The signature of single atoms in the vapor phase would be a shift to higher energy, while the observed low-energy shift indicates ejecta in

SCIENCE HIGHLIGHTS

CONDENSED MATTER PHYSICS



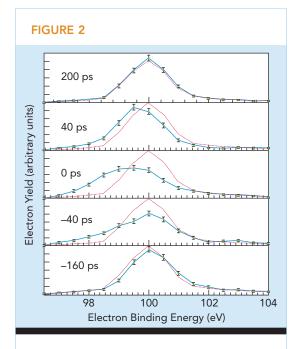
Laser-pump and x-ray-probe photoemission experiments to follow the chemical and structural dynamics of nanoparticle formation during short-pulse laser ablation. A femtosecond laser pulse, synchronized to the ALS storage ring, irradiates the silicon and initiates material ejection. An x-ray pulse whose arrival time relative to that of the laser pulse is controllable probes the ejecta by exciting silicon 2p photoelectrons that are recorded with an electron analyzer. The photoemission peak location varies with material phase (solid, liquid, or vapor), and time-dependent peak shifts reveal the transient shifts in the material phase.

liquid form. These findings suggest a highly inhomogeneous early phase of expansion in which the average density drops but the local density remains high, permitting the overlap of wave functions from neighboring atoms that characterizes a condensed phase.

Previous studies of silicon ejecta produced by long-pulse (nanosecond) laser ablation showed a very different initial ejecta composition in which isolated atoms and ions predominate, with clusters forming later (10–100 ns) by vapor condensation. We believe that isolated atoms and ions are produced after irradiation by long pulses because material is ejected while an intense laser field is still present, so that these particles are produced by secondary laser–ejecta interactions (ionization, etc.). By contrast, with ultrashort, femtosecond pulses, the laser field has decayed before material is ejected. The size distribution

of ejected particles is then determined by a material-fracture process driven by the local stresses associated with vacuum expansion (a process known as fragmentation).

Thus the initial ejecta composition suggests fundamentally different particle synthesis mechanisms for long as compared to short laser pulses: vapor condensation with long pulses and fragmentation with short pulses. The mean particle size in the femtosecond experiments is estimated to be > 1 nm, with better estimates expected from improved energy and time resolution. We further observed a rapid (< 50 ps) return of the photoemission peak (Figure 2), a signature of a liquid–solid phase transition that must have been driven by extreme undercooling to well below the solidification temperature during vac-



Temporal sequence of silicon 2p photoemission peak at specified pump–probe delays. A positive delay indicates x rays probing before arrival of the laser pump. A reference spectrum at +240 ps is shown (red). When pump and probe arrive "simultaneously" (i.e., within the x-ray pulse width of ~80 ps), photoemission peak distortion and a shift to lower binding energy (~1 eV) is observed. These peak modifications indicate that ejected material is in liquid form. The full sequence reflects the highly transient nature of the photoemission peak shift, indicating rapid (< 50 ps by deconvolution) solidification of ejected liquid droplets.

uum expansion. Extreme undercooling may prove useful as a way to "trap" novel material states associated with impulsive superheating.

INVESTIGATORS

T.E. Glover, G.D. Ackermann, P.A. Heimann, Z. Hussain, H.A. Padmore, and W.F. Steele (ALS); A. Belkacem, C. Ray, and R.W. Schoenlein (Berkeley Lab); and R.W. Lee and D.A. Young (Lawrence Livermore National Laboratory).

FUNDING

U.S. Department of Energy, Office of Basic Energy Sciences.

PUBLICATIONS

T.E. Glover et al., "Metal-insulator transitions in an expanding metallic fluid: Particle formation kinetics," *Phys. Rev. Lett.* **90**, 236102 (2003).

T.E. Glover et al., "Metal-insulator transitions in an expanding metallic fluid: Particle formation during femtosecond laser ablation," *Chem. Phys.* **299**, 171 (2004).

::

Nanodiamonds Show Buckyball Surface

Nanodiamonds—particles of diamond dust measured in nanometers—have been found in meteorites, protoplanetary nebulae, and interplanetary dust. On Earth, nanodiamonds can be produced by high-explosive detonation and chemical vapor deposition. Interest in laboratory-produced nanodiamonds has grown recently in proportion to their potential technological applications. As lightemitting semiconductors, nanodiamonds may be used in optoelectronic components that process both light and electricity. Diamond's hardness and fracture strength make it attractive for miniaturized mechanical devices such as cantilevers and gears. Diamond "nanodots" and "nanofilms," composed solely of carbon atoms, would be compatible with biological materials and may be used for neuronal imaging, integrating biological systems with electronic devices, or detecting biological or chemical warfare agents. All of these applications, however, depend on scientists' understanding of diamond's behavior at the nanoscale. In this research, Raty et al. report that, in fact, diamonds don't last forever: they begin to morph into buckyballs (at least on the surface) if broken up into small enough pieces.

Our team from the Lawrence Livermore National Laboratory has found that diamonds made of up to a few hundred carbon atoms do not exhibit the smooth, faceted surfaces commonly associated with crystals. Instead, at this scale, portions of the diamond's surface will spontaneously buckle into the curved, geodesic-dome structure found in buckyballs. We came to this surprising conclusion after performing ab initio calculations as well as x-ray absorption and emission experiments on nanodiamonds synthesized in detonation waves from high explosives. The discovery of this new family of carbon clusters, dubbed "bucky diamonds," may have implications for a wide range of areas, from astronomy, where diamonds are studied as a constituent of meteorites and interplanetary dust, to optoelectronics, where nanodiamonds might be used as photonic switches and tunable lasers.

Diamond, like silicon and germanium, is a semiconductor whose behavior depends on the size of its optical gap-the energy difference between its valence and conduction bands. At the nanometer scale, quantum confinement effects on electrons and holes typically result in a widening of the optical gap, which causes a blueshift in the material's absorption and emission peaks. Thus, a potentially useful property of nanosemiconductor particles is their ability to emit light at different wavelengths depending on particle size. Previous studies have demonstrated this effect for silicon and germanium particles as large as 7 nm in diameter. Our group extended these studies to nanodiamonds and found them to be unusual in both their electronic and geometric structure.

Using density functional theory and quantum

SCIENCE HIGHLIGHTS

CONDENSED MATTER PHYSICS

12

Monte Carlo calculations, we modeled the electronic structure of nanodiamond clusters. The results indicated that there is no appreciable quantum confinement effect on the optical gap of nanodiamonds until they get down to about 2 nm in diameter, contrary to what is found for silicon and germanium using the same theoretical tools. Geometrically, we found that as a nanodiamond gets smaller, its structure becomes unstable. Quantum simulations revealed graphitization of the first atomic layer, followed by the formation of pentagons linking the graphene fragments with the atoms underneath. This provided further curvature to the surface, which

The results of the calculations and simulations were consistent with x-ray emission and absorption spectra taken at ALS Beamline 8.0.1 and Stanford Synchrotron Radiation Laboratory. Emission and absorption spectroscopy together reveal the optical gap in semiconductors, with emission revealing the valence band maximum and absorption revealing the conduction band

eventually adopted a geometry similar to that of

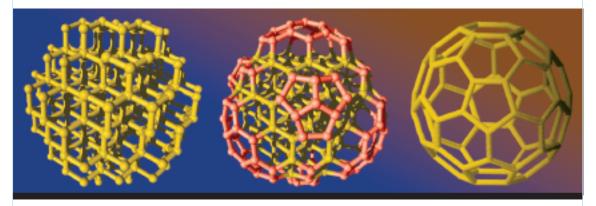
half a buckyball (Figure 3).

minimum. The techniques also reflect the density of states around the band gap—a sensitive fingerprint of atomic bonding configurations.

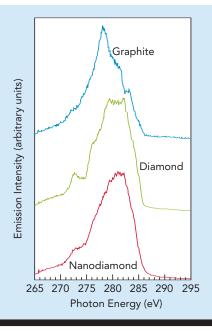
The sample nanodiamond sizes $(4 \pm 1 \text{ nm})$ and crystallinity were verified by electron diffraction and high-resolution transmission electron microscopy. The samples were also heated and cooled several times to remove impurities. The carbon K-edge emission and absorption spectra for nanodiamonds showed the same basic features as that of bulk diamond and graphite. In particular, we observed no blueshift in the position of the nanodiamond valence and conduction band edges in comparison to those of bulk diamond (Figure 4). Furthermore, the nanodiamond absorption spectra showed a pre-edge peak at 286.7 eV not observed in the bulk. Comparison to the density of unoccupied states derived for bucky diamond (Figure 5) suggests that the feature is the signature of the pentagonal and hexagonal bonding configurations found on buckyball-like surfaces.

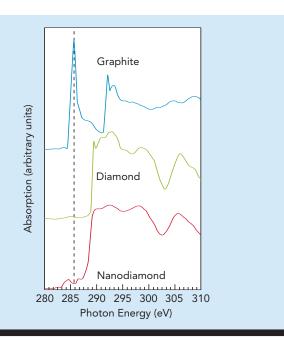
Interest in and funding for nanoscience has increased dramatically in recent years, reflecting

FIGURE 3



Left: Ball-and-stick representation of a 1.4-nm diamond with 275 atoms. Right: Representation of a classic 60-atom buckyball. Center: Representation of bucky diamond cluster with 275 atoms, 1.4 nm in diameter, showing diamond core (yellow) and a fullerenelike reconstructed surface (red).





Valence and conduction spectra of nanodiamond clusters compared to those of bulk diamond and graphite, as obtained using x-ray emission (left) and absorption (right) techniques, respectively. The energy scale of the absorption spectra was calibrated to the π resonance of highly oriented pyrolytic graphite, set to 285.38 eV.

> breakthroughs as well as practical applications. Studies such as this one are a necessary first step toward understanding the molecular building

the field's enormous potential for theoretical

blocks that will be utilized in the nanotechnologies of the future.

INVESTIGATORS

J.-Y. Raty (Lawrence Livermore National Laboratory and University of Liège, Belgium) and Galli, C. Bostedt, T.W. van Buuren, and L.J. Terminello (Lawrence Livermore National Laboratory).

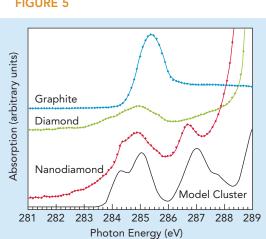
FUNDING

U.S. Department of Energy, Office of Basic Energy Sciences; Lawrence Livermore National Laboratory; and National Fund for Scientific Research, Belgium.

PUBLICATIONS

J.-Y. Raty et al., "Quantum confinement and fullerenelike surface reconstructions in nanodiamonds," Phys. Rev. Lett. 90, 037401 (2003).





Pre-edge peaks in nanodiamond absorption spectra (red) are compatible with the calculated signatures (black) of a mixture of pentagons and hexagons found on buckyball-like surfaces.

SCIENCE HIGHLIGHTS

CONDENSED MATTER PHYSICS

н

Buckyball Monolayer Electronic Structure

The energy scales of mobile electrons in solids are limited mainly by the difficulty of motion. In normal metals, the electrons move between atoms rather easily and reach a much higher energy than that associated with other motions, such as that of atomic vibrations. However, things are very different in solids composed of buckyballs, large carbon molecules discovered in 1985 and resembling American architect R. Buckminster Fuller's geodesic domes. Since it is very hard for electrons to hop between buckyballs, physicists expected the range of energies accessible to the mobile electrons (the conduction band width) to be small and even comparable to that of molecular vibrations of the buckyballs. However, a decade of intensive effort had not validated this expectation. Working at the ALS, Yang et al. have now provided the first direct experimental evidence for this conjecture, which not only relates to several questions of fundamental interest but may also lead to practical applications.

SCIENCE HIGHLIGHTS

CONDENSED MATTER PHYSICS

14

The 1980s witnessed the discovery of fullerenes, whose novel properties have been intensively studied by experiment and theory but remain incompletely understood. Among the fullerenes, for example, the solid formed from C₆₀ (buckyball) molecules exhibits superconductivity at the relatively high temperature of about 40 K when doped with alkali metal atoms (only the high-T_c cuprate superconductors have higher transition temperatures). Our international collaboration working at the ALS has now reported angle-resolved photoemission measurements of C₆₀ monolayers doped with potassium. We were able to detect, for the first time, both the band structure and a Fermi surface, two classical electronic structure features that surprisingly survive in the presence of the

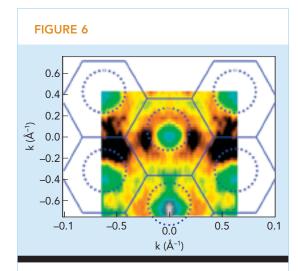
strong interactions in this material.

Condensed matter scientists agree that, as a molecular solid, doped C₆₀ (fullerides) should have a narrow band width. This feature combined with strong interactions, both between the electrons themselves (electron–electron) and between the electrons and the lattice vibration modes (electron–phonon), makes fullerides more challenging to study than other systems. Moreover, some even doubted whether a band dispersion of the type found in normal crystalline materials actually exists in fullerides because the strong interactions, whose energies are comparable to those of electrons, may disturb the electrons so much that bands could not form at all.

Electron–phonon interactions are of particular interest because they are a keystone of the theory that explains superconductivity in conventional metal superconductors. Whether high- T_c superconductivity in cuprates is due to electron–phonon interactions is still one of today's most interesting physics problems, but such interactions are also widely, if not universally, held to drive superconductivity in C_{60} compounds.

To study this interesting but complex physics in the C_{60} system, measurements of the energy band structure are of fundamental importance. Angle-resolved photoemission probes this structure directly by measuring the intensity, kinetic energy, and direction (momentum) of the photoelectrons excited by synchrotron radiation. However, after more than a decade of intense effort, direct observation of the momentum dependence (dispersion) of the electron bands remained elusive, owing to technical challenges imposed by both intrinsic features of the material and certain experimental effects.

Our collaboration was able to overcome these difficulties in our experiments on ALS Beamline 10.0.1, where we determined the Fermi surface (Figure 6) and band structure (Figures 7 and 8). The observed conduction band exhibits a small dispersion with an energy range of only 100 meV,

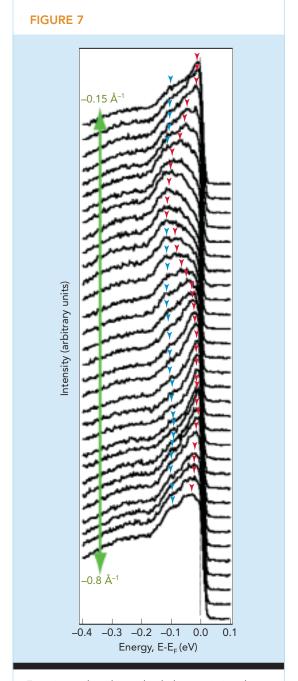


Buckyball Fermi surface. The hexagonal symmetry of the buckyball monolayer is reflected in the Fermi surface. Darker color indicates higher intensity. Blue lines are the Brillouin zone boundaries.

in sharp contrast to the 500-meV peak width seen in conventional angle-integrated photoemission spectra from the same conduction band. This substantial difference suggests the existence of strong interactions that broaden the peak width in photoelectron spectra but do not seem to affect the electronic structure, which exhibits a robust dispersion and classical Fermi surface.

We then turned to quantum mechanical calculations conducted at Berkeley Lab's National Energy Research Scientific Computing Center (NERSC). There, we calculated the band dispersion and compared the result to the experimental data. It turned out that the simulated band width was much larger than the experimental value, though the basic shapes are consistent. This difference was attributed to electron–phonon coupling.

Fulleride monolayers provide a rare testing ground for exploring key conceptual issues involving strong interactions in materials with novel properties. The persistence of a clear classical (quasiparticle) electronic structure in the presence of strong interactions may imply that the electronic properties rely more on localized features, a distinction that could also be very important in understanding novel behaviors in



Experimental angle-resolved photoemission data showing photoelectron intensity as a function of energy for several values of momenta (green arrow). The red arrows point to the conduction band energy at each momentum. The blue arrows are phonon satellites.

other materials, such as high-T_c superconductivity. Further investigations are underway to reveal still more interesting and deeper physics in these molecular crystals.

SCIENCE HIGHLIGHTS

CONDENSED MATTER PHYSICS

Buckyball monolayer band structure. The photoelectron intensity map shows the energy-momentum dispersion (darker color indicates higher intensity). The band width (maximum energy below the Fermi energy) is about 100 meV.

INVESTIGATORS

FIGURE 8

W.L. Yang, V. Brouet, and X.J. Zhou (Berkeley Lab and Stanford University); H.J. Choi, S.G. Louie, and M.L. Cohen (Berkeley Lab and University of California, Berkeley); S.A. Kellar, P.V. Bogdanov, A. Lanzara, and Z.-X. Shen (Stanford University); Z. Hussain (ALS); A. Goldoni (Sincrotrone Trieste, Italy); and F. Parmigiani (Università Cattolica del Sacro Cuore, Brescia, Italy).

FUNDING

U.S. Department of Energy, Office of Basic Energy Sciences; Office of Naval Research; and National Science Foundation.

PUBLICATIONS

W.L. Yang et al., "Band structure and Fermi surface of electron-doped C_{60} monolayers," *Science* **300**, 303 (2003)

Low-Temperature Electronic Properties of a Quasi-1D Metal

Cars caught in stop-and-go traffic on a one-lane road can be described as "strongly interacting" components of a one-dimensional (1D) system. They are strongly interacting because, being restricted to one lane, the motion of each car is tied to the motion of its nearest neighbors, and traffic will tend to bunch up into "car-density waves" rather than flow homogeneously (as on a four-lane freeway where there is room to pass). In the 1930s, physicist Rudolf Peierls theorized that electrons confined to a 1D metal crystal at low temperature would interact strongly with one another and with the crystal lattice to form chargedensity waves (CDWs). Although the existence of CDWs was detected in the 1970s, CDW materials are again the subject of intense research. In addition to serving as a conveniently observable model system for complex dynamical theories, CDW materials exhibit many exotic properties that may one day find practical applications as memory devices, tunable capacitors, or extremely sensitive optical detectors.

One-dimensional systems can be approximated by ultrathin wires or crystals with unidirectional bonds that confine electron motion to one dimension. At low temperatures, some 1D systems undergo a phase transition where interactions between the lattice and the electrons create a CDW in the material, which then exhibits highly nonlinear electrical behavior. The electronic structure of materials is particularly accessible with angle-resolved photoemission spectroscopy (ARPES). Our research group from Germany and the U.S. performed a photoemission study at the ALS of a quasi-1D metal, providing the first direct spectroscopic observation

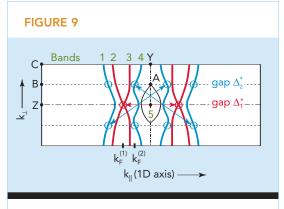
SCIENCE HIGHLIGHTS

CONDENSED MATTER PHYSICS

at low temperature of the electronic structure of the CDW system niobium triselenide (NbSe₃).

An ideal CDW conductor will show an energy gap in its electronic energy bands, resulting in reduced conductivity. In real materials that are not perfectly 1D, the gapping may be incomplete, with portions of the electron bands remaining metallic. NbSe₃ is a multiband Peierls system that is known to undergo two CDW transitions, one at $T_1 = 145$ K and another at $T_2 = 59$ K. Its Fermi surface (which decribes the location of the conduction electrons in reciprocal space) as calculated by density functional theory (DFT) consists of five electron bands (Figure 9). In this system, the presence of CDWs is signaled by the so-called "nesting" of its lattice distortion vectors in reciprocal space (i.e., for each CDW, vectors span a pair of bands in the Fermi surface).

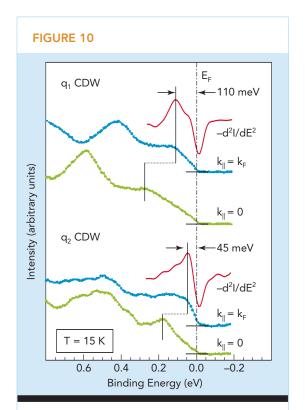
Single-crystal NbSe₃ "whiskers" were grown via vapor transport and cleaved into fine fibers in ultrahigh vacuum. High-resolution ARPES data at $T=15\,$ K were obtained from the tiny samples using the microfocused synchrotron beam at ALS Beamline 10.0.1. At low temperature, energy gaps are expected to occur in the Fermi surface where the lattice distortion vectors \mathbf{q}_1 and \mathbf{q}_2 are nested. However, theNbSe₃ spectra obtained do not display well-defined gaps; instead, pseudogap



Schematic of the Fermi surface of NbSe $_3$ calculated with DFT. Five bands are seen in a cross section along the chain direction (1D axis) and K_{\perp} . "Nesting" vectors connect bands 2 and 3 (red) and 1 and 4 (blue).

behavior is observed, with the photoemission intensity continuously decreasing toward the Fermi energy E_F (Figure 10). Extrinsic defect scattering is an unlikely cause of this since many other spectral features are rather sharp. We therefore concluded that the pseudogaps are intrinsic properties of the CDW phase. Photoemission intensity in the gap region can be generated by quantum fluctuations. Also, an imperfectly nested Fermi surface with permanently metallic sections may cause additional interactions that contribute to the gap spectral function. Effective gap values of $\Delta_1^*=110\pm20$ meV and $\Delta_2^*=45\pm10$ meV were obtained for the ${\bf q}_1$ and ${\bf q}_2$ CDWs, respectively.

Nominally metallic bands are encountered at the boundaries of the Brillouin zone, where the

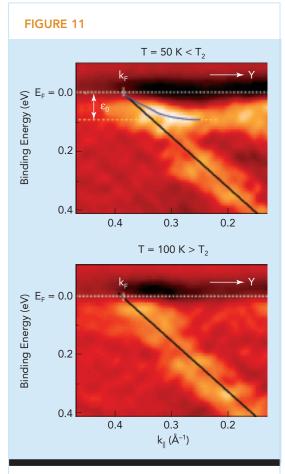


Spectral functions from ARPES line scans at $k_{\parallel}=0$ and at k_{F} for the effective gaps Δ_{1}^{\star} and $\Delta_{2}^{\star}.$ Gap spectra are identified by "nesting" conditions in reciprocal space. They are inherently broad and are complemented with second derivatives $-d^{2}I/dE^{2}.$

SCIENCE HIGHLIGHTS

CONDENSED MATTER PHYSICS

bands do not match a CDW nesting condition. Here, a low-energy shoulder near E_F is also observed (Figure 11). It displays a much-reduced dispersion that is equivalent to a particularly heavy electron mass. Such an effect has been



Top: Modified electron band dispersion along the Y-C direction in the Brillouin zone, where nominally metallic bands are expected (intensity displayed as $-d^2I/dE^2$). The branch with shallow slope is representative of an enhanced electron mass over an energy window of about 90 meV. *Bottom:* Above T_2 , the effect is no longer detected.

known to occur from "dressing" of the electron with phonons. In the present data, the shallow slope indicates an enhanced electron mass over an energy window of about 90 meV, coinciding with a value for the energy gap of $2\Delta_2$ *. The effect disappears above $T_2 = 59$ K, supporting a connection to the \mathbf{q}_2 CDW phase. The effect may be caused by the reduced phase space available for electron scattering that results from the gapped regions. However, a theoretical description of the effect is not yet available.

In conclusion, this study elucidates the nature of the energy gaps in the multiband environment encountered in many quasi-1D systems, where the energy gaps deviate from simple gap behavior. Nondistorted parts of the electron bands do not show a conventional Fermi edge, and the electronic dispersion exhibits the signature of electron mass enhancement on the energy scale of the full gap, $2\Delta_2^*$. Thus, both gapped and permanently metallic parts of the Fermi surface seem to mutually influence each other.

INVESTIGATORS

J. Schäfer, M. Sing, and R. Claessen (Universität Augsburg, Germany); E. Rotenberg (Berkeley Lab); X.J. Zhou (Berkeley Lab and Stanford University); R.E. Thorne (Cornell University); and S.D. Kevan (University of Oregon).

FUNDING

German Research Foundation and Bavaria California Technology Center.

PUBLICATIONS

J. Schäfer et al., "Unusual spectral behavior of chargedensity waves with imperfect nesting in a quasi-onedimensional metal," *Phys. Rev. Lett.* **91**, 066401 (2003).

н

A "Nearly-Free" Electron Metal in Two Dimensions

The electrons that conduct electricity in metals and semiconductors are important because they determine all of the important properties of conductors: not only those that have been understood for many years but also exotic phenomena discovered more recently, such as high-temperature superconductivity (disappearance of electrical resistance in certain ceramics at much higher temperatures than in metals), colossal magnetoresistance (drastically increased change in electrical resistance in a magnetic field), and fractional charge (apparent electric charge less than 1 under certain circumstances). These behaviors tend to be enhanced in so-called low-dimensional materials like layers only a few atoms thick and lines a few atoms wide. To study low-dimensional materials in controlled circumstances, scientists prepare "model" systems that exhibit the behaviors under investigation but avoid unrelated complication. Rotenberg et al. have constructed such a system comprising a layer of indium only one atom thick on a silicon substrate and showed that the indium acts like a textbook example of a two-dimensional (2D) metal without hindrance from the underlying silicon.

Because of burgeoning interest in nanostructures, the effects of low dimensionality in solids assume not just fundamental interest but also technological importance. Two-dimensional systems are particularly interesting because of their suspected role in many exotic phenomena and also because of their intermediate status between one dimension (where metals are intrinsically unstable) and ordinary three-dimensional (3D) metals. Here, we present angle-resolved photoemission findings for a single monolayer of indium atoms deposited on (111)-oriented silicon. The Fermi surface consists of an array of circular

contours on a square lattice, showing that the electronic states take the particularly simple and elegant form of a "nearly-free" metal. It is also a striking experimental realization of a simple model presented in most elementary textbooks on solid state physics.

It is now clear that the interaction of electrons with each other and with vibrations, spin waves, or other quantum-mechanical excitations is what underlies recently discovered exotic phenomena such as high-temperature superconductivity, colossal magnetoresistance, and fractional charge, as well as other more complex behaviors. The effect of these interactions increases as the electrons are confined to successively fewer dimensions of motion.

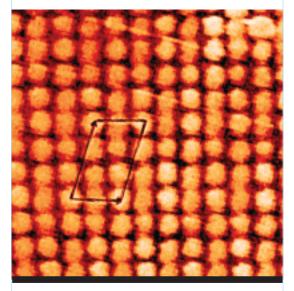
In fact, the relative role of disorder (leading to insulating behavior) and charge pairing (leading to superconductivity) in determining the ground state of 2D metals is currently unresolved, with most measurements in the field done by transport of electrons confined to buried interfaces. As an alternate model system for 2D metals, electrons can be confined to a material's surface. This surface confinement has the advantage that electronic spectral functions may be probed directly through surface probes, such as photoemission or scanning tunneling microscoscopy (STM), rather than indirectly through transport measurements.

The atomic structure of an indium monolayer on silicon is shown in a previously measured STM image (Figure 12) and consists of a simple, nearly square lattice of indium atoms similar to a single atomic plane from a bulk indium crystal. Figure 13 shows the momentum distribution of the least-bound (Fermi) electrons, which constitutes the so-called Fermi surface of the material, obtained by angle-resolved photoemission measurements at the Electronic Structure Factory at ALS Beamline 7.0.1.

There are three important findings. First, the predominant square-lattice symmetry of the Fermi surface suggests that electrons "feel" the indium atoms much more than they do the underlying silicon atoms, which is an indication of the high degree of electron confinement to the surface

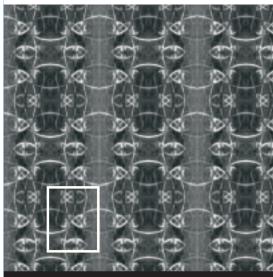
SCIENCE HIGHLIGHTS

CONDENSED MATTER PHYSICS



The atomic arrangement of a single monolayer of indium atoms, indium $\sqrt{7} \times \sqrt{3}$ on Si(111), determined by J. Kraft et al. from STM measurements [Surf. Sci. Lett. **372**, 271 (1997)].

FIGURE 13



The momentum-space distribution of electronic states at the Fermi level determined in the present study. The raw data (rectangle) are tiled to highlight the square lattice arrangement of the features.

SCIENCE HIGHLIGHTS

CONDENSED MATTER PHYSICS

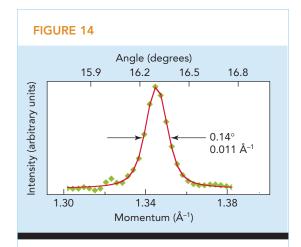
20

metallic layer. The largely square symmetry of the Fermi surface reflects the internal structure of the indium layer, in contrast to the substrate's threefold symmetry, which induces only weak modifications to the pattern's overall square arrangement.

Second, quantitative analysis shows that almost all of the Fermi-surface electrons participate in metallic bonding of the indium lattice, with only a minority of electrons participating in covalent bonds to the silicon substrate. In fact, about half of the electrons from dangling bonds in the silicon surface are donated to the metallic indium layer, adding further stability to the system. In effect, most of the electronic "glue" holding the system together is within the indium layer, with relatively few electrons bonding the layer to the substrate.

Third, the dramatic sharpness of the bands, indicated by the momentum distribution curve (Figure 14), attests to the high quality of the films. The mean free path of electrons must be in excess of 150 Å and is probably limited by

the size of the atomically flat terraces on our substrate wafers. The sharpness also attests to the high degree of angular resolution of the instrument, which is now estimated to be 0.086°.



A momentum distribution curve of one of the Fermi contours. The sharpness of the features indicates a mean free path > 150 Å and results from the high angular resolution obtained in the instrument (better than 0.09°).

INVESTIGATORS

E. Rotenberg, H. Koh, and K. Rossnagel (ALS); H.W. Yeom (Yonsei University, Korea); J. Schäfer (Universität Augsburg, Germany); and B. Krenzer, M.P. Rocha, and S.D. Kevan (University of Oregon).

FUNDING

U.S. Department of Energy, Office of Basic Energy Sciences, and Korean Science and Engineering Foundation.

PUBLICATIONS

E. Rotenberg et al., "Indium $\sqrt{7} \times \sqrt{3}$ on Si(111): A nearly free electron metal in two dimensions," *Phys. Rev. Lett.* **91**, 246404 (2003).

Universal Nodal Fermi Velocity in High-Temperature Superconductors

Superconductivity, the loss of electrical resistance when certain metals and compounds are cooled to cryogenic temperatures, was already of some commercial importance in late 1986, when the first of several families of so-called high-temperature superconductors was discovered. Ceramics rather than metals, these materials immediately became the focus of an intense effort both to figure out how to make them in useful forms, such as flexible wires, and to understand the origin of the superconductivity. High-temperature superconductivity lies at the frontier of condensed matter physics, where strong interactions between one electron and another and between electrons and other entities, such as lattice vibrations and magnetic phenomena, play the dominant role. However, a bewildering array of experimental results and theoretical models must be sorted through and reconciled to reach a solution. Zhou et al. have added one more piece to fit into the puzzle with their unexpected discovery that the velocity of certain electrons is constant and independent of the composition of the high-temperature superconductor.

Even after more than 15 years of intense experimental and theoretical effort at laboratories around the world, the mechanism causing high-temperature superconductivity in copper oxide materials (cuprates) is unresolved. Our international collaboration, comprising members drawn from Japan, China, Germany, and the U.S., has made the unexpected observation that the velocity of electrons near the Fermi level (low-energy or Fermi velocity) in high-temperature superconductors is the same (universal) for all compositions not only within one superconductor families.

The parent compounds from which the high-temperature superconductors are derived are antiferromagnetic insulators. As an increasing number of charge carriers (electrons or holes) are introduced into the insulator by changing the composition slightly, a process called doping, the material soon becomes a superconductor and eventually transforms into a normal metal. This dramatic change in physical properties with doping seems to imply that doping dependence (nonuniversality) is a general feature of these materials. Our results with high-resolution angle-resolved photoemission, which can directly probe how electrons move in materials, show that this is not the case for the Fermi velocity.

We measured five different families of cuprates with various hole dopings, including $(La_{2-x}Sr_x)CuO_4$ (LSCO) and $(La_{2-x-y}Nd_ySr_x)CuO_4$ (Nd-LSCO), $Bi_2Sr_2CaCu_2O_8$ (Bi2212), $Bi_2Sr_2CuO_6$ (Bi2201), $(Ca_{2-x}Na_x)CuO_2Cl_2$ (Na-CCOC), and $Tl_2Ba_2CuO_6$ (Tl2201). We made a particular effort to investigate the LSCO system across the entire doping range ($0 \le x < 0.3$) over which the physical properties vary from insulator ($0 \le x \le 0.03$) to superconductors (0.05 < x < 0.25) to overdoped nonsuperconducting metal (x > 0.25). Except for Na-CCOC, for which data were taken at the Stanford Synchrotron Radiation Laboratory, all the samples were measured at ALS Beamline 10.0.1.

SCIENCE HIGHLIGHTS

CONDENSED MATTER PHYSICS

CONDE

SCIENCE HIGHLIGHTS

CONDENSED MATTER PHYSICS

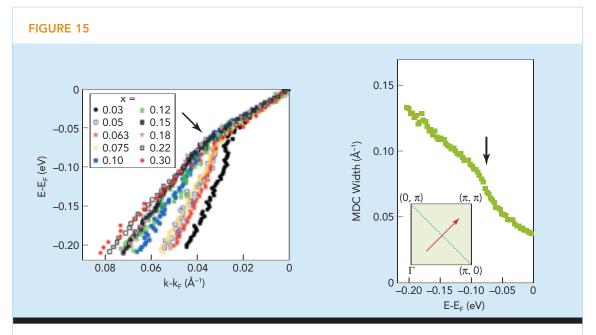
22

The energy–momentum (dispersion) curves of LSCO with various dopings ($0 < x \le 0.3$), measured along the (0,0)– (π,π) diagonal direction in the Brillouin zone in reciprocal space, are shown in Figure 15. In these superconductors, this direction is called the nodal direction because the superconducting gap, whose size varies with direction in the Brillouin zone, as well as the similarly anisotropic normal-state pseudogap, is zero. For all doping levels, there is clearly a kink at an energy of about 70 meV that separates the dispersion into a high-energy part (i.e., farther from the Fermi energy) and a low-energy part (i.e., closer to the Fermi energy) with different slopes.

Although the slope in the high-energy part varies with doping, the slope within about 50 meV of the Fermi energy is independent of doping. In addition, for the LSCO (x = 0.063) sample, we observed a drop in the electron scattering rate at

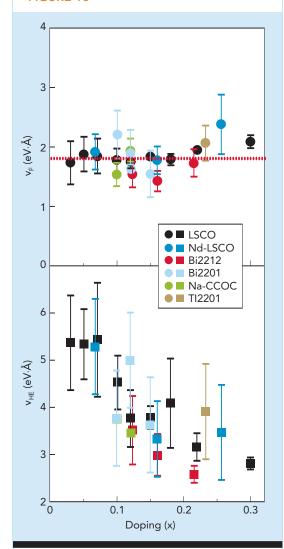
an energy of about 70 meV, as indicated in Figure 15. The electron velocity can be quantitatively extracted from the slope of the dispersion ($v = \partial E/\partial k$). Figure 16 shows the high- and low-energy velocities as a function of doping for all five families of materials. Indeed, the low-energy velocity (the Fermi velocity, v_F) is nearly a constant for all materials and dopings within an experimental error of about 20%. In contrast, the high-energy velocity, v_{HF} , varies strongly with doping.

The invariance of the nodal Fermi velocity in cuprates is surprising given the range over which many other physical properties vary with doping. This universal behavior, together with the ubiquitous existence of a kink in dispersion and a drop in the scattering rate, are all pieces that must be fit into the puzzle that when completed will reveal the mystery of high-temperature superconductivity.



Electron dynamics in LSCO. Left: Dispersion of LSCO with various dopings (x = 0.03 to 0.30) measured at a temperature of 20 K along the (0,0)–(π , π) nodal direction (the red arrow in the Brillouin zone in the inset at right). The dispersion is obtained from momentum distribution curves (MDCs), which represent the photoelectron intensity as a function of momentum at a given energy. The arrow indicates the position of the kink that separates the dispersion into high-energy and low-energy parts with different slopes. *Right:* The scattering rate obtained from the MDC full width at half maximum (FWHM) of the LSCO (x = 0.063) sample measured at 20 K. The MDC width is proportional to the scattering rate of electrons. The arrow indicates a drop at an energy of about 70 meV.

FIGURE 16



Velocities of electrons as a function of doping in various cuprates. *Top:* The low-energy Fermi velocity (v_F) obtained by linearly fitting the dispersion between 0 and -0.05 eV. The dashed line represents an average over all the measured values. *Bottom:* The high-energy velocity (v_{HE}) obtained by linearly fitting the dispersion between the energy range of -0.1 and -0.2 eV. These velocity values are averaged over many different measurements.

INVESTIGATORS

X.J. Zhou, A. Lanzara, and W.L. Yang (Stanford University and ALS); T. Yoshida (Stanford University and University of Tokyo, Japan); P.V. Bogdanov, S.A. Kellar, K.M. Shen, F. Ronning, T. Sasagawa, and Z.-X. Shen (Stanford University); T. Kakeshita, T. Noda, H. Eisaki, S. Uchida, and A. Fujimori (University of Tokyo, Japan); C.T. Lin (Max-Planck-Institut für Festkörperforschung, Germany); F. Zhou, J.W. Xiong, W.X. Ti, and Z.X. Zhao (Chinese Academy of Sciences, China); and Z. Hussain (ALS).

FUNDING

U.S. Department of Energy, Office of Basic Energy Sciences; National Science Foundation; Ministry of Education, Culture, Sports, Science, and Technology of Japan; New Energy and Industrial Technology Development Organization, Japan; National Natural Science Foundation of China; and Ministry of Science and Technology of China.

PUBLICATIONS

X.J. Zhou et al., "High-temperature superconductors: Universal nodal Fermi velocity," *Nature* **423**, 398 (2003).

SCIENCE HIGHLIGHTS

CONDENSED MATTER PHYSICS

MATERIALS SCIENCE

::

Time-Resolved X-Ray Absorption of Warm, Dense Matter

While 5000 degrees on any temperature scale would seem to be off the chart, to solid state physicists studying matter under extreme conditions, this temperature qualifies as merely warm because it is not enough to vaporize the material into a plasma of ions and electrons. Even so, the temperature is more than sufficient to pose severe experimental and theoretical challenges to those scientists who specialize in solid-density materials that are rapidly heated by extremely short bursts of laser light lasting less than one trillionth of a second (1 picosecond). Not only do such investigations provide information about the fundamental physics of how matter melts, but there is a practical aspect as well: processing the silicon from which computer chips are patterned can involve laser heating. Johnson et al. have demonstrated the ability to conduct x-ray absorption measurements of laser-melted silicon with a time resolution of only a few picoseconds, an important beginning in acquiring an armamentarium of tools for dissecting so-called warm, dense matter.

Experiments in the warm, dense matter regime are challenging, since it is difficult to sustain such extreme thermodynamic conditions under laboratory conditions long enough for conventional measurements. However, with experimental techniques capable of ultrafast time resolution, one can perform measurements on these rapidly evolving systems. To this end, our multi-institutional group has demonstrated transmission x-ray absorption measurements on a laser-heated silicon foil with picosecond time

resolution. This work represents a first step toward acquiring a comprehensive experimental capability to study solid-density matter under conditions of extremely high temperature.

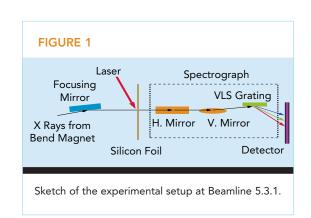
Warm, dense matter lies between the regimes of condensed matter physics and plasma physics in a part of thermodynamic phase space where existing theories have a difficult time. For example, consider a solid that is rapidly heated to just below the liquid-vapor "critical temperature" (the temperature past which the liquid-vapor equilibrium line does not exist). At such high temperature and density, is it more appropriate to describe the material as a hot liquid or as a cold plasma? Extensions of models of solid state materials to higher temperatures and of plasmas to the strongly coupled regime need to be tested.

Figure 1 is a sketch of our apparatus at ALS Beamline 5.3.1 for our pump-probe experiment. The pump was a 150-fs laser pulse that heats a portion of a 500-Å-thick silicon foil, rapidly melting and heating it to almost 5000 K. The probe was a 70-ps pulse of broad-spectrum x rays from a bend magnet focused onto the heated region of the foil. A grating spectrograph spectrally dispersed the transmitted x-ray spectrum onto a position-sensitive detector.

We used two different types of detectors. For slower time resolution, we used a pair of gated microchannel plates coupled to a CCD camera.

SCIENCE HIGHLIGHTS

MATERIALS SCIENCE



With this detection scheme, the temporal resolution was set by the duration of the x-ray pulse to about 70 ps. For faster time resolution (approximately 5 ps), we used an ultrafast x-ray streak camera that could resolve changes in the transmission spectrum during the x-ray pulse. Owing to irreversible damage of the irradiated areas, we were limited to about 200 shots per foil.

A comparison of the L absorption edges of solid and liquid silicon (Figure 2) revealed that the absorption of the liquid was significantly different from that of the solid. Measurements near the L_{II,III} edge taken with the streak camera confirmed that the drop in the magnitude of the absorption occurred in less than 5 ps, in agreement with previous measurements of laserinduced "ultrafast melting" in silicon.

To model the data, we used tight-binding molecular dynamics simulations to obtain the atomic structure of liquid silicon and then calculated an absorption spectrum based on this structure with FEFF, an ab initio scattering code. The comparison of the calculated and measured

absorption at the $L_{\rm II,III}$ edge (Figure 3) shows that the model reproduces the observed shift and decrease in absorption in the broad peak near 125 eV, a change that indicates a 0.15 \pm 0.07 Å increase in the nearest-neighbor distance upon melting.

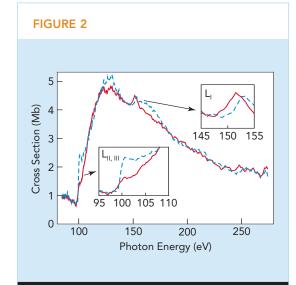
Plots from the simulations of the s-projected density of unoccupied states (inset of Figure 3) show that just above the Fermi level, the liquid has about 50% fewer states than the solid, which is consistent with the experimental absorption spectrum near the edge threshold. Model spectra and density-of-states calculations of the L_I edge also reproduce a shift on melting. Finally, the model predicts a large increase in structural disorder that results in washing out the absorption fine structure above 160 eV in the liquid.

Our group is now completing additional studies to examine the properties of liquid carbon. We expect that the application of a broad range of ultrafast, time-resolved x-ray techniques will offer a unique opportunity to investigate the regime of warm, dense matter.

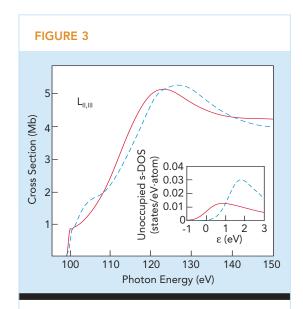
SCIENCE HIGHLIGHTS

MATERIALS SCIENCE

25



Absorption spectra of solid silicon (blue) and heated silicon 100 ps after laser excitation (red). The insets are detailed views of the $L_{\rm II,III}$ and $L_{\rm I}$ edges.



Model calculation of solid silicon (blue) and liquid silicon (red) near the $L_{\rm II,III}$ absorption edge. The inset shows the s-projected density of states for each material near the Fermi level.

INVESTIGATORS

S.L. Johnson (Paul Scherrer Institut, Switzerland), P.A. Heimann (ALS), A.M. Lindenberg (Stanford Linear Accelerator Center), H.O. Jeschke (Rutgers University), M.E. Garcia (Freie Universität Berlin), R.W. Lee (Lawrence Livermore National Laboratory), Z. Chang (Kansas State University), J.J. Rehr (University of Washington, Seattle), and R.W. Falcone (University of California, Berkeley).

FUNDING

U.S. Department of Energy, Office of Basic Energy Sciences and High-Energy-Density Grants Program; Lawrence Livermore National Laboratory; and German Research Foundation.

PUBLICATIONS

S.L. Johnson et al., "Properties of liquid silicon observed by time-resolved x-ray absorption spectroscopy," *Phys. Rev. Lett.* **91**, 157403 (2003).

S.L. Johnson, "Ultrafast x-ray absorption spectroscopy: Properties of liquid silicon and carbon," Ph.D. thesis, University of California, Berkeley (2002).

SCIENCE HIGHLIGHTS

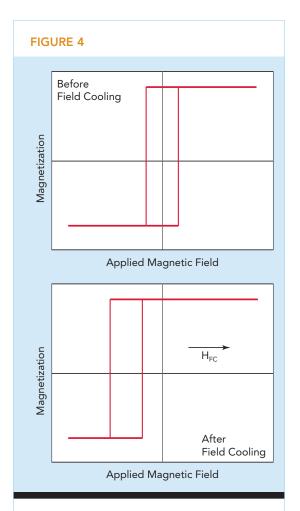
MATERIALS SCIENCE

26

Pinning Down Exchange Bias

The ability to rapidly and accurately "read" the stored data in today's desk- or laptop computers is due to an ultrathin sandwich of magnetic and nonmagnetic materials in a read head that sits closely over a rapidly whirling disk. Exchange bias is a phenomenon that provides a magnetic reference, so that the read head can sense which of two binary bits of information is present. How exchange bias works has been a mystery for 50 years. Various models are based on the idea that magnetic atoms are like tiny spinning tops that generate minute magnetic fields. A model in which the spin directions are aligned in the interface region between the layers of the sandwich can explain exchange bias, but this simple model results in an effect that is many factors of 10 too large. Ohldag et al. have used an x-ray spectroscopy technique that is sensitive to the interface to show that only about 5 percent of the spins there contribute to exchange bias, thereby bringing the model into line with reality.

Exchange bias refers to a preferred direction of magnetization of a ferromagnet in contact with an antiferromagnet. It is due to a shift in the hysteresis loop (magnetization vs. external magnetic field) when cooling the sample in an external field (field cooling) to below the antiferromagnet's ordering (Néel) temperature (Figure 4). Magnetic devices based on exchange bias are of considerable commercial importance for data storage, but the mechanism behind it has evaded detection for 50 years. Our collaboration, drawn from the Stanford Synchrotron Radiation Laboratory, the ALS, the Swiss Light



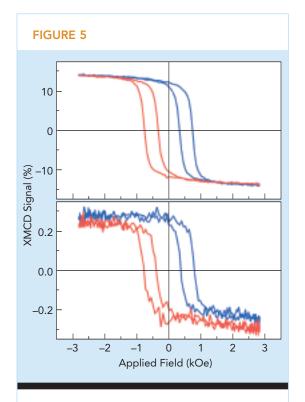
Exchange bias. The hysteresis loop of a ferromagnet in contact with an antiferromagnet shifts after cooling in an external field to a temperature below the Néel temperature (field cooling), so that one magnetization direction becomes preferred.

Source, and Hitachi Global Storage Technologies, has now shown that a relatively small number of "pinned" spins in the interface layer of the antiferromagnet are the cause.

Exchange bias can be understood qualitatively by a simple model. In an external field and above the Néel temperature (T_N) , antiferromagnetic spins located at the interface with the ferromagnet are aligned, like the ferromagnet, with the field. Once cooled below T_N , these interface spins thereafter keep their orientation and appear "pinned" because they are tightly locked to the spin lattice in the bulk of the antiferromagnet, which is not sensitive to external fields. Consequently these pinned spins produce a constant magnetic field at the interface that causes the hysteresis loop of the ferromagnet to shift. However, this intuitive picture overestimates the magnitude of the loop shift by orders of magnitude.

Numerous efforts have been made to explain the difference, but the problem has been the missing knowledge about the actual spin structure at the interface, which need not be the same as in the bulk. The goal of the collaboration was to detect pinned interfacial spins and use the information to find a direct correlation between their number and the size of the loop shift. The unique ability of x-ray magnetic circular dichroism (XMCD) to probe magnetic properties of individual elements in thin-film samples was the key to success.

For this purpose, we used elliptically polarizing undulator Beamline 4.0.2 at the ALS to measure hysteresis loops of interfacial spins in samples comprising thin layers of exchange-biased ferromagnetic cobalt or cobalt–iron on thicker layers of antiferromagnetic iridium–manganese, platinum–manganese, or nickel oxide, all on silicon substrates. In each case, we measured hysteresis loops in two sample orientations that gave loop shifts parallel and antiparallel to the positive field direction, respectively. By tuning the photon energy to the manganese or nickel



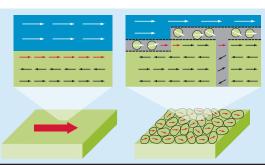
Hysteresis loops of cobalt (top) and manganese (bottom) in an exchange-biased layer of ferromagnetic cobalt on antiferromagnetic iridium—manganese. The loops for both elements shift, with the direction of the shift depending on the sample geometry. In addition, there is a vertical shift between the manganese loops. Both shifts are due to a small fraction of pinned spins at the interface.

absorption edges, we detected the extremely small XMCD signal arising only from the interfacial spins in the antiferromagnet (there is no signal from the antiferromagnet itself). These hysteresis loops exhibit a vertical shift in addition to the horizontal shift (Figure 5). Like the preferred magnetization direction, the vertical shift reverses if the sample geometry is reversed.

Two important conclusions follow from the interface hysteresis loops. First of all, most of the interfacial spins couple strongly to the ferromagnet on top and follow its magnetization, thereby exhibiting the same hysteretic behavior. Second, only a small fraction (5%) of interfacial spins is actually pinned, and these cause the horizontal hysteresis loop shifts (Figure 6). In addition, the vertical shift is caused by these pinned interfacial

SCIENCE HIGHLIGHTS

MATERIALS SCIENCE



Left: In an ideal, single-crystal antiferromagnet (green), all spins at the smooth interface (red arrows) are pinned and contribute in the same way to the internal field acting on the top ferromagnetic layer (blue). Right: In a real sample with a rough interface and grain boundaries (gray), most spins at the interface (small white arrows) are not pinned and follow the magnetization of the ferromagnet. The small number of pinned spins (red arrows) causes exchange bias.

spins, which were aligned by the cooling field and remain pointing in a fixed direction. The very small number of pinned spins observed explains why it was not possible to detect these spins with conventional magnetometry techniques. Also, it shows that the simple model for exchange bias is correct in principle, if one assumes "mixed coupling" across an imperfect antiferromagnetic/ferromagnetic interface instead of ideal interfaces. A next-generation photoemission electron microscope (PEEM-3) coming to the ALS will help clarify the origin of the pinning.

INVESTIGATORS

H. Ohldag (Stanford Synchrotron Radiation Laboratory, ALS, and Universität Düsseldorf, Germany); A. Scholl, E. Arenholz, and A.T. Young (ALS); F. Nolting (Swiss Light Source); S. Maat and M. Carey (Hitachi Global Storage Technologies); and J. Stöhr (Stanford Synchrotron Radiation Laboratory).

FUNDING

U.S. Department of Energy, Office of Basic Energy Sciences.

PUBLICATIONS

H. Ohldag et al., "Correlation between exchange bias and pinned interfacial spins," *Phys. Rev. Lett.* **91**, 017203 (2003).

Antiferromagnetic Domain Walls in Nickel Oxide

Magnets are magnetic because there are extended regions in which the quantum mechanical spins of atoms are aligned to generate a measurable magnetic field. Real magnets consist of multiple domains with different orientations that are separated by transition regions called domain walls. Antiferromagnets are special materials that can be visualized as two interpenetrating lattices of aligned spins, with the spins on one lattice being antiparallel to the spins on the other. The result is that there is no net magnetic field, but there is a definable magnetic axis, and there are walls between domains with differently oriented axes. All of this would be academic, but it turns out that antiferromagnetic materials are key players in modern information-storage technologies, such as that underlying the hard disk in your computer. Weber et al. have used an x-ray microscopy technique that is sensitive to the direction of the antiferromagnetic axis to visualize these walls. Based on their observations, they have devised a model for the forces that drive wall formation.

Since there is no net magnetization, virtually all techniques in use for ferromagnetic materials are ineffective for antiferromagnets. The same limitation also applies to domain walls in antiferromagnets, i.e., the transition region between domains with different orientations of the antiferromagnetic order parameter. However, photoemission electron microscopy offers sufficiently high spatial resolution and sensitivity to the antiferromagnetic order parameter to directly image antiferromagnetic walls, and we have imaged domain walls in nickel oxide by this technique. Modeling the resulting wall profiles showed that a magnetoelastic interaction determines the widths of domain walls and is the prime source

SCIENCE HIGHLIGHTS

MATERIALS SCIENCE

for the formation of antiferromagnetic domains.

The macroscopic properties of magnetically ordered materials are to a large extent dependent on the presence of domains and their properties—size, topology, and the ease with which they may be modified by external parameters like magnetic field, temperature, stress, or interlayer coupling in heterogeneous multilayer systems. Like walls in ferromagnets, domain walls in antiferromagnets can be characterized by a single vector, the antiferromagnetic (AF) vector, whose origin lies in strong exchange interactions and whose orientation is defined by the local magnetic axis.

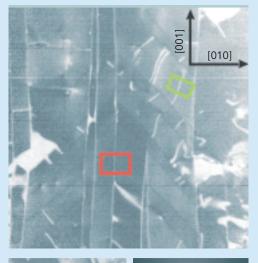
For our studies of antiferromagnetic domains in nickel oxide, we measured x-ray magnetic linear dichroism (XMLD) with the PEEM-2 photoemission electron microscope at ALS Beamline 7.3.1.1. For nickel oxide, the XMLD manifests itself at the nickel 2p_{1/2} absorption edge, which has a double peak. The relative strength of the two peaks depends on the angle θ between the linear polarization and the orientation of the magnetic axis, and the variation has the form $3\cos^2\theta - 1$. A typical domain pattern observed on a NiO(100) surface by taking the ratio of intensities obtained at the two nickel 2p absorption peaks is shown in Figure 7 (bottom left). The domains appear as stripes parallel to [100] and [110] directions within the surface.

The contrast between domains disappears whenever the angle θ is the same for two neighboring domains, as shown in Figure 7 *(top)*. Although the contrast between the domains themselves has disappeared, the image has narrow lines, which by comparison to the domain image can be identified as domain walls. The appearance of domain walls under such conditions means that the AF vector in the walls has a different orientation from that in the domains. The contrast also demonstrates that in the wall, the AF vector rotates within the surface plane, rather than rotating out of the surface, so that

the (100) walls between the domains can be classified as Néel type. A line scan across the wall in the red rectangle of Figure 7 shows a width of about 160 nm (Figure 8).

We also observed a second type of domain wall separating regions that appear with the same

FIGURE 7







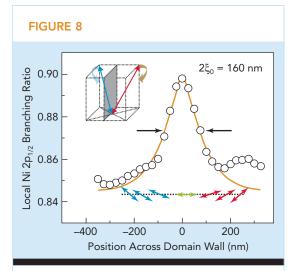
Antiferromagnetic domain walls on the NiO(100) surface imaged by photoemission microscopy. Bottom left: A typical domain pattern in which the domains appear as stripes parallel to [100] and [110] directions within the surface. Top: The contrast between domains disappears when the light polarization is parallel to a [010] direction within the surface, so that the only contrast is due to the domain walls. The walls along [001] appear brighter; walls parallel to [011] or [011] appear darker than the interior of the domains. Bottom right: A topography image formed from the mean photoelectron intensity obtained at 871 and 872 eV shows no features that may influence the domain structure, so that all the features seen in the other images are of magnetic origin. The field of view is about $35 \times 35 \,\mu\text{m}^2$.

SCIENCE HIGHLIGHTS

MATERIALS SCIENCE

MATERIALS

SCIENCE



Profile of the domain wall averaged along the wall in the the red rectangle of Figure 7. The points are experimental data, and the solid line was calculated. The width (FWHM) of the AF domain wall is about 160 nm. The inset shows a schematic representation of the (001) domain wall. Double-ended arrows show the orientation of the AF vector inside the domain wall.

contrast under all light polarizations or sample orientations (green rectangle). While the domains on both sides are identical, nevertheless, there is a domain wall. This new type of wall is interpreted as arising from a stacking fault of the AF stacking of the (111) planes (or an antiphase boundary). The widths of these walls are slightly larger than that of the walls discussed above. Furthermore it appears that they are not tied to low-index crystallographic directions.

We have modeled the wall profiles by introducing an effective magnetic anisotropy, which accounts for the influence of magnetostriction on the local magnetic anisotropy. The magnetoelastic interaction is the essence of what distinguishes the antiferromagnetic walls discussed here from the commonly encountered domain walls in ferromagnetic materials, where the magnetic anisotropy is uniform throughout the sample and across the wall. In contrast to a previous model based solely on indirect evidence of domain wall properties, the wall is significantly wider, and the energy per unit area of domain wall is smaller by two orders of magnitude.

INVESTIGATORS

N.B. Weber and H. Ohldag (Heinrich-Heine-Universität Düsseldorf, Germany) and H. Gomonaj and F.U. Hillebrecht (Max-Planck-Institut für Mikrostrukturphysik, Germany).

FUNDING

U.S. Department of Energy, Office of Basic Energy Sciences.

PUBLICATIONS

N.B. Weber et al., "Magnetostrictive domain walls in antiferromagnetic NiO," *Phys. Rev. Lett.* **91**, 237205 (2003).

:

Learning How Magnets Forget

A magnetic material immersed in an external magnetic field has a magnetization. As the external field cycles between positive and negative values, the magnetization traces out a hysteresis loop. While hysteresis underlies all magnetic datastorage technology, it is not understood at the microscopic level. Nevertheless, the magnetic disk drive industry has had a cumulative growth rate for the past decade that dwarfs even the celebrated Moore's Law growth rate for microcircuits. A number of technological innovations have made this growth possible, including the use of thin layers of magnetic materials into which a certain amount of disorder has been introduced in a controllable way. Pierce et al. have developed an x-ray analogue of the laser speckle well known to anyone who has seen the pattern created when laser light strikes a dusty mirror. They have used their technique to track quantitatively the evolution of magnetic domains as the magnetic layer cycles through various hysteresis loops, thereby directly probing how hysteresis unfolds at the microscopic level.

Despite decades of intense study, we still do not have a fully satisfactory microscopic understanding of magnetic hysteresis. To study the evolution of magnetic domains in magnetic-memory materials as they are cycled around their major and minor hysteresis loops, we developed a new form of coherent, reconstructionless x-ray speckle metrology and used it to demonstrate in thin, perpendicularly magnetized cobalt-platinum multilayers that the speckle patterns act as a fingerprint of the domain configurations and allow the ensemble of microscopic magnetic domains to be monitored. By auto- and cross-correlating the speckle patterns, we obtained a quantitative measure of the domain evolution and directly probed the microscopic mechanisms of hysteresis.

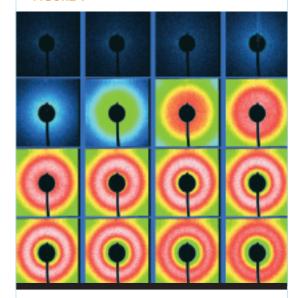
To obtain the desired hysteretic behavior, the magnetic-storage industry deliberately introduces carefully controlled disorder into its storage materials. Over the past 40 years, such magnetic hardening has developed into a high art form. To continue its phenomenal growth, the industry now believes that it will need to switch from longitudinal to perpendicular magnetic media in the next few years. Our group wanted to study the fundamental physics of the magnetic domains and of magnetic hardening in perpendicular magnetic media. Our idea was to use coherent soft x-ray magnetic scattering to study the magnetic structure at the magnetic domain length scale (~200 nm).

In particular, we investigated the phenomenon of magnetic return point memory (RPM). Suppose a magnetic system on the major hysteresis loop is subject to a change in the applied field that causes an excursion along a minor hysteresis loop inside the major loop; if the applied field is readjusted back to its original value and the sample returns to its initial magnetization, then macroscopic RPM is said to exist, but how do the ferromagnetic domains behave on a microscopic level? Do the domains remember (i.e., return precisely to) their initial states, or does just the ensemble average remember?

Microscopic RPM can be determined very precisely from magnetic speckle patterns. These patterns are produced by the (almost) randomly located magnetic domains. Changes in the magnetic speckle pattern will be produced by even small changes in the magnetic domains and can be determined by cross-correlating the magnetic speckle patterns, which is much easier than first inverting the speckle patterns to determine the real-space structure and then cross-correlating.

We performed our experiments at ALS Beamline 9.0.1, where the raw undulator beam is the most intense source of soft x rays in the world at the cobalt L_3 -edge resonant photon energy of 778 eV. To achieve transverse coherence, the raw undulator beam was passed through a 35-micron-diameter pinhole before

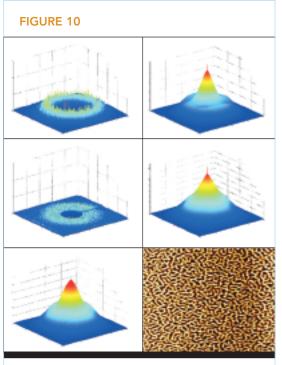
FIGURE 9



Measured magnetic speckle pattern versus applied magnetic field over the major hysteresis loop from -3000 to +1250 Oe. The pattern evolves from the featureless configuration in the magnetically saturated region of the hysteresis curve to the disk-like shape characteristic of a 2D gas of random domains to the annular shape characteristic of a 2D liquid of interacting domains at zero field. The shadow of the beam stop and the beam-stop support are visible in the center of and below each pattern. The color intensity scale is logarithmic.

SCIENCE HIGHLIGHTS

> MATERIALS SCIENCE



Coherent x-ray speckle metrology. *Top:* The measured speckle pattern at zero field and its autocorrelation function. *Center:* The measured speckle pattern at 2300 Oe and its autocorrelation function. *Bottom:* The cross-correlation function between the speckle patterns at 0 and 2300 Oe and the realspace magnetic force microscopy image of the magnetic domains (image size is $10 \times 7.5 \ \mu m$). The very sharp spike in the center of the auto- and cross-correlation functions is due to the speckles produced by the coherent scattering; the broad mountain under the coherent spike is due to the smooth average (incoherent) scattering.

being scattered in transmission by the sample. The resonant magnetic scattering was collected by a soft x-ray CCD camera. For samples, we deliberately introduced interfacial disorder into thin, multilayer, perpendicular cobalt–platinum magnetic-memory materials. With an electromagnet to apply fields perpendicular to the film,

we performed speckle measurements at various points around the hysteresis loops (Figure 9). The total number of photons in each speckle pattern was about 10⁹.

Our measurements of the speckle patterns and their analysis by auto- and cross-corrrelation (Figure 10) are the first direct determinations of the effects of disorder on major and minor loop microscopic RPM. We discovered that, contrary to the best current theories, our disordered magnetic storage materials partially remember their microscopic domain configuration, even after saturation.

The new coherent x-ray scattering cross-correlation method that we developed can also be used to study a wide variety of materials that also exhibit other types of hysteresis and memory effects for which we do not yet have a satisfactory microscopic understanding, including those in ferroelectrics, spin glasses, and shape memory materials.

INVESTIGATORS

M.S. Pierce, C.R. Buechler, R.G. Moore, and L.B. Sorensen (University of Washington); J.J. Turner and S.D. Kevan (University of Oregon); K.M. Chesnel and J.B. Kortright (Berkeley Lab); O. Hellwig and E.E. Fullerton (Hitachi Global Storage Technologies); and J. Hunter-Dunn (MAX-lab, Sweden).

FUNDING

U.S. Department of Energy, Office of Basic Energy Sciences, and German Research Foundation.

PUBLICATIONS

M.S. Pierce et al., "Quasistatic x-ray speckle metrology of microscopic magnetic return-point memory," *Phys. Rev. Lett.* **90**, 175502 (2003).

н

Magnetic Phase Transition in Coupled Magnetic Layers

Among the frontier areas of solid state research are magnetism, phase transitions from one form of matter to another, and so-called low-dimensionality materials (materials in the form of very thin sheets, wires, or dots). So it should be of no surprise that the study of magnetic phase transitions in ultrathin films is drawing a lot of attention, both for its fundamental importance to solid state theory and its centrality in advanced magnetic devices. Magnetic phase transitions include the switch from a magnetic to a nonmagnetic state when a material is heated above a "critical" temperature. It turns out that the critical temperature is lowered for thin layers by the effect of reduced dimensionality. Even more surprising, for two magnetic layers, each only a few atoms thick, separated by a nonmagnetic spacer layer, the critical temperatures are not always independent. Instead, the two layers talk to one another, as it were, through the spacer. Won et al. have used an x-ray microscope to make a detailed map (a phase diagram) of magnetic transitions in cobalt and nickel layers of varying thicknesses.

A magnetic phase transition occurs at a critical temperature (the Curie temperature for ferromagnetic materials) above which magnetic long-range order is lost. In addition to thermal fluctuations, the dimensionality of a ferromagnetic system plays a crucial role in magnetic phase transitions, making the Curie temperature of a ferromagnetic thin film lower than its corresponding bulk value. We have used x-ray photoemission electron microscopy to investigate the effect of magnetic interlayer coupling on magnetic phase transitions of magnetic nanostructures consisting of cobalt and nickel layers separated by copper or

iron spacer layers. With our data, we constructed a complete magnetic phase diagram in the cobaltnickel thickness plane.

Recently, many exotic phenomena have been explored in magnetic nanostructures that are due to the interlayer coupling between ferromagnetic layers across a nonmagnetic spacer layer. We focused on the interesting question: How does the magnetic interlayer coupling affect the magnetic phase transition of a coupled magnetic system? Experimental study of this topic was not possible until the development of x-ray magnetic circular dichroism (XMCD), which enables element-specific magnetic measurements. The photoemission electron microscope (PEEM-2) at ALS Beamline 7.3.1.1 was designed to take advantage of XMCD and thus was ideal for studying magnetic phase transitions in coupled magnetic systems.

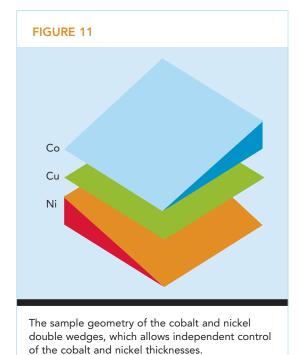
We investigated cobalt/copper/nickel and cobalt/iron/nickel sandwiches grown on copper(100) single-crystal substrates, where the cobalt and nickel ferromagnetic thin films are magnetically coupled across the thin copper and face-centered cubic (nonmagnetic) iron spacer layers. PEEM measurements can track separately the magnetic phase transitions of the cobalt and nickel layers. Because the Curie temperature of a thin film increases with film thickness, magnetic measurement as a function of film thickness at a fixed temperature (room temperature for our case) reveals a critical thickness at which the magnetic phase transition occurs. Then the effect of interlayer coupling on the magnetic phase transition can be explored by studying its effect on the critical thickness.

To precisely control the film thicknesses, we grew the cobalt and nickel films as crossed wedges (Figure 11), which we then scanned under the PEEM microscope. At each point, the microscope imaged only a small area in which the thicknesses were approximately constant. Magnetic domain images of the cobalt and nickel films were constructed by taking the ratio of intensities at the

SCIENCE HIGHLIGHTS

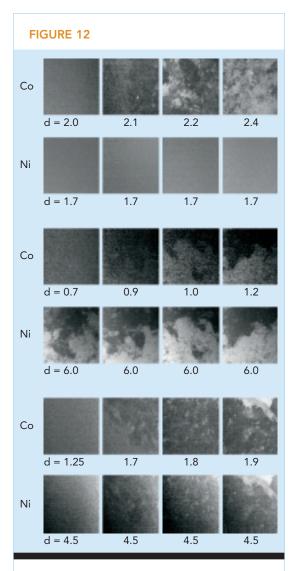
MATERIALS SCIENCE

SCIENCE HIGHLIGHTS



L₃ and L₂ edges of the cobalt and of the nickel, respectively. The critical thickness of cobalt or nickel film could be easily identified as that at which the magnetic domains disappeared (Figure 12). From these measurements, we constructed a complete magnetic phase diagram identifying three types of magnetic phase transitions as the film thicknesses increased (Figure 13). We also performed Monte Carlo simulations to better understand the phase transitions.

The first type of transition (from region I to region II or III) begins with both films in the paramagnetic state, and one film stays in the paramagnetic state while the other film undergoes the magnetic phase transition. For this case, the paramagnetic film has no effect on the phase transition of the other layer. In the second type of transition (from region II or III to region IV), one film stays in the ferromagnetic state and the other layer undergoes the magnetic phase transition. For this case, the ferromagnetic layer reduces the critical thickness of the other film (or increases the Curie temperature of the other film). In the third type of transition (from region I to region IV), both cobalt and nickel films undergo a single phase transition, even when one of the



PEEM images of the cobalt and nickel magnetic domains with changing layer thicknesses show the three types of magnetic phase transitions: type 1 (top), type 2 (center), and type 3 (bottom). Thicknesses d are given in monolayers (ML).

film thicknesses remains unchanged. For this case, the magnetic fluctuations of the two films are linked together by interlayer coupling.

INVESTIGATORS

C. Won, Y.Z. Wu, N. Kurahashi, H.W. Zhao, and Z.Q. Qiu (University of California, Berkeley) and A. Scholl and A. Doran (ALS).

FUNDING

U.S. Department of Energy, Office of Basic Energy Sciences; National Science Foundation; and Chinese Academy of Science. Magnetic phase diagram of cobalt/copper(2ML)/ nickel/copper(100). The triangles and squares are the cobalt and nickel critical thicknesses that define the magnetic phase transitions. The table

lists the magnetic states of the cobalt and nickel films in the four regions of the phase diagram.

PUBLICATIONS

C. Won et al., "Magnetic phase transition in Co/Cu/Ni/Cu(100) and Co/Fe/Ni/Cu(100)", *Phys. Rev. Lett.* **91**, 147202 (2003).

33

X-Ray Microdiffraction of Stress Gradients in Thin Metallic Films

A key metric in the economics of microchip fabrication is the yield, the fraction of chips manufactured that do not have fatal defects. The value of your semiconductor stock may depend on the company's ability to consistently achieve a respect-

able yield during the lengthy sequence of chip processing steps. One potential source of decreased yield that is of increasing concern as the metal conductors on chips become ever narrower is the generation of mechanical stresses during those processing steps where chips are heated to several hundred degrees centigrade and then cooled. These stresses can cause deformation in the metal that ultimately leads to circuit failure. Spolenak et al. have taken advantage of the ability of x-ray beams focused to very small spots less than one micrometer in diameter to measure the stresses in metal layers on semiconductor substrates after heating and cooling. Their discovery of microscopic variations (gradients) in the stress distributions may lead to a strategy for reducing stress and damage.

Metallic microcomponents are usually subject to relatively high mechanical stresses during the manufacture of integrated circuits. At first thought, one would assume that the deformation of a thin film on a substrate when heated and cooled would be uniform because the strain induced by the substrate is uniform. However, the voids and hillocks observed in thin-film systems indicate the contrary. Our industry/university/national laboratory collaboration has used x-ray microdiffraction to investigate local effects in an Al–0.5%Cu thin film, a typical alloy in microelectronics. Our observation of stress gradients within individual grains of the film suggests ways of minimizing damage during processing.

The stresses arise because the metal thin films are usually deposited onto semiconductor or ceramic substrates. Since most metals have a significantly higher coefficient of thermal expansion than their substrates, even small changes in temperature will lead to significant strains in the metallic layer and, consequently, to large mechanical stresses. For example, cooling an aluminum thin film on silicon from 400 °C to room temperature leads to a strain of roughly 0.8%. Even thin films, which can exhibit a sig-

SCIENCE HIGHLIGHTS

MATERIALS SCIENCE

nificantly higher yield stress than their bulk counterparts, deform plastically at such high strains.

The most appropriate way to investigate these effects is by measuring stresses and strains locally. Beamline 7.3.3 at the ALS provides an ideal tool to measure stresses by white-beam x-ray microdiffraction. With a spot size well below 1 μ m in diameter, even stress changes smaller than 20 MPa within a single grain can be determined. Laue patterns, which serve as the basis for stress analysis, are obtained for every spot on the sample. By moving the sample underneath the beam, complete stress maps are obtained.

Figure 14 shows stress maps in an Al-0.5%Cu thin film after cooling from 400 °C of the main deviatoric stress components and

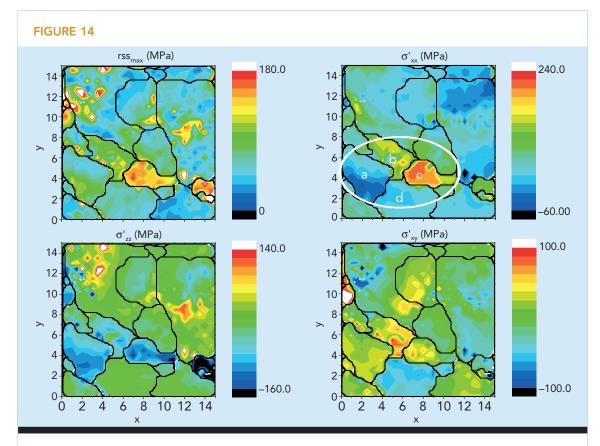
the maximum resolved shear stress (obtained by projecting the complete deviatoric stress tensor on all possible glide systems of a face-centered cubic lattice). The interesting observation is that not only do the stresses vary significantly from grain to grain, but they also exhibit gradients within single grains. Figure 15 illustrates how the observed gradients could arise: two grains with different yield stresses (stress at which dislocation motion causes plastic deformation) lead to shear stresses at the grain boundary and gradients in their neighbors.

The inability of the dislocations to move raises the yield stress. Usually in thin films, dislocation motion is constrained by the film thickness and the grain size. In particular, dislocations will travel only over a distance where the stresses

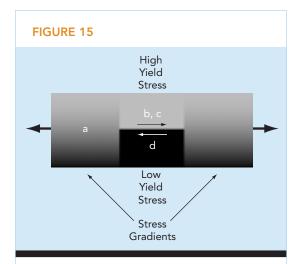
SCIENCE HIGHLIGHTS

MATERIALS SCIENCE

36



Deviatoric stress maps of a 15- μ m² area in the center of a 1.5- μ m-thick Al–0.5%Cu layer on a 200-nm-thick SiN $_x$ membrane. Top left: Resolved shear stress (rss $_{max}$) on the glide system experiencing the highest shear stress. Bottom left: Out-of-plane deviatoric stress in z (σ'_{zz}). Top right: In-plane deviatoric stress in x (σ'_{xx}). Bottom right: In-plane deviatoric shear stress in xy (σ'_{xy}). In σ'_{xx} , the area of interest is outlined with a white border, and the grains of interest are labeled alphabetically.

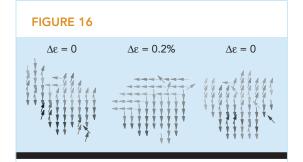


Schematic of stress scenario seen in a thin film. Two grains of different yield stresses lead to shear stresses at the grain boundary (arrows) and gradients in their neighbors. Shading from dark to light indicates increasing stress. The letters correspond to the analogous regions identified in Figure 14.

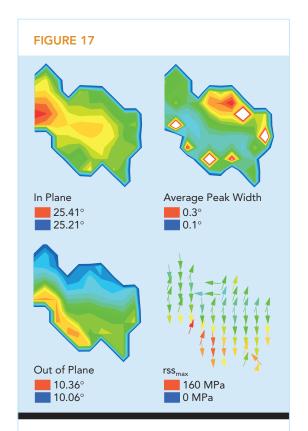
are uniform. Figure 16 shows that these stress "domains" within a grain can change their sign and size upon external stressing. Thus, the size of stress domains is an additional parameter that influences the yield stress of thin films. The smaller these domains are, the higher the yield stress will become in a particular grain.

Evidence that the grains investigated actually are at their yield stress is found in Figure 17. The change in crystal orientation over the width and length of the grain in conjunction with the local broadening of Laue peaks can only be accounted for by geometrically necessary dislocations that lead to grain rotation, a form of plastic deformation.

In summary, one can say that a significant step has been made toward understanding thinfilm plasticity. Damage in thin films and thus the reliability of microcomponents are strongly influenced by the local stress distribution. Finding the key parameters that will reduce the width of the distribution and eliminate high stresses will help the design of more reliable devices. The most promising candidates for process optimization are grain size and orientation distributions (texture).



Evolution of maximum resolved shear stress in grain a as a function of macroscopic strain ϵ in a bulge test (same grain as in Figure 15) up to 0.2% total strain. The vector plots show the projection of the glide directions experiencing the highest resolved shear stress, where the gray level corresponds to magnitude (white: 0 MPa, black: 140 MPa).



Single-grain analysis of grain a. Top left: In-plane orientation given by the angle between the [100] vector and the x axis. Bottom left: Out-of-plane orientation given by the angle between the surface normal and the [111] direction. Top right: Average peak width. Bottom right: Vector plot of the projection of glide directions experiencing the highest resolved shear stress. The color corresponds to the magnitude of the respective quantities.

SCIENCE HIGHLIGHTS

MATERIALS SCIENCE

INVESTIGATORS

R. Spolenak and W.L. Brown (Agere Systems); N. Tamura, A.A. MacDowell, R.S. Celestre, and H.A. Padmore (ALS); B. Valek and J.C. Bravman (Stanford University); T. Marieb and H. Fujimoto (Intel Corporation); and B.W. Batterman and J.R. Patel (ALS and Stanford Synchrotron Radiation Laboratory).

FUNDING

U.S. Department of Energy, Office of Basic Energy Sciences, and Intel Corporation.

PUBLICATIONS

R. Spolenak et al., "Local plasticity of Al thin films as revealed by x-ray microdiffraction," *Phys. Rev. Lett.* **90**, 096102 (2003).

N. Tamura et al., "Scanning x-ray microdiffraction with submicrometer white beam for strain/stress and orientation mapping in thin films," *J. Synch. Radiation.* **10** (Part 2), 137 (2003).

M. Phillips et al., "X-ray microdiffraction: Local stress distribution in polycrystalline and epitaxial thin films," *Microelectronic Engineering* **75**, 117 (2004).

SCIENCE HIGHLIGHTS

MATERIALS SCIENCE

ENVIRONMENTAL AND EARTH SCIENCE

::

High-Quality X-Ray Scattering Data for Water

For all its importance to our very existence, water continues to evade complete scientific understanding. Its structure (i.e., the locations of the atoms) is a case in point. In the main form of solid water (ice), each water molecule is bonded to four water neighbors in a rigid structure made up of connected hexagonal rings. When the ice melts, there is a broader distribution of bonding configurations, including a variety of polygons of varying sizes and degrees of puckering or distortion, that make the structure of liquid water more difficult to determine. The venerable technique of x-ray scattering (in which an x-ray beam shining on a sample emerges with different intensities at various directions) has long been used to study the structure of liquid water. Hura et al. have not only improved this technique, but they have combined it with a comparison of measured scattering patterns with those calculated from theoretical models of liquid water to determine the best model over a wide range of biologically relevant temperatures.

Given the importance of water, it is no surprise that determining the geometrical structure of this life-giving liquid has a long history. In principle, an accurate characterization of the structure of liquid water can be obtained from x-ray and neutron scattering experiments. However, the inconsistency in the experimental results over the past 30 years means that an accurate measurement of water structure is still needed. Our group from the University of California, Berkeley, and Berkeley Lab has now reported x-ray scattering data for pure water taken over the biologically relevant temperature range of 2–77 °C that is not only of higher quality than that obtained in the

past, but whose x-ray scattering intensities are qualitatively different from older x-ray data.

Structural information in the form of radial distribution curves can be derived from scattering data by Fourier transformation of the measured intensity curve as a function of the momentum transfer, O, to give the molecular centers distribution function of water (Figure 1). But before this transformation, it is necessary to correct the experimental data for several factors. Our new data from ALS Beamline 7.3.3 spans work over the last two years, in which we were able to gather high-quality x-ray scattering data for water over a range of temperatures relevant to most life processes. The error estimates for the data were smaller than the discrepancies between data sets collected in past x-ray experiments (Figure 2). This achievement was due to

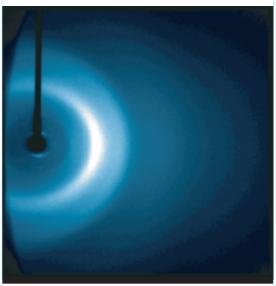
HIGHLIGHTS

ENVIRONMENTAL AND EARTH SCIENCE

39

SCIENCE

FIGURE 1

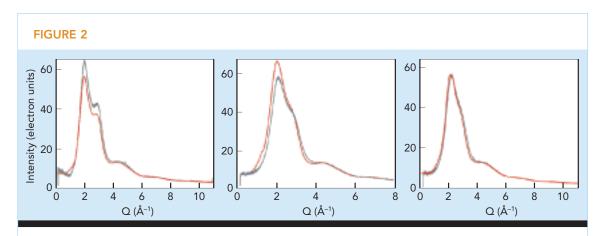


X-ray scattering pattern of liquid water at room temperature and pressure. Structural information can be extracted from the pattern either by Fourier transformation or by comparing it directly with patterns calculated from models of water.



ENVIRONMENTAL AND EARTH SCIENCE

40



Comparison of ALS experiments (gray) with older x-ray experiments (red) at three temperatures from 2 °C (left) to 77 °C (right) shows a qualitative difference that lies outside the error bars of the ALS experiment.

the use of a highly monochromatic source (the ALS), a well-characterized polarization correction, a Compton scattering correction that includes electron correlation effects, and better resolution and more accurate intensities from a modern CCD detector.

In addition to gathering data over a range of temperatures important to water, we introduced a new approach to interpreting the data. The common practice has been to report both the intensity curve and the radial distribution functions extracted from it, but the proper extraction of the real-space pair-correlation functions from scattering data is very difficult because of uncertainty introduced in the experimental corrections; the proper weighting of oxygen-oxygen, oxygen-hydrogen, and hydrogen-hydrogen contributions; and numerical problems of Fouriertransforming data truncated in Q-space. Instead, our group undertook the alternative strategy of directly calculating the x-ray scattering spectra from electron densities derived from density functional theory based on real-space configurations generated with classical water models. The model providing the most accurate simulation of the experimental intensity was then used to calculate the real-space pair-correlation functions (Figure 3).

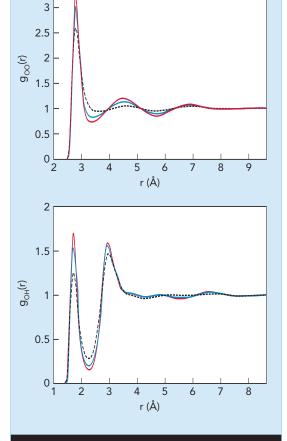
Water models start with "normal" ice (at least 13 other structures are known), in which a

water molecule is hydrogen bonded to four water neighbors in a tetrahedral structure, resulting in a crystal comprising connected hexagonal rings. In liquid water, the greater translational and rotational motion of the water molecules yields a broader distribution of hydrogen-bonded configurations. As temperature and pressure are increased or decreased, the structure of the 3D hydrogen-bonded network of water changes, giving rise to the well-known anomalous properties of liquid water. These altered water properties expand the functional versatility of the liquid solvent.

Models of the structure of water range from those derived from empirical force fields, to more recent models that incorporate manybody effects through polarizability, and finally to first-principles molecular dynamics studies based on well-defined approximations to the Schrödinger equation. We found that among the models showing very good agreement with the experimental intensities, the polarizable water model TIP4P-Pol2 shows quantitative agreement over the full temperature range. The resulting radial distribution functions calculated from TIP4P-Pol2 provide the current best benchmarks for real-space water structure over the biologically relevant temperature range studied in these experiments.

FIGURE 3

3.5



Real-space pair-distribution functions from the TIP4P-Pol2 model, which best reproduces the experimental x-ray scattering intensity curves for oxygen-oxygen (top) and oxygen-hydrogen (bottom) at 2 °C (red), 25 °C (blue), and 77 °C (dashed).

INVESTIGATORS

G. Hura, D. Russo, R.M. Glaeser, and T. Head-Gordon (University of California, Berkeley, and Berkeley Lab); M. Krack (Swiss Center for Scientific Computing, Manno, Switzerland); and M. Parrinello (ETH-Zurich, Switzerland).

FUNDING

National Institutes of Health, National Science Foundation, and Berkeley Lab Laboratory Directed Research and Development.

PUBLICATIONS

G. Hura et al., "Water structure as a function of temperature from x-ray scattering experiments and ab initio molecular dynamics," *Phys. Chem. Chem. Phys.* **5**, 1981 (2003).

T. Head-Gordon and G. Hura, "Water structure from scattering experiments and simulation," *Chem. Rev.* **102**, 2651 (2002).

SCIENCE HIGHLIGHTS

ENVIRONMENTAL AND EARTH SCIENCE

STRUCTURAL BIOLOGY

::

Designing a Novel Globular Protein Fold

DNA provides the starting recipe for the manufacture of proteins, large molecules that carry out much of the work that make up the daily life of a cell. How proteins do this work depends on their 3D structure, which is replete with folds, crevices, and other features that form from strings of molecules known as amino acids. But given only the sequence of amino acids specified by DNA, scientists cannot predict the final folded and compacted protein structure and, hence, how it works. Being able to predict structures could also confer to biologists the ability to design artificial protein structures that might themselves be useful. Kuhlman et al. have made a major advance toward this goal with a mathematical technique that takes the reverse approach of determining which amino-acid sequence will result in a specified protein structure. The researchers have tested their technique by designing a protein that does not exist in nature, synthesizing the protein, and verifying its structure at the ALS.

A major challenge of computational structural biology has been to create, from scratch, new proteins with heretofore unobserved 3D structures. Our collaboration from the University of Washington, Seattle, the University of North Carolina, Chapel Hill, and the Fred Hutchinson Cancer Research Center has now developed and demonstrated a methodology for protein structure prediction and design by creating the first artificial globular protein with a novel topology, a 93-residue protein called Top7. Significantly, the x-ray structure of Top7 agreed almost precisely with the structure specified by the computational model.

Protein function depends on the complex geometries assumed as sequences of amino acids (each comprising a carboxyl group, an amino group, and a side chain) link into chains of residues that form local structural units such as α helices and β strands, and finally fold into compact, 3D globular domains and multidomain structures. Previous computational protein design attempts have focused primarily on redesigning the sequence of naturally occurring proteins to enhance their stability or to achieve new functionality.

These methods generally start with a known, high-resolution structure of the target protein and then try to optimize the packing of different amino-acid side chains while keeping the backbone template (carboxyl and amino groups) fixed to arrive at new low-energy sequence solutions. The key features of these methods are an efficient search protocol for sampling the theoretically vast number of sequence permutations and an energy function designed to model the physical forces that hold natural proteins together.

We extended these concepts in our RosettaDesign method. However, we were faced with the additional challenge of sampling proteinbackbone structural space as well as sequence space, since our goal was the creation of a novel fold (where no natural backbone template was available). To this end, we constructed Rosetta-Design to iterate between full-scale optimization of the sequence for a fixed-backbone conformation and gradient-based optimization of the backbone coordinates for a fixed sequence. Beginning with a simple back-of-the-envelope sketch of the target, a novel α/β fold, and this protocol, we designed Top7, a 93-residue α/β protein with a topology not observed in the Protein Database (PDB), i.e., an artificial protein.

By means of a variety of biophysical techniques, we determined the synthesized Top7

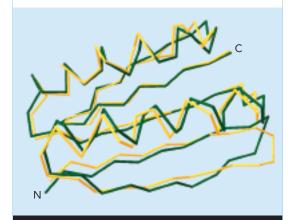
SCIENCE HIGHLIGHTS

STRUCTURAL BIOLOGY

protein to be monomeric, highly soluble, and extremely stable to chemical and thermal denaturation. Preliminary nuclear magnetic resonance (NMR) analysis also showed that Top7 had a rigid structure consistent with the target topology. Finally, thanks to the ALS Howard Hughes Medical Institute Beamline 8.2.1, we solved an x-ray structure of a single selenomethionyl-substituted variant of Top7 to 2.5-Å resolution with single-wavelength anomalous diffraction data.

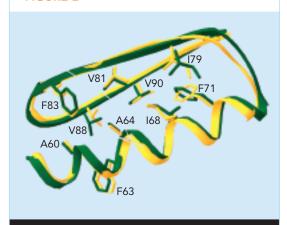
This high-resolution crystal structure revealed that the Top7 protein adopted the designed topology and in fact was strikingly similar to the design model at atomic resolution (1.17-Å root-mean-square deviation, or RMSD, over all backbone atoms, Figure 1). The two models differ most in the region surrounding the first N-terminal (amino-group end) hairpin, but even here the all-atom RMSD did not exceed 2.8 Å. In contrast, the C-terminal (carboxyl-group end) halves of the crystal structure and the designed model are very similar, and core side-chain atoms are virtually superimposable (Figure 2).

FIGURE 1



Comparison of the x-ray crystal structure of Top7 (yellow) to the computationally designed model (green). The $C-\alpha$ overlay of the structure and model shows the overall high accuracy of the design (1.17-Å RMSD).

FIGURE 2



Comparison of the x-ray crystal structure of Top7 (yellow) to the computationally designed model (green). The side chains in the core of the C-terminal portion of the Top7 structure are effectively superimposable with the model.

The successful design of Top7 has two major implications. First, it is a strong validation of the understanding and description of the energetics of proteins and other macromolecules, much of which, incidentally, has been a consequence of the determination of high-resolution structures of those macromolecules. Second, it suggests that the development of protein therapeutics and molecular machines need not be limited to the structures sampled by the biological evolutionary process.

INVESTIGATORS

G. Dantas, G. Varani, and D. Baker (University of Washington, Seattle); B. Kuhlman (University of North Carolina, Chapel Hill); and G.C. Ireton and B.L. Stoddard (Fred Hutchinson Cancer Research Center, Seattle).

FUNDING

National Institutes of Health and Cancer Research Fund of the Damon Runyun–Walter Winchell Foundation.

PUBLICATIONS

B. Kuhlman et al. "Design of a novel globular protein fold with atomic-level accuracy," *Science* **302**, 1364 (2003)

SCIENCE HIGHLIGHTS

STRUCTURAL BIOLOGY

::

Structure of Telomere-Protecting Proteins

Chromosomes in the nuclei of cells contain DNA with the recipe for life, so it is fortunate indeed that nature has devised ways to protect and repair chromosomes. One protection mechanism comes in the form of telomeres, highly specialized complexes of DNA and protein molecules that form end caps for chromosomes, including regions at the very tip of single- rather than double-stranded DNA. Since the normal DNA-replication process during cell division doesn't work in this region, an enzyme called telomerase takes care of this. Protection of telomeres (Pot1) proteins have now been found in organisms ranging from yeasts to humans and appear to be essential to the endcapping process. They may also be part of the process by which the telomere is made available to telomerase during replication. Lei et al. have obtained a high-resolution structure of the portion of a Pot1 protein with a region of single-stranded DNA (ssDNA) in yeast. The details of their structure provide a framework for understanding telomere functions at the molecular level.

Telomeres are specialized protein–DNA complexes that cap the ends of linear chromosomes in eukaryotic cells. Recent discoveries in organisms from yeasts to humans have shown that Pot1 (protection of telomeres) proteins are involved in the chromosome capping, but the molecular mechanism for the binding between Pot1 and DNA remained unknown. Our group from the University of Colorado at Boulder and the Stowers Institute for Medical Research has now obtained high-resolution x-ray crystallography structures of complexes comprising a DNA-binding domain of Pot1 and sections of DNA in yeast that explain the binding specificity.

Telomeres play an essential role in maintain-

ing the integrity of the chromosome, protecting it from degradation and from end-to-end fusion with other chromosomes. They also serve as substrates for the enzyme telomerase, which is reponsible for replicating the end region in cell division. The DNA component of telomeres usually begins with a double-stranded region consisting of repeated sequences of five to nine base pairs, where the number of base pairs varies from species to species. It then ends with a single-stranded region rich in guanine (G) and thymine (T) bases called a 3' overhang that bends back on itself to facilitate a protective t-loop structure.

Among proteins specific for this singlestranded overhang, Pot1 proteins provide the most widespread solution to chromosome endcapping in eukaryotes. Our previous biochemical work showed that the N-terminal DNA-binding domain Pot1pN in the fission yeast Schizosaccharomyces pombe, a popular model organism, had a sequence similarity to the first OB (oligonucleotide/oligosaccharide binding) fold of the α subunit of the telomere end-binding protein of the ciliated protozoan Oxytricha nova. However, without any structural information, the molecular basis for the DNA-binding specificity that ensures that Pot1 only binds to single-stranded G-rich telomeric DNA was not revealed.

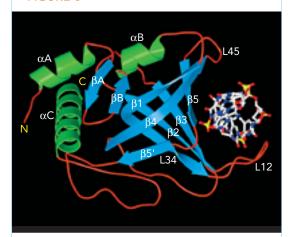
To explore the molecular mechanism of this binding specificity, we crystallized Pot1pN in three different forms in complex with either the pentanucleotide GGTTA or the hexanucleotide GGTTAC. From data obtained at ALS Beamlines 8.2.1 and 8.2.2, we solved the structure of one Pot1pN–GGTTA crystal form by means of single-wavelength anomalous dispersion and refined the structure to a resolution of 1.9 Å. Then we determined the structures of the other two crystal forms by molecular replacement and a searching model without the ssDNA. We found that the structures were essentially identical in all three crystal forms.

The crystal structure shows that Pot1pN consists of a compact single domain, the OB fold,

SCIENCE HIGHLIGHTS

STRUCTURAL BIOLOGY

FIGURE 3



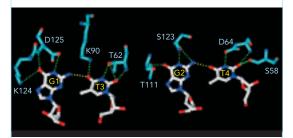
Structure of the Pot1pN-ssDNA complex. Ribbon diagram of Pot1pN exhibits β -strands (cyan), α -helices (green), and loops (red). The DNA, shown in a stick representation with carbon (white), nitrogen (blue), oxygen (red), and phosphorus (yellow), fits into a groove formed by one side of the β barrel and two protruding loops.

comprising a highly curved, five-stranded, antiparallel β barrel, as implied by the sequence alignment. The single-stranded DNA binds in a basic concave groove, a characteristic of OB-fold proteins, formed by one side of the β barrel and two protruding loops (Figure 3).

More importantly, the structure explains the exceptionally high sequence specificity of protein binding. An unanticipated ssDNA self-recognition involving novel G-T base pairing compacts the DNA (Figure 4), and this folded DNA structure is bound by the protein through stacking and hydrogen bonding. Any base sequence change would disrupt the ability of the DNA to fold into this structure, thus preventing it from contacting the array of protein hydrogen-bonding groups. Mutational analysis established the in vivo biological importance of the Pot1-ssDNA interaction by showing that two residues that were already implicated by the structure in DNA binding are also important for telomere maintenance and cell survival (Figure 5).

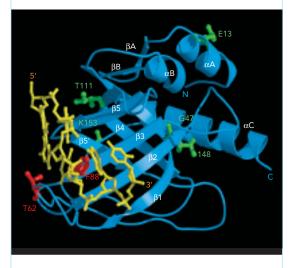
The structure will serve as a framework for understanding telomere functions at the molecular

FIGURE 4



Self-recognition of ssDNA by G-T base pairing interactions and binding with the protein. Owing to the ssDNA intramolecular hydrogen bonds (yellow), the donor/acceptor groups of the bases face the inner side of the binding groove, thus encouraging extensive intermolecular hydrogen bonding interactions with the protein (green).

FIGURE 5



The in vivo biological importance of the Pot1–ssDNA interaction. Mutational analysis of residues important to the interaction of Pot1pN (blue) and ssDNA (yellow) showed that the red mutations, T62 and F88, already implicated by the structure in DNA binding, are also important for telomere maintenance and cell survival. The mutated residues are shown as green and red ball-and-stick models.

level. These functions include Pot1 protein's essential role in chromosome end-capping in *S. pombe*, its contribution to regulation of telomerase in human cells, and its proposed role in switching telomeres between the protective t-loop and an open structure accessible to telomerase during replication.

SCIENCE HIGHLIGHTS

STRUCTURAL BIOLOGY

INVESTIGATORS

M. Lei, E.R. Podell, and T.R. Cech (University of Colorado) and P. Baumann (Stowers Institute for Medical Research).

FUNDING

National Institutes of Health, Stowers Institute for Medical Research, and Helen Hay Whitney Foundation.

PUBLICATIONS

M. Lei et al., "DNA self-recognition in the structure of Pot1 bound to telomeric single-stranded DNA," *Nature* **426**, 198 (2003).

:::

Structure of RNA Polymerase II and Initiation of Transcription

SCIENCE HIGHLIGHTS

STRUCTURAL BIOLOGY

46

It does no good to have a huge library if there is no way to access the books and read them. It's the same story with genetic information. DNA gets all the attention as the library for genes, but constructing a functioning human requires translating them into the molecules of which we are made. The first step in this transformation is transcribing the genetic information into carrier molecules called messenger RNA. As with almost every cellular function, enzymes catalyze the biochemical reactions that make up the transcription process. In humans, the enzyme comes in three varieties: RNA polymerase I, II, and III. Bushnell and Kornberg have determined the atomic structure of the complete RNA polymerase II (pol II). The details of the structure show how the enzyme grasps the DNA so that it can be read to make RNA. Understanding pol II is of great importance, since it should provide insight into gene expression and the many processes that are affected by gene expression.

Before the genetic information that is stored in a cell can be put to use, DNA must first be

transcribed into messenger RNA, which is then translated to produce a protein. Transcription is directed by an enzyme called RNA polymerase, the most of important of which for higher organisms, like humans, is RNA polymerase II, or pol II. We have been able to crystallize the full 12-subunit, initiation-competent form of pol II and have determined the structure to a resolution of 4 Å by x-ray crystallography. The new structure clarifies the important role of the two subunits, Rpb4 and Rpb7, in initiating transcription by clamping the DNA so that its sequence can be read.

There are three closely related RNA polymerases termed RNA polymerase I, II, and III. While the three polymerases are related, RNA polymerase II or pol II is responsible for the vast majority of messenger RNA produced. If we understand how pol II works, we should gain insight into gene expression and the many processes that are affected by gene expression. Pol II is a large protein complex with a mass about 0.5 Mda and up to 12 subunits. This complex molecular machine is capable of unwinding DNA, making RNA, and proofreading the RNA. The atomic structure of pol II should give insights into how it works, and scientists have spent much effort attempting to solve its structure. In 2001, after 10 years of effort, the atomic model of the core 10 subunits of pol II was solved to 2.8 Å by means of x-ray crystallography at high-intensity sources.

To start transcription, pol II requires two additional subunits: Rpb4 and Rpb7. These two subunits are known to form a stable complex that can disassociate from pol II, but little is known about their role in transcription initiation. In bakers' yeast, the most-studied form of pol II, Rpb7 is required for cell viability and has OB (oligonucleotide/oligosaccharide binding) and RNP (ribonucleoprotein) domains, both of which can interact with RNA. Rpb4, however, is not essential, and its only distinct sequence characteristic is a highly charged domain. The next

obvious step was to add subunits Rpb4 and Rpb7 to the 10-subunit core and see what the initiation-competent form of the enzyme looked like.

We were eventually able to grow crystals, which we took to ALS Beamline 8.2.1, where we collected diffraction data to 4 Å. This resolution was sufficient to dock the 10-subunit pol II structure and the structure of archaeal homologs of Rpb4 and Rpb7. For the first time, we understood how the Rpb4 and Rpb7 subunits were associated with pol II. We found that they were located next to a large mobile region of pol II termed the clamp, which resides along one of the two possible RNA exit channels (Figure 6). The clamp had previously been shown to move by as much as 18 Å, and the state of the clamp is important for RNA and DNA interaction.

Only when the clamp is closed is pol II in a state where DNA can be read to make RNA. Rpb4 and Rpb7 buttress the clamp into a closed state by connecting it to a nonmobile region of

pol II. Forcing the clamp closed in this way leaves pol II in a state where it can interact with DNA properly to make RNA. Once the DNA is threaded and RNA production has started, the clamp will stay closed and Rpb4 and Rpb7 can leave. It is possible that the RNA-binding site of Rpb4 plays an additional role by interacting with the newly synthesized RNA, but this hypothesis requires further investigation.

INVESTIGATORS

D.A. Bushnell and R.D. Kornberg (Stanford University).

FUNDING

National Institutes of Health, American Cancer Society, and U.S. Department of Energy, Office of Biological and Environmental Research.

PUBLICATIONS

D.A. Bushnell and R. D. Kornberg, "Complete, 12-subunit RNA polymerase II at 4.1-Å resolution: Implications for the initiation of transcription," *Proc. Nat. Acad. Sci.* **100**, 6969 (2003).

FIGURE 6

Clamp

RNA Exit Path 1

Ribbon representation of the complete pol II structure. Views from the top (*Ieft*) and back (*right*) show the Rpb4 (*red*), the N-terminal half of Rpb7, which contains the RNP domain (*dark blue*), and the C-terminal half of Rpb7, which contains the OB fold (*light blue*). The locations of the clamp and of the previously proposed RNA exit path 1 are indicated. This figure was generated with Swiss-PDB viewer and POV-ray.

SCIENCE HIGHLIGHTS

STRUCTURAL BIOLOGY

н

The Unusual Open-Ring Structure of the Rho Transcription Termination Factor

Decoding the genetic information held in doublestranded DNA begins with the process called transcription, which produces single-stranded messenger RNA. An important question for organisms from humans to bacteria is how to terminate transcription in time to insure that only the proper information is decoded, since the messenger RNA migrates to the cellular factory where the molecules of life are manufactured. It turns out that bacteria accomplish this task via an enzyme known as the Rho transcription termination factor, or simply the Rho factor. A great deal of research has revealed the basics of how the Rho factor works, but without an atomic structure of the molecule, many mysteries remained. Skordalakes and Berger have obtained such a structure for the Rho factor in contact with a segment of messenger RNA. Their structure, which includes an unusual openring conformation, not only answers many questions regarding the function of Rho in transcription termination, but it probably also represents a general operating mechanism for a number of essential molecular machines.

The proper termination of the transcription of DNA into messenger RNA is essential for gene expression. In bacteria, one mechanism of transcription termination requires the action of a hexameric, $5'\rightarrow 3'$ RNA/DNA helicase known as the Rho factor. Despite a plethora of available biochemical, genetic, and electron microscopy information, many mechanistic questions regarding the function of Rho in transcription termination have remained unanswered. To help address these issues, we have solved the structure of the

full-length Rho hexamer in complex with a nucleic acid substrate and an adenosinetriphosphate (ATP) mimic at 3.0-Å resolution.

Rho initially binds about 40 bases of cytosinerich, single-stranded RNA (ssRNA) in a nascent transcript via its primary RNA binding site, which is located in its N-terminal domains. Once Rho attaches, the RNA is passed on to a set of secondary RNA binding sites, located in its C-terminal domains. Binding at the secondary sites activates ATP hydrolysis, a function essential to the activity of Rho. Once activated in this manner, Rho uses energy derived from ATP hydrolysis to translocate along the messenger RNA until it reaches an RNA polymerase stalled at a pause site. Rho then unwinds the RNA/DNA duplex trapped in the polymerase, terminating transcription.

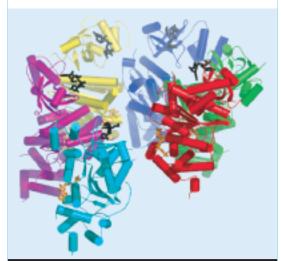
Our structure, based on data obtained at ALS Beamline 8.3.1, showed that within the hexamer, the N- and C-terminal domains of each subunit are organized to position the primary RNA binding site adjacent to the secondary RNA binding sites (Figure 7). The result of this arrangement is that each primary site is poised to

SCIENCE HIGHLIGHTS

STRUCTURAL BIOLOGY

48

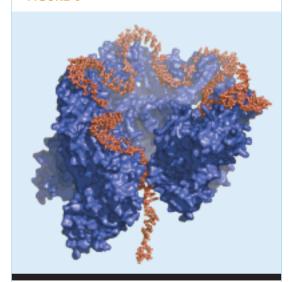
FIGURE 7



Structure of Rho transcription termination factor in complex with ssRNA (black) and the ATP analogue ANPPNP (orange).

feed the 3' end of the bound RNA segment into the hole of the ring where translocation occurs. Interestingly, biochemical studies have shown that Rho can bind over 70 nucleotides of RNA; this capability derives from arranging the six primary RNA binding sites such that the RNA "zigzags" from site to site around the perimeter of the ring (Figure 8).

FIGURE 8



Model of the Rho transcription termination factor bound to an extended ssRNA segment. The ssRNA "zig-zags" about the periphery of the interior of the N-terminal domains, an arrangement that feeds the 3' end of the RNA into the hole of the ring. Perspective is as in Figure 7.

The Rho structure also revealed a key and unexpected conformational state of the helicase: rather than being closed, the molecule forms a ring that is split open at one point. The opening gives rise to a single gap that breaches the ring. The width of the gap is about 12 Å, a distance sufficient to accommodate the entry of single-stranded nucleic acid into the hole of the ring. As a result, the structure appears to represent a conformation of Rho that is likely accessed when it loads onto RNA.

Finally, the structural model helps explain how a number of conserved signature sequence motifs—the P, Q, and R loops—communicate with each other during Rho function. Each of these regions turns out to be co-localized in the interior of the hexamer. The result of this arrangement is that any RNA that binds in the hole of the ring would contact some of these loops (the Q and R motifs) directly, an interaction that would in turn be communicated to catalytic elements responsible for ATP liganding and hydrolysis (the P loop). By this route, Rho is therefore organized to couple the chemical energy of ATP to translocation along RNA.

One additional feature of note in this regard is that we observed the Rho hexamer bound to the ATP analogue ANPPNP in all six of its ATP binding sites, and for this to occur, it appears that the ATP-binding pocket needs to be further conformationally rearranged, an event that could occur upon closure of the hexameric ring, as the appropriate contacts are formed between Rho and its messenger RNA substrate.

In conclusion, we note that the unusual open-ring arrangement of the Rho hexamer has significance for the action of a number of other essential motor proteins, and it probably represents a general mechanism by which some of these molecular machines likewise associate with their target substrates.

INVESTIGATORS

E. Skordalakes and J.M. Berger (University of California, Berkeley).

FUNDING

G. Harold and Leila Y. Mathers Charitable Foundation.

PUBLICATIONS

E. Skordalakes and J.M. Berger, "Structure of the Rho transcription terminator: Mechanism of mRNA recognition and helicase loading," *Cell* **114**, 135 (2003).

SCIENCE HIGHLIGHTS

STRUCTURAL BIOLOGY

н

Protein Pump Reveals Secrets of Drug Resistance

They say that what doesn't kill you makes you stronger. Despite the development in the twentieth century of "miracle drugs" such as penicillin, scientists have begun to report the emergence of drug-resistant strains of bacteria that were once considered in check. Antibiotics, if used judiciously and conscientiously, can eradicate a bacterial infection; however, their inappropriate or incomplete use provides an opportunity for any drugresistant mutations in a population to flourish. As a result, bacteria that were once considered benign or controllable, such as those responsible for food poisoning, tuberculosis, and pneumonia, are reemerging in more aggressive forms that are more difficult to treat. Basic research plays a critical role in responding to this problem. The AcrB pump, as revealed by the atomic structure determined by Yu et al., is extremely versatile in trapping and expelling toxins (including antibiotics) from bacteria. Although strategies for inhibiting these pumps are still at the early stages of research, structural knowledge about such bacterial defense mechanisms can lead to more effective avenues for drug-based counterattack.

In the race to stay one step ahead of drugresistant bacteria, our group from the University of California, Berkeley, and Berkeley Lab obtained high-resolution structures of AcrB, a bacterial protein complex that repels a wide range of antibiotics. The structures offer new insight into how bacteria survive attacks from different antibiotics, a growing health problem called multidrug resistance. As we learned, these robust defenses are rooted in the protein complex's remarkable ability to capture and pump out a spectrum of structurally diverse compounds. The research may inform the development of antibiotics that either evade or inhibit these pumps, allowing drugs to slip inside bacteria cells and kill them.

AcrB is a protein that resides in the inner membrane of Escherichia coli cells. It works in unison with two other proteins to rid the bacteria of toxins. Based on earlier studies, we knew that AcrB boasts a large cavity capable of binding with a vast range of antibiotics and other molecules. But precisely how this cavity accommodates so many shapes and sizes remained unclear. To witness this trickery, we crystallized the protein in the presence of four molecules an antibiotic, a dye, a disinfectant, and a DNAbinding molecule-and exposed the crystals to extremely bright x rays at ALS Beamline 8.2.2. The resulting 3.5- to 3.8-Å-resolution images provide the closest look yet at a phenomenon common to all living cells: the ability to expel a diverse flotilla of toxins using one pump.

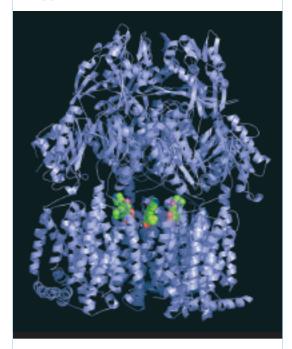
Multidrug pumps such as AcrB play important, but double-edged, roles. Normally, harmless colonies of E. coli inhabit animal intestines. In this environment, scientists theorize that AcrB's chief function is to trap and expel bile salt, which is toxic to the bacteria. Unfortunately, if a mutated form of E. coli causes food poisoning, a broad regimen of antibiotics is needed to fight the infection because AcrB shields the bacteria from many more compounds in addition to bile salt. In the structures obtained at the ALS, each of the four molecules crystallized with AcrB bonded to a different location in the protein's cavity, and each bond utilized a different set of amino-acid residues (Figure 9). The researchers suspect the cavity possesses areas where many types of antibiotics could be captured.

These results underscore the need to pursue alternative ways of fighting drug resistance. Currently, pharmaceutical researchers combat resistance by tweaking an antibiotic's molecular structure so that it isn't compatible with a pump's binding site. This is difficult work to begin with, largely because antibiotics must adhere to strict potency and safety regulations that limit the

SCIENCE HIGHLIGHTS

STRUCTURAL BIOLOGY

FIGURE 9



Even ciprofloxacin, an antibiotic used to treat a variety of bacterial infections including inhaled anthrax, is no match for AcrB. In this image, the drug (green) is firmly ensnared in the protein's cavity.

extent to which they can be modified. Add to these restrictions a better understanding of AcrB's readiness to bind with an array of compounds, including the most carefully engineered antibiotics, and the job appears even more difficult.

Instead, we believe our work supports another strategy in which the multidrug pump is disabled. In *E. coli*, such monkey-wrenching is possible because AcrB connects to a funnel-shaped protein embedded in the bacteria cell's outer membrane. This protein ejects the antibiotics trapped in the AcrB cavity. If a specially designed molecule could lodge inside the funnel, the pump would be rendered useless and antibiotics would be allowed to slip inside the cell unhindered.

To support these advancements in drug design, our team will next use the ALS to more fully explore how AcrB binds with a structurally diverse range of antibiotics. We believe a fuller understanding of the *E. coli* multidrug pump will shed light on similar pumps found in other harmful

bacteria, which could lead to better treatments for a variety of infections.

INVESTIGATORS

E.W. Yu, H.I. Zgurskaya, H. Nikaido, and D.E. Koshland, Jr. (University of California, Berkeley) and G. McDermott (Berkeley Lab).

FUNDING

Howard Hughes Medical Institute and National Institutes of Health.

PUBLICATIONS

E.W. Yu et al., "Structural basis of multiple drug-binding capacity of the AcrB multidrug efflux pump," *Science* **300**, 976 (2003).

-

Glycoprotein Receptor Yields Clues to Platelet "Stickiness"

Most of us are fortunate indeed that our blood clots. Otherwise, like those suffering from bleeding disorders such as hemophilia, we would find injuries as trivial as paper cuts to be life-threatening. Sometimes clotting is not so beneficial, as those surviving heart attacks and strokes resulting from narrowed arteries blocked by clots know full well. Clotting itself is a quite complex process ending in the production of fibrin molecules that clump together into an insoluble mesh and capture red blood cells and platelets, thereby forming a clot. One of the many key steps is that by which the platelets become sticky. The enzyme thrombin plays a role, when it binds to GpIb α , a receptor on the surface of platelets. Dumas et al. have determined the molecular structure of the part of the receptor involved in the binding while the binding is underway. Understanding the binding mechanism offers opportunities for developing drugs to treat coronary artery and related diseases by controlling overzealous clotting.

SCIENCE HIGHLIGHTS

STRUCTURAL BIOLOGY

Glycoprotein Ibα (GpIbα), a receptor on the surface of platelets in the blood, binds to several signaling molecules including thrombin, an enzyme released from damaged tissue that is required for blood clotting. Abnormal (both too much and too little) GpIbα-thrombin binding is associated with many pathological conditions, including the formation of blood clots that can cause heart attacks and strokes by blocking arteries (thrombosis) and bleeding disorders such as hemophilia. To gain insight into the adhesive mechanism by which platelet receptors regulate formation of a blood clot, our group from Wyeth Research has determined the crystal structure of a key portion of the GpIbα receptor in complex with thrombin.

Direct interaction between GpIba and thrombin is essential for initiation of platelet procoagulant activity, and exposure to very small concentrations (< 1 nM) of thrombin is sufficient to induce aggregation and activation at sites of vascular injury. The portion of the GpIbα receptor we studied is the extracellular domain, which resides outside the platelet membrane. The crystal structure of the complex, obtained to a resolution of 2.6 Å at ALS Beamline 5.0.1, operated by the Berkeley Center for Structural Biology, provides important details of GpIbα-thrombin interactions, thereby opening promising avenues both for further investigation and for development of novel antithrombotic drugs to treat coronary artery and other diseases that involve reduced blood flow.

The structure reveals that both the GpIb α and thrombin molecules are bivalent. Two highly electronegative regions on the surface of GpIb α simultaneously interact with two positively charged surface patches or "exosites" located on opposite poles of thrombin (exosites I and II). In the crystals, pairs of GpIb α and thrombin molecules associate as crystallographically independent complexes (Figure 10). Two types of GpIb α -thrombin interfaces that are related by crystal symmetry are evident within adjacent

Inhibitory Peptide Region Exosite I C Linker C Anionic Region Exosite II Thrombin

Ribbon representation of two Gplb α -thrombin complexes related by crystal symmetry. The asymmetric unit contains one molecule of Gplb α (green) and one molecule of thrombin (blue), which associate as a crystallographically independent complex. The anionic region of Gplb α (red), a region corresponding to a peptide that inhibits thrombin-mediated aggregation (gold), and thrombin exosite I and exosite II (dark blue) are highlighted.

complexes of oligomeric arrays in which the two distinct binding sites continuously alternate throughout the crystal (Figure 11).

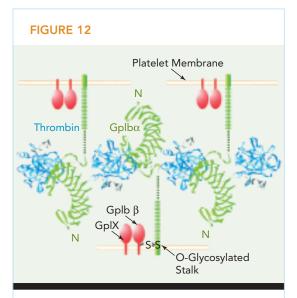
The first interface involves interactions between thrombin exosite I and a site on GpIba that spans a surface area of about 1400 Å². The binding interactions between GpIba residues and residues of exosite I are predominantly electrostatic. A second binding interface lies between exosite II of a second thrombin molecule and two adjacent regions of GpIba (the C-terminal end of the extracellular domain and the convex surface). This extensive interface covers a surface area of about 2000 Å². About 60% of this interface consists of a network of hydrogen bonds between the sulfated anionic region of GpIbα and highly basic residues in thrombin exosite II. Three tyrosine (Tyr) residues in this anionic region, including attached sulfate groups (necessary for optimal binding in vivo), participate in ionic and hydrophobic interactions with exosite II. In the remaining part of the GpIb α -exosite II interface, residues on the convex face of GpIba make mostly

The interacting surfaces of Gplb α and thrombin colored according to electrostatic potential (red is negative and blue is positive). Top: The charge distribution on the surface of thrombin highlights the high electropositivity at exosites I and II. The Gplb α receptor is shown as green ribbons with the surface rendered transparent. Bottom: The charge distribution on the surface of Gplb α highlights the highly electronegative regions that bind to exosites I and II. Thrombin is shown as blue ribbons with a transparent surface. The bottom view is rotated about the x-axis to present the Gplb α binding surface to the viewer.

hydrophobic contacts with thrombin.

In the context of cell–cell recognition and GpIb α -dependent platelet adhesion, the high affinity of thrombin for platelets and the associated thrombotic activity at physiologically relevant, low thrombin concentrations are likely accounted for by additive energetic contributions from individual GpIb α -exosite interfaces. In this regard, fortuitous crystal packing of the GpIb α receptor relative to thrombin provides a scaffold that could support tight multivalent adhesive interactions between platelets in vivo.

Given the mode of assembly depicted, a GpIbα receptor projecting from the cell membrane would interact with another GpIbα receptor indirectly through an intervening thrombin molecule (Figure 12). In this arrangement, GpIbα receptors from different membranes are aligned in alternating fashion, and the active site of thrombin remains accessible for other physiological substrates. This linear zipper configuration resembles the "cell-adhesion zipper" seen in other proteins involved in cell adhesion.



Schematic diagram of thrombin and Gplb-IX complexes in the region between platelets. Gplb α and thrombin molecules are arranged as an adhesive ribbon structure, as observed in the crystals. The green dotted lines depict the region between the last residue observed in Gplb α and the stalk region.

INVESTIGATORS

J.J. Dumas, R. Kumar, J. Seehra, W.S. Somers, and L. Mosyak (Wyeth Research).

FUNDING

Wyeth Research.

PUBLICATIONS

J.J. Dumas et al., "Crystal structure of the Gplb α -thrombin complex essential for platelet aggregation," *Science* **301**, 222 (2003).

SCIENCE HIGHLIGHTS

STRUCTURAL BIOLOGY

ATOMIC AND MOLECULAR SCIENCE

::

Ultrafast XANES Technique Reveals Photochemical Transients

Without chemical reactions induced by light (photochemistry), plants would not be able to convert sunlight via photosynthesis into energy for growth, nor would we be able to see the plants. But scientists motivated to study these and a host of other natural and industrial photochemical reactions face a problem. The reactions often comprise a sequence of events that follow each other extremely rapidly, sometimes in less than a trillionth of a second. Ultrafast lasers have been widely and successfully applied to the problem, but they are not a universal solution. X-ray spectroscopy can provide essential information, but until now, the combination of high-speed x-ray sources and experimental setups optimized for the weak signals generated have not been available. Saes et al. have recorded x-ray spectra of shortlived photochemical structures involving ruthenium metal in solution with a time resolution of about 100 trillionths of a second. While slower than the fastest lasers, their experiments constitute a proof of principle that the era of ultrafast x-ray spectroscopy has now arrived.

Ultrafast, time-resolved x-ray experiments are on the frontier of synchrotron radiation science with several demonstrations of white-light (Laue) x-ray diffraction to track structural changes on the picosecond time scale. Comparable experiments with x-ray absorption are more challenging because data must be recorded at each photon energy over the spectral range of interest. Transient, photochemical intermediate states in solution pose the additional difficulty of a solvent whose

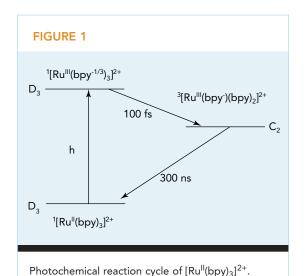
effects must be accounted for. Our team of researchers from the University of Lausanne, the Swiss Light Source, the University of California, Berkeley, and the ALS have paved the way for experiments of this type by using x-ray absorption near-edge structure spectroscopy (XANES, also known as NEXAFS) to detect the change in oxidation state of the central ruthenium atom in a laser-excited ruthenium complex in solution.

Charge-transfer processes during photochemical reactions occur in a large class of systems from small molecules to large metalloproteins. One thinks of photosynthesis in plants and vision in animals as prime examples in the natural world, but industrial instances abound as well. In principle, XANES is the ideal tool for studying the electronic structure of laser-excited transient states. Similarly, extended x-ray absorption fine structure spectroscopy (EXAFS) would be the choice for elucidating the changes in geometrical structure in these noncrystalline systems. Synchrotron sources are fast and intense enough to probe transients lasting 100 ps or longer. But there have been no reports of synchrotron-based, time-resolved x-ray absorption spectroscopy of transient, photochemical intermediate states with subnanosecond time resolution.

To record these short-lived states, we used an experimental setup sensitive enough to record the weak signals, reduce background to the shot-noise level of the pulsed x-ray source, and minimize interference from the solvent. For our pump–probe measurements, we chose ruthenium (II) tris-2,2'-bipyridine [Ru^{II}(bpy)₃]²⁺, a model transition-metal complex for studies of ultrafast electron-transfer processes, dissolved in a free-flowing jet of water. As the probe, we used x rays from ALS Beamline 5.3.1 with the ALS operating in its "camshaft" mode with a single, bright pulse of x rays in the midst of a 100-nslong dark interval. An amplified, frequency-

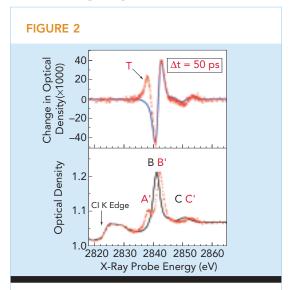
SCIENCE HIGHLIGHTS

ATOMIC AND MOLECULAR SCIENCE



doubled titanium-sapphire femtosecond laser, synchronized with the ALS, served as the pump.

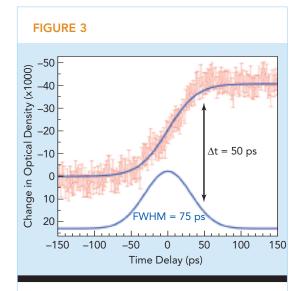
Laser excitation creates a ruthenium (III) singlet state that decays in 100 fs to a triplet state, ³[Ru^{III}(bpy⁻)(bpy)₂]²⁺, which has a lifetime



Top: Transient x-ray absorption spectrum of photoexcited aqueous $[Ru^{II}(bpy)_3]^{2+}$ measured 50 ps after laser excitation (red) with a fitted curve (blue) that accounts for the blue shift of the static absorption after photoexcitation. The peak near T is a new feature that occurs in the photoexcited intermediate. Bottom: Static L₃-edge x-ray absorption spectrum of ground-state $[Ru^{II}(bpy)_3]^{2+}$ (black) measured 0.5 ms before the laser strikes the sample, and excited-state absorption spectrum (red) generated from the transient data curve T in the upper panel. The blue shift B → B' and the new peak A' are evident.

of 300 ns and is the transient whose electronic structure was studied by XANES (Figure 1). As a baseline for the ruthenium (II) and ruthenium (III) states, respectively, we measured the static XANES spectrum of the unexcited complex and added from the literature a spectrum for [Ru^{III}(NH₃)₆Cl₂]. We then made the transient measurements in such a way that only the change in absorption (the transient part) was recorded (Figure 2). We determined the temporal resolution of the measurements to be 100 ps, governed by the x-ray pulse width, from the temporal evolution of the absorption at a particular wavelength as the delay between the exciting laser pulse and the probe x-ray pulse increased (Figure 3).

Two independent approaches to analyzing the transient absorption agreed that the basic features of the transient ruthenium (III) state are



Temporal evolution of the transient absorption is a step function whose shape is governed by the cross-correlation function between the exciting fs laser and the probing ps x-ray pulses. The derivative is Gaussian with a FWHM around 70–80 ps, which corresponds to the electron bunch length of the x-ray pulse (lower blue). With this precise timing measurement, one can then set a fixed time delay between the laser and the x-ray pulses with better than 10 ps accuracy (the arrow indicates a delay of 50 ps).

SCIENCE HIGHLIGHTS

ATOMIC AND MOLECULAR SCIENCE

SCIENCE HIGHLIGHTS

ATOMIC AND MOLECULAR SCIENCE

56

a 1.2-eV shift to higher energy of a pre-edge feature at 2841 eV due to a $2p_{3/2} \rightarrow 4d_{3/2}(e_g)$ transition and the onset of a new absorption due to a $2p_{3/2} \rightarrow 4d_{5/2}(e_g)$ transition. Both of these features, present in the static spectra, were already known, but this is the first time that such details have been extracted from transient XANES. We believe that the same approach can be applied to EXAFS measurement of local structural changes.

INVESTIGATORS

M. Saes (Université de Lausanne and Swiss Light Source, Switzerland); C. Bressler and M. Chergui (Université de Lausanne); R. Abela and D. Grolimund (Swiss Light Source); S.L. Johnson (University of California, Berkeley); and P.A. Heimann (ALS).

FUNDING

Swiss National Science Foundation, Swiss Light Source, and U.S. Department of Energy, Office of Basic Energy Sciences.

PUBLICATIONS

M. Saes et al., "Observing photochemical transients by ultrafast x-ray absorption spectroscopy," *Phys. Rev. Lett.* **90**, 047403 (2003).

Why Alcohol and Water Don't Mix

Imbibers have long been combining alcohol and water in myriad beverage concoctions. For example, Homer's account of the Trojan War reported that the Greeks mixed their wine with water to avoid insanity. Scientists, for entirely different reasons, have spent the past four decades studying how alcohol and water mix at the molecular level. Alcohol in water is one of the fundamental liquid—liquid solutions endemic to countless chemical and biological processes. Until now, however, experimental data on the molecular properties of such solutions came primarily from neutron diffraction analysis and sent mixed messages. The study

by Guo et al. of methanol, a nondrinkable form of alcohol that can provide insights into the behavior of other alcohols, sheds light on a 40-year controversy over what kinds of molecular structures are formed in pure liquid methanol. It also suggests an explanation for the well-known puzzle of why alcohol and water do not mix completely: the system must balance nature's tendency toward greater disorder (entropy) with the molecules' tendency to form hydrogen bonds.

The ability to determine the mixing properties of different liquids is of great importance: many vital chemical and biological processes take place in aqueous solutions. Our group has used x-ray absorption and selectively excited xray emission spectroscopy to study the electronic states of liquid water mixed with the simplest type of alcohol, methanol. The emission spectra obtained in this study reveal that the water and alcohol molecules in solution form complex hydrogen-bonded networks and mix very little at the microscopic level. The results illustrate the technique's potential to provide new and valuable information about the microscopic origins of the properties of liquids and solutions.

Our knowledge about the geometry and electronic structure of molecules in the liquid phase is very limited. Not only do the molecular arrangements change rapidly—on the scale of picoseconds to femtoseconds—but the properties of the individual molecules are also constantly changing, and interactions between the molecules cannot be neglected. Thus, it is not surprising that there is still much to learn about common and simple liquids.

One big mystery has involved the fact that, when alcohol and water mix, the disorder or entropy in the resulting system does not increase as expected for ideal solutions. This anomaly has traditionally been explained in terms of hydrophobic interactions involving alcohol molecules that induce a static, ice-like structure in the sur-

rounding water. However, despite a great deal of effort spanning four decades, a convincing description of the details of the incomplete mixing is lacking, and no consensus on the correct explanation has been reached.

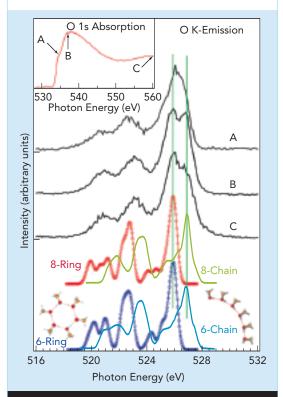
To shed light on this puzzle, we turned to ALS Beamline 7.0.1, where we studied the absorption and emission of x rays by liquid methanol in and out of solution with water. The spectra obtained reflect the local electronic structure; in particular, the oxygen line shape is sensitive to the hydrogen bonding configurations. Information about the molecular arrangements can therefore be obtained by comparison to theoretical predictions.

The results show that the structure of liquid methanol at room temperature is a combination of rings and chains, each made up of either 6 or 8 methanol molecules (Figure 4). When water is added, the methanol chains interact with varying numbers of water molecules. These "bridging" water molecules bend the chains into open-ring structures that are stable because their glue-like hydrogen bonds are saturated (Figure 5). This means that the mixing of alcohol and water on the microscopic level is incomplete no matter how long you wait.

The high degree of order in these clusters reduces the overall entropy of the liquid. Yet entropy must either stay the same or increase in the liquid. So to preserve the second law of thermodynamics, nature discourages the formation of too many such clusters in the liquid. Indeed, the measurements indicate that only a portion of the chains are being bridged. While the formation of clusters prevents full mixing, the second law of thermodynamics limits the degree of order in the system, suggesting a competition between increasing entropy and hydrogen bonding of clusters.

Devotees of scotch and water should now be advised they may never attain the perfect blend. While methanol is poisonous when consumed, its molecular behavior when mixed with water is

FIGURE 4



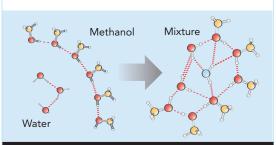
Experimental oxygen emission spectra recorded at three excitation energies (A, B, and C) compared with theoretical emission spectra of chain and ring structures in methanol. The inset shows the points on the absorption spectrum for the three excitation energies.

SCIENCE HIGHLIGHTS

ATOMIC AND MOLECULAR SCIENCE

57

FIGURE 5



At the molecular level, very little mixing of alcohol and water occurs in solution. Instead, chains of methanol molecules react with clusters of water molecules to form stable open-ring structures, which lower the solution's entropy.

SCIENCE HIGHLIGHTS

ATOMIC AND MOLECULAR SCIENCE

58

expected to be the same as that of ethanol, the drinkable form of alcohol. Beyond advances in mixology, however, this study establishes a valuable tool for probing the molecular properties of liquids and solutions, something that until now has been difficult to do. The results have substantially refined both our knowledge of structure and order in methanol and methanol—water solutions and our understanding of the unusual thermodynamic properties of this common liquid mixture.

INVESTIGATORS

J.-H. Guo and D.K. Shuh (Berkeley Lab); Y. Luo, S. Kashtanov, and H. Agren (Royal Institute of Technology, Sweden); and A. Augustsson, J.-E. Rubensson, and J. Nordgren (Uppsala University).

FUNDING

U.S. Department of Energy, Office of Basic Energy Sciences; Swedish National Science Foundation; Swedish Natural Science Research Council; and National Supercomputer Center of Sweden.

PUBLICATIONS

J.-H. Guo et al., "The molecular structure of alcoholwater mixtures," *Phys. Rev. Lett.* **91**, 157401 (2003).

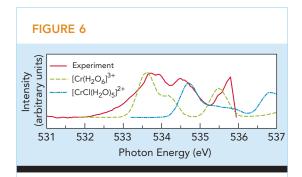
Orbital Mixing Between Water and Dissolved Ions

Water is a coolant, a heat reservoir, an acid, a base, a nearly universal solvent, and a weak electrical conductor; it plays a wide range of roles from regulating the Earth's climate to affecting the way proteins fold. Many of water's unusual properties arise from its propensity to form hydrogen bonds with nearby molecules. Hydrogen bonds are relatively "loose," based on attractions between opposite electrical charges. To better understand what happens when such bonds are formed between water molecules and dissolved ions, Näslund et al. studied the electron orbital structure of oxygen using an x-ray absorption spec-

troscopy technique that allows measurement of aqueous solutions at atmospheric pressure and room temperature with great sensitivity to the local environment of the dissolved ions. With this technique, combined with a powerful computational theory, the researchers gained insight into the local electronic structure of a hydrogenbonded liquid and were able to identify the "fingerprint" of the molecules in direct contact with a dissolved (solvated) metal ion.

The essential role of water as a solvent in chemistry and biology is closely connected to the chemical interactions between dissolved ions and the water molecules immediately surrounding them (the "first hydration shell"). With recent developments in soft x-ray absorption spectroscopy (XAS) applied to liquids under ambient conditions, selectively measuring the electronic structure of such water molecules in the solution is now possible. By combining such measurements with density functional theory (DFT) calculations, our collaboration involving researchers from Sweden and the U.S. has demonstrated that the molecular orbitals of the water molecules in the first hydration shell will mix with the d orbitals of a dissolved transition-metal ion, resulting in characteristic pre-edge features in the oxygen 1s XAS spectrum. The technique is sensitive enough to easily detect an additional chlorine ion in the hydration shell.

We made our measurements at ALS Beamline 8.0.1. The experimental oxygen 1s XAS spectrum of water with dissolved chromium chloride [CrCl₃(aq)] has a pre-edge region (532–536 eV) containing features not seen in the spectrum of water with dissolved aluminum chloride [AlCl₃(aq)]. This difference arises because the chromium's empty d states (characteristic of transition metals) cause it to bond differently with the surrounding water molecules than the (non-transition-metal) aluminum. A subtraction procedure enhances the differences and reveals three peaks (Figure 6).



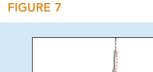
Features in the difference spectrum between CrCl₃(aq) and AlCl₃(aq) (red) and in the calculated spectra of $[Cr(H_2O)_6]^{3+}$ (green) and $[CrCl(H_2O)_5]^{2+}$ (blue) serve as a spectroscopic proof of d-orbital interaction between the Cr³⁺ ion and the water molecules in the first hydration shell.

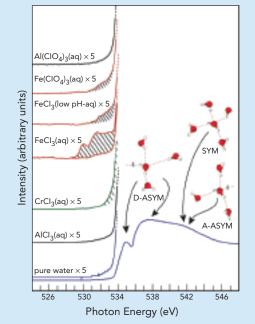
Our DFT calculations for the chromiumwater cluster $[Cr(H_2O)_6]^{3+}$ assign the two features at 533.8 and 535.8 eV to molecular orbitals having strong metal d character. In the computed spectrum of a similar complex in which one chloride replaces a water molecule in the first hydration shell [CrCl(H₂O)₅]2+, the spectrum is shifted upward by about 1 eV, generating a feature at 534.5 eV. The conditions of the experiment were such that an equal mixture of $[CrCl(H_2O)_5]^{2+}$ and $[Cr(H_2O)_6]^{3+}$ must be expected, and this expectation is beautifully confirmed in the resulting soft x-ray spectrum.

To show that the mixing between the molecular orbitals of water and the Cr3+ d orbitals represents a specific example of a more general phenomenon, we also studied solutions of another transition metal, iron, which has a much more complicated solution chemistry. The bonding of the Fe³⁺ ion is strong enough to cause deprotonation of the surrounding water molecules, resulting in hydroxide ions (OH-) in the first hydration shell. Alternatively, the addition of hydrochloric acid to the solution lowers the pH, inhibits deprotonation, and promotes the presence of chlorine ions in the first hydration shell.

Spectra of a sequence of Fe³⁺ complexes allow a definite assignment of the distinct and complicated d-orbital features at 530.0, 531.6, and 532.8 eV in the FeCl₃(aq) spectrum (Figure 7).

Computed x-ray absorption spectra indicate that the first peaks in the FeCl₃(aq) spectrum, at 530.0 and 531.6 eV respectively, are due to the interaction between OH- molecular orbitals and d orbitals in the metal. This is confirmed by the absence of these two peaks in the low-pH FeCl₃ spectrum (where OH- is replaced by Cl-). The broad peak at 532.8 eV is then assigned to the d interaction of the water molecules in the Fe³⁺ ion hydration shell. Overall, it was possible to assign all the peaks in the spectrum based on computed spectra for various possible compositions of the first hydration sphere.





Experimental oxygen 1s x-ray absorption spectra of various aqueous solutions. Extra pre-edge features (shaded areas) only appear if the dissolved ion is a transition metal. Differences between the spectra of the various Fe³⁺ complexes are due to the interaction between OH⁻ orbitals and d orbitals in the metal. Also shown is the oxygen 1s x-ray absorption spectrum of pure water, with features attributable to three configurations (symmetric and asymmetric) of water molecules.

SCIENCE HIGHLIGHTS

ATOMIC AND **MOLECULAR** SCIENCE

SCIENCE HIGHLIGHTS

ATOMIC AND MOLECULAR SCIENCE

60

Although the interaction between the water and the transition-metal d orbitals was anticipated in the literature, until now, there was no direct experimental evidence for it. XAS, combined with DFT calculations, is the only technique sensitive and selective enough to directly probe local orbital changes resulting from such a weak interaction. Soft x-ray measurements on ionic solutions have thus been demonstrated to provide unique information on electronic structure, bonding, and composition in the first hydration

INVESTIGATORS

shell of dissolved ions.

L.-Å. Näslund (Stockholm University and Uppsala University); M. Cavalleri, H. Ogasawara, L.G.M. Pettersson, and M. Sandström (Stockholm University); A. Nilsson (Stockholm University and Stanford Synchrotron Radiation Laboratory); P. Wernet (Stanford Synchrotron Radiation Laboratory); and D.C. Edwards and S. Myneni (Princeton University).

FUNDING

U.S. Department of Energy, Office of Basic Energy Sciences; Swedish Royal Academy of Science; Göran Gustafsson Foundation; National Science Foundation; Swedish Natural Science Research Council; Foundation for Strategic Research; and Swedish Center for Parallel Computing.

PUBLICATIONS

L.-Å. Näslund et al., "Direct evidence of orbital mixing between solvated transition-metal ions: An oxygen 1s XAS and DFT study of aqueous systems," *J. Phys. Chem.* A **107**, 6869 (2003).

н

First Photoelectron Imaging Studies of Pure Helium Nanodroplets

Among the behaviors of matter that are peculiar to quantum mechanics is superfluidity, the ability of a substance to flow without friction when it is cooled to within a few degrees of absolute zero. While superfluidity does have technological applications, chemists would also like to use superfluid helium in studies of gas molecules. When a single molecule is dissolved in a nanometer-sized droplet of superfluid (a nanodroplet), the molecule behaves exactly as it would in the gas phase but in a controlled environment. Before this type of experiment can be come routine, however, researchers need to understand the properties of isolated helium nanodroplets. For this purpose, lasers have been widely exploited, but they have limitations. Peterka et al. have instead employed a short-wavelength ultraviolet technique (vacuum ultraviolet photoelectron spectroscopy) in which they effectively take snapshots of individual electrons' velocities as they fly away from the droplet after absorbing ultraviolet light. Their experiments represent the first step in characterizing helium droplets by this method.

The quest to understand the properties of dilute quantum fluids has stimulated the development of laser cooling and trapping, atom lasers, and renewed interest in fundamental quantum mechanics. One dense quantum liquid, superfluid liquid helium, has been the subject of study since its discovery in 1908. In the past decade, impurity-doped, cold liquid helium nanodroplets (0.38 K) have been studied extensively as an "ultracold nanolaboratory." To avoid some of the limitations of lasers, we have performed the first photoelectron spectroscopy experiments on He_N droplets, with the number N of helium atoms per droplet ~10⁴. Our results

show strong evidence for many-body effects and final-state interactions between the photoelectrons and the helium atoms in the droplet.

Quantum fluids have provided both experimentalists and theorists challenges and pleasures. Among the experimental challenges have been optical studies of pure helium nanodroplets. The optically allowed electronic transitions of helium droplets lie well above the energy range accessible to laser spectroscopy, restricting experiments to synchrotron light sources. Thus far, fluorescence excitation spectra between 20-25 eV have been measured, as has the photoionization efficiency as a function of photon energy and droplet size. These experiments raise the issues of the mechanism of ionization in pure helium droplets, the competition between the mechanisms leading to ionization and fluorescence, and the interaction of the photoelectron with the atoms in the droplet.

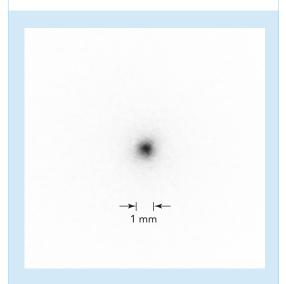
To address these and other issues, we turned to photoelectron spectroscopy. Our experiments were carried out at the Chemical Dynamics Beamline 9.0.2 at the ALS. Vacuum ultraviolet (VUV) radiation from a 10-cm-period undulator was dispersed by a 3-m, normal-incidence, off-plane Eagle monochromator, yielding more than 10^{13} photon/s at 25 eV with a bandwidth of 15 meV. The droplets were produced by expanding high pressures of helium gas through a 5- μ m cooled aperture (10–18 K), resulting in droplets of 10^3 – 10^4 helium atoms.

The VUV light crossed the helium-droplet beam perpendicular to the axis of the electron-detection system, which uses the technique of velocity-map photoelectron imaging. In this configuration, all electrons with the same momentum in the plane parallel to the detector were imaged to the same point, eliminating spatial blurring and offering exquisite sensitivity to low-energy electrons with 100% collection efficiency. The image obtained is the 2D projection of the nascent 3D distribution of emitted photoelectrons. Standard tomographic methods allow the direct inversion of the image to extract the pho-

toelectron velocity distribution.

Typical of our results are a photoelectron image (Figure 8), obtained following illumination of the droplet with 23.8-eV photons, and the associated distribution of the electron kinetic energy, E_k (Figure 9). The photoelectron spectra are dominated by very low energy electrons, with $\langle E_k \rangle$ less than 0.6 meV, that have an isotropic angular distribution. The bandwidth of the excitation light is 25 times greater then the average electron energy, clearly indicating decoupling of the excitation from the subsequent relaxation event. Over a range of photon energies (23-24.5 eV), the kinetic-energy distributions are nearly identical to the one shown. These results are attributed to the formation and autoionization of highly vibrationally excited He_n* Rydberg states within the cluster; the resulting electrons then undergo thermalizing collisions within the droplet before being emitted.





Typical integrated velocity-map photoelectron image from a helium droplet after illumination with 23.8-eV photons. In velocity-mapped images, electrons with zero velocity appear in the center of the image, and faster electrons are located away from the center, with the direction and distance from the center proportional to the electrons' velocity.

SCIENCE HIGHLIGHTS

ATOMIC AND MOLECULAR SCIENCE

SCIENCE HIGHLIGHTS

Photon Energy: 23.80 eV Photon Energy: 23.80 eV 2 4 6 8 10 Electron Kinetic Energy (meV)

Typical distribution of the photoelectron kinetic energy. The photoelectron spectra are dominated by electrons with very low energies and isotropic angular distributions.

These experiments represent the first step in characterizing the photoelectron spectra of helium droplets. Future experiments include measurement of the photoelectron spectra above the helium ionization potential, where new ionization channels will be energetically accessible, and a study of cluster-size effects on the ionization process.

INVESTIGATORS

D.S. Peterka, L. Poisson, A. Lindinger, and D.M. Neumark (University of California, Berkeley, and Berkeley Lab) and M. Ahmed (Berkeley Lab).

FUNDING

U.S. Department of Energy, Office of Basic Energy Sciences

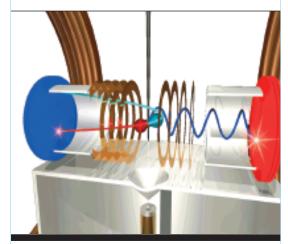
PUBLICATIONS

D.S. Peterka et al., "Photoelectron imaging of helium droplets," *Phys. Rev. Lett.* **91**, 043401 (2003).

Femtosecond Timer for Dancing Molecules

From the time the earliest humans tamed fire, fascination with burning and combustion has been a moving force behind many crucial discoveries. Today, the burning of fossil fuels is the major source of industrial power for the planet. Those studying the physics of atoms and molecules have a definite role to play in the quest to find ways to burn fossil fuels more efficiently and cleanly, thus minimizing their effects on the environment. Acetylene, for example, is a very commonly used flammable gas with a simple molecular structure that makes it possible to conceive and execute experiments that generate fundamental and useful information. Osipov et al. have drawn on a recently developed experimental technique called COLTRIMS that tracks every ion and electron that emerges from a molecule that is ionized by x rays. They have used this method to measure the time it takes for acetylene to transform to a related molecule (isomer) with the same composition, thereby showing its value as a tool for clocking molecular rearrangements, including those in combustion.

Acetylene, besides being one of the most common flammable gases, has long been a subject of interest because of its simple molecular structure and the existence of its isomer, vinylidene. A novel approach to measuring the time scale for the isomerization of acetylene to vinylidene was recently introduced by our collaboration of scientists from Kansas State University, the University of Frankfurt, Berkeley Lab, and Western Michigan University. Cold-target recoilion momentum spectroscopy (COLTRIMS), with the capability to measure electron momentum, was used to conduct the kinematically complete experiment (Figure 10). We found that the x-ray K-shell photoionization of the cold acetylene



Schematic diagram of the COLTRIMS apparatus, showing a beam of the molecules to be photoionized and the paths of positively charged ions, drawn to the position- and time-sensitive blue detector, and the negatively charged electron, drawn to the position- and time-sensitive red detector, after the photoionization event and the subsequent Coulomb explosion.

molecule leads to an Auger decay followed by the Coulomb explosion of the doubly charged ion.

Acetylene (C₂H₂) has a well-known linear molecular configuration, with a triple bond between the carbons and a hydrogen atom at each end. It has an isomer, vinylidene, in which both hydrogen atoms reside on the same side of the molecule and are connected to the same carbon atom. The ground state of the neutral C₂H₂ molecule prefers to be in the acetylene (A) configuration. However, even a slight disturbance of the molecule—excitation, addition or removal of an electron—can make the vinylidene (V) configuration energetically preferred. The molecule is then likely to undergo a rearrangement process and convert its configuration from A to V.

The simplest model for this rearrangement is the tangential motion of the hydrogen atom around the molecule. Until recently, this process has been studied mainly through theoretical calculations of the intermediate transition states and experimental identification of these states in x-ray absorption and transmission spectra. Even a simple characteristic such as the time scale for this rearrangement has been widely debated, and experiments that provide direct information about this time scale are rare.

Our experiment involved the K-shell photo-ionization of acetylene and was carried out on Beamlines 4.0.2 and 9.3.2 during two-bunch operation at the ALS, which is an essential requirement for the time-of-flight measurements in COLTRIMS experiments. The measured flight times and positions of the photoelectrons and molecular fragments were converted into the corresponding vector momenta. From these momenta, the photoelectron angular distributions were obtained. The formation of vinylidene was clearly identified from the recoil-ion momentum spectra of the breakup fragments.

In the body-fixed frame of the initial molecule, the photoelectron distributions were found to exhibit very sharp angular features (Figure 11). These sharp features were used much like the hands of a clock to determine the angle through which the carbon-carbon bond had rotated between the excitation of the target, initially in the acetylene configuration, and the final decay of the molecule through the vinylidene decay channel. This angle, together with an estimation of the initial angular momentum of the molecule-the rotation speed of the clock hands-gave the time duration between the K-shell photoionization and the Coulomb explosion. Since the isomerization happens between those two events, this time can be considered an upper bound of the rearrangement duration. It was found to be around 60 fs.

Although the acetylene-vinylidene rearrangement study was the main point of this experiment, our technique of measuring the time scales of molecular rearrangements and fragmentation pathways can be applied to other systems. For example, it has also been recently used for determination of the lifetimes of the long-lived states of the carbon monoxide doubly charged ions produced after carbon K-shell photoionization, and it has been used to measure hydrogen migration times for molecules excited by intense laser pulses.

SCIENCE HIGHLIGHTS

SCIENCE HIGHLIGHTS

ATOMIC AND MOLECULAR SCIENCE

64

Top: Polar plot of photoelectrons in the body-fixed frame for the A channel. Bottom: Same type of plot for the V channel. The angle through which the carbon–carbon bond rotated during the isomerization is indicated by the clock hands. In the plots, the angle measures the direction of the photoelectron momentum, and the radial distance gives the probability for the electrons to travel in that direction.

330

240 270 300

INVESTIGATORS

T. Osipov and C.L. Cocke (Kansas State University); R. Dörner, Th. Weber, O. Jagutszki, L. Schmidt, and H. Schmidt-Böcking (University of Frankfurt, Germany); A. Landers (Western Michigan University); and M.H. Prior (Berkeley Lab).

FUNDING

U.S. Department of Energy, Office of Basic Energy Sciences.

PUBLICATIONS

T. Osipov et al., "Photoelectron-photoion momentum spectroscopy as a clock for chemical rearrangements: Isomerization of the di-cation of acetylene to the vinylidene configuration," *Phys. Rev. Lett.* **90**, 233002 (2003).

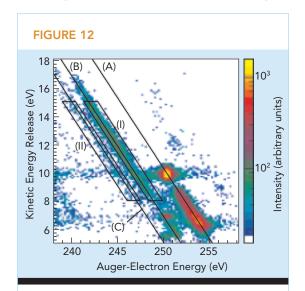
Auger-Electron Emission from Fixed-in-Space CO

When an atom or molecule absorbs an x ray, two things can then happen. First, one or more of the electrons gain energy from the x ray, creating an excited molecule. Second, the electrons lose some or all of the energy by a variety of decay processes. In 1926, French scientist Pierre Auger discovered one of the fundamental decay processes of excited atoms and molecules: the emission of an energetic electron (Auger electron). But even such basic information as the direction the Auger electron takes when leaving the atom or molecule has remained unknown. Scientists have also wondered whether the excitation and decay are two independent events or inseparable aspects of one event. The ability to answer such questions demonstrates that a solid understanding of the quantum mechanics that governs all matter, not just atoms and molecules, is in hand. Weber et al. have used a device sometimes called a momentum microscope to track the Auger decay of carbon monoxide in unprecedented detail, thereby boosting confidence in our ability to answer fundamental questions.

One of the longstanding and previously experimentally unresolved questions of molecular physics involves the direction in which a molecule emits Auger electrons. Using a powerful many-particle, multicoincidence imaging technique known as cold-target recoil-ion momentum spectroscopy (COLTRIMS), we can answer this question and unravel Auger decay in unprecedented completeness and detail. Specifically, for the Auger decay of carbon K-shell-ionized CO+, we have measured the Auger-electron energy and angle in coincidence with the energy and angle of both fragment ions of the CO²⁺.

The questions we addressed in our experiment were as follows: What is the direction of the Auger electron? Which states are involved and how does the direction depend on them? And finally, does the Auger decay have a memory of the photoionization step that created the decaying inner-shell hole? Our experiment was performed at ALS Beamline 4.0.2 to take advantage of the outstanding circular polarization properties of the beamline's elliptically polarizing undulator. The photon beam intersected a supersonic CO gas jet inside a momentum spectrometer that uses electric and magnetic fields to guide simultaneously the Auger electrons and recoiling ions onto large-area, position-sensitive detectors. From the measured flight times and impact positions, the trajectories can be reconstructed.

The total energy available in the decay of the core-ionized CO⁺ is shared between the Auger electron, the kinetic energy release (KER), and the internal electronic excitation energy in the ionic fragments. The correlation between Auger



Auger decay of CO⁺ after photon absorption at 305 eV leads to C⁺ + O⁺. The diagonal lines correspond to decays of the CO⁺ ground state to the different final states at the ionic fragments (A) $C^{+}(^{2}P) + O^{+}(^{4}S)$ (ground state); (B) $C^{+}(^{2}P) + O^{+}(^{2}D)$; and (C) $C^{+}(^{2}P) + O^{+}(^{2}P)$.

energy and KER is shown in Figure 12. Each of the final ionic states leads to a diagonal line. The electronic ground state and the two first excited states are indicated by solid lines.

As an example, we focus on the narrow ${}^{1}\Sigma^{+}$ line (B state) at around 250.5 eV in the energy diagram. An Auger-electron dependence on the direction of polarization of the photon that created the K-hole would indicate a breakdown of the widely accepted independent two-step model. This model plausibly assumes that if the Auger electron and photoelectron have very different energies, one can treat the first core-level photoionization and the second core-hole Auger-decay steps as independent processes, i.e., the Auger decay has no memory of how the K-hole was produced. The data shown in Figure 13 corroborate this idea because the Auger angular distributions are, indeed, polarization independent and, hence, are consistent with the two-step model.

Figure 14 shows the Auger-electron angular distributions for the regions I and II in Figure 12. For the transitions to the ${}^{1}\Pi$, ${}^{3}\Pi$, and ${}^{1}\Delta$ states in region I, the emission is mainly perpendicular to the molecular axis, as one expects for a Π wave. A completely different pattern is found in Figure 14 for the transition to the third ${}^{1}\Sigma^{+}$ state, located along line C in region II in Figure 12. The fine structure is due to a diffraction of the Auger-electron wave in the two-center potential.

There is also a very narrow peaked emission of the electrons along the molecular axis in the direction of the oxygen. Such emission into the direction of the neighboring atom is known from photoelectron diffraction as "forward focusing." The screened Coulomb potential next to the source of a photoelectron wave can act as a lens that collects a large amount of the electron flux into the forward direction. This analogy suggests that the Auger-electron wave does not emerge from a delocalized orbital spread over the whole molecule but from a localized region close to the carbon nucleus.

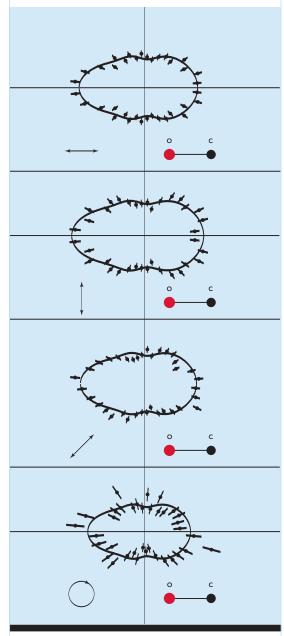
SCIENCE HIGHLIGHTS

ATOMIC AND MOLECULAR SCIENCE

SCIENCE HIGHLIGHTS

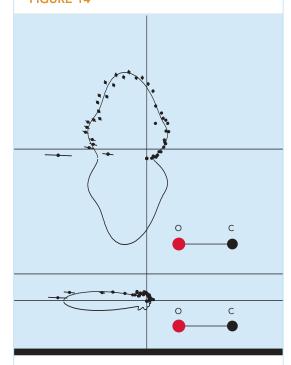
ATOMIC AND MOLECULAR SCIENCE

66



Angular distribution of Auger electrons from the narrow $^1\Sigma^+$ line at 250.5 eV (B state in Figure 12) for variably polarized light propagating into the plane of the figure. The orientation of the molecule is horizontal with the oxygen to the left, as indicated. The polarization vector for linearly polarized light is indicated by the double-headed arrow and the sense of circularly polarized light (bottom) by the circle and arrow head. The radial distance measures the magnitude of the Auger-electron momentum, and the angle gives the direction.

FIGURE 14



Angular distribution of Auger electrons from CO⁺. Top: From region I in Figure 12 for a CO⁺ $(^1\Sigma^+) \rightarrow$ CO²⁺ $(^1\Delta, \,^3\Pi, \,^1\Pi)$ transition. Bottom: From region II for a CO⁺ $(^1\Sigma^+) \rightarrow$ CO²⁺ $(^1\Sigma)$ transition. The full lines in the figures are a fit of Legendre polynomials to guide the eye.

INVESTIGATORS

Th. Weber, M. Weckenbrock, M. Balser, L. Schmidt, O. Jagutzki, O. Hohn, M. Schoeffler, H. Schmidt-Böcking, and R. Dörner (University of Frankfurt, Germany); L. Foucar and M.H. Prior (Berkeley Lab); E. Ahrenholz and T. Young (ALS); T. Osipov and C.L. Cocke (Kansas State University); A. De Fanis (Tohoku University, Japan), R. Díez Muiño (Donostia International Physics Center, and Spain).

FUNDING

Federal Ministry of Education and Research, Germany; German Research Foundation; and U.S. Department of Energy, Office of Basic Energy Sciences.

PUBLICATIONS

Th. Weber et al., "Auger electron emission from fixed-in-space CO," *Phys. Rev. Lett.* **90**, 153003 (2003).

NEW X-RAY TECHNIQUES

::

Demonstration of Coherent X-Ray Diffraction Imaging

For scientists in the burgeoning realms of nanotechnology and life science at the molecular level who want to peer at 3D images of objects with features measured in billionths of a meter (nanometers), there is no lens that can do the imaging. For samples consisting of a very large number of identical objects arrayed in a regular pattern (e.g., atoms in a crystal), a lensless alternative is to mathematically reconstruct the object (i.e., its atomic positions) from the intensities and directions of beams that are deflected (diffracted) as they pass through the sample. A growing number of researchers are now taking image reconstruction from diffraction patterns a big step further by studying individual, nonrepeating objects by the new technique of coherent x-ray diffraction imaging. Marchesini et al. are the first to accomplish lensless imaging without any supplementary information whatsoever (working with the diffraction pattern only), as shown by their 2D images of clusters of gold balls 50 nm in diameter.

In order to image the interiors of intrinsically noncrystalline objects with nanometer resolution, several groups have been developing the technique of coherent x-ray diffraction (or lensless) imaging; however, up until now they have required the use of additional image information to supplement the diffraction pattern. Our collaboration comprising researchers from Lawrence Livermore National Laboratory, Arizona State University, and the ALS has demonstrated the ability to make 2D images of clusters of gold balls 50 nm in diameter from diffraction data alone with a Rayleigh resolution of 10 nm.

The inversion of a diffraction pattern offers aberration-free, diffraction-limited, 3D images without the resolution and depth-of-field limitations of lens-based tomographic systems. Radiation damage becomes the main limiting factor. The best-known example, crystallography, is possible owing to special conditions, namely the existence of crystalline samples and auxiliary techniques for obtaining phase information. Coherent x-ray diffraction imaging (CXDI) eliminates the need for periodic arrays of identical objects and solves the phase problem mathematically.

Three ideas developed over half a century have contributed to the development of CXDI. In 1952, David Sayre (IBM T.J. Watson Research Center) noticed that conventional crystallography, by recording discrete Bragg diffraction spots, "undersampled" the diffraction intensity relative to a theorem of the late information theorist Claude Shannon (AT&T Bell Laboratories). In the 1980s, James R. Fienup (University of Rochester) developed iterative algorithms that efficiently extracted phase information from adequately sampled diffraction patterns like the continuous patterns from nonperiodic samples. Finally, in 1999, Jianwei Miao (now at the Stanford Synchrotron Radiation Laboratory) and colleagues working at the National Synchrotron Light Source reconstructed 2D images of lithographically prepared objects with a resolution of 75 nm. A number of groups have since achieved higher resolution and 3D imaging with both x rays and electrons.

In Fienup's hybrid input-output algorithm, one starts with a diffraction pattern with random phases and then iteratively transforms between real space (the image) and back to reciprocal space (the diffraction pattern with phases). Each transform to reciprocal space provides improved phases for the next cycle. An essential constraint is the requirement that the intensity of the dif-

SCIENCE HIGHLIGHTS

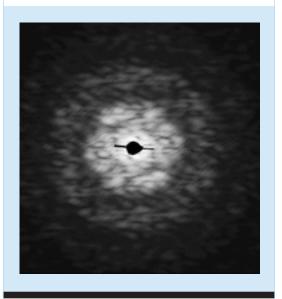
NEW X-RAY TECHNIQUES

fraction pattern be zero outside the boundary of the object (the support). The better the support is known, the faster the iterations converge to an accurate image. Most researchers have relied on x-ray microscopy or other techniques to supply this information.

Our collaboration has been working to eliminate the need for supplementary experiments. Previously, we had succeeded by preparing on a silicon nitride substrate clusters of gold balls 50 nm in diameter together with an isolated single gold ball as reference that generated the information needed to construct the support. Now, we have done away with even that requirement with a new "shrink-wrap" algorithm. We use a transform of the diffraction pattern as the initial support (Figure 1). At intervals, we generate a new support from the transform of the current diffraction pattern. In this way, the support converges to a tight boundary around the cluster of balls, and the image also emerges (Figure 2). The reconstruction is superior to that from the hybrid input-output algorithm in the presence of noise, except when the initial knowledge of the support is known perfectly (Figure 3).

Work on 3D images from a series of diffraction patterns obtained at many illumination angles is underway. In the meantime, we believe that a resolution of 10 nm will be possible for

FIGURE 1



Measured x-ray diffraction pattern of two clusters of gold balls 50 nm in diameter.

FIGURE 2

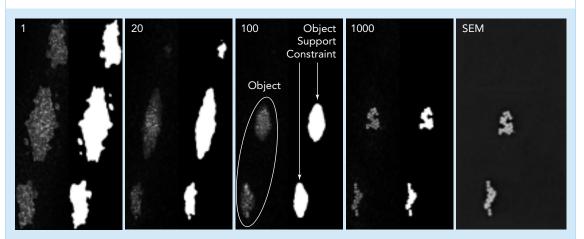
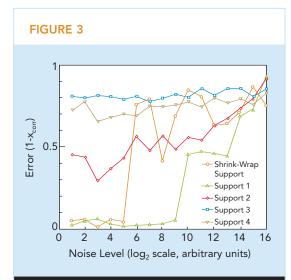


Image reconstruction of two clusters of gold balls showing the convergence of both the reconstructed image and the support as the number of iterations increases (*left to right*) from 1 to 1000. For comparison, a scanning electron microscope (SEM) image is also shown. The Rayleigh resolution of the reconstructed image is 10 nm.



Effect of noise on reconstruction error. The shrink-wrap algorithm (yellow) is superior to hybrid input-output algorithms with fixed support, except for the case when the support is known perfectly (green). The accuracy of the supports decreases from support 1 to support 4.

life-science samples, where radiation damage is an issue, and 2 nm for solids. A dedicated CXDI beamline at the ALS after a planned brightness upgrade could improve the figure to 1 nm, owing to an increase in imaging speed. The ultrabright, femstosecond x-ray pulses expected when the Stanford Synchrotron Radiation Laboratory's Linac Coherent Light Source comes online around 2008 may enable atomic-resolution imaging of single molecules.

INVESTIGATORS

S. Marchesini, H.N. Chapman, S.P. Hau-Riege, and A. Noy (Lawrence Livermore National Laboratory); H. He and M. Howells (ALS); and U. Weierstall and J.C.H. Spence (Arizona State University).

FUNDING

U.S. Department of Energy, Office of Basic Energy Sciences, and National Science Foundation.

PUBLICATIONS

S. Marchesini et al., "X-ray image reconstruction from a diffraction pattern alone," *Phys. Rev. B* **68**, 140101(R) (2003).

H. He et al., "Inversion of x-ray diffuse scattering to images using prepared objects," *Phys. Rev. B* **67**, 174114 (2003).

SCIENCE HIGHLIGHTS

NEW X-RAY TECHNIQUES





Composite photo of ALS: then and now.

Reflections on the ALS

Commemorating our Tenth Anniversary of Operation

As we go about our daily routines, year in and year out, carried along by the momentum of recent highs and lows and focused on getting over the next hump, it's easy to lose sight of the larger landscape in which we travel. Where did we come from? How did we get here? Where are we going? These are questions that, unfortunately, often get deferred until, with some surprise, we realize that, say, ten years have gone by since some milestone event and that many of our fellow travelers don't share our vivid memories of the byways through which we have passed.

A decade after it first began operations in 1993, the ALS is at such a point in its history. Recent years have seen the buildout of the facility with all straight sections either occupied or spoken for. Superbends were suc-

cessfully retrofitted into the storage ring to extend the ALS's range of photon energies. Plans for near-future upgrades include switching to a "top-off" injection mode and the replacement of older insertion devices with newer, chicaned versions. Further off in the distance lies the prospect of a "light-source campus" with proposed sister facilities such as CIRCE and LUX. As the ALS community contemplates its strategic direction for the next 5 to 10 years, we pause here to look back on the challenges, setbacks, and ultimately, the successes of those who, ten years ago, turned a vision into reality.

н

The Impossible Dream

Although 1993 marked the start of ALS operations, the true beginnings of the ALS date as far back as 1980, when David Shirley became Berkeley Lab director. Dave was a veteran synchrotron user at the Stanford Synchrotron Radiation Laboratory (SSRL). He felt strongly that synchrotron radiation could play a large role in U.S. science and that the West Coast in particular needed a lowenergy machine. At about the same time, Klaus Halbach had realized that iron-free permanentmagnet wigglers and undulators could be built that would revolutionize synchrotron light sources. This was a technology that would make the ALSthe prototype "third-generation" light source possible. In 1981, Jay Keyworth, President Reagan's science advisor, was in Berkeley for the Lab's 50th anniversary celebration. Dave pitched him the idea of the ALS as part of a National Center for Advanced Materials (NCAM). In January 1983 the proposal was added on to the federal budget for fiscal year 1984, bypassing the DOE and the peer-review process. Understandably, the scientific community balked, insisting that users be out in front, driving the process. The "addon" was removed from the budget, and the ALS was back to square one.

THE ALS: FROM VISION TO REALITY

1980	David Shirley becomes Berkeley Lab director DECEMBER Klaus Halbach's undulator installed at SSRL
1981	OCTOBER Jay Keyworth at Berkeley Lab's 50th Anniversary Celebration
1983	JANUARY NCAM/ALS added on to FY84 budget OCTOBER DOE Eisenberger-Knotek review
1984	MARCH NAS Seitz-Eastman review
1985	NOVEMBER Workshop on an Advanced Soft X-Ray and Ultraviolet Synchrotron Source: Applications to Science and Technology
1986	FEBRUARY Reagan's State of the Union Address, \$1.5 million authorized for engineering design JULY Conceptual Design Report published (Pub-5172 Rev.)
1987	JUNE Jay Marx becomes ALS project director DECEMBER Congress approves first \$18 million for ALS construction
1988	AUGUST Groundbreaking ceremony
1989	SEPTEMBER Charles Shank becomes Berkeley Lab director OCTOBER Last major concrete pour for floor and foundation
1990	MARCH First section of the booster ring lowered into the shielding enclosure
1991	MARCH Linear accelerator produces beam on first try
1992	OCTOBER Brian Kincaid becomes ALS director DECEMBER Storage ring completed
1993	MARCH Beam current reaches 290 mA OCTOBER First light delivered to Beamline 10.3.1 OCTOBER ALS dedication ceremony



The ALS team in 1987 sitting in the gap of the 184-inch cyclotron. Dave Attwood, Alan Paterson, Brian Kincaid, Alan Jackson, Ron Yourd, Klaus Berkner, Henry Lancaster, and Werner Ganz, among others, are seated in the front row.

REFLECTIONS ON THE ALS

78



Groundbreaking ceremony launches construction in 1988: David Shirley, Jo Ann Elferink (Manager, DOE San Francisco Operations Office), Donna Fitzpatrick (DOE Associate Under Secretary/Under Secretary), and Steve Kevan (UEC Chair).

After this false start, the normal peer-review process for the ALS began in October 1983, with the DOE's Eisenberger-Knotek review of major facilities for materials science. The case for the ALS was made further in March 1984, at the Seitz-Eastmann review sponsored by the National Academy of Sciences (NAS). These reviews were very supportive of the idea of a soft x-ray facility, although a higher priority was given to building a hard x-ray facility. Philip Abelson, editor of Science magazine, was in the audience of the Seitz-Eastmann review and was impressed enough to feature an article about the ALS in the June 1985 issue. The article was very helpful in getting the case out into the larger scientific community, where many people found it hard to believe that you could get coherence out of uncorrelated electrons.

That summer, the National Science Foundation decided not to go forward with Aladdin, a soft x-ray facility at the University of Wisconsin-Madison. Although Aladdin has been operating now for many years, at the time it was having problems coming online. Its apparent demise created an opening for the ALS. A workshop was quickly organized for November 1985 to restate the case for the ALS and submit a report by December 1,

an important deadline in the federal budget process. The report carefully laid out the broad community of support that had been built up over the past several years under the leadership of Herman Grunder, Martha Krebs, and Dave Attwood. Dave was told by Judy Bostock of the White House Office of Management and Budget to listen carefully to the President's State of the Union address in February. If the ALS gets mentioned, she said, you're in. If not, good luck next year. Dave recalls clearly that he was driving in downtown San Francisco, listening to the speech on the radio when President Reagan spoke about aspiring "to discover a new universe inside a tiny silicon chip or a single human cell." That was it! The ALS would be in the budget. "I was so shaken," he said, "I had to pull off the road!"

That initial pot of money (\$1.5 million), although not the full amount needed for construction, was enough to get started on detailed engineering. Klaus Berkner and Max Cornacchia led the production of the ALS "bible," the Conceptual Design Report (Pub. 5172 Rev.), published in July 1986. This report incorporated major design improvements, including the use of the triple-bend achromat structure in the lattice. After a grueling review by a DOE commit-



The ALS construction site, while boasting a spectacular view, posed many challenges: then, as now, space was scarce.

tee with technical experts from around the world, the CDR became the basis for realistic funding, scheduling, and technical goals. The wheels of government slowly turned, and in December 1987, Congress authorized the first \$18 million needed to begin construction of the ALS. A groundbreaking ceremony was held in August 1988.

FACILITY REPORT

REFLECTIONS ON THE ALS



Project leaders Jay Marx, Ron Yourd, Brian Kincaid, and Alan Jackson in 1989.



"Assembly line" of dipole (blue) and quadrupole (gold) magnets.

REFLECTIONS ON THE ALS

80

Construction Challenges

By this time, Jay Marx had been named ALS project director. Jay came in with a background as a user of high-energy physics facilities. As he says, "I knew how to pick up the phone and scream 'More beam!'" He soon discovered that this project was going to be fraught with technical challenges, including dealing with the limited space, decomissioning the existing cyclotron, stability issues, reliability for users, beam dynamics in the storage ring, vacuum chamber and undulator design, heat loads on x-ray optics, and on and on, not to mention management challenges such as a changing regulatory environment and looming budget cuts. Jay credits Ron Yourd, the ALS project manager, with building the ALS while Jay fended off the outside world.

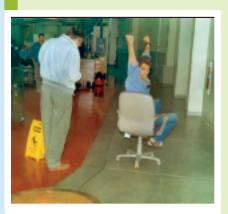
Sometimes, however, challenges and delays turn out to be blessings in disguise. In October 1989, the project was about a week behind schedule when the Bay Area was hit with the 7.1-



A section of the ALS storage-ring vacuum chamber atop an aluminum blank.

RACING AROUND . . .

The first operating ALS beamline was bending-magnet Beamline 10.3.1. In October 1993, the moment of truth—first light at the first ALS beamline—had arrived. Well, not quite. It turned out that, once the beamline was



Drew Kemp celebrates his finish in the chair race, while Jim Underwood records his time.

ready to go, there were still a couple of hours to kill while the control room cranked up the beam in the storage ring. Instead of kicking back and relaxing, members of the Beamline 10.3.1 team decided to blow off steam by staging chair races around the empty experiment floor, scooting around the perimeter

using a simple but reliable foot-propulsion method. The official record shows that Tom Swain crossed the finish line first in a (still unbroken) record time of 1 minute 31 seconds. Eric Gullikson came in second at 1:44, and Ray Thatcher came in third at 1:57.

... SEEING THE LIGHT

First Light at the ALS was clearly a momentous occasion in ALS history, one that begged to be captured on film for posterity. Of course, x-ray "light" is invisible to the eye as well as to conventional photographic film, so a phosphor-

coated screen had to be placed in the path of the beam to produce a visible manifestation of the arrival of the first x rays at an ALS beamline. Typically, such screens glow bright green when struck by x rays. Thinking that a



"Official" photo of First Light at the ALS, 12:20 A.M., October 5, 1993.

warm orange glow would make for a better image, Al Thompson got some red phosphor particles from Dean Chapman at the National Synchrotron Light Source and sprinkled them on a sticky foil. It worked beautifully. The resulting photo (a copy of which, signed by those present that day, is still on display at Beamline 10.3.1), evokes the image of a rising sun, an appropriate symbol of the dawning of a new era at the ALS.

magnitude Loma Prieta earthquake. The steel framework for the experiment hall was still stacked around the site perimeter at the time. If the girders had been in the process of being erected that day per the schedule, there is a good chance there would have been serious damage. As it turned out, the ALS escaped unscathed. Jay remembers that he was in Washington at the time, and it took him seven hours to get through by phone to his family and three hours to call the ALS.

While the walls were still going up, work on accelerator and booster-ring components continued in parallel. This work was being done all over the place, not just under the dome–for example, magnets were

being assembled and stored in separate buildings. An interesting aside is that, in selecting the distinctive color scheme of the magnets, Jay confesses that he punted to Ron, who chose blue and gold in honor of his alma mater, Berkeley. In any case, at one point, before the magnets could be installed, it started raining and a roof started leaking onto these precise, complex assemblies. People from all over the Lab rushed over to help fix the leak and move magnets.

Another nerve-wracking episode involved the milling of the vacuum chamber. The chamber is the backbone of the storage ring and consists of large aluminum panels milled with computer-aided precision to accommodate the electron beam and lattice compo-



ALS dedication ceremony on October 22, 1993: Jay Marx, Don Pearman (head of the DOE Oakland Site Office), Martha Krebs, David Shirley, Gayle Wilson (wife of then-Governor Pete Wilson), Brian Kincaid, Charles Shank, and Herman Grunder.

REFLECTIONS ON THE ALS

82

nents. Each aluminum panel measured 5×33 ft, weighed 8690 lbs, and cost \$17,500. Twenty-six panels were shipped to a company in Los Angeles for milling. However, before it could start the job, the company went bankrupt. To avoid a delay of up to six months while the courts sorted out the company's assets, ALS engineers were immediately dispatched to LA, where they hired a trucking company, arranged for storage facilities, and reclaimed the aluminum panels literally hours before the padlocks went up on the doors.

The vacuum chamber episode is emblematic of the dozens of tales of the ingenuity, initiative, and dedication of the people who built the ALS, too numerous to mention in this short space. Because of them, despite all the challenges

inherent in building an incredibly complex scientific facility, the ALS was completed on schedule and within budget (with \$2,200 left over). In October 1992, as the ALS construction was nearing completion, Jay Marx handed the baton to Brian Kincaid, who guided the ALS through its commissioning and early years as a productive scientific facility. The official dedication ceremony was held on October 22, 1993. How did they do it? Bill Oosterhuis, representing the DOE's Materials Sciences and Engineering Division at the 2003 ALS Users' Meeting, summed it up this way: "First, you get really good people. Second, you give them enough resources so that they can do the job without cutting corners. The third thing is you get the hell out of their way."



The ALS project team was huge, and while there is no single photo of everyone gathered in one spot, this photo shows many of the people involved in construction, ca. 1993.

OPERATIONS

Ben Feinberg, Division Deputy for Operations

:::

Operations and Availability

The mission for the ALS is to "support users in doing outstanding science." Critical to that support is the delivery of high-quality beam. Delivering beam according to the published schedule, along with an efficient, effective safety program, allows ALS researchers to make maximum use of the limited beam time. In 2003, the ALS maintained its exemplary operations record while continuing to make improvements in beam quality and reliability. In addition, the Operations groups worked with the Experimental Systems Group (ESG) and other groups at Berkeley Lab to bring online five new beamlines, including an elliptically polarized insertion-device beamline dedicated to molecular and environmental science (MES), two protein crystallography beamlines on superbends, one with the added capability of

small-angle scattering, and two bend-magnet beamlines, one for LIGA (deep-etch lithography) and one for diagnostic use by the Accelerator Physics Group. In addition, the Scientific Support Group (SSG) in conjunction with the Center for X-Ray Optics (CXRO) has commissioned a new coherent soft x-ray science branchline in Sector 12.

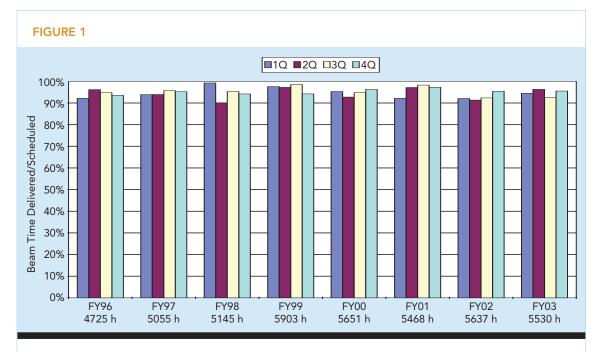
The research community at the ALS has become accustomed to high operational efficiency and reliability, and it was not disappointed during this period. As shown in Figure 1, the ALS delivered beam to the users 95% of the time scheduled for user operations in fiscal year (FY) 2003, doing slightly better than last year.

As in years past, we look very carefully at our different systems to determine where to focus our resources to improve reliability. Figure 2 shows our "lost user beam analysis" over the past several years. These figures allow us to pinpoint the most frequent causes of lost user beam time. As a

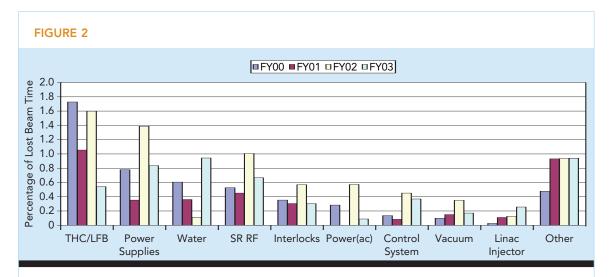
FACILITY REPORT

OPERATIONS

84



ALS operational availability (percentage of scheduled user beam time actually delivered).



Lost user beam analysis. The bars represent the percentage of user beam time lost over the last four fiscal years, separating out the various machine systems responsible. THC/LBF = third-harmonic cavities/longitudinal feedback; SR RF = storage-ring rf power.

result of the 2003 analysis, we are looking into improvements in some of our power supplies and continuing to work on our water systems to improve reliability.

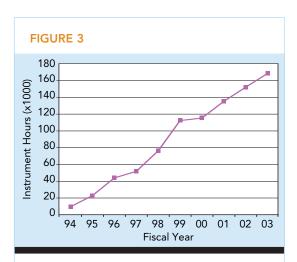
::

Changes in User and Instrument Hours

The monthly operations schedule continued to include a minimal number of maintenance and installation periods, which has been our practice for the last several years. Allowing approximately three days per month for needed maintenance and installation of new instrumentation has provided the maximum number of hours for user operations. In addition to these monthly periods, this year we had one four-week installation shutdown to install the new higher-order-mode (HOM) dampers in the third-harmonic cavities, improving the ability of the ALS damping systems to control beam instabilities, and to replace the superbend magnet cryocoolers. The delivered operating hours remained at the same level in FY 03 as in previous years.

With the constant number of operating

hours and the installation of new beamlines, we were able to increase the number of instrument hours (user hours multiplied by the number of simultaneous beamlines that can accept beam). We finished the fiscal year with 35 beamlines operating simultaneously, up from 30 at the end of the previous fiscal year. Figure 3 shows the growth in instrument hours since the first full year of ALS operations. The growth this year resulted in the delivery of about 169,000 instrument hours, an increase of 11% over FY 02.



Growth in the number of instrument hours (user hours multiplied by the number of simultaneously running beamlines) from year to year.

FACILITY REPORT
OPERATIONS

::

Facility Growth

In April, during our one major shutdown for the year, we installed the new diagnostic beamline and the higher-order-mode dampers in the third-harmonic cavities. The MES beamline was commissioned early in the fiscal year, and two new superbend crystallography beamlines were commissioned, as described above. In addition, a new bend-magnet beamline for LIGA and a new branchline for soft x-ray coherent science on the Sector 12 undulator were also commissioned this year. These new beamlines have enhanced our capacity in the hard x-ray region and opened up major new capabilities for MES research and coherent soft x-ray scattering within the core region of the ALS spectrum.

FACILITY REPORT

OPERATIONS

ACCELERATOR PHYSICS

David Robin, Accelerator Physics Group Leader

::

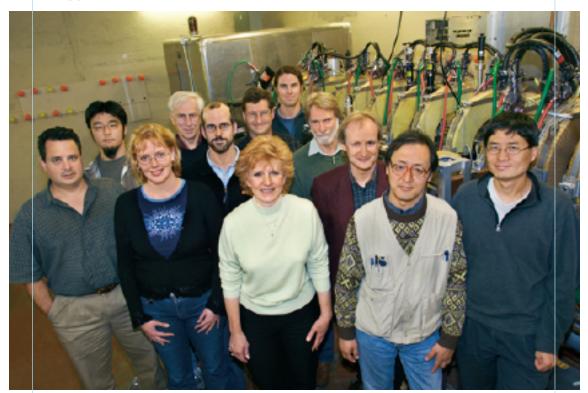
Introduction

To achieve the goal of supporting users in doing outstanding science, the ALS Accelerator Physics Group (Figure 1) plays several important roles. The first is to make certain that the ALS provides high-quality beam in a reliable manner to users. The second is to strive to understand and continually improve the performance of the facility, keeping it at the forefront of synchrotron radiation sources. The third role is to ensure that machine upgrades are implemented smoothly, minimizing any adverse impact to users. The fourth is to study potential upgrades

to the facility that will enhance the ALS's capabilities and capacities.

This past year significant gains were realized in understanding and improving the performance of the ALS storage ring. Last year marked the completion of Beamline 7.2, completely dedicated to beam diagnostics. In addition, a fast orbit feedback system was commissioned to improve the beam stability. Also, a lot of effort was directed at future projects and upgrades to the facility, particularly for the generation of femtosecond x rays, brightness increases, and farinfrared (IR) radiation. In preparation for the installation of a narrow-gap, in-vacuum insertion device for the generation of femtosecond x rays,

FIGURE 1



The Accelerator Physics Group. Front: Fernando Sannibale, Agusta Loftsdottir, Linda Senft, Hiroshi Nishimura, Weishi Wan. Middle: Toshiro Nishimura, Steve Lidia, Warren Byrne, Christoph Steier. Back: Harald Rose, David Robin, Tom Scarvie.

FACILITY REPORT

ACCELERATOR PHYSICS

ACCELERATOR PHYSICS

88

the effect of narrow-gap insertion devices on the beam lifetime was extensively studied. Also, planning began for the eventual transition to top-off injection operation.

Compared to the previous year, the ALS realized several improvements in operation. This was the first full year of operation with higherorder-mode (HOM) dampers in the radiofrequency (rf) system. Installation of HOM dampers in the main- and third-harmonic cavities reduced the thresholds of coupled-bunch instabilities. Before installation of the dampers, the driving terms of the HOMs were sufficiently large that if the beam was longitudinally unstable at large currents, it was impossible to restabilize the beam. A loss in longitudinal lock required approximately half an hour of user down time in which the beam energy was ramped down to the injection energy, the current scraped down, longitudinal lock recaptured, the beam current refilled, and the beam energy ramped back to user energy. Loss of longitudinal lock was one of the major causes of beam loss for users. The HOM dampers damped the modes to such a level that the coupled-bunch feedback systems could recapture longitudinal lock at full beam current, resulting in no loss of beam time.

In May 2004 additional dampers will be installed in the third-harmonic cavities. The goal of these dampers is to reduce the modes in those cavities that drive transverse instabilities. At the present time, if the parameters of the cavity such as temperature and tuner position are not properly adjusted, the beam becomes unstable. This happened on a number of occasions during this last year. Once the new dampers are installed, the beam will be much less sensitive to the cavity settings. This will improve the overall reliability of the ALS.

In the same May shutdown, a new W11 wiggler will be installed, replacing an older W16. This new wiggler has two functions. It will be a

source of hard x-ray radiation for the existing three protein crystallography beamlines in Sector 5. In addition, it will serve as the modulator for the femtosecond slicing beamlines planned for Sector 6. The big advantage of the W11 is that it will serve both the femtosecond and protein crystallography communities simultaneously. This was not possible with the W16.

This year a lot of work went into investigation of IR radiation in the storage ring. One of the interesting outcomes was the generation of enhanced radiation during the femtosecond slicing experiment. When the femtosecond laser modulates the stored beam, a longitudinal density modulation was created that enhanced the emission of coherent IR radiation. This radiation, which was measured at the IR beamline, was used as an effective diagnostic for the femtosecond experiment. This diagnostic had many advantages compared to other diagnostics used to optimize the laser beam interaction. It is a sensitive, continuous, nondestructive diagnostic of the effectiveness of the slicing and was fundamental for the users of the femtoslicing beamline.

This past year a lot of thought went into upgrades of the facility, prompted by a BESAC subcommittee workshop on producing a 20-year roadmap for Basic Energy Sciences facilities. The ALS presented plans for upgrades to the existing storage ring as well as plans for a new storage ring dedicated to far-IR radiation. The storage-ring upgrades are designed to improve brightness. The first step is to increase the time-averaged current by a factor of three. The plan is to go to a quasicontinuous injection scheme with the current increased to 750 mA. In addition, the brightness would be increased by operating with smaller vertical gaps in the insertion devices. This would also increase the range of undulator radiation to higher energies. The plan also calls for the replacement of the older, full-length, planer insertion devices with two half-length insertion devices

with chicanes. This would increase the capacity and productivity of the facility by allowing more "application specific" beamlines. The changes would be implemented gradually in typical annual shutdowns with minimal disruption for users. The plans for these short-term upgrades are discussed in more detail below.

Also at the BESAC workshop, plans for a new source of far-IR radiation was presented. This source, named CIRCE, would reside on top of the booster-ring shielding and would use the booster as an injector. CIRCE would be optimized for the generation of far-IR radiation by taking advantage of synchrotron radiation to shape the pulses and provide stable far-IR radiation many orders of magnitude higher than provided by conventional sources. The idea was experimentally verified at BESSY II. The effect of the synchrotron radiation impedance on the bunch distribution was first investigated by K. Bane et al. (American Institute of Physics Conference Proceedings, Vol. 367, p. 191), and in the past two years, scientists at Berkeley Lab and BESSY were able to expand upon the theory to quantitatively explain the BESSY results. In addition, the theory was used to design CIRCE to be fully optimized for the generation of far-IR radiation. These studies, together with engineering studies, were funded on strategic Laboratory Directed Research and Development (LDRD) funds.

The BESAC subcommittee recommended that the DOE organize a national workshop to explore the scientific advantages of research with terahertz radiation at user facilities. The workshop, sponsored by the DOE's Office of Basic Energy Sciences (BES), the National Institutes of Health (NIH), and the National Science Foundation (NSF), is scheduled for February 2004 and the CIRCE parameters will be presented there. The report of that workshop will determine how aggressively we pursue the CIRCE proposal.

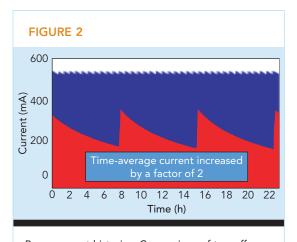
Top-Off Mode

The practical achievable brightness of the ALS is limited by beam lifetime. It is possible to increase the beam brightness by operating with higher currents, smaller beam sizes, and smaller insertion-device gaps. However, the operating conditions come with a penalty-a shorter lifetime, which is unacceptable to the users. To alleviate the impact of short beam lifetimes, the ALS is planning to upgrade the facility to operate in a quasi-continuous injection mode (topoff mode). In this mode, beam is injected into the ring approximately every minute to replenish lost electrons, keeping the beam current roughly constant. Operating the ring with constant beam current has an additional advantage. Top-off operation would improve the thermal stability of many of the storage ring and beamline components. The short-term plan is to operate with top-off injection at 500 mA. The actual time between fills is a function of the electron-beam parameters and depends upon such things as the acceptable change in current with refilling and the beam lifetime (Figure 2, Table 1). As seen in Figure 3, there are brightness gains in all sources. These gains result from the doubling of the



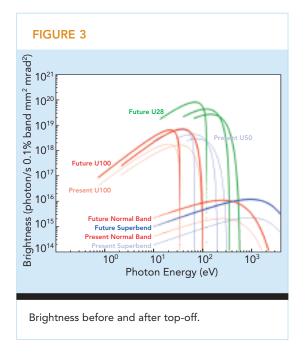
ACCELERATOR PHYSICS

89



Beam-current histories: Comparison of top-off mode (blue) to present mode (red).

	δi (mA)	Δt (s)	δt (ms)	$oldsymbol{arepsilon}_{v}$	σ _h (μm)	σ _y (μm)	σ΄ _h (µrad)	σ' _ν (µrad)
Operational 2003	1.5	72	≤ 50	150×10^{-12}	298	23	22	6
Intermediate	1.5	32	≤ 50	30×10^{-12}	298	10	22	3
Smallest ever	1.5	14.4	≤ 50	5×10^{-12}	298	4	22	1



ACCELERATOR **PHYSICS**

90

average current, smaller vertical beam sizes, and smaller vertical gaps.

For top-off injection, the injector energy has to be increased from 1.5 to 1.9 GeV. This requires an upgrade of parts of the booster injector (particularly rf components and power supplies) as well as an upgrade of the some of the pulsed-injection elements. Also, top-off operation requires that the beamline shutters remain open during injection. We received some initial funding this past year for refining the scope of the top-off upgrade. The effort was concentrated in three areas. A major part of the work was to study the key injection components to be upgraded. Also, a series of experiments were performed with various user groups to identify issues with top-off mode. Of particular concern

was the injection process, which would perturb the beam current and beam orbit. We identified a few types of experiments (particularly involving microscopes with short integration times) where injection was not transparent and found gating schemes to mitigate the problem. Finally, we are studying plans for modifications to the radiation protection system. By the end of this year, the scope of the upgrade will be well defined. The plan is to complete the upgrade by the end of FY 07.

Impact of Narrow-Gap Insertion Devices

Christoph Steier, David Robin, Weishi Wan

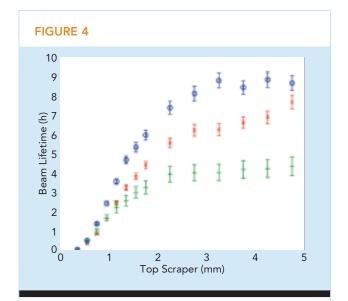
For permanent-magnet and superconducting insertion devices, performance depends strongly on the minimum gap of the magnetic structure. Lowering the minimum possible gap, which at the ALS is currently slightly below 14 mm for out-of-vacuum devices, will allow us to deliver photon beams with higher brightness, broader tuning range, or covering new spectral regions (especially at higher photon energies).

One of the major concerns with lowering the vacuum gap is that there will be an increase in the electron-beam loss rate. Increasing the electron losses shortens the beam lifetime and increases the radiation levels. The primary mechanism for particle-beam loss at the ALS is intrabeam (so-called Touschek) scattering. During a Touschek scatter, two particles collide—one gains energy and the other loses energy. If the change

in energy is sufficiently large, an electron's subsequent motion can reach an amplitude such that it strikes the vacuum chamber wall—typically the smallest vertical aperture. The amount of energy that a particle can gain or lose and still stably remain in the ring is called the momentum aperture. The beam lifetime is more than quadratically dependent upon the size of the momentum aperture. Therefore it is important to understand and optimize the dependence of the momentum aperture on the vertical physical aperture to maximize the performance of narrow-gap insertion devices.

Before the installation of the superbends at the ALS, the vertical aperture at which the lifetime began to deteriorate significantly was about 8 mm (corresponding to an out-of-vacuum magnetic gap of about 14 mm). Modifications were made to the storage-ring magnetic lattice. In particular, a change was made in the manner in which we controlled the vertical beam size. Previously, skew quadrupoles were used to excite a linear horizontal-to-vertical coupling resonance, thus increasing the vertical beam size. Now, skew quadrupoles are used to introduce a vertical dispersion wave to increase the vertical beam size. We found that for the present ALS lattice, the dependence of the momentum aperture (lifetime) on the vertical physical aperture became much weaker, allowing us to reduce the vertical physical aperture significantly without compromising the beam lifetime.

Figure 4 shows the dependence of the beam lifetime on the position of a scraper (i.e., the vertical half aperture) for three different cases. The *red* and *blue* cases both correspond to a vertical emittance of 150 pm, whereas the *green* case corresponds to a vertical emittance of about 30 pm. In the *red* case, the vertical emittance is artificially increased (to increase the lifetime) by exciting a coupling resonance. This is how the vertical beam size has been controlled historically at the ALS. The *blue* case has the same vertical emit-



Measured lifetime of the ALS versus top scraper position (half aperture) in one straight for three different cases: excited coupling resonance (red), vertical dispersion wave (blue), and corrected coupling and vertical dispersion (green). The two cases with excited coupling resonance and dispersion wave were measured for identical vertical emittance.

tance, but instead of increasing the coupling, the coupling is corrected, and a coupling-free global dispersion wave is used to generate vertical emittance. The *green* case shows a future upgrade scenario, where both coupling and vertical dispersion are corrected, providing higher brightness, but because of the higher bunch density, a necessarily smaller lifetime.

For both the case with corrected vertical emittance (green) and the case with vertical dispersion wave (blue), the change in lifetime is fairly small down to a half aperture of 2.1 mm and 2.6 mm, respectively. For the case with artificially excited coupling resonance (red), however, the lifetime in this aperture range is already dropping significantly. Combined with the improvements in the lattice implemented three years ago and better correction of lattice symmetry errors, the improved coupling control will enable the ALS to reduce the physical gap of insertion devices from the current 8–9 mm down to about 5 mm. A first in-vacuum permanent-magnet undulator

FACILITY REPORT

ACCELERATOR PHYSICS

ACCELERATOR PHYSICS

92

with a 5.5-mm minimum magnetic gap will be installed early in 2005.

The injection efficiency for smaller vertical gaps was studied as well, and no showstoppers have yet been found. We plan to install a collimator system to protect all insertion devices in the ALS from injection losses during top-off operation. There are other issues associated with insertion devices with very small apertures and/or high magnetic fields. Some of these effects that have been studied-to name just a few examples—is the effect of the fields of the insertion devices on the nonlinear dynamics, resistive wall-heating effects, impedance issues, and the effects of the field imperfections of the devices (coupling, focusing, and orbit errors). Cooperating closely with the magnet group of the ALS, an extensive set of specifications is written for every new insertion device being built, to ensure smooth integration into the operation of the ALS.

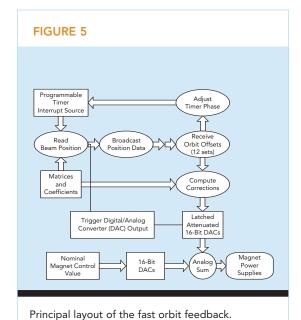
**

Commissioning of the Fast Orbit Feedback

Christoph Steier, Eric Williams, Ed Domning, Tom Scarvie

Employing a combination of good passive measures and careful engineering of noise sources like power supplies and the cooling system, the short-term closed-orbit stability of the ALS has so far fulfilled user requirements. In the range between 0.1 and 500 Hz, the integrated closed-orbit motion in the insertion-device straights is below 2 μ m in the vertical plane and about 3 μ m in the horizontal plane (one-sigma beam sizes at 1.9 GeV at that position are about 23 μ m vertical and 300 μ m horizontal).

The constant expansion of the ALS creates new sources of closed-orbit noise. EPUs, for example, require fast focusing and coupling compensation to minimize their influence on the beam size, which in turn creates fast distortions of the orbit. Other noise sources include active tune/chromaticity compensation schemes and the cryogenics of superconducting magnets or beamlines. To prevent the deterioration of the current orbit stability due to those upgrade projects and to ultimately provide a short-term submicron orbit stability, a fast, global orbit feedback system was designed similar to those found at several other light sources (Figure 5). The initial goal was to operate at an update rate of up to 1 kHz.

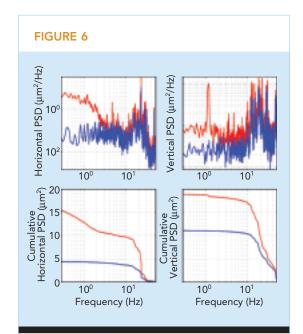


The commissioning of the fast orbit feedback started in late 2002. Initially the system was configured as a single-channel local feedback to simplify the optimization. Later it was tested in its full configuration with 24–40 beam position monitors (BPMs) in each plane and 22 corrector magnets in each plane distributed at 12 distinct

After the solution of many software and hardware problems, a reasonable system performance was achieved, correcting all orbit noise

locations.

below 15 Hz down to the BPM noise floor (Figure 6), without exciting higher frequencies in a significant way. This is a significant improvement over the slow orbit feedback used so far, which was only capable of suppressing noise below about 0.1 Hz. The slow orbit feedback will continue to be used together with the fast orbit feedback, since it allows a better localized slow correction using more BPMs and correctors. Problems coordinating the slow and fast feedback systems that showed up at other light sources were solved in our implementation from the beginning. Initial tests with a few users have been carried out, and the system will be used in routine user operation starting in early 2004.



Performance of the fast orbit feedback at the ALS. The left plots show horizontal closed-orbit motion and the right ones, vertical orbit motion. The upper plots show the power spectral density (PSD), whereas the lower ones show the square of the integrated root-mean-square (rms) orbit motion integrated from high to low frequencies. One can see that the system is very effective below 15 Hz. The 3-dB point of the closed-loop disturbance rejection is about 40 Hz.

**

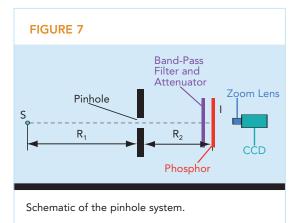
Beamline 7.2: A Second Beam Diagnostics Line

Fernando Sannibale

For the last two years, a mixed ALS and Engineering Division group has been working on a second ALS beamline completely dedicated to beam diagnostics. Beamline 7.2 was installed in August and successfully commissioned in September. The design of the beamline is optimized for the measurement of the momentum spread and emittance of the ALS beam in combination with the existing diagnostic beamline, Beamline 3.1. Before Beamline 7.2 became available, the momentum spread, a fundamental parameter in a storage ring, was not directly measurable at the ALS. Analysis of the experimental error in the emittance-momentum spread measurement allowed us to define the system parameters. We found a simple and reliable system based on an x-ray pinhole system (Figure 7) to be an ideal match for the requirements. The design of the beamline is based on two similar diagnostic beamlines at BESSY II. This approach allowed significant savings in time, cost, and engineering effort. Figure 8 shows a 3D view of Beamline 7.2 with its major subsystems. The entire beamline is located inside the ALS shielding.

FACILITY REPORT

ACCELERATOR PHYSICS



X-Ray BPM

Beamline 7.2 3D layout.

FACILITY REPORT

ACCELERATOR PHYSICS

94

For an electron beam at equilibrium, the transverse beam size is defined by the combined contribution of the emittance and momentum spread terms. For the horizontal rms size, we can write,

$$x_{rmr} = \left(\beta_{\kappa} \varepsilon \frac{1}{1+\kappa} + \left(\eta_{\kappa} \frac{\sigma_{p}}{p}\right)^{2}\right)^{1/2}$$

where β_x and η_x are the horizontal beta function and dispersion at the point of observation, ε is the natural emittance, κ is the emittance ratio, and σ_p/p is the rms relative momentum spread. If the optical functions at the source points are known and the horizontal beam size in two different points of the ring are measured, then the

TABLE 2 Comparison of source-point parameters.*

	Beamline 7.2	Beamline 3.1
$eta_{\!\scriptscriptstyle X}$ (m)	0.9	0.35
$\eta_{\scriptscriptstyle extsf{X}}$ (m)	0.07	0.03
x _{rms} (µm)	105	57.1

^{*}At 1.9 GeV, 400 mA, 3.07 keV critical energy.

emittance and the energy spread can be easily evaluated. The source point of Beamline 7.2 is situated in the central magnet of the triple-bend achromat (TBA) cell of the ALS, while for Beamline 3.1, the source point is in the external bend of the TBA. Table 2 shows the parameters for both the source points.

The filter shown in Figure 7 consists of a variable-thickness molybdenum target with the double role of variable attenuator and filter for the selection of the hard x-ray portion of the spectrum as required

for resolution preservation. The phosphor screen converts the x rays to visible light, and the image is finally acquired and digitized by a CCD camera. Table 3 shows the main pinhole system parameters, and Table 4 summarizes the performance of the system for different measurements. It must be remarked that the experimental error for the emittance–momentum spread measurement is dominated by the contribution of the optical functions at the source points and cannot be significantly reduced by a further adjustment of the Beamline 7.2 parameters.

Beamline 7.2 also includes an x-ray BPM for measuring the electron-beam orbit position and angle at the Beamline 7.2 source point. The system is based on the differential measurement of the electron secondary emission induced on two metallic blades by the synchrotron radiation. Finally, a special second port dedicated to visible and IR light can be used for several different electron-beam measurements, including longitudinal distribution profile and motion, transverse motion, and coherent effects at the IR and far-

TABLE 3 Beamline 7.2 pinhole system characteristics.

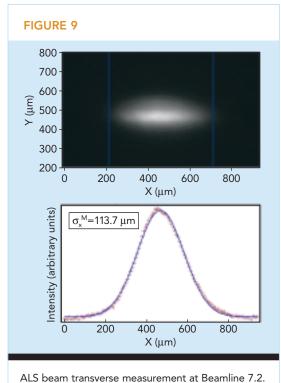
Parameter	Value
R1 (m)	6.08
R2 (m)	2.04
Pinhole Diameter (μm)	20
Photon Energy (keV)	16.3
Resolution (µm)	22

IR wavelengths. These last two systems are expected to be operational at the end of 2004.

Commissioning of Beamline 7.2 began in September 2003. Figure 9 shows a typical example of a transverse beam-size measurement. On the top is a very clean image of the ALS beam with an extremely low-level, uniform the background. On the bottom, the experimental points (crosses) for the horizontal distribution are nicely fitted by a Gaussian function (solid line). The resolution of the system has been measured by performing combined measurements of the size and lifetime of the ALS beam.

TABLE 4 Beamline 7.2 calculated performances.

Measurement	Experimental Error (rms value)
Momentum Spread	5.6%
Horizontal Emittance	6.6%
Horizontal Beam Size	1.3%
Horizontal Dispersion	1.2%
Horizontal Distribution Center of Mass	1.1%



FACILITY REPORT ACCELERATOR PHYSICS

EXPERIMENTAL SYSTEMS

Howard Padmore, Experimental Systems Group Leader

::

Introduction

The roles of the Experimental Systems Group (Figure 1) can be split into several categories: (1) to design and build beamlines and endstations based on the demands of the user program, (2) to conduct forefront research in science and instrumentation that will push the boundaries of the application of synchrotron radiation techniques, and (3) to give support to existing user programs, usually in areas of high technical complexity. Approximately 50% of the group's activity is in this latter area of direct user support. In this short report, I will give several examples of work in the two former areas and summarize our group's activity over the broader range of our work.



96



FIGURE 1

The Experimental Systems Group. Jinghua Hao, James Glossinger, Sirine Fakra, Tony Young, Dana Weinstein, Cathy Cooper, Jim Patel, Simon Clark, Tony Warwick, Andrew Doran, Jun Feng, Wayne McKinney, Alastair MacDowell, Jamie Nasiatka, Sug-Bong Choe, Peter Schmid, Martin Kunz, Matthew Marcus, Donnacha Lowney, Nobumichi Tamura, Howard Padmore, Ernie Glover, Andreas Scholl, Sander Caldwell, Rich Celestre, and Dave Walker.

::

X-Ray Tomography

The ALS has developed a wide range of imaging techniques, and the latest in this suite of methods is hard x-ray tomography, which allows deep penetration into solids and 3D visualization. This complements other techniques used at the ALS that look at surface or near-surface regions. The new superbend Beamline 8.3.2 was developed in collaboration with a consortium of users from Lawrence Livermore National Laboratory (LLNL), Berkeley Lab's Earth Sciences Division, and UC San Francisco (UCSF).

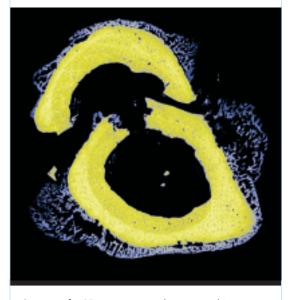
Beamline 8.3.2 is an unfocused beamline with a monochromator that allows the use of wide-bandpass multilayer mirrors or crystals or that can be rotated out of the beam path for white-light operation. The system normally uses W/B₄C multilayer mirrors with 2.5-nm lattice spacing for an energy range from 8-40 keV. A minihutch, as used for protein crystallography, houses the endstation, a state-of-the-art tomography system developed at LLNL by J. Kinney. The endstation is equipped with a tomographic camera that can zoom to a pixel size of 1 micron, so that by choosing an appropriate pixel resolution and photon energy, a wide range of sample volumes can be studied. The system is currently used to study a wide range of materials problems, including engineering materials and failure mechanisms, the porosity and connectivity of oil-bearing rock, the structure of gas clathrates, and the growth of bone.

Figure 2 shows a cross section from a 3D reconstruction of a section of bone from a rat femur, showing excellent differentiation between soft and hard bone regions. The image is 24 × 24 mm with a pixel size of 12 microns, and 360 images were acquired at 25 ms/frame. This bone imaging work by Kinney and co-workers is designed to address the issue of bone regrowth following hormone treatment for osteoporosis.

Although bone regrowth occurs with the stimulation of hormone treatment, very often the bone formed is of a high-density type susceptible to fracture. The key is to find a treatment that causes regrowth of the connective "spongy" bone network characteristic of normal bone.

While the system has been immediately successful in application to a wide range of problems involving imaging large objects, there are many areas that can be improved. To improve resolution without paying the normal flux penalty imposed by the use of very thin phosphors, we are investigating the use of highly asymmetric Bragg crystals as magnifying devices, as pioneered recently at the Swiss Light Source. We are also actively investigating column-parallel readout CCDs for a range of applications, including tomography, where very high frame rates with high digitization accuracy are required.

FIGURE 2



Section of a 3D reconstructed tomographic image from bone, highlighting high- and low- density regions. Image size is 24×24 mm with a pixel size of 12 microns. The reconstruction used 360 views, with exposure times of 25 ms/frame.

FACILITY REPORT

EXPERIMENTAL SYSTEMS

н

Small-Molecule Chemical Crystallography

Beamline 11.3.1 has been developed in collaboration with the UC Berkeley (UCB) Chemistry Department, for the examination of microcrystalline samples that could not otherwise be analyzed by bench-top x-ray diffraction instruments. The sample sizes that we are able to analyze are currently down to 10 microns on a side. Normally, such small crystals would be analyzed using powder techniques, but these are highly limited in terms of the complexity of the crystal structure that can be extracted, with 50 atoms per unit cell an upper maximum. Many of the compounds that chemists produce are more complex than this, or a level of structural accuracy is needed beyond that which can be extracted from powder data.

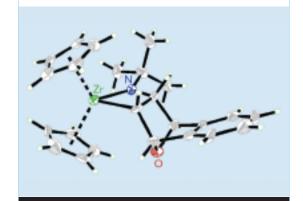
Beamline 11.3.1 uses a novel design in which a miniature, cryocooled, channel-cut monochromator and a 1:1-focusing toroidal mirror are located inside the shield wall, reducing the size and complexity of the system. Outside the shield wall is a small hutch and a standard Bruker SMART diffractometer and camera. In essence, the synchrotron provides a bright x-ray source for what is otherwise a standard laboratory x-ray instrument. This enables users to quickly and efficiently perform their experiments without a steep learning curve on how to operate the instrument. Collection time for a complete data set (100% coverage of reflection data) is on the order of 1.5 hours, and data can be collected and solved on crystals so small that conventional laboratory x-ray diffractometers would not be able to record even single diffraction patterns from them.

Figure 3 shows a structure solved from data taken on Beamline 11.3.1. The sample was produced by R.G. Bergman's group in the UCB Chemistry Department. The primary thrust of

this research is the analysis and development of compounds that can be utilized in catalysis. Often these materials contain transition metals that allow for controlled functionalization and modification of the compounds to form catalysts. The data for this sample were collected on a crystal that measured 28 microns on edge and refined to an R factor of 6.71%. Data were taken at 1 frame/s, and 750 frames were measured in total. Research undertaken at the UCB College of Chemistry covers a range of fields from synthesis of new catalysts, to solid-state materials for use in storage units in hydrogen fuel cells, to the total synthesis of natural compounds found in sponges, fungi, and other living things. This breadth reflects the general strength and diversity of the community of chemists that uses smallmolecule chemical crystallography as a standard tool.

Although Beamline 11.3.1 is now working well, there are a number of improvements that can be made and a number of new areas that can be addressed. In terms of improvements, we are working on adding a multilayer monochromator to the system to increase flux and enable

FIGURE 3



Structure of the zirconium complex ($C_{24}H_{27}NOZr$) solved on Beamline11.3.1 to 0.85-Å resolution. Carbon atoms are given by gray ellipses, hydrogen atoms by green open circles, and Zr, N, and O, respectively by green, blue, and red ellipses.

FACILITY REPORT

EXPERIMENTAL SYSTEMS

work on much smaller crystal volumes. Higher flux also increases throughput, and already in many cases, the data acquisition time is significantly shorter than the time needed to move the goniometer and read out the detector. The high spectral resolution of the current Si(111) monochromator is not required because of the typically small size of the unit cells that are measured. We also expect that it should be possible to extract the structure of long-lived photoexcited molecules using pump-probe laser techniques. Finally, we are examining the details of moving the system to a superbend location. Access to higher photon energies will significantly enhance the accuracy of our structural data. We are currently limited to around 16 keV on a normal bend magnet, and we would use typically around 30 keV on a superbend beamline. In doing so, we would expect to drive the resolution down to around 0.4 Å and make chargedensity measurements much more routine than they are at present.

::

SIBYLS Beamline 12.3.1 for Structural Biology

The Structurally Integrated BiologY for Life Sciences (SIBYLS) program is headed by J. Tainer of The Scripps Research Institute and P. Cooper of Berkeley Lab's Life Sciences Division. The beamline was funded by the DOE's Office of Biological and Environmental Research (OBER) and is part of a larger National Cancer Institute–funded program on the Structural Biology of DNA Repair (SBDR). The beamline and endstation are aimed at the study of the large complexes involved in DNA repair mechanisms and therefore have characteristics that are unique among the array of protein crystallography beamlines at the ALS. The endstation (Figure 4) is separated into two parts, an

upstream small-angle x-ray scattering (SAXS) station and a downstream protein crystallography (PX) station.

The PX station uses an ADSC Q315 detector capable of retracting to 1 m from the sample, allowing the beam to be focused either on the detector or on the sample. For large-unit-cell structures, it is important to have very good spot-to-spot resolution, and so in this mode, the

FIGURE 4



Layout of the SIBYLS beamline, showing the upstream SAXS station (*left*) and the downstream PX station (*right*).

detector is moved away from the sample, and the beamline is adjusted to put the focus at the detector plane. This requires that the M2 mirror angle and bend be changed slightly, and therefore the sample goniometer and all its associated instrumentation are moved vertically to accommodate the small vertical position displacement of the beam.

The upstream SAXS station is used for the study of proteins in solution. The solution cell is at the front of the hutch, and a MAR165 detector is approximately 1.5 m downstream. In SAXS mode, the beamline is refocused onto the SAXS detector. For time-resolved work, typically 5% of the detector is exposed, and the rest is used as fast memory. Also, as SAXS does not require high energy resolution, a multilayer monochromator is used that consists of two

FACILITY REPORT

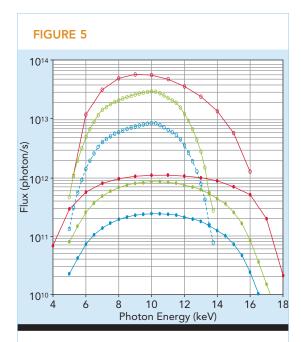
EXPERIMENTAL SYSTEMS

100

W/B₄C multilayer mirrors with 200 periods of 2.5-nm d-spacing, which give a measured efficiency (each) of 55% at 8.5 keV. The first multilayer is mounted off-axis on the rotation system of the first crystal of the monochromator in such a way that in going to small angles, lower than the normal crystal range, the first multilayer intercepts the beam. The second multilayer is then moved on its x-y table to give a fixed exit height. Thus, switching from crystal to multilayer mode is simple, fast, and reproducible. To further improve the changeover from PX to SAXS mode, the whole SAXS endstation system, including flight tube and detector, is mounted on a laterally translating table.

The beamline and PX endstation have been commissioned, and the PX endstation has begun routine data collection. The SAXS commissioning is just starting. Figure 5 shows the flux performance of the beamline in both SAXS and PX modes. The SAXS mode gives around 3×10^{13} photons/s (with multilayers) at the detector. It should be noted that the system is optimized for 10 keV, and because of the eccentric motion of the first multilayer, flux at higher energies falls off simply because the beam starts to miss the multilayer. However, almost all SAXS studies planned for this beamline will use 10 keV light, and so in practice, this compromise in performance has no practical effect; the positive benefit of the geometry, however, is that the system is simple, low in cost, and easy to operate. In PX mode, a 100-micron pinhole collimator is used, giving a flux of 2×10^{11} photons/s [with Si(111) crystal] for a 3-mrad convergence angle, commensurate with the Sector 8.2 superbend PX beamlines. The upper curves for the crystal and multilayer monochromators refer to use without a pinhole collimator.

Although SIBYLS is in many ways an optimum and flexible structural biology facility, in SAXS mode, there is significant room for improvement. The current CCD-based detector is excel-



Calculated and measured fluxes for the multilayer and Si(111) monochromators at the PX sample position. The upper plot is the total calculated flux from the multilayer mirrors (without pinhole collimator). The two plots slightly below it are the measured total flux and the measured flux through a 100-µm pinhole. The three lower curves are similar plots for the Si(111) crystals. Fluxes are for 400 mA at 1.9 GeV and full acceptance of the beamline, resulting in a convergence onto the sample of 3.0×0.31 mrad. The focused spot size was measured as 165×130 µm FWHM.

lent for static SAXS, but its limited readout speed means that for dynamic SAXS, i.e., for looking at the assembly of complexes, the detector has to be used in "streaked" mode. In this mode, typically 5% of the detector is used for data collection and 95% is used for memory. This is clearly wasteful, and for radiation-sensitive systems, it is far from ideal. A solution is to use much faster CCD detectors based on a columnparallel readout format, where each column of data is read by its own electronics channel. We are working on a program between Berkeley Lab and Fairchild Imaging to build such a system, utilizing the large-area CCDs that Fairchild has pioneered combined with the electronics that Berkeley Lab has developed for the SuperNova/ Acceleration Probe (SNAP) project. Such a system should have a 200-frame/s capability at 16-bit dynamic range. One of the issues with such a system is dealing with the huge data rate, and so a significant component of the system under study is the use of a field-programmable gate array (FPGA) backend for data reduction and compression. For SAXS, this is relatively easy as it only involves doing azimuthal integrals, but similar systems will be used for single-crystal diffraction where more complex analysis and compression algorithms will be needed.

н

High-Pressure X-Ray Diffraction

Beamline 12.2.2 is designed for collecting diffraction and x-ray spectroscopic data from materials held under extreme conditions of temperature and pressure. The scientific focus is on understanding Earth dynamics, investigating chemical reactivity, and probing the link between the meso- and nanoscale in materials. Construction and commissioning of the beamline is largely completed, and its performance has been measured to be close to predictions.

The endstation is highly complex and includes two workstations: the first utilizing resistively heated diamond-anvil cells and the second, a laser-heating system. The laser-heating system is working off-line and is ready for installation in the hutch. Currently, the plan is to install the first workstation during the May 2004 shutdown and the second workstation in August 2004. The beamline design is almost identical to that of the SIBYLS beamline, employing a vertically collimating, side-cooled Si mirror inside the shield wall, a two-crystal [Si(111)] monochromator, and a 2:1 (horizontal) toroidal refocusing mirror. The beamline also uses the same dual-monochromator scheme, with an off-axis multilayer mirror pair (for an optimum energy

of 25 keV) for high flux, and the normal Si(111) constant exit-height system. The only major difference is that the mirror grazing angles are reduced to 2 mrad from 4.5 mrad, to give an upper operating energy of 40 keV. The upstream endstation will utilize the native beam size (150 × 100 microns), and the second endstation will refocus this object using a Kirkpatrick-Baez (K-B) mirror pair to 10 microns. The upstream endstation is now complete and undergoing commissioning; the downstream endstation and its K-B mirror system are under construction.

Development of this beamline has been a collaboration between the UCB Earth and Planetary Science Department (R. Jeanloz), the UCB Chemistry Department (A.P. Alivisatos), the UC Santa Cruz Earth Sciences Department (E.B. Knittle and Q.C. Williams), the UC Los Angeles Chemistry and Biochemistry Department (S.H. Tolbert), LLNL (J. Zaug), and the ALS. It has been supported through major grants from DOE BES as well as from LLNL. The National Science Foundation Consortium for Materials Properties Research in Earth Sciences (COMPRES) supports geoscience users on Beamline 12.2.2 and single-crystal studies on Beamline 11.3.1.

During the construction of Beamline 12.2.2, we have been developing protocols for collecting high-pressure data using a temporary set-up on Beamline 7.3.3. Such work by UCB researchers K.K.M. Lee and R. Jeanloz resulted in a major step forward in our understanding of the Earth's core [Geophys. Res. Lett. 30, 2212 (2003)]. Their work on the high-pressure and -temperature alloying of potassium and iron, not possible at ambient conditions because of incompatible electronic structures, shows that potassium and its long-lived radioactive isotope (40K) can be incorporated into the Earth's iron-rich core, providing a heat source to drive the Earth's magnetic field and mantle dynamics. This alloying was discovered through the use of

FACILITY REPORT

EXPERIMENTAL SYSTEMS

synchrotron-based x rays at Beamline 7.3.3 and from earlier data taken at Stanford Synchrotron Radiation Laboratory (SSRL) that show that the unit-cell volume increases with the incorporation of K into Fe at elevated pressures (Figure 6). Phase-transition pressures are indicated by vertical lines for Fe (solid) and K (dashed) with phase stability ranges labeled in between. The shaded vertical bar at 26 ± 3 GPa is the K-Fe alloy transition pressure.

FIGURE 6 12.0 ©080 d 11.5 0 0.11 7.00 (Å²) 0.01 0.01 40 ressure (GPa) 10.0 9.5 9.0^L 10 20 30 40 50 60 70 Pressure (GPa)

Iron unit-cell volumes observed for K + Fe samples, prior to heating above the sample solidi (solid circles) and after heating above the sample solidi (open circles), compared with those for pure Fe (solid squares). The inset shows the percent deviation from the expected Fe volume. Horizontal dashed lines at 0 and 2.1% correspond to no deviation, as observed for the volumes of unalloyed Fe (closed circles) and the average percent volume deviation of the Fe-K alloy (open circles).

FACILITY REPORT

EXPERIMENTAL SYSTEMS

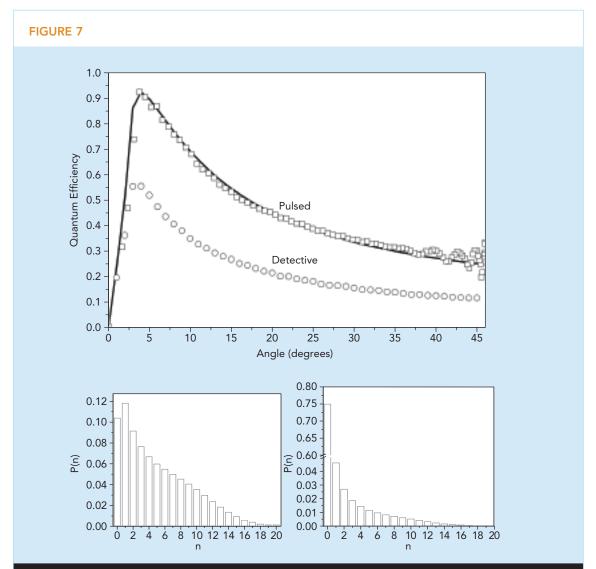
102

::

A Detector for the Study of Ultrafast Dynamics

We have a need for ultrafast detectors for a range of experiments that are based on streakcamera technology. X rays strike a photocathode and are converted to electrons; the electrons are accelerated to high energy (10 keV) and are deflected by a photo-switch-triggered sweep plate and dispersed onto an image-intensified CCD camera. An ultrafast detector would mainly be used (1) in conjunction with our Beamline 6.0 sliced x-ray source to reduce background and (2) for ultrafast magnetization experiments. Streak-camera detection complements the use of sliced pulses of x-rays in that they record an entire time sequence in one shot, they can work at a high repetition rate in principle, and can be used in conjunction with any ALS beamline.

Although streak cameras have been around for many years, they have a range of problems that we are trying to address. The most serious is that the conversion of x rays to electrons is inefficient, with a typical yield being a few percent in the soft x-ray range and less than this in the hard x-ray range. We have addressed this by examining the use of grazing-incidence photocathodes. The basic idea is very simple: to match the penetration of the x rays from the surface to the secondary escape depth, which can be done by going to a grazing geometry. Figure 7 shows the pulsed quantum efficiency (PQE) for CsI as a function of angle, and this demonstrates that a PQE of 100% can be reached. This particular measurement was for 1-keV x rays. The detective quantum efficiency (DQE) reached a maximum of around 60%, lower than the PQE because of the spread in the probability of exciting a particular number of electrons with each x-ray photon. This spread lowers the statistical certainty of a measurement and, hence, the DQE. A grazing-incidence



Top: Pulsed and detective quantum efficiencies of a grazing-incidence photocathode for use in a grazing-incidence streak camera. Bottom: Probability of detecting a defined number of electrons per x-ray photon, for 500 eV (*left*) and 1000 eV (*right*).

streak camera based on this concept has been designed and is due to be tested shortly.

A second issue with streak cameras is jitter between the excitation pulse and the sweep, caused by laser intensity jitter activating the photoconductive switch for the sweep plate at slightly different times. This jitter problem is being addressed by careful attention to laser intensity stability. In addition, we are developing a system that time stamps the sweep by putting a frequency-tripled ultraviolet (UV) pulse onto

the photocathode. Each frame is recorded, unlike in a conventional camera, and then jitter is removed on a shot-by-shot basis by referencing each sweep to the time zero established by the UV pulse signal. The challenge is to do this at the 5-kHz repetition rate of the camera.

We are also investigating the absolute time resolution set by space charge and by electron scattering within the photocathode, as well as ways to make an isochronous electron imaging system. One of the principal restrictions on FACILITY REPORT

EXPERIMENTAL SYSTEMS

temporal resolution is the chromaticity of the secondary electrons that produce the image. Electrons created at the same time but with different initial energies are swept to different positions on the detector. To counter this, an optimum design should be isochronous, i.e., electrons of any initial energy take the same time to pass through the optical system. Such systems are commonly used in some high-energy accelerators, and we are using similar methods in our initial studies of corrected isochronous cameras.

Other Ongoing Projects

The PEEM-3 beamline in Sector 11 is under construction, with first light expected early in 2005. The PEEM-3 microscope itself is an aberration-corrected photoemission electron microscope and should be ready for initial testing in spring 2005. Major components of these systems are now being fabricated. The beamline and microscope combined should give unprece-

dented performance, with around 1000 times the throughput and 5–10 times the resolution of PEEM-2.

The group is also working on an ultrafast x-ray science facility in Sector 6. The source is a 30-mm-period 1.5-T in-vacuum undulator/ wiggler. Short pulses of x-rays will be produced by laser-induced energy modulation combined with vertical dispersion and imaging. This "slicing" of the beam will produce pulses of x rays ~200 fs long. The first beamline, expected to be operational in spring 2005, will use a soft x-ray spectrometer system with an imaging detector, allowing whole spectra to be measured at once. A second beamline, to come online later, will be a conventional two-crystal monochromator beamline for higher-energy x rays.

We are also working on the details of moving the microdiffraction beamline to a superbend and on all aspects of the ALS upgrade. This will involve significant optics upgrades to most beamlines and the addition of more chicaned undulator beamlines. This is a major design and planning activity and is well underway.

FACILITY REPORT

EXPERIMENTAL SYSTEMS

SCIENTIFIC SUPPORT

Zahid Hussain, Scientific Support Group Leader; John Bozek, Scientific Support Group Deputy Leader

Introduction

The primary mission of the Scientific Support Group (Figure 1) is to support the efforts of researchers at the ALS through scientific and technical collaboration and scientific outreach. Working with the users, the SSG plays an important role in developing novel instrumentation that enables cutting-edge science. Depending on the needs of the user, the degree of collaboration can range from technical assistance with the beamline to full partnership in developing new research programs.

Scientific Outreach

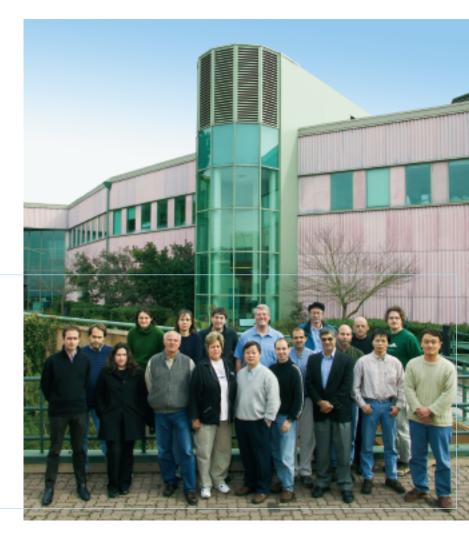
The SSG strives to expand the scientific program of the ALS and broaden its user base through publications and presentations. The group organizes a variety of seminars, including the weekly ALS/CXRO seminar series and a targeted weekly SSG lecture series. The weekly lectures cover a wide range of topics and are given by world-renowned scientists. The group also organizes the quarterly ALS Colloquium.

Working together with the Users' Executive Committee, the SSG also helps to organize workshops exploring new scientific opportunities and needs for new beamlines or experimental facilities. During the 2003 ALS Users' Meeting, six such workshops were heavily attended by enthusiastic scientists, triggering many fruitful discussions that should spark further advances at the ALS.

The ALS Doctoral Fellowship in Residence program, established in 2001, has been very popular among doctoral students and has been received with much appreciation. The doctoral fellowships enable students to acquire hands-on scientific training and develop professional

FIGURE 1

The Scientific Support Group. Front: Massimiliano Rossi, Alexandre Kouprine, Adriana Reza, Fred Schlachter, Cheryl Hauck, Jinghua Guo, Per-Anders Glans, Zahid Hussain, Yi-De Chuang, Simon Mun. Back: Karine Chesnel, Elke Arenholz, Rudy Kimmerling, Mike Martin, Mohammad Gharaibeh, Aran Guy, Bill Bates, David Kilcoyne, Eli Rotenberg. Not pictured: Glenn Ackerman, John Bozek, Jonathan Denlinger, Alexei Fedorov, Byron Freelon, Gennadi Lebedev, Bruce Rude, Michel Van Hove.



maturity for independent research. More details are given at the ALS Web site (www-als.lbl.gov/als/fellowships). A selection committee consisting of J. Doudna (Chair, UEC), F. Himpsel, Z. Hussain, S. Bader (Chair, Scientific Advisory Committee), and N. Smith recommended the following recipients for doctoral fellowships for academic year 2004 (Figure 2):

Yulin Chen (Stanford University, spin-resolved photoemission spectroscopy)

Mohammad Gharaibeh (University of Nevada, Reno, ion spectroscopy)

Darcy Peterka (UCB, photoionization and photoelectron imaging of nanodroplets)

Daniel Rolles (Freie University, Germany, atomic, molecular, and optical physics)

Zhe Sun (University of Colorado, angle-resolved photoemission spectroscopy)

Joshua Turner (University of Oregon, coherent soft x-ray magnetic scattering)

Mandana Veiseh (University of Washington, biomaterials/nanotechnology)

Feng Wang (University of Michigan, photoemission and spectroscopy of correlated systems)

Support

SSG members are responsible for the operation, upgrade, and maintenance of most of the facility beamlines and many of the permanent endstations at the ALS. The undulator-based beamlines—4.0.2, 7.0.1, 8.0.1, 10.0.1, a photo-emission branchline on 12.0.1, and a coherent science branchline 12.0.2—each have one to two SSG staff members responsible for their continued operation. The group is also playing an active role in fixing some of the problems in the operation of the chemical dynamics complex

FIGURE 2

ALS Doctoral Fellows: Zhe Sun, Mandana Veiseh, Mohammad Gharaibeh, Darcy Peterka. *Not pictured:* Yulin Chen, Daniel Rolles, Joshua Turner, Feng Wang.

FACILITY REPORT

SCIENTIFIC SUPPORT

(Beamline 9.0.2), which is operated by Berkeley Lab's Chemical Sciences Division under separate funding from BES. The SSG has also received \$3.5M in funding from BES for the development of a new meV-resolution beamline (MER-LIN) optimized for the study of inelastic x-ray scattering and ultrahigh-resolution photoemission. Members of the SSG put great emphasis on making the development of novel instrumentation more efficient and user friendly. Also in 2003, the group has designed and developed several new experimental systems, some of which are described bellow.

Member Research

Staff scientists within SSG are expected to maintain scientific and technical excellence in areas of synchrotron radiation research. Participation in active scientific programs is essential for such development, and all of the SSG scientists are active members of research programs at the ALS.

-

Coherent Soft X-Ray Magnetic Scattering at Beamline 12.0.2

A new endstation dedicated to coherent x-ray resonant magnetic scattering (CXRMS) has been installed and commissioned on Beamline 12.0.2. This instrument specializes in the use of coherent light to probe magnetic nanostructures, utilizing the high brightness and coherence properties of ALS soft x-ray undulator radiation. While magnetic scattering (with incoherent light) gives information about magnetic structure and correlation at long range, coherent light yields speckle patterns, which relate to short-range magnetic order. CXRMS will provide access to magnetic fluctuations on the nanometer length scale and

the microsecond time scale, providing an important conceptual bridge between the nano- and macroscopic scales.

Development of this instrument emerged from experiments in collaboration with S. Kevan (University of Oregon), L. Sorensen (University of Washington), J. Kortright (Berkeley Lab's Materials Science Division), and E. Fullerton (Hitachi Global Storage Technologies). By extracting a transversely coherent beam directly from the undulator radiation on ALS Beamline 9.0.1, speckle patterns were obtained from a Co/Pt multilayer, structured on the nanometer scale. A static soft x-ray speckle metrology technique was developed to test the microscopic memory of the magnetic domain pattern (see "Learning How Magnets Forget" in the Materials Science section of the Science Highlithst chapter). These promising results motivated the construction of a new endstation dedicated to CXRMS that will extend these static experiments into the time domain.

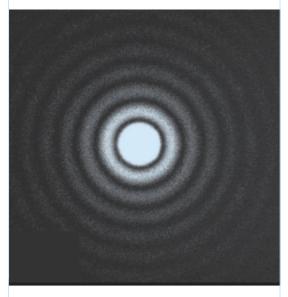
The design of Beamline 12.0.2 was specifically optimized to produce an intense, well focused beam of transversely coherent soft x rays, using a variable-line-spacing (VLS) grating monochromator with K-B refocusing mirrors. To illustrate the high degree of coherence, a diffraction pattern obtained from a circular pinhole is presented in Figure 3.

The new CXRMS endstation (Figure 4) includes an octopolar assembly of electromagnets capable of producing a magnetic field of up to 0.56 T with arbitrary orientation. The scattering chamber features a series of flanges in the vertical scattering plane. Scattered light can be measured either in transmission geometry using the main exit flange or in reflection geometry at angles from 0° (grazing incidence) to 180° (back scattering). The sample is mounted on a precision xyz stage through a side port. A cryogenic system allows temperature-dependent studies. Because the K-B mirrors focus the beam into a

FACILITY REPORT

SCIENTIFIC SUPPORT

FIGURE 3



Airy pattern obtained from a 2.5-µm pinhole at 500 eV (courtesy of K. Rosfjord and D. Attwood, CXRO).

FACILITY REPORT

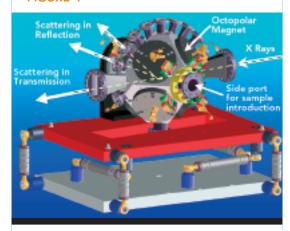
SCIENTIFIC SUPPORT

108

small spot, the system requires a small spatial filter pinhole and a correspondingly large speckle solid angle, so that the flux scattered into a single speckle will be enhanced. As shown in Figure 5, an array of micron-sized pinholes is mounted in front of the sample stage for spatial filtering. It can move independently in the horizontal and vertical directions thanks to an inchworm and a bender device. The distance between sample and pinhole is about 5 mm, thus giving near-field illumination and good oversampling conditions.

This new facility is now operational and the first experiments have been performed on reference magnetic systems. The study of magnetic speckle patterns at different resonance edges and

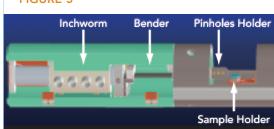
FIGURE 4



Schematic of CXRMS endstation showing the scattering chamber inserted in the octopolar magnet.

different scattering angles will provide information about the true local magnetic configuration within a material as well as spatial and temporal fluctuations under different parameters (magnetic field, temperature, etc). This technique can be used to study various types of magnetic systems, from thin films to nanoparticles.

FIGURE 5



Schematic of the cryogenic sample holder and enlarged view of the pinholes holder.

н

Vector Magnetometry Endstation Upgrades

The vector magnetometry endstation on EPU Beamline 4.0.2 allows polarization-dependent x-ray absorption measurements in magnetic fields applied in any direction relative to the incoming x-ray beam and the sample surface.

Replacing the steel poles used so far to obtain fields up to 0.9 T with newly fabricated aluminum poles allows us to sweep the field in $25-\mu T$ steps over the range of ± 0.15 T. For the study of very soft magnetic systems, the use of the remanence-free aluminum poles is clearly advantageous. Switching between the two sets of poles is possible within a few hours.

Recently, a cryogenic sample holder that covers temperatures from 15 to 450 K (measured at the sample) and with azimuthal and polar rotation capabilities was developed (Figure 6). Because access to the measurement chamber is limited (only 0.8 inches, set by the magnet dimensions), the main challenge was to design a very compact system that includes a bias mesh necessary to obtain high-quality data in electronyield measurements in an applied field.

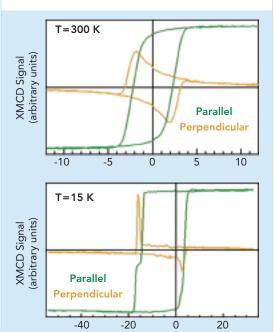
The new low-field and low-temperature capabilities of the system were recently employed to study magnetization reversal processes in Fe/MnF₂ bilayers (results are shown in Figure 7) in collaboration with K. Liu (UC Davis) and I.K. Schuller (UC San Diego).

FIGURE 6



New cryogenic sample holder used for the experiments.

FIGURE 7



XMCD measurements on an Fe/MnF $_2$ sample at room temperature and at 15 K after cooling in a magnetic field. The field dependence of the XMCD signal with the x-ray beam parallel and perpendicular to the applied field are shown in green and orange, respectively.

Field (mT)

FACILITY REPORT

SCIENTIFIC SUPPORT

н

ESF Chamber Goes to the Fourth Dimension

The Electronic Structure Factory (ESF) endstation at Beamline 7.0.1 has had a significant software upgrade this year to facilitate band mapping over a very wide range of 3D k-space values as well as to aid in data visualization. Users can now routinely acquire a 4D data set (energy, k_x, k_y, k_z) encompassing the band structure throughout most of a typical bulk Brillouin zone. The technique has significant advantages over other Fermi-surface mapping techniques because of its model-independent visualization of Fermi surfaces, the additional measurement of underlying band structure, and its applicability to disordered materials such as alloys as well as nonconductive materials. So far, the technique has been applied mainly toward electronic structure determination of magnetic metals.

Figure 8 illustrates a "brute-force" collection of band-structure data sampled uniformly throughout 3D **k** space for a hydrogenated tungsten (110) surface and obtained in about 90 min-

utes (right panel). Selective constant-energy cuts of the resulting 4D data set show cross sections of 3D surfaces which can be directly compared to calculated Fermi surfaces (left panel). In addition, the underlying bands can be interpolated along any arbitrary trajectory through the complete data set. Also useful is the straightforward identification of surface states whose geometry is conserved with respect to momentum perpendicular to the surface.

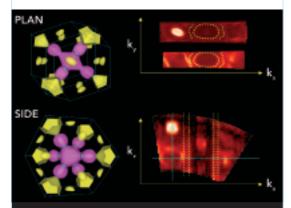
Figure 9 illustrates data acquisition along arbitrary trajectories in **k** space by coordinated movement of the monochromator and sample goniometer. The upper panel shows calculated 3D representations of the Fermi surface of bulk Cr metal consisting of electron and hole pockets. The lower panel shows cross sections of the electronic bands at constant energy for the Fermi energy, E_F (directly comparable to the upper figure), and for 0.21 eV below E_F. In contrast to conventional measurements at constant photon energy (*blue* line), the data were obtained

FACILITY REPORT

SCIENTIFIC SUPPORT

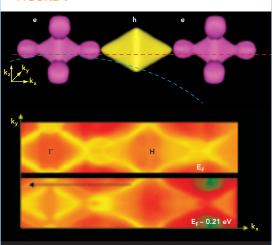
110

FIGURE 8



Calculated (left) and measured (right) Fermi surfaces for bulk tungsten. In the upper right panel, two planes of constant k_z are shown that cut the center of the electron pocket (left, purple sections) and hole pocket (left, yellow ellipse at center). Surface states are indicated by yellow lines.

FIGURE 9



Photoemission data along an arbitrary trajectory in \mathbf{k} space. *Top:* Calculated Fermi surface of paramagnetic Cr metal, consisting of electron (e) and hole (h) pockets. *Bottom:* Experimental constantenergy surfaces acquired at the Fermi level E_F and 0.21 eV below E_F along a true linear trajectory in \mathbf{k} space (red line).

in a plane with k_z (along surface normal) held fixed (*red* line), which cuts through the symmetry plane in a much more useful fashion. The ability to record a wide range of binding energies simultaneously allows us to see a backfolding of the hole pocket from the H symmetry point toward Γ , indicating the presence of a symmetry change from paramagnetic to antiferromagnetic metal caused by a commensurate spin-density wave (arrow). T.S. Choy et al. (University of Florida) worked out the theory and E. Rotenberg (ALS) and S.D. Kevan (University of Oregon) did the experiment.

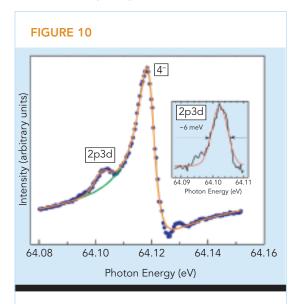
As a result of these developments, a typical one-week photoemission run now yields in excess of 10 gigabytes of data. The adoption of large-scale data storage and fast processors, once the exclusive territory of protein crystallography or microscopy users, has now become routine for angle-resolved photoemission practitioners.

::

Resolving Power of the ARPES Branch of Beamline 12.0.1

Development of the Beamline 12.0.1 ARPES endstation equipped with the highly efficient SES-100 electron spectrometer brought a new challenge for the beamline staff and the community of scientists interested in performing ARPES experiments. The large gap between the resolving power delivered by the existing VLS plane-grating monochromator (~1200, or $\Delta E =$ 50 meV at 60-eV photon energy) and the energy resolution of the SES-100 (~5 meV) called for a sharp boost in the resolving power of the monochromator. Although a tenfold increase in the resolving power of a beamline designed for high throughput and low resolution seemed a huge stretch, the year-long effort shared by the SSG and CXRO was a success, and a resolving power

of 10,000 has been obtained (Figure 10). This was achieved with a new VLS grating that, unlike the original 200-line/mm grating, was blazed to operate in a negative diffraction order. The new grating, designed by E. Gullikson (CXRO), has both 300- and 600-line/mm rulings on a single substrate. The grating was ruled by T. Tanaka



Rydberg series of doubly excited helium measured at Beamline 12.0.1 using the newly installed 600-line/mm VLS grating. Experimental width of the 2p3d resonance is ~6 meV. This measurement demonstrates a resolving power of 10,000.

(Hitachi High-Technologies Corporation) on a gold-coated substrate supplied by CXRO. The coating process developed by CXRO proved to be the key to creating a high-efficiency grating (Figure 11).

The scientific program was mainly devoted to studies of strongly correlated materials, including high-temperature superconductors, colossal magnetoresistance (CMR) compounds, and exotic superconductors (e.g., doped cobalt oxides). A UCB group led by A. Lanzara studied the electronic structure of carbon nanotubes and diluted magnetic semiconductors. Responding to the wishes of many users, we have designed and built a new sample manipulator capable of three rotational degrees of freedom. It is coupled to

FACILITY REPORT

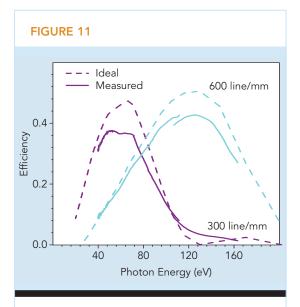
SCIENTIFIC SUPPORT

FACILITY REPORT

SCIENTIFIC SUPPORT

112

the liquid-helium cryostat, which can cool the sample down to 13 K. Another important upgrade is a sample load-lock chamber allowing simultaneous loading and storage of up to six samples. The load-lock chamber is also equipped with a compact electron-beam heater and thermocouple. Hence, samples can be annealed at temperatures of up to 3000 °C. Since many of the compounds studied at the ARPES endstation have a limited lifetime in the vacuum chamber



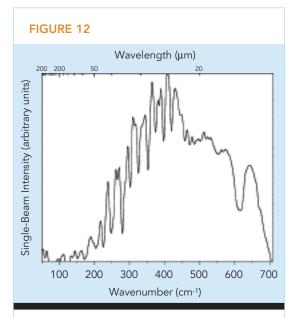
Diffraction efficiency of the new Beamline 12.0.1 VLS gratings measured at a constant deviation angle of 14° at Beamline 6.3.2. Note the excellent agreement between measured and ideal diffraction efficiency.

and are generally not available in big quantities, much time was spent improving the vacuum conditions. For example, the CMR material LaSrMnO (probably the most sensitive) does not show signs of aging during the typical eight-hour period required for its complete measurement.

First Far-IR Microscopy at Beamline 1.4.3

Extending the reach of synchrotron IR microscopy to longer wavelengths will allow users to measure lower-frequency vibrational modes. At present, the IR microscope on Beamline 1.4.3 has an MCT-A detector with a low-frequency cut-off of ~650 cm⁻¹. The KBr beam splitter will, in principle, allow measurements down to about 400 cm⁻¹. Measurement of lower frequencies will require a different beam splitter and a different detector.

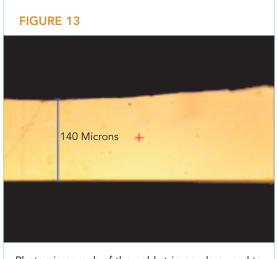
To test the longer-wavelength capabilities of the beamline and instrumentation, we purchased a solid-silicon beam splitter (nominal range 50-700 cm⁻¹), and we manually added a flat mirror inside the microscope's detector compartment to direct the light from the sample out the



Single-beam far-IR intensity measurement of the synchrotron source through the Beamline 1.4.3 Nic-Plan IR microscope and using a silicon beam splitter and liquid-helium-cooled silicon bolometer detector. The series of absorption bands below ~425 cm⁻¹ are due to water vapor in the air. These will be reduced significantly with the addition of a purge box for the external detector optics.

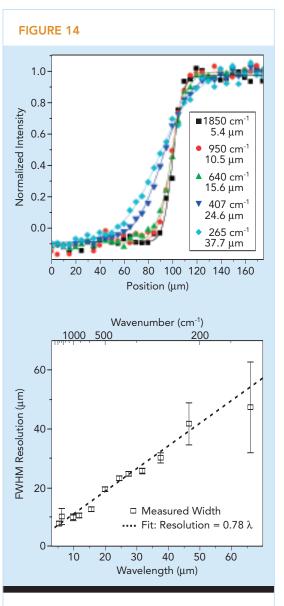
side of the microscope. This light was then focused using an off-axis parabolic mirror onto the entrance cone of a liquid-helium-cooled silicon bolometer. This bolometer was used with its 700-cm⁻¹ cut-on filter and a low-noise amplifier. The detected IR signal was sent back into the spectrometer for interferrogram acquisition and subsequent Fourier-transform processing. The side of the microscope cover and the parabolic mirror were located in air for these initial tests, so the far-IR water-vapor spectrum will be a limitation in performance. In the future, we will enclose and purge this part of the optical path.

The measured raw single-beam far-IR spectrum is shown in Figure 12. It was obtained using the synchrotron source in reflection off of a gold-coated microscope slide and the 15× objective, with 128 scans, 4-cm⁻¹ resolution, a scanning mirror velocity of 1.266 cm/s, and amplified 20 times with 100-Hz roll-on and 10-kHz roll-off filters. One-hundred-percent signal-to-noise lines show 1% rms noise from 220 to 675 cm⁻¹ and usable signal to about 200 cm⁻¹, with the water-vapor absorption locations degrading the signal-to-noise ratio at each dip around this low frequency. Purging the space between the microscope and the IR detector sig-



Photomicrograph of the gold strip on glass used to test the spatial resolution of the synchrotron beam as a function of wavelength. nificantly improved this low end, pushing the usable signal to below 150 cm⁻¹.

To test the spatial resolution of the focused synchrotron spot in the microscope and determine if we are indeed maintaining diffraction-limited performance into the far IR, a line scan with 5-micron steps across a test sample was performed. The test sample consisted of a



Plot of intensity vs. position for five representative wavelengths. The sharpness of the measured edge allows the determination of resolution. The measured resolution as a function of wavelength is shown in the inset.

SCIENTIFIC SUPPORT

FACILITY REPORT

SCIENTIFIC SUPPORT

114

140-micron-wide sharp edge of gold evaporated onto a glass slide (Figure 13).

The measured intensity was integrated over numerous ~50-cm⁻¹-wide regions wherever there was significant intensity in the spectra as a function of distance across the line map. Several representative intensity vs. position graphs are plotted in Figure 14. One can immediately recognize that the sharpness of this step in intensity changes as a function of wavelength, with short wavelengths showing a sharper rise than longer wavelengths, as expected. The solid lines in Figure 14 are fits to the data, and these fits allow us to determine a spatial resolution for each wavelength. The measured resolution is plotted as a function of wavelength in the inset. The slope of the dashed line-0.78-indicates that the spot size is 0.78 λ . The error bars are large at the longest wavelengths as these signals were quite low.

This new far-IR capability is important for matching astronomical observations, studying low-frequency metallo-organic modes, surface electrochemical products, impurities in semiconductors, etc. It is a collaborative project between the ALS (M.C. Martin, J. Singley) and LLNL (S. Bajt).

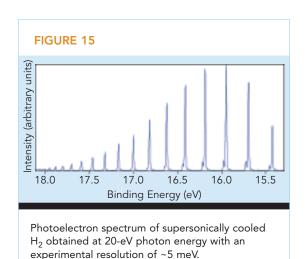
Recent Advances in AMO Science on Beamline 10.0.1

On the atomic, molecular, and optical (AMO) physics front, a few major changes occurred on Beamline 10.0.1, including the addition of a new beamline scientist, David Kilcoyne. Previously affiliated with H. Ade and the University of North Carolina, David was responsible for the design, construction, commissioning, and operation of the scanning transmission x-ray microscope (STXM) on Beamline 5.3.2. He brings extensive experience in designing and building complicated experimental endstations as well as considerable experience in atomic and molecular photoionization experiments.

On the fiscal front, our users have been successful in applying for grants to improve the beamline and update its suite of endstations. K. McLaughlin (Loras College) received an NSF grant to partially fund a new grating for the beamline and extend its utility to lower photon energies. While the spherical grating monochromator (SGM) covers energies from 18 to ~350 eV with three different gratings, the undulator can cover a much broader range, from ~11 to over 700 eV at 1.9 GeV. The AMO group is interested in both lower and higher energies, but the included angle of the monochromator, 165°, restricts its usefulness at higher energies because of low reflectivity. The addition of a grating to the monochromator requires the use of dual groove patterns on a single substrate because the design of the monochromator mechanism allows for only three gratings to be installed in the vacuum chamber. The new grating is expected to be installed and in use providing lower-energy photons to users in mid-2005. Also, N. Berrah (Western Michigan University) and J. Bozek (ALS) received a grant to expand the capabilities of the AMO endstations. Preliminary plans call for upgrading the Scienta electron spectrometer and building a new ion-photon endstation for crossed-beam experiments, as well as other projects. These upgrades will be implemented over the next two to three years.

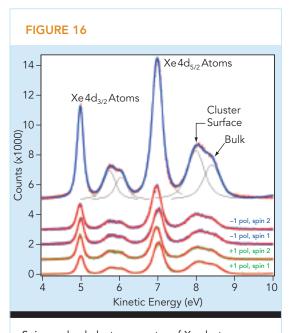
Notable developments in the scientific program include successful experiments involving supersonic jets. Very high resolution electronenergy measurements of gaseous targets can become dominated by Doppler broadening in light targets or at high electron kinetic energies. To overcome this limitation, gas jets in which all of the atoms are traveling in the same direction are typically employed. We have previously used a nonsupersonic jet with an electron spectrometer on Beamline 9.0.1 to measure "sub-Doppler" spectra of H₂ [G. Ohrwall et al., *J. Phys. B* **32**, 51 (1999)]. In that work, the molecules were not cooled, although the spectra were sufficiently

resolved to exhibit several rotational states accompanying the vibrational peaks. Recently, however, we have employed a precooled supersonic continuous gas jet to produce a beam of rotationally cooled H₂ and found that the spectra exhibit only two rotational levels (Figure 15). Rotational cooling will be essential for achieving higher-resolution photoelectron spectra for larger polyatomic systems. With the demonstration of cooling in H₂, we are confident of further successes with larger molecules in the near future.



The supersonic jet is also useful for producing van der Waals clusters of rare-gas atoms. We recently performed electron-spin measurements on Xe clusters using the circular polarization capabilities of Beamline 4.0.2. The measurements were made during two-bunch operation and utilized the electron time-of-flight spectrometer fit

with a Mott detector from N. Berrah's group. The spectra, shown in Figure 16, were obtained with both left and right circularly polarized light and fit with peaks representing the atoms and surface and bulk constituents of the clusters. The resulting electron-spin polarizations, obtained from the areas of the peaks in the four spin-resolved spectra shown in the figure, indicate that electrons from the bulk atoms are less polarized than those from atoms at the surface of the cluster or those from the free atoms also present in the beam. These preliminary results indicate a fruitful new direction for AMO science and will be followed up in the next year.



Spin-resolved electron spectra of Xe clusters obtained with circularly polarized light. The top curve is the sum of the four lower curves.

SCIENTIFIC SUPPORT

USER SERVICES

Gary Krebs, User Services Group Leader

::

Introduction

The User Services Group provides an interface to the ALS for new and continuing users. The group is made up of the User Services Administration, Beamline Coordination, Materiel Management, and Technical Information Sections. These groups work together to provide the users with a wide range of services. It is the goal of the ALS to continue to provide these varied services in a friendly and efficient manner.

::

User Services Administration

The User Services Office is located on the mezzanine floor of the ALS, just to the left of the reception area. The User Services Office is staffed by administrative personnel (Figure 1) who help new users through the registration process required before beginning work at the ALS. All users receive an electronic identification key card, which allows them access to Berkeley

FACILITY REPORT

USER SERVICES

116

FIGURE 1

The User Services Administration Section. Sharon Fujimura, Gary Krebs, Molly Stoufer, Jeff Troutman, David Malone. *Not pictured:* Adriana Reza, Barbara Phillips, Zalashya Lowry.



Lab and the ALS experiment floor. About 1700 users had access to the experiment floor in 2003. New users also watch a short safety video that describes some of the potential safety hazards at the facility and outlines the experiment safety checkout process. New users can complete much of the processing before they arrive by preregistering on the ALS Web site (www-als.lbl.gov). Through its oversight of the registration process, the User Services Administration Section also collects data about user publications and demographics. As a national user facility, the ALS is required to report these statistics annually to the U.S. Department of Energy.

In another of its many functions, the User Services Administration Section coordinates the allocation of beam time through a peer-review process. For all the sciences except protein crystallography, general user requests for beam time are received through the ALS Web site twice annually. Protein crystallography proposals, also submitted over the Web, are received and evaluated bimonthly to better serve the rapid-access needs of the crystallography community. Proposals for beam time are ranked by a Proposal Study Panel (PSP), and beam time is allocated based on principles and guidelines agreed upon by the ALS and the Users' Executive Committee (UEC). These principles and guidelines adhere to those of the International Union of Pure and Applied Physics. The UEC, elected annually by the users, is the voice of that diverse group and represents them at the ALS as an advisory body. PSP members are chosen in consultation with the UEC to cover the wide range of sciences represented at the ALS. The User Services Administration Section provides administrative and logistical support to both the PSPs and the UEC.

FIGURE 2



The ALS apartments are conveniently located near downtown Berkeley along the main shuttle bus route.

The proposal submission and beam time allocation process is described in greater detail on the ALS Web site (www-als.lbl.gov/als/quickguide/independinvest.html).

The User Services Office can also help out-of-towners find a place to stay while working at the ALS. The office manages the ALS apartments (Figure 2), which are located near Berkeley Lab on the main shuttle-bus route. The apartments are available to all ALS users, and detailed information about costs and other factors can be found on the Web (www-als.lbl.gov/als/quick-guide/housing.html).

The User Services Administration Section is managed by Jeff Troutman and includes Sharon Fujimura, Zalashya Lowry, Barbara Phillips, Molly Stoufer, and Adriana Reza. FACILITY REPORT

USER SERVICES

::

Beamline Coordination

The Beamline Coordination Section (Figure 3) serves as a point of contact for users on the experiment floor. Section members act as liaisons between users and ALS and Berkeley Lab resources. A crucial function of this group is to ensure that all user experiments are checked for safety. Section members work closely with various Berkeley Lab safety specialists in the areas of electrical, mechanical, chemical, radiation, seismic, and laser safety. This safety checkout process is required in order to assure the safety of all users on the experiment floor. Upon the successful completion of the required safety checks, section members enable the beamline to receive light. The Beamline Coordination Section is led by Donna Hamamoto and includes John Pruyn and David Malone.

FACILITY REPORT

USER SERVICES

118

FIGURE 3



The Beamline Coordination and Materiel Management Sections. Ken Winters, Todd Anderson, Tony Marquez, David Malone, Gary Giangrasso, John Pruyn, and Donna Hamamoto.

...

Materiel Management

The Materiel Management Section (Figure 3) provides shipping, receiving, temporary storage, and endstation setup services. The section maintains a stock room of parts and equipment commonly needed by ALS users and ALS technicians (Figure 4). These supplies are accessible by key card 24 hours a day. The section is managed by Gary Giangrasso and includes Todd Anderson, Tony Marquez, and Kenneth Winters.

FIGURE 4



Commonly needed parts and equipment are available in a user stock room available 24 hours a day by key card.

::

Technical Information

The Technical Information Section (Figure 5) provides information about the science carried out at the ALS to the scientific and technical community, government officials, and the general public. The members of this section are responsible for this Activity Report as well as the science highlights on display in the ALS lobby and on the ALS Web site. The section maintains and develops the ALS Web site and produces the electronic newsletter, ALSNews. The group's members also prepare special brochures and create posters and announcements for countless workshops and conferences. The group maintains strong ties to the educational community within the state of California, around the U.S., and abroad. The Technical Information Section is led by Art Robinson and includes Annette Greiner, Elizabeth Moxon, Lori Tamura, and Greg Vierra.

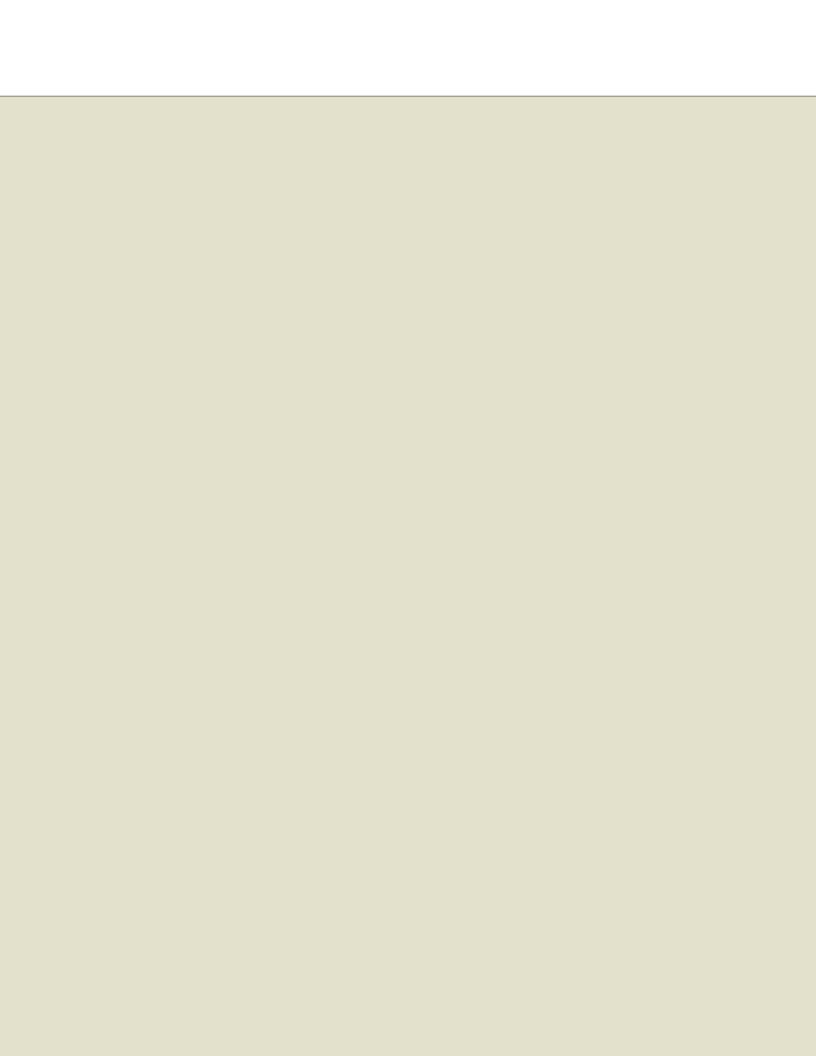
FIGURE 5

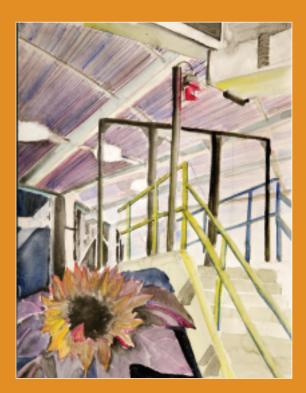


The Technical Information Section. Annette Greiner, Art Robinson, Lori Tamura, Greg Vierra, and Elizabeth Moxon.

FACILITY REPORT

USER SERVICES





SPECIAL EVENTS



Eighth International Conference on Synchrotron Radiation Instrumentation (SRI03)

San Francisco, August 25–29

SPECIAL EVENTS

122

An exciting and comprehensive program of plenary talks, parallel sessions, and posters attracted more than 750 attendees to the beautiful Yerba Buena Center for the Arts in downtown San Francisco for SRI03. For four days, meeting participants were treated to an outstanding array of speakers and topics covering every-

ON SYNCHROTRON RADIATION INSTRUMENTATION

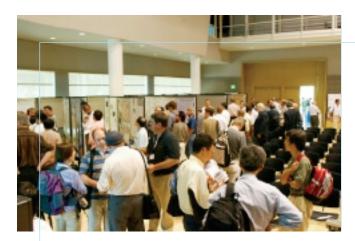
During the opening session, SRI03 cochairs Howard Padmore (ALS) and Jo Stöhr (Stanford University) welcomed an overflow crowd to the conference. thing from new developments in synchrotron radiation sources to advanced techniques in spectroscopy, beamline instrumentation, and the development of novel radiation sources. All conference talks are posted on the Web at www.sri2003.lbl.gov/html/presentations.html.

Also included in this year's meeting was a Public Science Day designed to introduce the general public to synchrotron-related science. The day was capped with a public lecture by Berkeley Lab's award-winning astrophysicist Saul Perlmutter, who spoke to an audience of over 400 on "Supernovae, Dark Energy, and the Accelerating Universe." The meeting concluded with tours of the facilities that co-sponsored the event, the ALS and the Stanford Synchrotron Radiation Laboratory.





SPECIAL EVENTS







Parallel sessions, vendor exhibits, and posters sessions drew enthusiastic crowds daily.

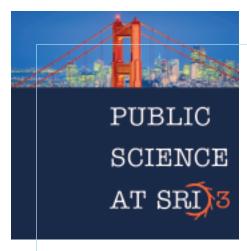


Lunch breaks were an opportune time to stroll in Yerba Buena Gardens or relax and chat with colleagues.

SPECIAL EVENTS

On the final day of the conference, attendees were bused to the ALS for a half-day tour of the facility.





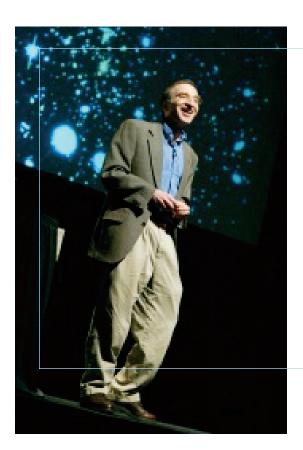




Visitors to the public science exhibits viewed ALS-themed artwork by UC Berkeley students and tried their hand at the linear accelerator model.

SPECIAL EVENTS

125



Saul Perlmutter entertained a capacity audience of SRI03 attendees and the general public during his talk about supernovae and the accelerating universe.

ALS Users' Meeting

Berkeley Lab, October 6-8

This year's meeting drew a capacity crowd of users, staff, and vendors interested in hearing about recent research conducted at the ALS over the last year. In addition to the usual meeting program of facility updates, scientific highlights, vendor exhibits, poster sessions, and the awards banquet, meeting attendees were treated to a special session of talks and displays celebrating the 10-year anniversary of ALS operations. Two of the key players in the early history of the ALS, David Attwood and Jay Marx, provided intriguing glimpses into the trials and tribulations of funding and building the facility. Their talks were followed by a reception on the patio, where current and former ALS staffers had the chance to view a display of photographs chronicling the construction and commissioning of the ALS.

ADVANCED LIGHT SOURCE
USERS' MEETING

October 6-1, 2011

MORKENDERS

Industrial States Deliver to Constitute to Control Springs

Industrial States to Control Springs

Applications of Periodic Affairmance to Control Springs

Industrial Affairmance to Control Springs

Applications of Periodic Affairmance to Control Springs

Industrial Affairmance

Applications of Periodic Affairmance to Control Springs

Industrial Affairmance

Applications of Periodic Affairmance

Applications of Perio

SPECIAL EVENTS

126



ALS Division Director Daniel Chemla answers users' questions after giving his talk on the state of the ALS.









Scientific highlight speakers included Sheryl Tsai (UC Irvine), Norman Mannella (UC Davis), Byron Freelon, Carolyn Larabell, and Karine Chesnel (all from Berkeley Lab).



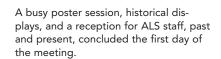


During the special retrospective session, Berkeley Lab's David Attwood gave an entertaining talk about securing funding for the construction of the ALS entitled, "The Impossible Dream."



SPECIAL EVENTS







Ruth Halbach presented the Klaus Halbach Award for Innovative Instrumentation at the ALS to Mark Le Gros (Physical Biosciences Division) for developing an automated tomography station for x-ray microscopy of biological materials. Mrs. Halbach also presided over the dedication of the main ALS conference room to the memory of her late husband, whose invention of permanent-magnet insertion devices revolutionized third-generation synchrotron light sources.

Following the dinner buffet on the patio, award recipients posed for a photo. From left: Tonio Buonassisi (UC Berkeley), winner of the student poster competition for a study of copper contaminants in polycrystalline silicon solar cell material; presenter Ruth Halbach; Mark Le Gros (noted above); Donna Hamamoto (ALS Beamline Coordination), recipient of the Tim Renner User Services Award; and Xing-Jiang Zhou (Stanford University and Berkeley Lab), who took home the David A. Shirley Award for Outstanding Science for his angle-resolved photoemission studies of high-temperature superconductors.





SPECIAL EVENTS

WIRMS 2003

Lake Tahoe, July 8–11

On the sunny shores of Lake Tahoe, more than 75 representatives from the infrared scientific programs at 13 light sources and 10 free-electron laser facilities convened for a series of talks and poster presentations covering recent advances in infrared science. The International Workshop on

Infrared Microscopy and Spectroscopy with Accelerator-Based Sources (WIRMS 2003), sponsored by the ALS and Stanford University, included sessions about biomedical spectroscopy, terahertz microscopy, environmental and planetary sciences, and strongly correlated materials.

SPECIAL EVENTS

130



WIRMS participants take a break by the lake between sessions.

High-Pressure Structure and Reactivity Workshop

Berkeley Lab, December 4-7

Nearly 100 people attended this ALS workshop that focused on the use of crystallographic techniques to study of chemical reactions and phase transitions induced by the application of high pressure. Sponsored by the International Union of Crystallography (IUCr) and the Consortium for Materials Properties Research in

Earth Sciences (COMPRES), the workshop provided an active forum for participants to discuss the current state of the field and future courses of research. The workshop was preceded by a one-day practicum that attracted more than 60 participants interested in hands-on instruction in high-pressure synchrotron techniques.

Practicum participants got a close look at the infrared microscope with ALS beamline scientist Mike Martin.



SPECIAL EVENTS

Congressional Tour

In April, members of the House Energy and Water Development Appropriations
Subcommittee—a key congressional panel for science funding—visited the ALS as part of a larger visit to Bay Area national laboratories and water projects. The committee chair, Rep. David Hobson, along with Rep. Marion Berry and Rep. Michael Simpson, met with senior Berkeley Lab management and heard about Lab programs such as advanced scientific computing (NERSC), the supernova satellite project (SNAP), and the Molecular Foundry. At the ALS, Director Daniel Chemla gave a brief introduction to the ALS, a few vital statistics,



Congressman David Hobson (right), discusses recent advances in protein crystallography with Sue Bailey (left) of the Physical Biosciences Division.

and a survey of future developments. The congressional delegation was then escorted to the experiment floor, where they visited several beamlines.

SPECIAL EVENTS

132



Michael Rubiano (right), representing Congresswoman Barbara Lee of California's Ninth District, presents Neville Smith with a framed copy of the October 20, 2003, edition of the U.S. Congressional Record. In honor of the ALS's tenth anniversary, Rep. Lee cited the ALS as "one of our Nation's premier scientific research centers."

ALS Tenth Anniversary

To honor the tenth anniversary of the ALS, Berkeley Lab sponsored a special program of talks that included a retrospective of the construction of the synchrotron by former ALS Project Manager Jay Marx, and a look into the future direction of scientific research at the facility by ALS Deputy Division Director Neville Smith. The talks were followed by tours of the ALS for lab employees and a cake-cutting ceremony in the ALS lobby.

Beamline 12.0.2 Dedication

On April 22, ALS Director Daniel Chemla and Berkeley Lab Director Charles Shank cut the ribbon on the new coherent soft x-ray Beamline 12.0.2. A joint project of the ALS, the Center for X-Ray Optics (CXRO), and the University of Oregon, the beamline will produce microwatts of tunable coherent soft x rays to do a wide range of experiments in both scattering and optics.



Joining in the dedication are (from left) Steve Kevan from the University of Oregon, CXRO Head Erik Anderson, and ALS Scientific Support Group Leader Zahid Hussain. Watching the proceedings behind Anderson is CXRO's Dave Attwood. Also on hand were (left to right in back) Ron Oort, Patrick Naulleau, Kevin Bradley, Bryan Hoef, Paul Denham, Rene Delano, Gideon Jones, Ken Goldberg, Hanjing Huang, and Drew Kemp.

SPECIAL EVENTS

133

purchase and based about 2 is a series of the series of th

LLNL representative Lou Terminello (at left, holding check) presents a symbolic check for \$150,000 to ALS Deputy for Science Neville Smith (right) as CALIPSO program manager Simon Clark (in yellow tie) looks on.

CALIPSO Grows

The California High-Pressure Science Observatory (CALIPSO) program welcomed new member Lawrence Livermore National Laboratory in August. CALIPSO, a consortium of seven institutions, is currently focused on developing a new beamline at the ALS designed for studying materials held in diamond-anvil cells and heated with lasers.

Art Students at the ALS

ALS staff and users were treated to a unique event in May when students from UC Berkeley displayed their artistic impressions of the ALS on the outdoor patio. The students, from the art, architecture, and engineering departments on campus, had recently spent two evenings at the ALS painting and drawing at various locations around the experiment floor. The result of their

efforts was a colorful array of images of everything from wiring and monochromators to the historic ALS dome. For ALS staff, it was a rare opportunity to see their environment through the fresh eyes of artists, and for the students, it was an intriguing glimpse into the big research facility up on the hill. The artwork of several of the students is featured on the divider pages of this report.

SPECIAL EVENTS



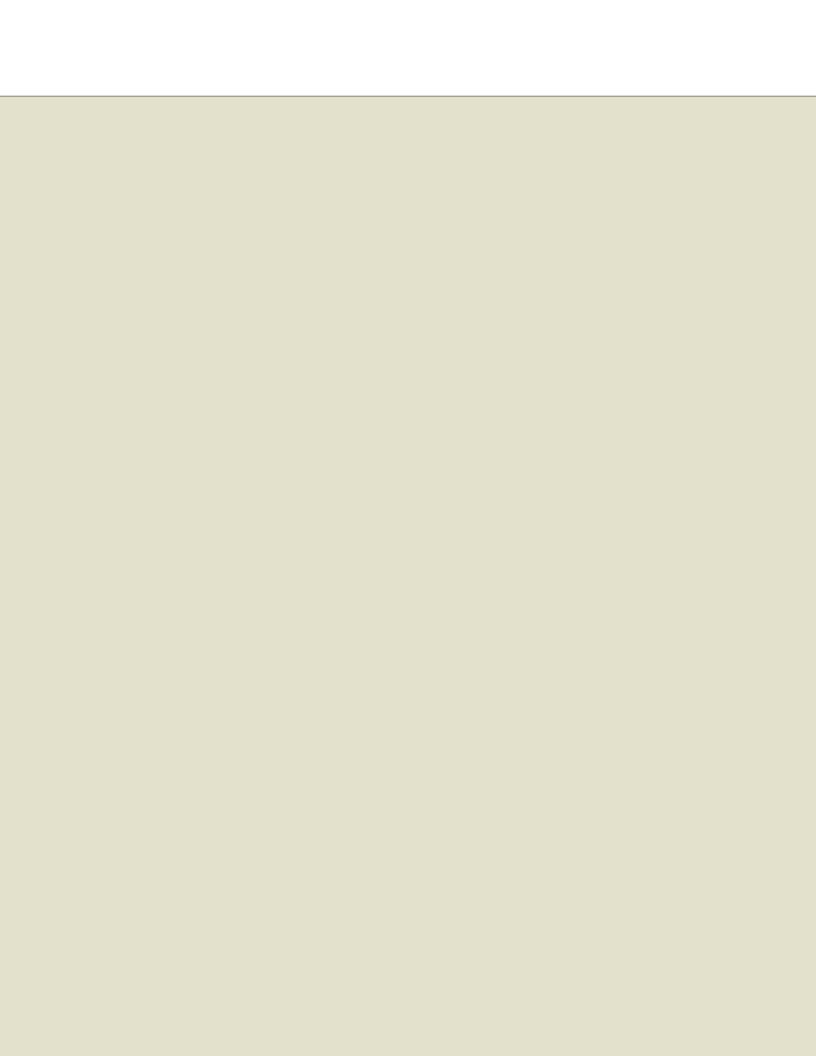
ALS in the Movies

The ALS suffered a little movie fever this year when it played a supporting role in this year's blockbuster movie "Hulk." Actors and technicians spent a week filming a series of scenes using the ALS and the surrounding area.



Director Ang Lee (second from right) and his staff review footage during a film shoot under the ALS dome.

SPECIAL EVENTS





ABOUT THE ALS

ALS ADVISORY PANELS

Scientific Advisory Committee

Samuel Bader, Argonne National Laboratory Ernst G. Bauer, Arizona State University James Berger, University of California, Berkeley John Carruthers, Intel Corporation Jennifer Doudna (ex-officio), Berkeley Lab Wolfgang Eberhardt, BESSY GmbH, Germany Roger Falcone, University of California, Berkeley Yves Idzerda, Montana State University Stephen D. Kevan (chair), University of Oregon Anders Nilsson, SSRL/Stockholm University, Sweden Sunil Sinha, University of California, San Diego Janet L. Smith, Purdue University

Donald L. Sparks, University of Delaware

John Spence, Berkeley Lab

Anthony Starace, University of Nebraska-Lincoln

J. Friso van der Veen, Paul Scherrer Institut

Science Policy Board

Massimo Altarelli, Elettra Sincrotrone Trieste, Italy

Paul Fleury, University of New Mexico

Franz J. Himpsel, University of Wisconsin, Madison

Stephen E. Kevan (ex-officio), University of Oregon

Walter Kohn, University of California, Santa Barbara

Yuan T. Lee, Academia Sinica, Taiwan

Albert Narath (retired), Lockheed Martin Corporation

Yves Petroff, European Synchrotron Radiation **Facility**

Alan Schriesheim, Argonne National Laboratory Robert Tjian, University of California, Berkeley Eberhard Umbach, University of Würzburg, Germany

ABOUT THE ALS

ALS ADVISORY PANELS

Users' Executive Committee

Jennifer Doudna (chair), University of California, Berkeley

John Bozek, Advanced Light Source, Berkeley Lab

Sophie Canton (student), University of Western Michigan

Gregory Denbeaux, Advanced Light Source, Berkeley Lab

Dan Dessau, University of Colorado

Keith Jackson, Center for X-Ray Optics, Berkeley Lab

Dennis W. Lindle (vice chair), University of Nevada, Las Vegas

Gerry McDermott, Physical Biosciences Division, Berkeley Lab

Gary E. Mitchell, Dow Chemical Company

Alexander Moewes, University of Saskatchewan

Yasuji Muramatsu, Japan Atomic Energy Research Institute

Eli Rotenberg, Advanced Light Source, Berkeley Lab



Members of the Users' Executive Committee pose with visiting members of DOE BES during the 2003 ALS Users' Meeting. From left: Dennis Lindle, Eli Rotenberg, Dan Dessau, John Bozek, Jennifer Doudna, Alexander Moewes, Pedro Montano (BES Division of Scientific User Facilities), Bill Oosterhuis (BES Division of Materials Sciences and Engineering), Gary E. Mitchell, Greg Denbeaux, Gerry McDermott, and BES Associate Director Pat Dehmer.

ABOUT THE ALS

ALS ADVISORY PANELS

ALS STAFF

This is a cumulative list of all those who worked at the ALS during the 2003 calendar year. The list includes visitors, students, as well as staff members from other divisions who were matrixed to the ALS.

Division Management

D. Chemla

B. Feinberg

J. Krupnick

Y. Petroff

N. Smith

Accelerator Physics

D. Robin, Group Leader

J. Byrd, Deputy Leader

S. Lidia

A. Loftsdottir*

H. Nishimura

H. Sannibale

T. Scarvie

C. Steier

W. Wan

Administration

B. Dixon

C. Cooper

A. Reza

E. Saucier

L. Senft

Budget

J. Dahlgard

J. Coyne

Controls

A. Biocca, Group Leader

C. Timossi, Deputy Leader

E. Domning

C. Ikami

S. Jacobson

J. McDonald

A. Robb

J. Spring

R. Steele

M. Urashka

E. Williams

Electrical Engineering

W. Barry, Group Leader

G. Stover, Deputy Leader

B. Bailey

M. Balagot

K. Baptiste

M. Bell

R. Benjegerdes

K. Bolin

R. Candelario

M. Chin

R. Cole

R. Colston

S. Cooper

P. Cull

A. Detzner

L. Dominguez

J. Elkins

M. Estrema

D. Edwards

M. Fahmie

M. Foster

R. Gassaway

R. Gervasoni

A. Geyer

J. Gregor

J. Hellmers

M. Hilburn

L. Holzer

L. Jordan

I. Iulian

T. Kuneli

S. Kwiatkowski

E. Lee

A. Lindner

W. Mattson

P. Molinari

R. Mueller

T. Nhan

J. Nomura

F. Ottens

S. Patterson

A. Ritchie

S. Rogoff

P. Rosado

H. Scheid

A. Sippio R. Slater

G. Stover

M. Szajbler

M. Thomas

R. Valasco M. Vinco

I. Weber

M. Williams

K. Woolfe

Environment, Health, and Safety

R. Baker

B. Fairchild

T. Kuneli

R. Mueller

G. Perdue

Experimental Systems

H. Padmore, Group Leader

A. Warwick, Deputy Leader

W. Caldwell

R. Celestre

S.-B. Choe

S. Clark

A. Doran

ABOUT THE ALS

ALS STAFF

J. Feng A. Franck E. Glover J. Hao E. Harvey H. He P. Heimann M. Howells S. Irick A. MacDowell M. Marcus W. McKinney J. Nasiatka P. Schmid A. Scholl R. Sublett N. Tamura A. Thompson A. Young

S. Fakra

Mechanical Engineering

A. Paterson, Group Leader R. Schlueter, Deputy Leader N. Andresen R. Armstrong D. Baum R. Beggs J. Bercovitz L. Bonifas D. Calais D. Cambie K. Carter M. Coleman D. Colomb J. Comins C. Corradi C. Cummings

M. Decool

A. Demello

S. Dimaggio

R. Duarte

K. Franck

A. Gavidia

D. Fritz

D. Ellis

D. Gibson C. Hopkins D. Hull D. Jones J.-Y. Jung N. Kelez K. Kennedy S. Klingler M. Knolls C. Knopf M. Kritscher K. Krueger A. Lim R. Low S. Lundgren D. MacGill S. Marks P. McKean H. Meyer T. Miller V. Moroz G. Morrison D. Munson W. Ogelsby I. Osborne E. Palmerston R. Patton J. Pepper K. Peterman P. Pipersky D. Plate S. Prestemon K. Sihler T. Stevens H. Stewart M. Thomas W. Thur R. Weidenbach M. Wingert E. Wong

F. Zucca Operations

B. Samuelson, Group Leader T. Byrne, Deputy Leader M. Beaudrow D. Bentsen J. Bishop
D. Brothers
E. Diaz
O. Jones
K. Osborne
J. Pusina
D. Richardson
S. Stricklin
M. Wolfe

Procedure Center

R. Jones

Project Management

A. Catalano J. Harkins S. Rossi

Quality Assurance

E. Lampo

B. Rude

F. Schlachter

M. Van Hove

Scientific Support

ABOUT THE ALS

ALS STAFF

141

Z. Hussain, Group Leader J. Bozek, Deputy Leader G. Ackerman E. Arenholz W. Bates K. Chesnel Y.-D. Chuang J. Denlinger A. Federov B. Freelon J. Guo A. Guy C. Hauck D. Kilcoyne R. Kimmerling G. Lebedev M. Martin S. Mun E. Rotenberg

User Services

G. Krebs, Group Leader

A. Robinson, Deputy Leader

T. Anderson

J. Coyne

S. Fujimura

G. Giangrasso

A. Greiner

D. Hamamoto

A. Lobodovsky

Z. Lowry

D. Malone

A. Marquez

J. McClain

E. Moxon

J. Murray

B. Phillips

J. Pruyn

M. Stoufer

J. Troutman

L. Tamura

G. Vierra

K. Winters

ABOUT THE ALS

ALS STAFF

142

Visitors and **Students**

A. Aguilar* A. Augustsson*

B. Batterman

R. Bilodeau

P. Bogdanov* V. Brouet

S. Canton

H. Chong*

S. Chourou

J. Diaz

C. Dong

D. Edwards*

J. Glossinger*

J. Graf

G.-H. Gweon

Z. Hasan*

N. Khan

J. Kirz

A. Lanzara

S. Locklin*

D. Lowney*

A. MacPhee

A. Manceau K. Opachich

M. Paik*

J. Patel

M. Salim

E.J. Singley

C. Slim*

J. Spence

W. Stolte

G. Turri

D. Weinstein

K. Wilson*

C. Won*

W. Yang

H.-S. Youn

X. Zhou

ALS Doctoral Fellows

Y. Chen*

M. Gharaibeh*

D. Peterka*

D. Rolles*

Z. Sun*

J. Turner* M. Veiseh*

F. Wang*

*Graduate Student Research Assistant

FACTS AND FIGURES

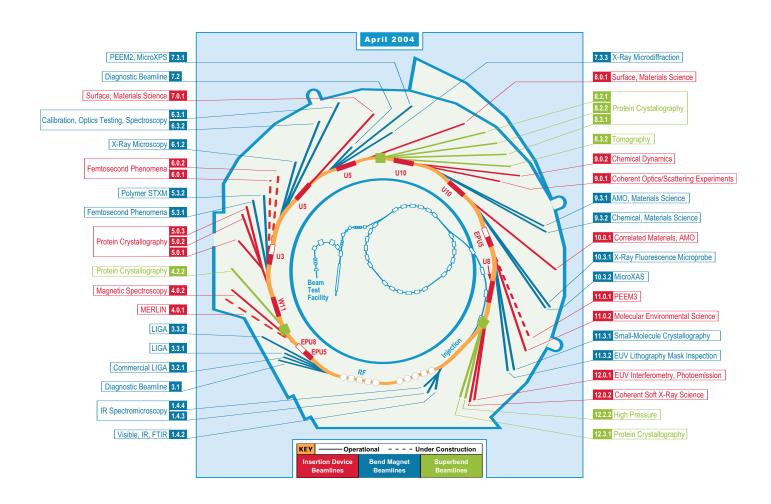
Using the Advanced Light Source

The ALS, a Department of Energy national user facility, welcomes researchers from universities, industry, and government laboratories. Qualified users have access as members of either participating research teams (PRTs), approved programs (APs), or as general users. PRTs and APs (groups of researchers with related interests from one or more institutions) construct and operate beamlines and have primary responsibility for experiment endstation equipment. They are entitled to a certain percentage of their

beamline's operating time commensurate with the resources that they have contributed to the beamline. Through a peer-reviewed proposal process, the remaining beam time is granted to general users, who may provide their own endstation or negotiate access to a PRT- or APowned endstation.

The ALS does not charge users for beam access if their research is nonproprietary. Users performing proprietary research are charged a fee based on full cost recovery. All users are responsible for the day-to-day costs of research (e.g., supplies, phone calls, technical support).

The nominal operating energy of the ALS



storage ring is 1.9 GeV, although it can run from 1.0 to 1.9 GeV, allowing flexibility for user operations. At 1.9 GeV, the normal maximum operating current is 400 mA in multibunch operation. The spectral range of undulator and wiggler beamlines extends from photon energies of roughly 5 eV to 21 keV; on superbend beamlines the range is between 2.4 and 60 keV. Bend

magnets produce radiation from the infrared to about 20 keV.

The ALS is capable of accommodating approximately 50 beamlines and more than 100 endstations. The first user beamlines began operation in October 1993, and there were 36 operating beamlines, with several more under construction, by the end of 2003.

ALS Beamlines*

Beamline	Source	Areas of Research/Techniques	Monochromator	Energy Range	Operational
1.4.2	Bend	Visible and infrared FTIR	Interferometer	0.002-3 eV (15-25,000 cm ⁻¹)	Now
1.4.3	Bend	Infrared spectromicroscopy	Interferometer	0.01-1 eV (100-10,000 cm ⁻¹)	Now
1.4.4	Bend	Infrared spectromicroscopy	Interferometer	0.05-1 eV (550-10,000 cm ⁻¹)	Now
3.1	Bend	Diagnostic beamline	Mirror/filter	1–2 keV	Now
3.2.1	Bend	Commercial LIGA	None	3–12 keV	Now
3.3.1	Bend	LIGA	None	1–20 keV	Now
3.3.2	Bend	LIGA	None	1–20 keV	Now
4.0.1	EPU8	Magnetic and Polymer Nanostructures (MERLIN)	SGM	15–150 eV	2005
4.0.2	EPU5	Magnetic spectroscopy			
		XMCD chamber	Variable-included-angle PGM	52–1900 eV	Now
		X-ray absorption chamber	Variable-included-angle PGM	52–1900 eV	Now
		Advanced photoelectron spectrometer/diffractometer	Variable-included-angle PGM	52–1900 eV	Now
		Gas-phase absorption cell	Variable-included-angle PGM	52–1900 eV	Now
		L-edge chamber with superconducting spectrometer	Variable-included-angle PGM	52–1900 eV	Now
		XMCD chamber (6 T, 2 K)	Variable-included-angle PGM	52–1900 eV	Now
		Photoemission electron microscope	Variable-included-angle PGM	52–1900 eV	Now
4.2.2	SB	MAD and monochromatic PX	Double crystal	6–18 keV	Now
5.0.1	W11	Monochromatic PX	Curved crystal	12.4 keV	Now
5.0.2	W11	MAD and monochromatic PX	Double crystal	3.5–14 keV	Now
5.0.3	W11	Monochromatic PX	Curved crystal	12.4 keV	Now
5.3.1	Bend	Femtosecond phenomena	Double crystal	1.8–12 keV	Now
5.3.2	Bend	Polymer scanning transmission x-ray microscopy	SGM	250-700 eV	Now
6.0.1	U3	Femtosecond phenomena	Double crystal	2.2-10 keV	2006
6.0.2	U3	Femtosecond phenomena	VLS-PGM	130–1800 eV	2005
6.1.2	Bend	High-resolution zone-plate microscopy	Zone-plate linear	300-1000 eV	Now
6.3.1	Bend	Calibration and standards, EUV/soft x-ray optics testing, solid-state chemistry	VLS-PGM	300–2000 eV	Now

^{*} The information in this table is valid as of May 2004. The most current information about ALS beamlines is available on the Web at www-als.lbl.gov/als/als_users_bl/bl_table.html.

continued

ABOUT THE ALS

FACTS AND FIGURES

Beamline	Source	Areas of Research/Techniques	Monochromator	Energy Range	Operational
6.3.2	Bend	Calibration and standards; EUV optics testing; atomic, molecular, and materials science	VLS-PGM	50–1300 eV	Now
7.0.1	U5	Surface and materials science, spectr	omicroscopy		
		Scanning photoemission microscope (SPEM)	SGM	100-800 eV	Now
		Electronic Structure Factory (ESF)	SGM	60–1200 eV	Now
		Soft x-ray fluorescence spectrometer (SXF)	SGM	80–1200 eV	Now
7.2	Bend	Diagnostic beamline	Filter/none	Far IR–17 keV	Now
7.3.1.1	Bend	Magnetic microscopy, spectromicroscopy	SGM	175–1500 eV	Now
7.3.1.2	Bend	Surface and materials science, micro x-ray photoelectron spectroscop	SGM py	175–1500 eV	Now
7.3.3	Bend	X-ray microdiffraction	White light, two or four crystal	6–12 keV	Now
8.0.1	U5	Surface and materials science, imagir	ng photoelectron spectroscopy, s	oft x-ray fluorescence	
		Ellipsoidal-mirror electron- energy analyzer (EMA)	SGM	65–1400 eV	Now
		Soft x-ray fluorescence spectrometer (SXF)	SGM	65–1400 eV	Now
8.2.1	SB	MAD and monochromatic PX	Double crystal	5–17 keV	Now
8.2.2	SB	MAD and monochromatic PX	Double crystal	5–17 keV	Now
8.3.1	SB	MAD and monochromatic PX	Double crystal	2.4–18 keV	Now
8.3.2	SB	Tomography	Double crystal	3–60 keV	Now
9.0.1	U10	Coherent optics/scattering experiments	None or off-axis zone plate	10-800 eV	Now
9.0.2	U10	Chemical reaction dynamics, photoch photoelectron and photoionization in		ectron and photoionization	spectroscopy,
		Crossed molecular beam	White light, off-plane Eagle	5–30 eV	Now
		Molecular-beam photoelectron/ photoion spectroscopy	White light, off-plane Eagle	5–30 eV	Now
		Molecular-beam photoelectron/ photoion imaging and spectroscopy	White light, off-plane Eagle	5–30 eV	Now
		Flame chamber	White light, off-plane Eagle	5–30 eV	Now
		Ablation chamber	White light, off-plane Eagle	5–30 eV	Now
		Aerosol machine	White light, off-plane Eagle	5–30 eV	Now
9.3.1	Bend	Atomic, molecular, and materials scie	nce		
		Angle-resolved time-of-flight electron spectrometer	Double crystal	2.2–5.5 keV	Now
		lon time-of-flight spectrometer	Double crystal	2.2–5.5 keV	Now
		Magnetic mass analyzer	Double crystal	2.2-5.5 keV	Now
		Polarized-x-ray emission spectrometer	Double crystal	2.2–5.5 keV	Now
		X-ray absorption cell	Double crystal	2.2–5.5 keV	Now
		XAFS station	Double crystal	2.2–5.5 keV	Now
9.3.2	Bend	Chemical and materials science, circu	llar dichroism, spin resolution		
		Advanced materials chamber (AMC)	SGM	30-1400 eV	Now
		Ambient pressure photoemission	SGM	30-1400 eV	Now

ABOUT THE ALS

FACTS AND FIGURES

145

continued

Beamline Source Areas of Research/Techniques Monochromator **Energy Range** Operational 10.0.1 U10 Photoemission of highly correlated materials; high-resolution atomic, molecular, and optical physics High energy resolution SGM 17-340 eV Now spectrometer (HERS) Electron spin polarization (ESP) SGM 17-340 eV Now High-resolution atomic and molecular SGM 17-340 eV Now electron spectrometer (HiRAMES) Ion-photon beamline (IPB) 17-340 eV Now 10.3.1 Bend X-ray fluorescence microprobe White light, multilayer mirrors 3-20 keV Now 10.3.2 Bend Environmental and materials science, White light, two crystal 2.5-17 keV Now micro x-ray absorption spectroscopy 11.0.1 EPU5 VLS-PGM 100-2000 eV 2004 Magnetic microscopy, spectromicroscopy (PEEM3) 11.0.2 EPU5 Molecular environmental science Variable-included-angle PGM 95-2000 eV Wet spectroscopy Now High-pressure photoemission Now Variable-included-angle PGM 95-2000 eV spectroscopy Scanning transmission x-ray Variable-included-angle PGM 130-2000 eV Now microscope (STXM) 11.3.1 Bend Small-molecule crystallography Channel-cut Si(111) 6-17 keV Now 12.0.1 U8 EUV optics testing and interferometry, angle- and spin-resolved photoemission EUV interferometer (2 available) VLS-PGM 60-320 eV Now Angle- and spin-resolved VLS-PGM 20-320 eV Now photoemission 12.0.2 U8 Coherent soft x-ray science Coherent optics VLS-PGM 200-1000 eV Now Coherent scattering VLS-PGM 200-1000 eV Now 12.2.2 SB California High-Pressure Science Observatory (CALIPSO) Nanoscience/materials chemistry Double crystal 6-40 keV Now Solid state physics/geoscience Double crystal 6-40 keV Now 5.5-17 keV SB Double crystal and double 12.3.1 Structurally Integrated Biology Now for Life Sciences (SIBYLS) multilayer BTF Beam Test Facility 50-MeV electrons Now Linac None

ABOUT THE ALS

FACTS AND FIGURES

146

 $Bend = bend \ magnet$

EPUx = x-cm-period elliptically polarizing undulator

EUV = extreme ultraviolet

FTIR = Fourier transform infrared

LIGA = deep-etch x-ray lithography

MAD = multiple-wavelength anomalous diffraction

PX = protein crystallography

SB = superconducting bend magnet

Ux = x-cm-period undulator

Wx = x-cm-period wiggler

XAFS = x-ray absorption fine structure

XMCD = x-ray magnetic circular dichroism

ALS Insertion Device Parameters

Device	Beamline	Status	Energy Range at 1.5 GeV (eV)	Energy Range at 1.9 GeV (eV)	Period (cm)	No. of Periods	Operating Gap Range (cm)	Peak Effective Field Range
U5	8.0	Operational	50–1900	80–3000	5.0	89	1.4–4.5	0.85–0.10
U5	7.0	Operational	50-1900	80-3000	5.0	89	1.4-4.5	0.85-0.10
U8	12.0	Operational	18–1200	20–1900	8.0	55	2.5-8.3	0.80-0.07
U10	9.0	Operational	5–950	8-1500	10.0	43	2.4–11.6	0.98-0.05
U10	10.0	Operational	8–950	12–1500	10.0	43	2.4–11.6	0.80-0.05
EPU5	4.0	Operational	60–1000*	100–3000*	5.0	37	1.45–5.5	0.79–0.10 (vertical) 0.54–0.10 (horizontal)
EPU5	11.0	Operational	60–1000*	100–3000*	5.0	37	1.45–5.5	0.79–0.10 (vertical) 0.54–0.10 (horizontal)
W16	5.0	Operational	5000-13000	5000–21000	16.0	19	1.4–18.0	2.1–0.03

^{*} Elliptical polarization mode

ALS Storage Ring Parameters

Parameter	Value
Beam particle	Electron
Beam energy	1.0–1.9 GeV
Injection energy	1.0-1.5 GeV
Beam current multibunch mode two-bunch mode	400 mA 2 × 30 mA
Filling pattern (multibunch mode)	276 to 320 bunches possibility of 10-mA "camshaft" bunch in filling gap
Bunch spacing multibunch mode two-bunch mode	2 ns 328 ns
Circumference	196.8 m
Number of straight sections	12
Current number of insertion devices	8
Radio frequency	499.642 MHz
Beam size in straight sections, rms (1.9-GeV multibunch mode)	310 (h) × 23 (v) microns

Parameter V	alue at 1.5 GeV	Value at 1.9 GeV
Beam lifetime multibunch mode two-bunch mode	~3.5 h at 400 mA not used	~8.0 h at 400 mA ~50 min. at 40 mA
Horizontal emittance	4.2 nm-rad	6.75 nm-rad
Vertical emittance*	0.2 nm-rad	0.15 nm-rad
Energy spread (ΔE/E, rms	8×10^{-4}	1×10^{-3}

^{*}Vertical emittance is deliberately increased to improve beam lifetime

ABOUT THE ALS

FACTS AND FIGURES

2003 PUBLICATIONS

Ade, H., A.L. Kilcoyne, T. Tyliszczak, P. Hitchcock, E. Anderson, B. Harteneck, E.G. Rightor, G.E. Mitchell, A.P. Hitchcock, and T. Warwick, "Scan-ning transmission x-ray microscopy at a bending magnet beamline at the Advanced Light Source," *Journal de Physique IV* **104**, 3 (2003); Proceedings of the 7th International Conference on X-Ray Micro-scopy, Grenoble, France, July 28–August 2, 2002.

Aguilar, A., A.M. Covington, G. Hinojosa, R.A. Phaneuf, I. Alvarez, C. Cisneros, J.D. Bozek, I. Dominquez, M.M. Sant'Anna, and A.S. Schlachter, "Absolute photoionization cross section measurements of O II ions from 29.7 to 46.2 eV," *Astrophysical Journal Supplement Series* 146, 467 (2003).

Aguilar, A., J.B. West, R.A. Phaneuf, R.L. Brooks, F. Folkmann, H. Kjeldsen, J.D. Bozek, A.S. Schlachter, and C. Cisneros, "Photoionization of isoelectronic ions: Mg⁺ and Al²⁺," *Phys. Rev. A* **67**, 012701 (2003).

Aguilar-Mendoza, A., "Photoionization of positive ions: The nitrogen isoelectronic sequence," Ph.D. thesis, University of Nevada, Reno (2003).

An, J.M., D. Raczkowski, Y.Z. Wu, C.Y. Won, L.W. Wang, A. Canning, M.A. Van Hove, E. Rotenberg, and Z.Q. Qiu, "Quantization condition of quantum-well states in Cu/Co(001)," *Phys. Rev. B* **68**, 045419 (2003).

Anders, S., M.F. Toney, T. Thomson, J.-U. Thiele, B.D. Terris, S. Sun, and C.B. Murray, "X-ray studies of magnetic nanoparticle assemblies," *J. Appl. Phys.* **93**, 7343 (2003).

Anders, S., M.F. Toney, T. Thomson, R.F.C. Farrow, J.-U. Thiele, B.D. Terris, S. Sun, and C.B. Murray, "X-ray absorption and diffraction studies of thin polymer/FePt nanoparticle assemblies," *J. Appl. Phys.* **93**, 6299 (2003).

Armitage, N.P., D.H. Lu, C. Kim, A. Damascelli, K.M. Shen, F. Ronnig, D.L. Feng, P. Bogdanov, X.J. Zhou, W.L. Yang, Z. Hussain, P.K. Mang, N. Kaneko, M. Greven, Y. Onose, et al., "An angle-resolved photoemission spectral function analysis of the electron-doped Nd_{1.85}Sr_{0.15}CuO₄," *Phys. Rev. B* **68**, 064517 (2003).

Audette, G.F., R.T. Irvin, and B. Hazes, "Purification, crystallization and preliminary diffraction studies of the *Pseudomonas aeruginosa* strain K122-4 monomeric pilin," *Acta Crystallogr., Sect. D* D59, 1665 (2003).

Augustsson, A., "RIXS studies of lithium intercalation in rechargeable battery systems," licentiate thesis, Uppsala University, Sweden (2003).

Augustsson, A., A. Henningsson, S.M. Butorin, H. Siegbahn, J. Nordgren, and J.-H. Guo, "Lithium ion insertion in nanoporous anatase TiO₂ studied with RIXS," *J. Chem. Phys.* **119**, 3983 (2003).

Augustsson, A., T. Schmitt, L.-C. Duda, J. Nord-gren, S. Nordlinder, K. Edstrom, T. Gustafsson, and J.-H. Guo, "The electronic structure and lithiation of electrodes based on vanadium-oxide nanotubes," *J. Appl. Phys.* **94**, 5083 (2003).

Barabash, R.I., G.E. Ice, N. Tamura, B.C. Valek, J.C. Bravman, R. Spolenak, and J.R. Patel, "Quantitative analysis of dislocation arrangements induced by electromigration in a passivated Al (0.5 wt % Cu) interconnect," *J. Appl. Phys.* **93**, 5701 (2003).

Barglik-Chory, Ch., D. Buchold, M. Schmitt, W. Kiefer, C. Heske, C. Kumpf, O. Fuchs, L. Weinhardt, A. Stahl, E. Umbach, M. Lentze, J. Geurts, and G. Müller, "Synthesis, structure, and spectroscopic characterization of water-soluble CdS nanoparticles," *Chem. Phys. Lett.* 379, 443 (2003).

Bell, J.K., D.H. Goetz, S. Mahrus, J.L. Harris, R.J. Fletterick, and C.S. Craik, "The oligomeric structure of human granzyme A is a determinant of its extended substrate specificity," *Nat. Struct. Biol.* **10**, 527 (2003).

Bernstein, D.A., M.C. Zittel, and J.L. Keck, "High-resolution structure of the *E. coli* RecQ helicase catalytic core," *EMBO J.* **22**, 4910 (2003).

Berry, E.A., and L.-S. Huang, "Observations concerning the quinol oxidation site of the cyto-chrome bc_1 complex," *FEBS Lett.* **555**, 13 (2003), 126th Nobel Symposium, Stockholm Sweden, August 22–24, 2003.

Bertone, J.F., J. Cizeron, R.K. Wahi, J.K. Bosworth, and

ABOUT THE ALS

2003 PUBLICATIONS

V.L. Colvin, "Hydrothermal synthesis of quartz nanocrystals," *Nano Letters* **3**, 655 (2003).

Boukhvalov, D.W., E.Z. Kurmaev, A. Moewes, D.A. Zatsepin, V.V. Cherkashenko, S.M. Nemnonov, L.D. Finkelstein, Y.M. Yarmoshenko, M. Neumann, V.V. Dobrovitski, M.I. Katsnelson, A.I. Lichtenstein, B.N. Harmon, and P. Kogerler, "Electronic structure of magnetic molecules V₁₅: LDA+U calculations, x-ray emission and photoelectron spectra," *Phys. Rev. B* **67**, 134408 (2003).

Boulanger, M.J., D.C. Chow, E. Brevnova, and K.C. Garcia, "Hexameric structure and assembly of the interleukin-6/IL-6 α -receptor/gp130 complex," *Science* **300**, 2101 (2003).

Bozek, J.D., S.E. Canton, E. Kukk, and N. Berrah, "Vibrationally resolved resonant Auger spectroscopy of formaldehyde at the C $1s^{-1}\pi^*$ resonance," *Chem. Phys.* **289**, 149 (2003).

Bruehwiler, D., and H. Frei, "Structure of Ni(II) and Ru(III) ammine complexes grafted onto mesoporous silicate sieve," *J. Phys. Chem. B* **107**, 8547 (2003).

Buonassisi, T., M. Heuer, O.F. Vyvenko, A.A. Istratov, E.R. Weber, Z. Cai, B. Lai, T.F. Ciszek, and R. Schindler, "Applications of synchrotron radiation x-ray techniques on the analysis of the behavior of transition metals in solar cells and single crystalline silicon with extended defects," *Physica B* **340**, 1137 (2003).

Bushnell, D.A., and R.D. Kornberg, "Complete, 12-subunit RNA polymerase II at 4.1-Å resolution: Implications for the initiation of transcription," *Proc. Natl. Acad. Sci.* **100**, 6969 (2003).

Cahill, C.F., "Asian aerosol transport to Alaska during ACE-Asia," *J. Geophys. Res.* **108**(D23), ACE 32-1 (2003).

Canton, S.E., A.A. Wills, T.W. Gorczyca, E. Sokell, J.D. Bozek, G. Turri, M. Wiedenhoest, X. Feng, and N. Berrah, "New low-lying mirroring singly and doubly excited resonances in neon," *J. Phys. B* **36**, L181 (2003).

Canton, S.E., A.J. Yencha, E. Kukk, J.D. Bozek, M.C.A. Lopes, G. Snell, and N. Berrah, "Canton et al. Reply," *Phys. Rev. Lett.* **90**, 249602 (2003).

Carr, G.L., M. Martin, W.R. McKinney, K. Jordan, G.R Neil, and G.P. Williams, "Very high power THz radiation sources," *Journal of Biological Physics* **29**, 319 (2003).

Chambers, S.A., T. Droubay, C.M. Wang, A.S. Lea, R.F.C. Farrow, L. Folks, V. Deline, and S. Anders, "Clusters and magnetism in epitaxial Co-doped TiO₂ anatase," *Appl. Phys. Lett.* **82**, 1257 (2003).

Chang, G., "Structure of MsbA from *Vibrio cholera*: A multidrug resistance ABC transporter homolog in a closed conformation," *J. Mol. Biol.* **330**, 419 (2003).

Chao, W., E. Anderson, G. Denbeaux, B. Harteneck, A.J. Liddle, A. Pearson, D. Olynick, F. Salmassi, C. Song, and D. Attwood, "Photon-based microscopy with 20-nm spatial resolution," *Optics and Photonics News* 14, 18 (2003).

Chao, W., E. Anderson, G. Denbeaux, B. Harteneck, J.A. Liddle, D. Olynick, A. Pearson, F. Salmassi, C. Song, and D. Attwood, "20-nm-resolution soft x-ray microscopy demonstrated using multilayer test structures," *Opt. Lett.* **28**, 2019 (2003).

Chao, W., E. Anderson, G. Denbeaux, B. Harteneck, J.A. Liddle, D. Olynick, A. Pearson, F. Salmassi, C. Song, and D. Attwood, "Demonstration of 20 nm half-pitch spatial resolution with soft x-ray microscopy," *J. Vac. Sci. Technol. B* **21**, 3108 (2003).

Chen, C., J. Liu, and C.Y. Ng, "Vacuum ultraviolet pulsed field ionization-photoelectron study for N₂O⁺ in the energy range of 16.3–21.0 eV," *J. Phys. Chem. A* **107**, 8086 (2003).

Choi, W.-J., T.-Y. Lee, K.-N. Tu, N. Tamura, R.S. Celestre, A.A. MacDowell, Y.-Y. Bong, and L. Nguyen, "Synchrotron radiation micro-diffraction study of Sn whiskers on Pb-free surface finish," *Acta Materialia* **51**, 6253 (2003).

Classen, S., S. Olland, and J.M. Berger, "Structure of the topoisomerase II ATPase region and its mechaABOUT THE ALS

PUBLICATIONS

nism of inhibition by the chemotherapeutic agent ICRF-187," *Proc. Natl. Acad. Sci.* **100**, 10629 (2003).

Cool, T.A., K. Nakajima, T.A. Mostefaoui, F. Qi, A. Mcllroy, P.R. Westmoreland, M.E. Law, L. Poisson, D.S. Peterka, and M. Ahmed, "Selective detection of isomers with photoionization mass spectrometry for studies of hydrocarbon flame chemistry," *J. Chem. Phys.* **119**, 8356 (2003).

Corbett, K.D., and J.M. Berger, "Structure of the topoisomerase VI-B subunit: Implications for type II topoisomerase mechanism and evolution," *EMBO J.* **22**, 151 (2003).

Corlett, J.N, W.A. Barletta, S. De Santis, L. Doolittle, W.M. Fawley, M.A. Green, P. Heimann, S. Leone, S. Lidia, D. Li, A. Ratti, K. Robinson, R. Schoenlein, J. Staples, W. Wan, R. Wells, A. Wolski, A. Zholents, et al., "A recirculating linac-based facility for ultrafast x-ray science," in *Pro-ceedings of the 2003 Particle Accelerator Conference*, Portland, Oregon, May 12–16, 2003.

Croll, L.M., A.P. Hitchcock, I. Koprinarov, D.W. Vanbesien, and H.D.H. Stöver, "Integrating near edge x-ray absorption fine structure (NEXAFS) microscopy and crystallography: The effects of molecular order on soft x-ray spectromicroscopy," *J. Synchrotron Radiat.* 10, 265 (2003).

Damascelli, A., Z. Hussain, and Z.-X. Shen, "Angle-resolved photoemission studies of the cuparte superconductors," *Rev. Mod. Phys.* **75**, 473 (2003).

Dang, L.T.N., W.C. Stolte, G. Ohrwall, M.M. Sant'Anna, I. Dominguez-Lopez, A.S. Schlachter, and D.W. Lindle, "Core-level anionic photofragmentation of OCS," *Chem. Phys.* **289**, 45 (2003).

Davies, D.R., H. Interthal, J.J. Champoux, and W.G. Hol, "Crystal structure of a transition state mimic for Tdp1 assembled from vanadate, DNA, and a topoisomerase I-derived peptide," *Chemistry and Biology* 10, 139 (2003).

Deganzo, S.M., J.P. Erzberger, W.M. Lam, E. Skordalakes, R. Zhang, A.A. Franco, S.J. Brill, P.D. Adams, J.M. Berger, and P.D. Kaufman, "Structure and function of the conserved core of histone deposition protein Asf1," *Curr. Biol.* **13**, 2148 (2003).

Delabarre, B., and A.T. Brunger, "Complete structure of p97/valosin-containing protein reveals communication between nucleotide domains," *Nat. Struct. Biol.* **10**, 856 (2003).

Doolittle, R.F., "Some notes on crystallizing fibrinogen and fibrin fragments," *Biophys. Chem.* **100**, 307 (2003).

Doolittle, R.F., "Structural basis of the fibrinogen-fibrin transformation: Contributions from x-ray crystallography," *Blood Reviews* 17, 33 (2003).

Doolittle, R.F., "X-ray crystallographic studies on fibrinogen and fibrin," *Journal of Thrombosis and Haemostasis* 1, 1559 (2003).

Dumas, J.J., R. Kumar, J. Seehra, W.S. Somers, and L. Mosyak, "Crystal structure of the GpIbα-thrombin complex essential for platelet aggregation," *Science* **301**, 222 (2003).

Eimueller, T., P. Fischer, P. Guttmann, G. Denbeaux, M. Scholz, M. Koehler, G. Schmahl, G. Bayreuther, and G. Schuetz, "Multilayered magnetic nanostrips studied by transmission x-ray microscopy," *Journal de Physique IV* **104**, 483 (2003); Proceedings of the 7th International Conference on X-Ray Microscopy, Grenoble, France, July 28–August 2, 2002.

Eisebitt, S., M. Lorgen, W. Eberhardt, J. Luning, J. Stöhr, C.T. Rettner, O. Hellwig, E.E. Fullerton, and G. Denbeaux, "Polarization effects in coherent scattering from magnetic specimen: Implications for x-ray holography, lensless imaging, and correlation spectroscopy," *Phys. Rev. B* **68**, 104419 (2003).

Endo, K., S. Koizumi, T. Otsuka, T. Ida, T. Morohashi, J. Onoe, A. Nakao, E.Z. Kurmaev, A. Moewes, and D.P. Chong, "Analysis of electron spectra of carbon allotropes (diamond, graphite, fullerene) by density functional theory calculations using the model molecules," *J. Phys. Chem. A* **107**, 9403 (2003).

Ernst, J.A., and A.T. Brunger, "High resolution structure, stability, and synaptotagmin binding of a truncated neuronal SNARE complex," *J. Biol. Chem.* **278**, 8630 (2003).

Farangis, B., P. Nachimuthu, T.J. Richardson, J.L. Slack, B.K. Meyer, R.C.C. Perera, and D.M. Rubin,

"Structural and electronic properties of magnesium-3D transition metal switchable mirrors," *Solid State Ionics* **165**, 309 (2003).

Farangis, B., P. Nachimuthu, T.J. Richardson, J.L. Slack, R.C.C. Perera, E.M. Gullikson, D.W. Lindle, and M. Rubin, "In situ x-ray-absorption spectroscopy study of hydrogen absorption by nickel-magnesium thin films," *Phys. Rev. B* **67**, 085106 (2003).

Ferre-D'Amare, A.R., "RNA-modifying enzymes," *Curr. Opin. Struct. Biol.* **13**, 49 (2003).

Fischer, P., G. Denbeaux, H. Stoll, A. Puzic, J. Raabe, F. Nolting, T. Eimueller, and G. Schuetz, "Magnetic imaging with soft x-ray microscopies," *Journal de Physique IV* **104**, 471 (2003); Proceedings of the 7th International Conference on X-Ray Microscopy, Grenoble, France, July 28–August 2, 2002.

Fischer, P., T. Eimuller, G. Schutz, and G. Den-beaux, "Imaging magnetic domain structures with soft x-ray microscopy," *J. Structural Chemistry* **14**, 39 (2003).

Franco, N., J.E. Klepeis, C. Bostedt, T. van Buuren, C. Heske, O. Pankratov, T.A. Callcott, D.L. Ederer, and L.J. Terminello, "Experimental and theoretical electronic structure determination of PtSi," *Phys. Rev. B* **68**, 045116 (2003).

Frank, M., S. Friedrich, J. Höhne, and J. Jochum, "Cryogenic detectors and their application to x-ray fluorescence analysis," *J. X-Ray Sci. Technol.* **11**, 83 (2003).

Friedman, J., L. Lad, R. Deshmukh, H. Li, A. Wilks, and T.L. Poulos, "Crystal structures of the NO- and CO-bound heme oxygenase from *Neisseriae meningitidis*: Implications for O₂ activation," *J. Biol. Chem.* **278**, 34654 (2003).

Friedrich, S., A. Vailionis, O. Drury, T. Niedermayr, T. Funk, W.N. Kang, E.M. Choi, H.J. Kim, S.I. Lee, S.P. Cramer, C. Kim, and S.E. Labov, "A multichannel superconducting tunnel junction detector for high-resolution x-ray spectroscopy of magnesium diboride films," *IEEE Transactions on Applied Superconductivity* 13, 1114 (2003).

Fullerton, E.E., O. Hellwig, K. Takano, and J.B. Kortright, "Soft x-ray magnetic scattering as a probe of

recording media," *Nucl. Instrum. Meth. B* **200**, 202 (2003).

Gambin, V., V. Lordi, W. Ha, M. Wistey, T. Takizawa, K. Uno, S. Friedrich, and J. Harris, "Structural changes on annealing of MBE grown (Ga,In)(N,As) as measured by x-ray absorption fine structure," *J. Cryst. Growth* **251**, 408 (2003).

Gassner, N.C., W.A. Baase, B.H. Mooers, R.D. Busam, L.H. Weaver, J.D. Linstrom, M.L. Quillin, and B.W. Matthews, "Multiple methionine substitutions are tolerated in T4 lysozyme and have coupled effects on folding and stability," *Biophys. Chem.* **100**, 325 (2003).

Gibson, N.D., C.W. Walter, O. Zatsarinny, T.W. Gorczyca, G.D. Ackerman, J.D. Bozek, M. Martins, B.M. McLaughlin, and N. Berrah, "K-shell photodetachment from C⁻: experiment and theory," *Phys. Rev. A* **67**, 030703 (2003).

Glover, T. E., "Hydrodynamics of particle formation following femtosecond laser ablation," *J. Opt. Soc. Am. B* **20**, 125 (2003).

Glover, T.E., G.D. Ackerman, A. Belkacem, P.A. Heimann, Z. Hussain, R.W. Lee, H.A. Padmore, C. Ray, R.W. Schoenlein, W.F. Steele, and D.A. Young, "Metal insulator transitions in an expanding metallic fluid: Particle formation kinetics," *Phys. Rev. Lett.* **90**, 236102 (2003).

Gordon, M.L., G. Cooper, T. Araki, C. Morin, C.C. Turci, K. Kaznatcheev, and A.P. Hitchcock, "Innershell excitation spectroscopy of the peptide bond: Comparison of the C 1s, N 1s and O 1s spectra of glycine, glycyl-glycine and glycyl-glycyl-glycine," *J. Phys. Chem. A* **107**, 6144 (2003).

Goudeau, P., P. Villain, N. Tamura, and H.A. Padmore, "Mesoscale x-ray diffraction measurement of stress relaxation associated with buckling in compressed thin films," *Appl. Phys. Lett.* **83**, 51 (2003).

Goudeau, P., P. Villain, N. Tamura, P.O. Renault, K.F. Badawi, and H.A. Padmore, "Elastic properties of supported polycrystalline thin films and multilayers: An x-ray diffraction study," *Mater. Sci. Forum* **426–432**, 3409 (2003); Proceedings of the 4th International Conference on Processing and Manufacturing of Advanced Materials, Madrid, Spain, July 7–11, 2003.

ABOUT THE ALS

2003 PUBLICATIONS

PUBLICATIONS

2003

Gromko, A.D., A.V. Fedorov, Y.-D. Chuang, J.D. Koralek, Y. Aiura, Y. Yamaguchi, K. Oka, Y. Ando, and D.S. Dessau, "Mass-renormalized electronic excitations at $(\pi,0)$ in the superconducting state of Bi₂Sr₂CaCu₂0_{8+ δ}," *Phys. Rev. B* **68**, 174520 (2003).

Guo, J.-H., Y. Luo, A. Augustsson, S. Kashtanov, J.-E. Rubensson, D.K. Shuh, H. Agren, and J. Nordgren, "Molecular structure of alcohol-water mixtures," *Phys. Rev. Lett.* **91**, 157401 (2003).

Harries, J.R., J.P. Sullivan, J.B. Sternberg, S. Obara, T. Suzuki, P. Hammond, J. Bozek, N. Berrah, M. Halka, and Y. Azuma, "Double photoexcitation of helium in a strong dc electric field," *Phys. Rev. Lett.* **90**, 133002 (2003).

Harries, J.R., J.P. Sullivan, S. Obara, P. Hammond, and Y. Azuma, "Doubly-excited states of helium observed in *N*- and *I*-specific partial photoionisation cross-sections using lifetime-resolved fluorescence spectroscopy," *J. Phys. B* **36**, L319 (2003).

Hartmann, R., J. Justesen, S.N. Sarkar, G.C. Sen, and V.C. Yee, "Crystal structure of the 2'-specific and double-stranded RNA-activated interferon-induced antiviral protein 2'-5'-oligoadenylate synthetase," *Mol. Cell* 12, 1173 (2003).

Hau-Riege, S.P., A. Barty, P.B. Mirkarimi, D.G. Stearns, H. Chapman, D. Sweeney, M. Clift, E. Gullikson, and M.S. Yi, "Multilayer defect repair in EUVL mask blanks," *Proc. SPIE* **5037** (2003); Proceedings of the 28th Annual SPIE International Symposium and Education Program on Microlithography, Santa Clara, California, February 23–28, 2003.

Hävecker, M., R.W. Mayer, A. Knop-Gericke, H. Bluhm, E. Kleimenov, A. Liskowski, D. Su, R. Follath, F.G. Requejo, D.F. Ogletree, M. Salmeron, J.A. Lopez-Sanchez, J.K. Bartley, G.J. Hutchings, and R. Schlögl, "In situ investigation of the nature of the active surface of a vanadyl pyrophosphate catalyst during *n*-butane oxidation to maleic anhydride," *J. Phys. Chem. B* **107**, 4587 (2003).

He, H., S. Marchesini, M. Howells, U. Weierstall, G. Hembree, and J. Spence, "Experimental lensless soft-xray imaging using iterative algorithms: Phasing diffuse scattering," *Acta Crystallogr., Sect. A* **A59**, 143 (2003).

He, H., S. Marchesini, M. Howells, U. Weierstall, H. Chapman, S. Hau-Riege, A. Noy, and J.C.H. Spence, "Inversion of x-ray diffuse scattering to images using prepared objects," *Phys. Rev. B* **67**, 174114 (2003).

He, X.L., J.F. Bazan, G. McDermott, K. Wang, J.B. Park, M. Tessier-Lavigne, Z. He, and K.C. Garcia, "Structure of the nogo receptor ectodomain: A recognition module implicated in myelin inhibition," *Neuron* **38**, 177 (2003).

Hellwig, O., G.P. Denbeaux, J.B. Kortright, and E.E. Fullerton, "X-ray studies of aligned magnetic stripe domains in perpendicular multilayers," *Physica B* **336**, 136 (2003); Proceedings of the 7th International Conference on Surface X-Ray and Neutron Scattering, Tahoe City, California, September 23–27, 2002.

Hellwig, O., T.L. Kirk, J.B. Kortright, A. Berger, and E.E. Fullerton, "A new phase diagram for layered antiferromagnetic films," *Nature Materials* 2, 112 (2003).

Hemmers, O., R. Guillemin, E.P. Kanter, B. Krassig, D.W. Lindle, S.H. Southworth, R. Wehlitz, J. Baker, A. Hudson, M. Lotrakul, D. Rolles, W.C. Stolte, I.C. Tran, A. Wolska, S.W. Yu, M.Ya. Amusia, K.T. Cheng, L.V. Chernysheva, W.R. Johnson, S.T. Manson, et al., "Dramatic nondipole effects in low-energy photoionization: Experimental and theoretical study of Xe 5s," *Phys. Rev. Lett.* **91**, 053002 (2003).

Hemphill, R.D., M. Hurwitz, and M.G. Pelizzo, "Osmium atomic-oxygen protection by an iridium overcoat for increased extreme-ultraviolet grating efficiency," *Appl. Optics* **42**, 5149 (2003).

Heske, C., "Studying buried interfaces with soft x-ray spectroscopy," *Synchrotron Radiation in Natural Sciences* **2**, 35 (2003).

Heske, C., U. Groh, O. Fuchs, L. Weinhardt, E. Umbach, M. Grün, S. Petillon, A. Dinger, C. Klingshirn, W. Szuszkiewicz, and A. Fleszar, "Studying the local chemical environment of sulfur atoms at buried interfaces in CdS/ZnSe superlattices," *Appl. Phys. Lett.* **83**, 2360 (2003).

Heske, C., U. Groh, O. Fuchs, L. Weinhardt, E. Umbach, Th. Schedel-Niedrig, Ch.-H. Fischer, M.Ch. Lux-Steiner, S. Zweigart, T.P. Niesen, F. Karg, J.D. Denlinger, B. Rude, C. Andrus, and F. Powell,

"Monitoring chemical reactions at a liquid-solid interface: Water on CuIn(S,Se)₂ thin film solar cell absorbers," *J. Chem. Phys.* **119**, 10467 (2003).

Hoelz, A., A.C. Nairn, and J. Kuriyan, "Crystal structure of a tetradecameric assembly of the association domain of Ca²⁺/calmodulin-dependent kinase II," *Mol. Cell* **11**, 1241 (2003).

Holbrook, E.L., U. Schulze-Gahmen, G.W. Buchko, S. Ni, M.A. Kennedy, and S.R. Holbrook, "Purification, crystallization and preliminary x-ray analysis of two nudix hydrolases from *Deinococcus radiodurans*," *Acta Crystallogr., Sect. D* D**59**, 737 (2003).

Holman, H.Y., M.C. Martin, and W.R. McKinney, "Synchrotron-based FTIR spectromicroscopy: Cytotoxicity considerations," *Journal of Biological Physics* **29**, 275 (2003).

Holman, H.Y., M.C. Martin, and W.R. McKinney, "Tracking chemical changes in a live cell: Biomed-ical applications of SR-FTIR spectromicroscopy," *Spectroscopy, an International Journal* 17, 139 (2003).

Holyoak, T., M.A. Wilson, T.D. Fenn, C.A. Kettner, G.A. Petsko, R.S. Fuller, and D. Ringe, "2.4 Å resolution crystal structure of the prototypical hormone-processing protease Kex2 in complex with an Ala-Lys-Arg boronic acid inhibitor," *Biochemistry–US* **42**, 6709 (2003).

Howard, B.R., F.F. Vajdos, S. Li, W.I. Sundquist, and C.P. Hill, "Structural insights into the catalytic mechanism of cyclophilin A," *Nat. Struct. Biol.* **10**, 475 (2003).

Huang, D.B., D. Vu, L.A. Cassiday, J.M. Zimmerman, L.J. Maher III, and G. Ghosh, "Crystal structure of NF-κB (p50)₂ complexed to a high-affinity RNA aptamer," *Proc. Natl. Acad. Sci.* **100**, 9268 (2003).

Huang, L.-S., D. Cobessi, and E.A. Berry, "Crystallizations of the cytochrome bc1 complex," in *Methods and Results in Membrane Protein Crystal-lization*, S. Iwata (IUL Biotechnology Series, La Jolla, 2003).

Huang, X., M. Begley, K. Morgenstern, Y. Gu, P. Rose, H. Zhao, and X. Zhu, "Crystal structure of an inactive Akt2 kinase domain," *Structure* 11, 21 (2003).

Hura, G., D. Russo, R.M. Glaeser, T. Head-Gordon, M. Krack, and M. Parrinello, "Water structure as a function of temperature from x-ray scattering experiments and ab initio molecular dynamics," *Phys. Chem. Chem. Phys.* 5, 1981 (2003).

Im, M.Y., P. Fischer, T. Eimueller, G. Denbeaux, and S.C. Shin, "Magnetization reversal study of CoCrPt alloy thin films on a nanogranular-length scale using magnetic transmission soft x-ray microscopy," *Appl. Phys. Lett.* **83**, 4589 (2003).

Ionov, L., S. Minko, M. Stamm, J.-F. Gohy, R. Jerome, and A. Scholl, "Reversible chemical patterning on stimuli-responsive polymer film: Environment-responsive lithography," *JACS* **125**, 8302 (2003).

Isaure, M.-P., A. Laboudigue, N. Tamura, and M.A. Marcus, "Zn speciation in a soil contaminated by the deposition of a dredged sediment by synchrotron x-ray techniques," *Journal de Physique IV* **107**, 657 (2003); Proceedings of the XII International Conference on Heavy Metals in the Environment, Grenoble, France, May 26–30, 2003.

Istratov, A.A., T. Buonassisi, E.R. Weber, R.C. McDonald, A.L. Smith, R. Schindler, J. Rand, and J.P. Kalejs, "Metal content of multicrystalline silicon for solar cells," *Solid State Phenomena* **95-96**, 175 (2003); Proceedings of the 10th Inter-national Autumn Meeting on Gettering and Defect Engineering in Semiconductor Technology, Brandenburg, Germany, September 21–26, 2003.

Istratov, A.A., T. Buonassisi, R.J. McDonald, A.R. Smith, R. Schindler, J.A. Rand, J.P. Kalejs, and E.R. Weber, "Metal content of multicrystalline silicon for solar cells and its impact on minority carrier diffusion length," *J. Appl. Phys.* **94**, 6552 (2003).

Jalil, P.A., M. Faiz, N. Tabet, N.M. Hamdan, and Z. Hussain, "A study of stability of tungstophosphoric acid, H₃PW₁₂O₄₀, using synchrotron XPS, XANES, hexane cracking, XRD and IR spectroscopy," *J. Catal.* **217**, 292 (2003).

Janke-Gilman, N.A.R., "Magnetism in thin transition metal films," Ph.D. thesis, Pennsylvania State University (2003).

Jimenez-Mier, J., D.L. Ederer, and T. Schuler, "Correlation effects in the resonant and nonresonant ABOUT THE ALS

2003 PUBLICATIONS

manganese 3s \rightarrow 2p photon emission in MnF₂," *Phys. Rev. A* **68**, 042715 (2003).

Jimenez-Mier, J., D.L. Ederer, T. Schuler, and T.A. Callcott, "Direct evidence for 3p→2p non-dipole x-ray emission in transition metals," *J. Phys. B* **36**, L173 (2003).

Johnson, S.L., P.A. Heimann, A.M. Lindenberg, H.O. Jeschke, M.E. Garcia, Z. Chang, R.W. Lee, J.J. Rehr, and R.W. Falcone, "Properties of liquid silicon observed by time-resolved x-ray absorption spectroscopy," *Phys. Rev. Lett.* **91**, 157403 (2003).

Juenger, M.C.G., V.H.R. Lamour, P.J.M. Monteiro, E.M. Gartner, and G.P. Denbeaux, "Direct observation of cement hydration by soft x-ray microscopy," *J. Mater. Sci. Lett.* **22**, 1335 (2003).

Juers, D.H., S. Hakda, B.W. Matthews, and R.E. Huber, "Structural basis for the altered activity of Gly794 variants of *Escherichia coli* β -galactosidase," *Biochemistry* 42, 13505 (2003).

Kaafarani, B.R., B. Wex, A.G. Oliver, J.A. Krause Bauer, and D.C. Neckers, "π-π stacking and nitro-π-stacking interactions of 1-(4-nitrophenyl)-4-phenyl-2,4-bis(phenylethynyl)butadiene," *Acta Crystallogr., Sect. E* **E59**, 227 (2003).

Kamtekar, S., W.D. Kennedy, J. Wang, C. Stathopoulos, D. Söll, and T.A. Steitz, "The structural basis of cysteine aminoacylation of RNA^{Pro} by prolyl-tRNA synthetases," *Proc. Natl. Acad. Sci.* **100**, 1673 (2003).

Keatinge-Clay, A.T., A.A. Shelat, D.F. Savage, S.-C. Tsai, L.J.W. Miercke, J.D. O'Connell III, C. Khosla, and R.M. Stroud, "Catalysis, specificity, and ACP docking site of *Streptomyces coelicolor* malonyl-CoA: ACP transacylase," *Structure* 11, 147 (2003).

Kilcoyne, A.L., T. Tyliszczak, W. Steele, S. Fakra, P.P. Hitchcock, K. Franck, E.H. Anderson, B. Harteneck, E.G. Rightor, G.E. Mitchell, A.P. Hitchcock, L. Yang, T. Warwick, and H. Ade, "Interferometer controlled scanning transmission x-ray microscopes at the Advanced Light Source," *J. Synchrotron Radiat.* 10, 125 (2003).

Kirpichtchikova, T., A. Manceau, B. Lanson, M.A. Marcus, and T. Jacquet, "Speciation and mobility of

Zn, Cu and Pb in a truck farming soil contaminated by sewage irrigation," *Journal de Physique IV* **107**, 695 (2003); Proceedings of the XII International Conference on Heavy Metals in the Environment, Grenoble, France, May 26–30, 2003.

Konya, Z., V.F. Puntes, I. Kiricsi, J. Zhu, J.W. Ager, M.K. Ko, H.M. Frei, P. Alivisatos, and G.A. Somorjai, "Synthetic insertion of gold nanoparticles into mesoporous silica," *Chem. Mater.* **15**, 1242 (2003).

Kortright, J.B., J.S. Jiang, S.D. Bader, O. Hellwig, D.T. Marguiles, and E.E. Fullerton, "Magnetism in heterogeneous thin film systems: Resonant x-ray scattering studies," *Nucl. Instrum. Meth. B* **199**, 301 (2003).

Krisch, M.J., J.L. Miller, L.J. Butler, H. Su, R. Bersohn, and J. Shu, "Photodissociation dynamics of ethyl ethynyl ether: A new ketenyl radical precursor," *J. Chem. Phys.* **119**, 176 (2003).

Krylova, I.N., "Biochemical studies on orphan nuclear receptor, SF-1," masters thesis, University of California, San Francisco (2003).

Kuepper, K., B. Schneider, V. Caciuc, M. Neu-mann, A.V. Postnikov, A. Ruediger, A.A. Grabar, and Y.M. Vysochanskii, "Electronic structure of Sn₂P₂S₆," *Phys. Rev. B* **67**, 115101 (2003).

Kuhlman, B., G. Dantas, G.C. Ireton, G. Varani, B.L. Stoddard, and D. Baker, "Design of a novel globular protein fold with atomic-level accuracy," *Science* **302**, 1364 (2003).

Kurmaev, E.Z., A. Moewes, L. Ouyang, L. Randaccio, P. Rulis, W.Y. Ching, M. Bach, and M. Neumann, "The electronic structure and chemical bonding of vitamin B12," *Europhys. Lett.* **62**, 582 (2003).

Kurmaev, E.Z., A. Moewes, S.M. Butorin, M.I. Katsnelson, L.D. Finkelstein, J. Nordgren, and P.M. Tedrow, "Half-metallic electronic structure of CrO₂ in resonant scattering," *Phys. Rev. B* **67**, 155105 (2003).

Kurmaev, E.Z., A. Moewes, T. Ida, S. Danielache, K. Endo, I.O. Bashkin, A.I. Harkunov, and A.P. Moravsky, "Isomer structure of high-pressure hydrofullerene probed by soft x-ray emission," *J. Mol. Struct.* **639**, 27 (2003).

Kurtis, K.E., and F.A. Rodrigues, "Early age hydration of rice hull ash cement examined by soft x-ray microscopy," *Cement Concrete Res.* **33**, 509 (2003).

Kurtis, K.E., and P.J.M. Monteiro, "Chemical additives to control expansion of alkali-silica reaction gel: Proposed mechanisms of control," *J. Mater. Sci.* **38**, 2027 (2003).

Kusinski, G.J., K.M. Krishnan, G. Denbeaux, and G. Thomas, "Magnetic reversal of ion beam patterned Co/Pt multilayers," *Scripta Materialia* **48**, 949 (2003).

Lad, L., J. Wang, H. Li, J. Friedman, B. Bhaskar, P.R. Ortiz de Montellano, and T.L. Poulos, "Crystal structures of the ferric, ferrous, and ferrous-NO forms of the Asp140Ala mutant of human heme oxygenase-1: Catalytic implications," *J. Mol. Biol.* **330**, 527 (2003).

Lawrence, J.R., G.D.W. Swerhone, G.G. Leppard, T. Araki, X. Zhang, M.M. West, and A.P. Hitchcock, "Scanning transmission x-ray, laser scanning, and transmission electron microscopy mapping of the exopolymeric matrix of microbial biofilms," *Applied and Environmental Microbiology* **69**, 5543 (2003).

Lee, K.K.M., and R. Jeanloz, "High-pressure alloying of potassium and iron: Radioactivity in the Earth's core?" *Geophys. Res. Lett.* **30**, 2212 (2003).

Lee, K.K.M., "Exploring planetary interiors: Experiments at extreme conditions," Ph.D. thesis, University of California, Berkeley (2003).

Lee, K.-S., S.-K. Kim, and J.B. Kortright, "Atomic-scale depth selectivity of soft x-ray resonant Kerr effect," *Appl. Phys. Lett.* **83**, 3764 (2003).

Lee, S-Y., A. De La Torre, D. Yan, S. Kustu, B.T. Nixon, and D.E. Wemmer, "Regulation of the transcriptional activator NtrC1: Structural studies of the regulatory and AAA+ ATPase domains," *Genes and Development* 17, 2552 (2003).

Leemans, W.P., C.G.R. Geddes, J. Faure, Cs. Toth, J. van Tilborg, C.B. Schroeder, E. Esarey, G. Fubiani, D. Auerbach, B. Marcelis, M.A. Carnahan, R.A. Kaindl, J. Byrd., and M.C. Martin, "Obser-vation of terahertz emission from a laser plasma accelerated electron bunch crossing a plasma-vacuum boundry," *Phys. Rev. Lett.* **91**, 4802 (2003).

Lei, M., E.R. Podell, P. Baumann, and T.R. Cech, "DNA self-recognition in the structure of Pot1 bound to telomeric single-stranded DNA," *Nature* **426**, 198 (2003).

Li, W., L. Poisson, D.S. Peterka, M. Ahmed, R. Lucchese, and A.G. Suits, "Dissociative photonization dynamics in ethane studied by velocity map imaging," *Chem. Phys. Lett.* **374**, 334 (2003).

Liu, J., M. Hochlaf, and C.Y. Ng, "Pulsed field ionization-photoelectron bands for CS₂⁺ in the energy range of 13.2–17.6 eV: An experimental and theoretical study," *J. Chem. Phys.* **118**, 4487 (2003).

Liu, J., W. Chen, M. Hochlaf, X. Qian, C. Chang, and C.Y. Ng, "Unimolecular decay pathways of state selected CO_2^+ in the internal energy range of 5.2–6.2 eV: An experimental and theoretical study," *J. Chem. Phys.* **118**, 149 (2003).

Liu, Y., "Coherence properties of extreme ultraviolet/ soft x-ray sources," Ph.D. thesis, University of California, Berkeley (2003).

Lodowski, D.T., W.D. Capel, J.A. Pitcher, R.J. Lefkowitz, and J.J.G. Tesmer, "Keeping G proteins at bay: A complex between G protein-coupled receptor kinase 2 and Gβγ," *Science* **300** 1256 (2003).

Lordi, V., V. Gambin, S. Friedrich, T. Funk, T. Takizawa, K. Uno, and J.S. Harris, "Nearest-neighbor configuration in (GaIn)(NAs) probed by x-ray absorption spectroscopy," *Phys. Rev. Lett.* **90**, 145505 (2003).

Luning, J., F. Nolting, A. Scholl, H. Ohldag, J.W. Seo, J. Fompeyrine, J.P. Locquet, and J. Stöhr, "Determination of the antiferromagnetic spin axis in epitaxial LaFeO₃ films by x-ray magnetic linear dichroism spectroscopy," *Phys. Rev. B* **67**, 214433 (2003).

Luz, J.G., C. Hassig, C. Pickle, A. Godzik, B.J. Meyer, and I.A. Wilson, "XOL-1, primary sex-determing sig-

ABOUT THE ALS

2003 PUBLICATIONS

nal of *C. elegans*, is a GHMP kinase family member and structural prototype for a class of developmental regulators," *Genes and Development* 17, 977 (2003).

Magnuson, M., J.-E. Rubensson, A. Fohlisch, N. Wassdahl, A. Nilsson, and N. Martensson, "X-ray fluorescence spectra of metals excited below threshold," *Phys. Rev. B* **68**, 045119 (2003).

Manceau, A., N. Tamura, R.S. Celestre, A.A. MacDowell, N. Geoffroy, G. Sposito, and H.A. Padmore, "Molecular-scale speciation of Zn and Ni in soil ferromanganese nodules from loess soils of the Mississippi Basin," *Environ. Sci. Technol.* 37, 75 (2003).

Manjasetty, B.A., "Crystal structure of a bifunction aldolase-dehydrogenase: Sequstering a reactive and volatile intermediate," *Proc. Natl. Acad. Sci.* **100**, 6992 (2003).

Marchesini, S., and C.S. Fadley, "X-ray fluorescence holography: Going beyond the diffraction limit," *Phys. Rev. B* **67**, 024115 (2003).

Marchesini, S., H. He, H.N. Chapman, S.P. Hau-Riege, A. Noy, M.R. Howells, U. Weierstall, and J.C.H. Spence, "X-ray image reconstruction from a diffraction pattern alone," *Phys. Rev. B* **68**, 140101(R) (2003).

Marchesini, S., H.N. Chapman, S.P. Hau-Riege, R.A. London, A. Szoke, H. He, M.R. Howells, H. Padmore, R. Rosen, J.C H. Spence, and U. Weierstall, "Coherent x-ray diffractive imaging: Applications and limitations," *Optics Express* 11, 2344 (2003).

Margarit, S.M., H. Sondermann, B.E. Hall, B. Nagar, A. Hoelz, M. Pirruccello, D. Bar-Sagi, and J. Kuriyan, "Structural evidence for feedback activation by Ras-GTP of the Ras-specific nucleotide exchange factor SOS," *Cell* **112**, 685 (2003).

Matsuo, S., P. Nachimuthu, D.W. Lindle, H. Wakita, and R.C.C. Perera, "Electronic structures of crystalline and aqueous solutions of LiBr, NaBr, KBr, and KBrO₃: In situ Br L-edge near-edge x-ray absorption fine structure," *J. Phys. Chem. B* **107**, 12562 (2003).

Maynes, J.T., C. Garen, M.M. Cherney, G. Newton, D. Arad, Y. Av-Gay, R.C. Fahey, and M.N.G. James, "The crystal structure of 1-D-*myo*-inosityl 2-acetamido-

2-deoxy-alpha-D-glucopyranoside deacetylase (MshB) from *Mycobacterium tuberculosis* reveals a zinc hydrolase with a lactate dehydrogenase fold," *J. Biol. Chem.* **278**, 47166 (2003).

McDonald, M., "Finding optical constants of uranium oxide mirrors using FORTRAN," masters thesis, Brigham Young University (2003).

McFarland, B.J., T. Kortemme, S.F. Yu, D.A. Baker, and R.K. Strong, "Symmetry recognizing asymmetry: Analysis of the interactions between the C-type lectin-like immunoreceptor NKG2D and MHC class I-like ligands," *Structure* 11, 411 (2003).

Miao, J., K.O. Hodgson, T. Ishikawa, C.A. Larabell, M.A. Le Gros, and Y. Nishino, "Imaging whole *Escherichia coli* bacteria by using single-particle x-ray diffraction," *Proc. Natl. Acad. Sci.* **100**, 110 (2003).

Miller, G.J., R. Mattera, J.S. Bonifacino, and J.H. Hurley, "Recognition of accessory protein motifs by the γ -adaptin ear domain of GGA3," *Nat. Struct. Biol.* **10**, 599 (2003).

Mo, S.-K., J.D. Denlinger, H.-D. Kim, J.-H. Park, J.W. Allen, A. Sekiyama, A. Yamasaki, K. Kadono, S. Suga, Y. Saitoh, T. Muro, P. Metcalf, G. Keller, K. Held, V. Eyert, V.I. Anisimov, D. Vollhardt, et al., "Prominent quasiparticle peak in the photoemission spectrum of the metallic phase of V₂O₃," *Phys. Rev. Lett.* **90**, 186403 (2003).

Moewes, A., E.Z. Kurmaev, L.D. Finkelstein, A.V. Galakhov, S. Gota, M. Gautier-Soyer, J.P. Rueff, and C.F. Hague, "X-ray emission spectroscopy study of the Verwey transition in Fe₃O₄," *J. Phys. Condens. Mat.* **15**, 2017 (2003).

Mol, C.D., A. Brooun, D.R. Dougan, M.T. Hilgers, L.W. Tari, R.A. Wijnands, M.W. Knuth, D.E. McRee, and R.V. Swanson, "Crystal structures of active fully assembled substrate- and product-bound complexes of UDP-N-acetylmuramic acid:L-alanine ligase (MurC) from *Haemophilus influenzae*," *J. Bacteriol.* **185**, 4152 (2003).

Mol, C.D., K.B. Lim, V. Sridhar, H. Zou, E.Y.T. Chien, B.-C. Sang, J. Nowakowski, D.B. Kassel, C.N. Cronin, and D.E. McRee, "Structure of a c-Kit product complex reveals the basis for kinase transactivation," *J. Biol. Chem.* **278**, 31461 (2003).

Moore, K.T., M.A. Wall, A.J. Schwartz, B.W. Chung, D.K. Shuh, R.K. Schulze, and J.G. Tobin, "Failure of Russell-Saunders coupling in the 5F states of plutonium," *Phys. Rev. Lett.* **90**, 196404 (2003).

Morales, A.M., G. Aigeldinger, M.A. Bankert, L.A. Domeier, J.T. Hachman, C. Hauck, P.N. Keifer, K.L. Krafcik, D.E. McLean, and P.C. Yang, "Sacrificial layer for the fabrication of electroformed cantilevered LIGA microparts," *Proc. SPIE* **4979**, 448 (2003); Proceedings of the Micromachining and Microfabrication Process Technology VIII Conference, Photonics West 2003, San Jose, California, January 27–29, 2003.

Morales, A.M., L.A. Domeier, M.G. Gonzales, J.T. Hachman, J.M. Hruby, S.H. Goods, D.E. McLean, N. Yang, and A.D. Gardea, "Microstructure and mechanical properties of nickel microparts electroformed in replicated LIGA molds," *Proc. SPIE* **4979**, 440 (2003); Proceedings of the Micromachining and Microfabrication Process Technology VIII Conference, Photonics West 2003, San Jose, California, January 27–29, 2003.

Morales, A.M., T.J. Garino, B.L. Boyce, L.A. Domeier, A.K. Gutmann, and D.E. McLean, "Micromolding and sintering of nanoparticle preforms into microparts," *Proc. SPIE* **4979**, 430 (2003); Proceedings of the Micromachining and Microfabrication Process Technology VIII Conference, Photonics West 2003, San Jose, California, January 27–29, 2003.

Müller, A., R.A. Phaneuf, A. Aguilar, M.F. Gharaibeh, A.S. Schlachter, I. Alvarez, C. Cisneros, G. Hinojosa, and B.M. McLaughlin, "Photoionization of C²⁺ ions," *Nucl. Instrum. Meth. B* **205**, 301 (2003).

Mura, C., J. Katz, S. Clarke, and D. Eisenberg, "Structure and function of an archaeal homolog of survival protein E (SurEα): An acid phosphatase with purine nucleotide specificity," *J. Mol. Biol.* **326**, 1559 (2003).

Muramatsu, Y., "Theoretically predicted soft x-ray emission and absorption spectra of graphitic-structured BC₂N," *Adv. Quantum Chem.* **42**, 353 (2003).

Muramatsu, Y., M. Fujino, T. Yamamoto, E.M. Gullikson, and R.C.C. Perera, "Soft x-ray emission and absorption spectroscopy in the Si L region of polysilanes," *Nucl. Instrum. Meth. B* **199**, 260 (2003).

Nachimuthu, P., S. Thevuthasan, Y.J. Kim, A.S. Lea, V. Shutthanandan, M.H. Engelhard, D.R. Baer, S.A. Chambers, D.K. Shuh, D.W. Lindle, E.M. Gullikson, and R.C.C. Perera, "Investigation of copper(I) oxide quantum dots by near-edge x-ray absorption fine structure spectroscopy," *Chem. Mater.* **15**, 3939 (2003).

Nachtegaal, M., "The influence of competing sor-bents on the dynamics and mechanisms of metal reactions in natural systems: A multiscale approach," Ph.D. thesis, University of Delaware (2003).

Nadolski, L., and J. Laskar, "Review of single particle dynamics for third generation light sources through frequency map analysis," *Phys. Rev. ST Accel. Beams* **6**, 114801 (2003).

Nagano, S., H. Li, H. Shimizu, C. Nishida, H. Ogura, P.R. Ortiz de Montellano, and T.L. Poulos, "Crystal structures of epothilone D-bound, epothilone B-bound, and substrate-free forms of cytochrome P450epoK," *J. Biol. Chem.* **278**, 44886 (2003).

Nagar, B., O. Hantschel, M.A. Young, K. Scheffzek, D. Veach, W. Bornmann, B. Clarkson, G. Superti-Furga, and J. Kuriyan, "Structural basis for the autoinhibition of c-Abl tyrosine kinase," *Cell* **112**, 859 (2003).

Nakamura, J., S.-Y. Nasubida, E. Kabasawa, H. Yamazaki, N. Yamada, K. Kuroki, M. Watanabe, T. Oguchi, S. Lee, A. Yamamoto, S. Tajima, Y. Umeda, S. Minakawa, N. Kimura, H. Aoki, S. Otani, S. Shin, T.A. Calcott, D.L. Ederer, J.D. Denlinger, and R.C.C. Perera, "Electronic structure of B 2pσ and pπ states in MgB₂, AlB₂, and ZrB₂ single crystals," *Phys. Rev. B* **68**, 064515 (2003).

Näslund, L.-A., M. Cavalleri, H. Ogasawara, A. Nilsson, L.G.M. Pettersson, P. Wernet, D.C. Edwards, M. Sandstrom, and S. Myneni, "Direct evidence of orbital mixing between water and solvated transitionmetal ions: An oxygen 1s XAS and DFT study of aqueous systems," *J. Phys. Chem. A* **107**, 6869 (2003).

Neil, G.R., G.L. Carr, J.F. Gubeli, K. Jordan, M.C. Martin, W.R. McKinney, M. Shinn, M. Tani, G.P. Williams, and X.C. Zhang, "Production of high power femtosecond terahertz radiation," *Nucl. Instrum. Meth. A* **507**, 537 (2003).

ABOUT THE ALS

2003 PUBLICATIONS

Nordlinder, S., A. Augustsson, T. Schmitt, J. Guo, L.C. Duda, J. Nordgren, T. Gustafsson, and K. Edstrom, "Redox behavior of vanadium oxide nanotubes as studied by x-ray photoelectron spectroscopy and soft x-ray absorption spectro-scopy," *Chem. Mater.* **15**, 3227 (2003).

Nyberg, M., M. Odelius, A. Nilsson, and L.G.M. Pettersson, "Hydrogen bonding between adsorbed deprotonated glycine molecules on Cu(110)," *J. Chem. Phys.* **119**, 12577 (2003).

Oganesyan, V., D. Busso, J. Brandsen, S. Chen, J. Jancarik, R. Kim, and S. Kim, "Structure of the hypothetical protein AQ_1354 from *Aquifex aeolicus*," *Acta Crystallogr., Sect. D* D59, 1219 (2003).

Ohldag, H., A. Scholl, F. Nolting, E. Arenholz, S. Maat, A.T. Young, M.J. Carey, and J. Stöhr, "Correlation between exchange bias and pinned interfacial spins," *Phys. Rev. Lett.* **91**, 017203 (2003).

Osipov, T., C.L. Cocke, M.H. Prior, A. Landers, Th. Weber, O. Jagutzki, L. Schmidt, H. Schmidt-Böcking, and R. Dörner, "Photoelectron-photoion momentum spectroscopy as a clock for chemical rearrangements: Isomerization of the di-cation of acetylene to the vinylidene configuration," *Phys. Rev. Lett.* **90**, 233002 (2003).

Ouyang, L., L. Randaccio, P. Rulis, E.Z. Kurmaev, A.P. Moewes, and W.Y. Ching, "Electronic structure and bonding in vitamin B12 cyanocobalamin," *J. Mol. Struct.* **622**, 221 (2003).

Pauly, T.A., J.L. Ekstrom, D.A. Beebe, B. Chrunyk, D. Cunningham, M. Griffor, A. Kamath, E. Lee, R. Madura, D. Mcguire, T. Subashi, D. Wasilko, P. Watts, B.L. Mylari, P.J. Oates, P.D. Adams, and V.L. Rath, et al., "X-ray crystallographic and kinetic studies of human sorbitol dehydrogenase," *Structure* 11, 1071 (2003).

Pauly, T.A., T. Sulea, M. Ammirati, J. Sivaraman, D.E. Danley, M.C. Griffor, A.V. Kamath, I.-K., Wang, E.R. Laird, A.P. Seddon, R. Menard, M. Cygler, and V.L. Rath, "Specificity determinants of human cathepsin S revealed by crystal structures of complexes," *Biochemistry* **42**, 3203 (2003).

Pecher, K.H., D.M. McCubbery, E.M. Kneedler, J. Rothe, J.R. Bargar, G. Meigs, L. Cox, K.H. Nealson,

and B.P. Toner, "Quantitative charge state analysis of manganese biominerals in aqueous suspension using scanning transmission x-ray microscopy (STXM)," *Geochim. Cosmochim. Acta* **67**, 1089 (2003).

Perez-Dieste, V., O.M. Castellini, J.N. Crain, M.A. Eriksson, A. Kirakosian, J.-L. Lin, J.L. McChesney, F.J. Himpsel, C.T. Black, and C.B. Murray, "Thermal decomposition of surfactant coatings on Co and Ni nanocrystals," *Appl. Phys. Lett.* **83**, 5053 (2003).

Peterka, D.S., A. Lindinger, L. Poison, M. Ahmed, and D.M. Neumark, "Photoelectron imaging of helium droplets," *Phys. Rev. Lett.* **91**, 043401 (2003).

Phillips, J.D., F.G. Whitby, J.P. Kushner, and C.P. Hill, "Structural basis for tetrapyrrole coordination by uroporphyrinogen decarboxylase," *EMBO J.* 22, 6225 (2003).

Pierce, M.S., R.G. Moore, L.B. Sorensen, S.D. Kevan, O. Hellwig, E.E. Fullerton, and J.B. Kortright, "Quasistatic x-ray speckle metrology of microscopic magnetic return point memory," *Phys. Rev. Lett.* **90**, 17552 (2003).

Podobnik, M., T.F. Weitze, M. O'Donnell, and J. Kuriyan, "Nucleotide-induced conformational changes in an isolated *Escherichia coli* DNA polymerase III clamp loader subunit," *Structure* 11, 253 (2003).

Prestemon, S., D.R. Dietderich, S.A. Gourlay, P. Heimann, S. Marks, G. Sabbi, R.M. Scanlan, R. Schlueter, B. Wahrer, and B. Wang, "Design and evaluation of a short period Nb₃Sn superconducting undulator prototype," in *Proceedings of the 2003 Particle Accelerator Conference*, Portland, Oregon, May 12–16, 2003.

Prilliman, S., "Synchrotron x-ray diffraction studies of phase transition and mechanical properties of nanocrystalline materials at high pressure," Ph.D. thesis, University of California, Berkeley (2003).

Qian, X.M., A.H. Kung, T. Zhang, K.C. Lau, and C.Y. Ng, "Rovibrational-state-selected photoionization of acetylene by the two-color IR + VUV scheme: Observation of rotationally resolved Rydberg transitions," *Phys. Rev. Lett.* **91**, 233001 (2003).

Qian, X.M., T. Zhang, C. Chang, P. Wang, C.Y. Ng, Y.H. Chiu, D.J. Levandier, J.S. Miller, R.A. Dressler, T. Baer, and D.S. Peterka, "High-resolution state-selected

ion-molecule reaction studies using pulsed field ionization photoelectron-secondary ion coincidence method," *Rev. Sci. Instrum.* 74, 4096 (2003).

Qian, X.M., T. Zhang, C.Y. Ng, A. Kung, and M. Ahmed, "Two-color photoionization spectroscopy using vacuum ultraviolet synchrotron radiation and infrared optical parametric oscillator laser source," *Rev. Sci. Instrum.* 74, 2784 (2003).

Qian, X.M., T. Zhang, Y. Chiu, D.J. Levandier, J.S. Miller, R.A. Dressler, and C.Y. Ng, "Rovibrational state-selected study of H_2^+ (X, $v^+ = 1-17$, $N^+ = 1$) + Ar using the pulsed field ionization-photoelectron-secondary ion coincidence scheme," *J. Chem. Phys.* **118**, 2455 (2003).

Qin, B.Y., C. Liu, S.S. Lam, H. Srinath, R. Delston, J.J. Correia, R. Derynck, and K. Lin, "Crystal structure of IRF-3 reveals mechanism of autoinhibition and virus-induced phosphoactivation," *Nat. Struct. Biol.* **10**, 913 (2003).

Raty, J.Y., G. Galli, C. Bostedt, T. van Buuren, and L.J. Terminello, "Quantum confinement and fullerenelike surface reconstruction in nanodiamonds," *Phys. Rev. Lett.* **90**, 037401 (2003).

Retzko, I., and W.E.S. Unger, "Analysis by carbon materials by x-ray photoelectron spectroscopy and x-ray absorption spectroscopy," *Advanced Engineering Materials* **5**, 519 (2003).

Rhie, H.-S., S. Link, H.A. Durr, W. Eberhardt, and N.V. Smith, "Systematics of image-state lifetimes on d band metal surfaces," *Phys. Rev. B* **68**, 033410 (2003).

Richardson, T.J., B. Farangis, J.L. Slack, P. Nachimuthu, R. Perera, N. Tamura, and M. Rubin, "X-ray absorption spectroscopy of transition metalmagnesium hydride thin films," *Journal of Alloys and Compounds* 356-357, 204 (2003).

Rigo, S., P. Goudeau, J.-M. Desmarres, T. Masri, J.-A. Petit, and P. Schmidt, "Correlation between x-ray micro-diffraction and a developed analytical model to measure the residual stresses in suspended structures in MEMS," *Microelectronics Reliability* **43**, 1963 (2003).

Roberts, D.R., A.C. Scheinost, and D.L. Sparks, "Zinc speciation in contaminated soils combining direct and

indirect characterization methods," in *Geochemical and Hydrological Reactivity of Heavy Metals*, H.M. Selim and W.L. Kingery (Lewis Publishers, Boca Raton, 2003).

Robien, M.A., B.E. Krumm, M. Sandkvist, and W.G.J. Hol, "Crystal structure of the extracellular protein secretion NTPase EpsE of *Vibrio cholerae*," *J. Mol. Biol.* 333, 657 (2003).

Robinson, J.C., N.E. Sveum, and D.M. Neumark, "Determination of absolute photoionization cross sections for vinyl and propargyl radicals," *J. Chem. Phys.* **119**, 5311 (2003).

Robinson, R., "Removing contaminants from silicon wafers to facilitate EUV optical characterization," masters thesis, Brigham Young University (2003).

Rocha, M.P., "A high-resolution study of the electronic structure of NbSe₃ in normal and charge density wave phases with angle resolved photo-emission spectroscopy," Ph.D. thesis, University of Oregon (2003).

Rogan, R.C., N. Tamura, G.A. Swift, and E. Ustundag, "Direct measurement of triaxial strain fields around ferroelectric domains using x-ray microdiffraction," *Nature Materials* 2, 379 (2003).

Rosengarth, A., and H. Luecke, "A calcium-driven conformational switch of the N-terminal and core domains of annexin A1," *J. Mol. Biol.* **326**, 1317 (2003).

Rotenberg, E., H. Koh, K. Rossnagel, H.W. Yeom, J. Schäfer, B. Krenzer, M.P. Rocha, and S.D. Kevan, "Indium $\sqrt{7} \times \sqrt{3}$ on Si(111): A nearly free electron metal in two dimensions," *Phys. Rev. Lett.* **91**, 6401 (2003).

Sablin, E.P., I.N. Krylova, R.J. Fletterick, and H.A. Ingraham, "Structural basis for ligand-independent activation of the orphan nuclear receptor LRH-1," *Mol. Cell* **11**, 1575 (2003).

Saes, M., C. Bressler, R. Abela, D. Grolimund, S.L. Johnson, P.A. Heimann, and M. Chergui, "Observing photochemical transients by ultrafast x-ray absorption spectroscopy," *Phys. Rev. Lett.* **90**, 047403 (2003).

Sali, A., R. Glaeser, T. Earnest, and W. Baumeister, "From words to literature in structural proteomics," *Nature* **422**, 216 (2003).

ABOUT THE ALS

2003 PUBLICATIONS

ABOUT THE ALS

2003 PUBLICATIONS

160

Salleo, A., S.T. Taylor, M.C. Martin, W.R. Panero, R. Jeanloz, F.Y. Genin, and T. Sands, "Laser-driven formation of a high-pressure phase in amorphous silica," *Nature Materials* **2**, 796 (2003).

Sandberg, R.L., D.D. Allred, J.E. Johnson, and R.S. Turley, "A comparison of uranium oxide and nickel as single-layer reflectors from 2.7 to 11.6 nm," *Proc. SPIE* **5193**, 191 (2003); Proceedings of the Advances in Mirror Technology for X-Ray, EUV Lithography, Laser, and Other Applications Conference, SPIE Annual Meeting 2003, San Diego, California, August 3–8, 2003.

Sannibale, F., D. Baum, N. Kelez, T. Scarvie, K. Holldack, "A second beam-diagnostic beamline for the Advanced Light Source," in *Proceedings of the 2003 Particle Accelerator Conference*, Portland, Oregon, May 12–16, 2003.

Sannibale, F., J.M. Byrd, A. Loftsdottir, M.C. Martin, and M. Venturini, "A model for producing stable, broadband terahertz coherent synchro-tron radiation in storage rings," in *Proceedings of the 2003 Particle Accelerator Conference*, Portland, Oregon, May 12–16, 2003.

Sarma, G.N., S.N. Savvides, K. Becker, M. Schirmer, R.H. Schirmer, and P.A. Karplus, "Glutathione reductase of the malarial parasite *Plasmodium falciparum*: Crystal structure and inhibitor development," *J. Mol. Biol.* **328**, 893 (2003).

Sarret, G., W.H. Schroeder, M.A. Marcus, N. Geoffroy, and A. Manceau, "Localization and speciation of Zn in mycorrhized roots by micro-SXRF and micro-EXAFS," *Journal de Physique IV* **107** (2003); Proceedings of the XII International Conference on Heavy Metals in the Environment, Grenoble, France, May 26–30, 2003.

Savage, D.F., P.F. Egea, Y. Robles-Colmenares, J.D. O'Connell III, and R.M. Stroud, "Architecture and selectivity in aquaporins: 2.5 Å x-ray structure of aquaporin Z," *PLoS Biology* 1(3), 334 (2003).

Savytskii, D.I., D.M. Trots, L.O. Vasylechko, N. Tamura, and M. Berkowski, "Twinning in La_{0.95}Sr_{0.05}Ga_{0.9}Mg_{0.1}O_{2.92} crystals studied by white beam (Laue) x-ray microdiffraction," *J. Appl. Crystallogr.* **36**, 1197 (2003).

Scarvie, T., N. Andresen, K. Baptiste, J. Byrd, M. Chin, M. Martin, W. McKinney, and C. Steier, "Noise reduction efforts for the infrared beamline at the Advanced Light Source," in *Proceedings of the 2003 Particle Accelerator Conference*, Portland, Oregon, May 12–16, 2003.

Schäfer, J., M. Sing, R. Claessen, E. Rotenberg, X.J. Zhou, R.E. Thorne, and S.D. Kevan, "Unusual spectral behavior of charge density waves with imperfect nesting in a quasi-one-dimensional metal," *Phys. Rev. Lett.* **91**, 066401 (2003).

Schäfer, J., S.C. Erwin, M. Hansmann, Z. Song, E. Rotenberg, S.D. Kevan, C.S. Hellberg, and K. Horn, "Random registry shifts in quasi-one-dimensional adsorbate systems," *Phys. Rev. B* **67**, 085411 (2003).

Schattke, W., and M.A. Van Hove, "Solid-state photoemission and related methods: Theory and experiment," in *Solid-State Photoemission and Related Methods: Theory and Experiment*, W. Schattke and M.A. Van Hove (Wiley-VCH Verlag, Berlin, 2003).

Schattke, W., M.A. Van Hove, F.J. García de Abajo, R. Díez Muiño, and N. Mannella, "Overview of core and valence photoemission," in *Solid-State Photoemission and Related Methods: Theory and Experiment*, W. Schattke and M.A. Van Hove (Wiley-VCH Verlag, Berlin, 2003).

Schippers, S., A. Müller, B.M. McLaughlin, A. Aguilar, C. Cisneros, E.D. Emmons, M.F. Gharaibeh, and R.A. Phaneuf, "Photoionization studies of the B+valence shell: Experiment and theory," *J. Phys. B* **36**, 3371 (2003).

Schippers, S., A. Müller, S. Ricz, M.E. Bannister, G.H. Dunn, A.S. Schlachter, G. Hinojosa, C. Cisneros, A. Aguilar, A.M. Covington, M.F. Gharaibeh, and R.A. Phaneuf, "Photoionization of Sc²⁺ ions: Measurements and absolute cross sections in the photon energy range 23–68 eV," *Phys. Rev. A* **67**, 032702 (2003).

Schippers, S., A. Müller, S. Ricz, M.E. Bannister, G.H. Dunn, J.D. Bozek, A.S. Schlachter, G. Hinojosa, C. Cisneros, A. Aguilar, A.M. Covington, M.F. Gharaibeh, and R.A. Phaneuf, "Photoionization of Sc²⁺: Experimental link with photorecombination of Sc³⁺ by application of detailed balance," *Nucl. Instrum. Meth. B* **205**, 297 (2003).

Schneider, G., G. Denbeaux, E.H. Anderson, W.A. Bates, F. Salmassi, P. Nachimuthu, A. Pearson, D. Richardson, D. Hambach, N. Hoffmann, W. Hasse, and K. Hoffmann, "Electromigration in integrated circuit interconnects studied by x-ray microscopy," *Nucl. Instrum. Meth. B* **199**, 469 (2003).

Scholl, A., "Applications of photoemission electron microscopy (PEEM) in magnetism research," *Current Opinion in Solid State & Material Sciences* 7, 59 (2003).

Schreiter, E.R., M.D. Sintchak, Y. Guo, P.T. Chivers, R.T. Sauer, and C.L. Drennan, "Crystal structure of the nickel-responsive transcription factor NikR," *Nat. Struct. Biol.* **10**, 794 (2003).

Schulze-Gahmen, U., J. Pelaschier, H. Yokota, R. Kim, and S.H. Kim, "Crystal structure of a hypothetical protein, TM841 of *Thermotoga maritima*, reveals its function as a fatty acid-binding protein," *Proteins:* Structure, Function, and Genetics **50**, 526 (2003).

Shin, D.H., A.Roberts, J. Jancarik, H. Yokota, R. Kim, D. Wemmer, and S.H. Kim, "Crystal structure of a phosphatase with a unique substrate binding domain from *Thermotoga maritima*," *Protein Sci.* **12**, 1464 (2003).

Shin, D.S., L. Pellegrini, D.S. Daniels, B. Yelent, L. Craig, D. Bates, D.S. Yu, M.K. Shivji, C. Hitomi, A.S. Arvai, N. Volkmann, H. Tsuruta, T.L. Blundell, A.R. Venkitaraman, and J.A. Tainer, "Full-length archaeal Rad51 structure and mutants: Mechanisms for RAD51 assembly and control by BRCA2," *EMBO J.* 22, 4566 (2003).

Skordalakes, E., and J.M. Berger, "Structure of the Rho transcription terminator: Mechanism of mRNA recognition and helicase loading," *Cell* **114**, 135 (2003).

Smith, A.D., P.F. Schofield, A. Scholl, R.A.D. Pattrick, and J.C. Bridges, "XPEEM valence state imaging of mineral micro-intergrowths with a spatial resolution of 100 nm," *Journal de Physique IV* **104**, 373 (2003); Proceedings of the 7th International Conference on X-Ray Microscopy, Grenoble, France, July 28–August 2, 2002.

Smith, A.D., T. Pradell, J. Molera, M. Vendrell, M.A. Marcus, and E. Pantos, "MicroEXAFS study into the oxidation states of copper coloured Hispano-Moresque lustre decorations," *Journal de Physique IV* **104**, 519 (2003); Proceedings of the 7th International

Conference on X-Ray Microscopy, Grenoble, France, July 28–August 2, 2002.

Smith, N.V., "Memory effects in the magnetotransport properties of the classical Drude metal," *Phys. Rev. B* **68**, 132406 (2003).

Sokolov, A.V., E.Z. Kurmaev, J. MacNaughton, A. Moewes, N.A. Skorikov, and L.D. Finkelstein, " σ and π -band dispersion of graphite from polarized resonant inelastic x-ray scattering measurements," *JETP Letters* 77, 108 (2003).

Sokolov, A.V., E.Z. Kurmaev, S. Leitch, A. Moewes, J. Kortus, L.D. Finkelstein, N.D. Skorikov, C. Xiao, and A. Hirose, "Band dispersion of MgB₂, graphite and diamond from resonant inelastic scattering," *J. Phys. Condens. Mat.* **15**, 2081 (2003).

Sondermann, H., S.M. Soisson, D. Bar-Sagi, and J. Kuriyan, "Tandem histone folds in the structure of the N-terminal segment of the Ras activator Son of Sevenless," *Structure* 11, 1583 (2003).

Spezzani, C., "Diffusion résonante des rayons X polarisés et couplage magnétique dans les multicouches Co/Cu," Ph.D. thesis, Université Paris-Sud, France (2003).

Spiller, E., S.L. Baker, P.B. Mirkarimi, V. Sperry, E.M. Gullikson, and D.G. Stearns, "High performance Mo/Si multilayer coatings for EUV lithography using ion beam deposition," *Appl. Optics* **42**, 4049 (2003).

Spolenak, R., W.L. Brown, N. Tamura, A.A. MacDowell, R.S. Celestre, H.A. Padmore, B.C. Valek, J.C. Bravman, T. Marieb, H. Fujimoto, B.W. Batterman, and J.R. Patel, "Local plasticity of Al thin films as revealed by x-ray microdiffraction," *Phys. Rev. Lett.* **90**, 09610211 (2003).

Staninec, M., J. Zie, C.Q. Le, and D. Fried, "Influence of an optically thick water layer on the bond-strength of composite resin to dental enamel after IR laser ablation," *Lasers in Surgery and Medicine* **33**, 264 (2003).

Steier, C., A. Biocca, E. Domning, S. Jacobson, G. Portmann, T. Scarvie, and E. Williams, "Commissioning results of the fast orbit feedback at the ALS," in *Proceedings of the 2003 Particle Accelerator Conference*, Portland, Oregon, May 12–16, 2003.

ABOUT THE ALS

2003 PUBLICATIONS

PUBLICATIONS

2003

Steier, C., D. Robin, A. Wolski, G. Portmann, and J. Safranek, "Coupling correction and beam dynamics at ultralow vertical emittance in the ALS," in *Proceedings of the 2003 Particle Accelerator Conference*, Portland, Oregon, May 12–16, 2003.

Steier, C., E. Forest, L. Nadolski, H. Nishimura, D. Robin, W. Wan, Y. Wu, and A. Zholents, "Accelerator physics challenges of the fs-slicing upgrade at the ALS," in *Proceedings of the 2003 Particle Accelerator Conference*, Portland, Oregon, May 12–16, 2003.

Stolte, W.C., M.M. Sant'Anna, G. Ohrwall, I. Dominguez-Lopez, M.N. Piancastelli, and D.W. Lindle, "Photofragmentation dynamics of core-excited water by anion-yield spectroscopy," *Phys. Rev. A* **68**, 022701 (2003).

Strong, R.K., M.A. Holmes, P. Li, L. Braun-Jones, N. Lee, and D.E. Geraghty, "HLA-E allelic variants: Correlating differential expression, peptide affinities, crystal structures and thermal stabilities," *J. Biol. Chem.* **278**, 5082 (2003).

Suer, S., S. Misra, L.F. Saidi, and J.H. Hurley, "Structure of the GAT domain of human GGA1: A syntaxin amino-terminal domain fold in an endosomal trafficking adaptor," *Proc. Natl. Acad. Sci.* **100**, 4451 (2003).

Sun, S., S. Anders, T. Thomson, J.E.E. Baglin, M.F. Toney, H.F. Hamann, C.B. Murray, and B.D. Terris, "Controlled synthesis and assembly of FePt nanoparticles," *J. Phys. Chem. B* **107**, 5419 (2003).

Suzer, S., M.M. Sayan, B. Holl, E. Garfunkel, Z. Hussain, and N. Hamdan, "Soft x-ray photo-emission studies of Hf oxidation," *J. Vac. Sci. Technol. A* **21**, 106 (2003).

Szpunar, D.E., Y. Liu, M.J. McCullagh, L.J. Butler, and J. Shu, "Photodissociation of allyl-d₂ iodide excited at 193 nm: Stability of highly rationally excited H₂CDCH₂ radicals to C–D fission," *J. Chem. Phys.* **119**, 5078 (2003).

Tabet, N., M. Faiz, N.M. Hamdan, and Z. Hussain, "High resolution XPS study of oxide layers grown on Ge substrates," *Surf. Sci.* **523**, 68 (2003).

Takenaka, H., K. Nagai, H. Ito, S. Ichimaru, T. Ohchi, Y. Muramatu, and E.M. Gullikson, "Highly reflective

Co_xCr_{1-x}/C multilayer mirror for use in x-ray photoemission spectroscopy in the wavelength region around 6 nm," in *Journal de Physique IV*, **104**, 255; Proceedings of the 7th International Conference on X-Ray Microscopy, Grenoble, France, July 28–August 2, 2002.

Takenaka, H., S. Ichimaru, T. Haga, T. Ohchi, H. Ito, Y. Muramatsu, E.M. Gullikson, and R.C.C. Perera, "Fabrication of soft x-ray beam splitters for use in the wavelength region around 13 nm," *Journal de Physique IV* **104**, 251 (2003); Proceedings of the 7th International Conference on X-Ray Microscopy, Grenoble France, July 28–August 2, 2002.

Tamura, N., A.A. MacDowell, R. Spolenak, B.C. Valek, J.C. Bravman, W.L. Brown, R.S. Celestre, H.A. Padmore, B.W. Batterman, and J.R. Patel, "Scanning x-ray microdiffraction with submicro-meter white beam for strain/stress and orientation mapping in thin films," *J. Synchrotron Radiat.* **10**, 137 (2003).

Terwilliger, T.C., et al., "The TB structural genomics consortium: A resource for *Mycobacterium tuberculosis* biology," *Tuberculosis* **83**, 223 (2003).

Theis, W., E. Rotenberg, K.J. Franke, P. Gille, and K. Horn, "Electronic valence bands in decagonal Al-Ni-Co," *Phys. Rev. B* **68**, 104205 (2003).

Thieme, J., G. Schneider, and C. Knoechel, "X-ray tomography of a microhabitat of bacteria and other soil colloids with sub-100 nm resolution," *Micron* **34**, 339 (2003).

Todd, E.C., and D.M. Sherman, "Surface oxidation of chalcocite (Cu_2S) under aqueous (pH = 2–11) and ambient atmospheric conditions: Mineralogy from Cu L- and O K-edge x-ray absorption spectroscopy," *Am. Mineral.* **88**, 1652 (2003).

Turri, G., G. Snell, B. Langer, M. Martins, E. Kukk, S.E. Canton, R.C. Bilodeau, N. Cherepkov, J.D. Bozek, and N. Berrah, "Molecular effects in the spin polarization of the sulfur 2p in OCS and H₂S molecules," *AIP Conference Proceedings* **697**, 48 (2003); Proceedings of the International Symposium on (e,2e), Double Photoionization and Related Topics and the Twelfth International Symposium on Polarization and Correlation in Electronic and Atomic Collisions, Königstein, Germany, July 30–August 2, 2003.

Valek, B.C., N. Tamura, R. Spolenak, W.A. Caldwell, A.A. MacDowell, R.S. Celestre, H.A. Padmore, J.C. Bravman, B.W. Batterman, W.D. Nix, and J.R. Patel, "Early stage of plastic deformation in thin films undergoing electromigration," *J. Appl. Phys.* **94**, 3757 (2003).

Van Hove, M.A., "Overview of Surface Structures," in *Solid-State Photoemission and Related Methods: Theory and Experiment*, W. Schattke and M.A. Van Hove (Wiley-VCH Verlag, Berlin, 2003).

Vila-Sanjurjo, A., W.K. Ridgeway, V. Seymaner, W. Zhang, S. Santoso, K. Yu, and J.H. Doudna Cate, "X-ray crystal structures of the WT and a hyper-accurate ribosome from *Escherichia coli," Proc. Natl. Acad. Sci.* **100**, 8682 (2003).

Walden, H., M. Podgorski, and B.A. Schulman, "Insights into the ubiquitin transfer cascade from the structure of the activating enzyme for NEDD8," *Nature* **422**, 330 (2003).

Walden, H., M.S. Podgorski, D.T. Huang, D.W. Miller, R.J. Howard, D.L. Minor, Jr., J.M. Holton, and B.A. Schulman, "The structure of the APPBP1-UBA3-NEDD8-ATP complex reveals the basis for selective ubiquitin-like protein activation by an E1," *Molecular Cell* 12, 1427 (2003).

Wang, Z., G. Benoit, J. Liu, S. Prasad, P. Aarnisalo, X. Liu, H. Xu, N.P.C. Walker, and T. Perlmann, "Structure and function of Nurr1 identifies a class of ligand-independent nuclear receptors," *Nature* **423**, 555 (2003).

Weber, N.B., H. Ohldag, H. Gomonaj, and F.U. Hillebrecht, "Magnetostrictive domain walls in antiferromagnetic NiO," *Phys. Rev. Lett.* **91**, 237205 (2003).

Weber, T., "Untersuchung der verschränkten Bewegung freier Elektronenpaare emittiert aus Ein- und Zweizentren Coulomb-Potentialen in Photoabsorptionsprozessen," Ph.D. thesis, University of Frankfurt, Germany (2003).

Weber, T.W., M. Weckenbrock, M. Balser, L. Schmidt, O. Jagutzki, W. Arnold, O. Hohn, M. Schöffler, E.

Arenholz, T. Young, T. Osipov, L. Foucar, A. DeFanis, R. Díez Muiño, H. Schmidt-Böcking, C.L. Cocke, H. Prior, and R. Dörner, "Auger electron emission from fixed-in-space CO," *Phys. Rev. Lett.* **90**, 153003 (2003).

Weinhardt, L., T.H. Gleim, O. Fuchs, C. Heske, E. Umbach, M. Bär, H.J. Muffler, C.H. Fischer, M.C. Lux-Steiner, Y. Zubavichus, T.P. Niesen, and F. Karg, "CdS and Cd(OH)₂ formation during Cd treatments of Cu(In,Ga)(S,Se)₂ thin film solar cell absorbers," *Appl. Phys. Lett.* **82**, 571 (2003).

Wetzel, M.A., G.E. Shaw, J.R. Slusser, R.A. Borys, and C.F. Cahill, "Physical, chemical, and ultraviolet radiative characteristics of aerosol in central Alaska," *J. Geophys. Res.* **108**, 4418 (2003).

Wheeler, C.R., D. Fried, J.D.B. Featherstone, L. Watanabe, and C.Q. Le, "Irradiation of dental enamel with Q-switched λ =355-nm laser pulses: Surface morphology, fluoride adsorption, and adhesion to composite resin," *Lasers in Surgery and Medicine* **32**, 310 (2003).

Wiedenhoeft, M., "Double photoionization of atoms," Ph.D. thesis, Western Michigan University (2003).

Wilson, J.J., O. Matsushita, A. Okabe, and J. Sakon, "A bacterial collagen-binding domain with novel calcium-binding motif controls domain orientation," *EMBO J.* **22**, 1743 (2003).

Won, C., Y.Z. Wu, A. Scholl, A. Doran, N. Kurahashi, H.W. Zhao, and Z.Q. Qiu, "Magnetic phase transition in Co/Cu/Ni/Cu(100) and Co/Fe/Ni/Cu(100)," *Phys. Rev. Lett.* **91**, 147202 (2003).

Won, C., Y.Z. Wu, H.W. Zhao, A. Scholl, A. Doran, and Z.Q. Qiu, "Effect of the interlayer coupling on the Ni spin reorientation in Ni/Fe/Co/Cu(100)," *Phys. Rev. B* **68**, 052404 (2003).

Won, C., Y.Z. Wu, N. Kurahashi, K.T. Law, H.W. Zhao, A. Scholl, A. Doran, and Z.Q. Qiu, "Evidence of the oscillatory magnetic anisotropy in Ni/Co/Ni/Cu(100)," *Phys. Rev. B* **67**, 174425 (2003).

Wood, Z.A., L.B. Poole, and P.A. Karplus, "Peroxire-doxin evolution and the regulation of hydrogen peroxide signaling," *Science* **300**, 650 (2003).

ABOUT THE ALS

2003
PUBLICATIONS

ABOUT THE ALS

2003 PUBLICATIONS

164

Wu, J., W. Walukiewicz, K.M. Yu, J.W. Ager, E.E. Haller, I. Miotkowski, A.K. Ramdas, C.H. Su, I.K. Sou, R.C.C. Perera, and J.D. Denlinger, "Origin of the large band-gap bowing in highly mismatched semiconductor alloys," *Phys. Rev. B* **67**, 035207 (2003).

Yang, W.L., V. Brouet, X.J. Zhou, H.J. Choi, S.G. Louie, M.L. Cohen, S.A. Kellar, P.V. Bogdanov, A. Lanzara, A. Goldoni, F. Parmigiani, Z. Hussain, and Z.X. Shen, "Band structure and Fermi surface of electron-doped C₆₀ monolayers," *Science* **300**, 303 (2003).

Yoshida, T., X.J. Zhou, T. Sasagawa, W.L. Yang, P.V. Bogdanov, A. Lanzara, Z. Hussain, T. Mizokawa, A. Fujimori, H. Eisaki, C. Kim, Z.-X. Shen, T. Kakeshita, and S. Uchida, "Metallic behavior of lightly doped La_{2-x}Sr_xCuO₄ with a Fermi surface forming an arc," *Phys. Rev. Lett.* **91**, 027001 (2003).

Young, T.A., B. Delagoutte, J.A. Endrizzi, and T. Alber, "Structure of *Mycobacterium tuberculosis* PknB supports a universal activation mechanism for Ser/Thr kinases," *Nat. Struct. Biol.* **10**, 168 (2003).

Yu, E.W., G. McDermott, H.I. Zgurskaya, H. Nikaido, and D.E. Koshland, Jr., "Structural basis of multiple drug-binding capacity of the AcrB multidrug efflux pump," *Science* **300**, 976 (2003).

Yu, S.W., W.C. Stolte, G. Ohrwall, R. Guillemin, M.N. Piancastelli, and D.W. Lindle, "Anionic and

cationic photofragmentation of core-excited N₂O," *J. Phys. B* **36**, 1255 (2003).

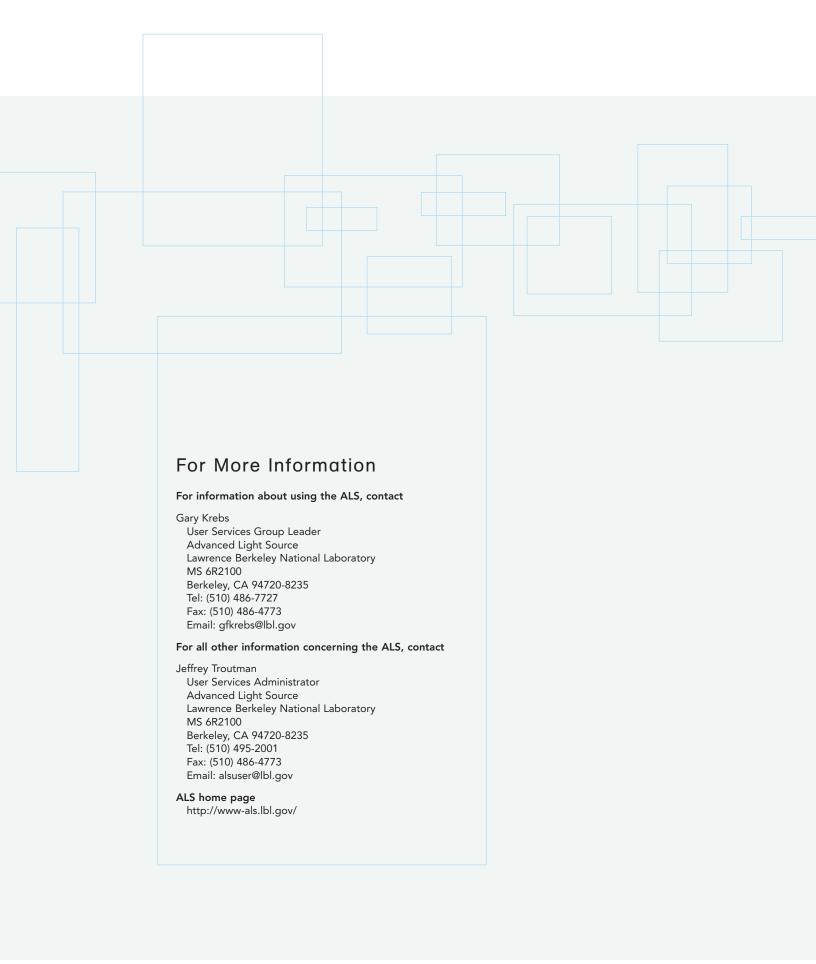
Zajonc, D.M., M.A. Elsliger, L. Teyton, and I.A. Wilson, "Crystal structure of CD1a in complex with a sulfatide self antigen at a resolution of 2.15 Å," *Nat. Immunol.* 4, 808 (2003).

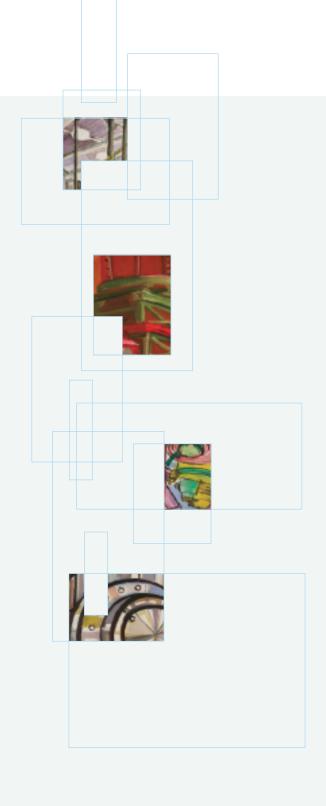
Zaziski, D.J., "Effects of the solid-solid transformation in nanocrystals," Ph.D. thesis, University of California, Berkeley (2003).

Zhang, T., X.-M. Qian, X.N. Tang, C.Y. Ng, Y. Chiu, D.J. Levandier, J.S. Miller, and R.A. Dressler, "A state-selected study of the H_2^+ (X, $v^+ = 0$ –17, $N^+ = 1$) + Ne proton transfer reaction using the pulsed-field ionization-photoelectron-secondary ion coincidence scheme," *J. Chem. Phys.* **119**, 10175 (2003).

Zhou, X.J., T. Yoshida, A. Lanzara, P.V. Bogdanov, S.A. Kellar, K.M. Shen, W.L. Yang, F. Ronning, T. Sasagawa, T. Kakeshita, T. Noda, H. Eisaki, S. Uchida, C.T. Lin, F. Zhou, J.W. Xiong, W.X. Ti, Z.X. Zhao, A. Fujimori, Z. Hussain, and Z.-X. Shen, "High-temperature superconductors: Universal nodal Fermi velocity," *Nature* 423, 398 (2003).

Zhu, X., A. Heine, F. Monnat, K.N. Houk, K.D. Janda, and I.A. Wilson, "Structural basis for antibody catalysis of a cationic cyclization reaction," *J. Mol. Biol.* **329**, 69 (2003).





Supported by the U.S. Department of Energy under Contract No. DE-AC03-76SF00098

